NASA TECHNICAL NOTE

NASA TN D-7690

NASA TN D-7690

PERFORMANCE OF FINNED THERMAL CAPACITORS

by William R. Humphries

George C. Marshall Space Flight Center
Marshall Space Flight Center, Ala. 35812

NATIONAL AERONAUTICS AND SPACE ADMINISTRATION • WASHINGTON, D. C. • JULY 1974

TECHNICAL REPORT STANDARD TITLE PAGE

1. REPORT NO.	2. GOVERNMENT ACCESSION NO.	3. RECIPIENT'S CATALOG NO.
NASA TN D-7690		

4. TITLE AND SUBTITLE	5. REPORT DATE
PERFORMANCE OF FINNED THERMAL CAPACITORS	July 1974
	6. PERFORMING ORGANIZATION CODE M-386
7. AUTHOR(S) William R. Humphries	8. PERFORMING ORGANIZATION REPORT #
9. PERFORMING ORGANIZATION NAME AND ADDRESS George C. Marshall Space Flight Center Marshall Space Flight Center, Alabama 35812	10. WORK UNIT NO. 11. CONTRACT OR GRANT NO.
12. SPONSORING AGENCY NAME AND ADDRESS National Aeronautics and Space Administration Washington, D. C. 20546	13. TYPE OF REPORT & PERIOD COVERED Technical Note 14. SPONSORING AGENCY CODE

15. SUPPLEMENTARY NOTES
Originally presented to the faculty of the graduate school of The University of Texas at Austin in partial fulfillment of the requirements for the Degree of Doctor of Philosophy.

16. ABSTRACT

The objective of this study was to investigate the performance of typical thermal capacitors, both in earth and orbital environments. Techniques which were used to make predictions of thermal behavior in a one-g earth environment are outlined. Orbital performance parameters are qualitatively discussed, and those effects expected to be important under zero-g conditions are outlined. A summary of thermal capacitor applications are documented, along with significant problem areas and current configurations. An experimental program was conducted to determine typical one-g performance, and the physical significance of these data is discussed in detail. Finally, numerical techniques were employed to allow comparison between analytical and experimental data.

17. KEY WORDS	18. DISTRIBUTION STATEMENT
	Cat. 03

19. SECURITY CLASSIF. (of this report)	20. SECURITY CLASSIF. (of this page)	21. NO. OF PAGES	22. PRICE
Unclassified	Unclassified	324	$7.25

For sale by National Technical Information Service, Springfield, Virginia 22151

TABLE OF CONTENTS

Chapter

LIST OF ILLUSTRATIONS

Figure

Page

LIST OF TABLES

DEFINITION OF SYMBOLS

Symbol	Definition
A	Area
A_{AP}	Apparent area
A_{BP}	Base plate area
A_b	Base plate surface area
A_t	Fin surface area
a	Arbitrary constant
Bo	Bond number = $\frac{\rho g L^2}{\sigma}$
b	Arbitrary constant
C	Carbon element
C_p	Specific heat at constant pressure
$\mathcal{L}$	Centerline
C_1	Arbitrary constant
C_2	Arbitrary constant
D	Diameter or cell spacing
d	Diameter
DCE	Drive Control Electronics
e	Energy per unit mass
g	Standard gravitational acceleration
Gr	Grashoff Number = $\frac{g\beta(T_w - T_\infty)\ L^3}{\nu^2}$
H	Hydrogen element

DEFINITION OF SYMBOLS (Continued)

Symbol	Definition
Ht	Height
h	Heat transfer coefficient
ΔH	Latent heat of fusion
ΔH_T	Latent heat of transition
i	Dummy index
j	Dummy index
K	Thermal conductivity
K_L	Liquid phase thermal conductivity
K_S	Solid phase thermal conductivity
Keff	Effective thermal conductivity
KW	Kilowatt
L	Length or characteristic dimension
LRV	Lunar Roving Vehicle
LCRU	Lunar Communications Relay Unit
m	Dummy index
M	Molecular weight
Ma	Marangoni Number = $\frac{\left(-\frac{d\sigma}{dT}\right)\left(\frac{dT}{dL}\right)L^2}{\rho\nu\alpha}$
n	Dummy index
Nu	Nusselt Number = $\frac{hL}{K}$
P	Pressure

DEFINITION OF SYMBOLS (Continued)

Symbol	Definition
Pr	Prandtl Number = $\frac{C_p \mu}{K}$
PCM	Phase Change Material
q	Heat flux per unit mass
Q	Heat flux
$\dot{Q}$	Heating flux rate
$\dot{Q}_{AP}$	Apparent heat flux rate
Ra	Rayleigh Number = Gr·Pr
RH	Horizontal resistor
RV	Vertical resistor
S	Phase front position
S_1	Bottom plate thickness
S_2	Fin thickness
S_3	Top plate thickness
s	Square node side dimension
SPU	Signal Processing Unit
T	Temperature
T_o	Initial temperature
T_w	Wall temperature
T_∞	Bulk fluid temperature
T_B	Base plate temperature

DEFINITION OF SYMBOLS (Continued)

Symbol	Definition
T_F	Fin temperature
T_{Fr}	Freeze temperature (also = T melt)
T_L	Liquid phase temperature
T_S	Solid phase temperature
T_T	Transition temperature
T_{CR}	Critical temperature
TC	Thermal capacitor
ΔT	Temperature difference
t	Time
Δt	Time difference
$\hat{U}$	Internal energy
V	Velocity
$\vec{V}$	Velocity vector
v	Volume
W	Width
Wt	Weight
Wt_c	Weight of container
Wt_{c+pf}	Weight of container plus paraffin
Wt_f	Weight of full container
w	Work per unit mass

DEFINITION OF SYMBOLS (Concluded)

Symbol	Definition
ρ	Density
μ	Absolute viscosity
ν	Viscosity
τ	Shear stress
θ_T	Total liquifaction period
θ_{EFF}	Effective temperature control period
α	Thermal diffusivity
α_S	Solid phase thermal diffusivity
α_L	Liquid phase thermal diffusivity
β	Coefficient of volumetric expansion
σ	Surface tension
σ_H	Hot liquid surface tension
σ_C	Cold liquid surface tension
σ_O	Initial surface tension

PERFORMANCE OF FINNED THERMAL CAPACITORS

By

William R. Humphries

SUMMARY

The objective of this study was to investigate the performance of typical thermal capacitors, both in earth and orbital environments. Techniques which were used to make predictions of thermal behavior in a one-g earth environment are outlined. Orbital performance parameters are qualitatively discussed, and those effects expected to be important under zero-g conditions are outlined. A summary of thermal capacitor applications are documented, along with significant problem areas and current configurations. An experimental program was conducted to determine typical one-g performance, and the physical significance of these data is discussed in detail. Finally, numerical techniques were employed to allow comparison between analytical and experimental data.

A transparent test specimen was built for the experimental study to allow visual observation of the phase change front. The test specimen

consisted of two compartments, a phase change material (PCM) housing and a finned fluid passage. The PCM housing contained aluminum fins, which partitioned the PCM compartment into 1.9-cm (3/4-in.), 1.27-cm (1/2-in.), and 0.635-cm (1/4-in.) cells. During all tests, nonadecane normal paraffin material was used as the PCM. By introducing Monsanto Coolanol-15 into the finned fluid passage, the PCM was either cooled or heated. Heating and cooling rates were varied by varying the coolanol inlet temperature from 1103.4 J/m^2-sec (350 BTU/ft^2-hr) to 204.9 J/m^2-sec (65 BTU/ft^2-hr), and from 567.5 J/m^2-sec (180 BTU/ft^2-hr) to 126.1 J/m^2-sec (40 BTU/ft^2-hr), respectively.

Instrumentation consisted of temperature sensors located in the paraffin, on the fins, in the fluid, and on the plate separating the PCM from the coolanol compartment. In addition, low speed 16-mm motion pictures were used to document freezing and melting rates.

Using an explicit forward finite differencing technique, analytical models of the 1.9-cm (3/4-in.) and 0.635-cm (1/4-in.) cells were developed. Experimental fin and plate temperatures were used as boundary values for analytical models and these models were used to generate PCM temperature profiles and interface positions.

The melt model, which utilized a Rayleigh number correlation to incorporate convection, satisfactorily predicted the melt front position.

However, a pure conduction model used to predict the freeze front position, lagged the expected positions. It was postulated that this discrepancy between the analytical model and the test data was due to the model using a planar interface rather than the actually observed irregular interface. The irregular interface was a result of numerous dendrites which formed at the liquid/solid boundary.

Zero-g investigations indicated that the most significant difference between one-g and zero-g thermal performance was the absence of buoyancy driven convection at zero-g. However, appreciable convection can be induced by surface tension forces. The ullage bubble, if present, could inhibit heat transfer at zero-g. However, this is very unlikely when paraffin is the PCM, due to its good wetting characteristics.

CHAPTER I

INTRODUCTION

Definition of a Thermal Capacitor

From an electrical analogy, any device which has the capacity to store quantities of thermal energy can be defined as a thermal capacitor (TC). However, for the purpose of this study, only a device that absorbs and rejects energy by using a material which undergoes a phase change will be considered a thermal capacitor. This definition is further restricted in this study to include only latent heat effects associated with the melting process and with solid-state structural changes of phase. Although these devices will be referred to as thermal capacitors, other names such as thermal flywheel, phase change device, and fusible mass device have been used to describe the same equipment concept.

Fundamentally there are three uses to which the TC has been applied: (A) Thermal damping of oscillatory outputs, (B) inhibiting thermal excusions, and (C) maintaining constant temperature. Thermal responses in these situations are illustrated in Figure 1.

Typically a TC is a passive device, having no moving parts, which is normally composed of three integral components: an external housing, an

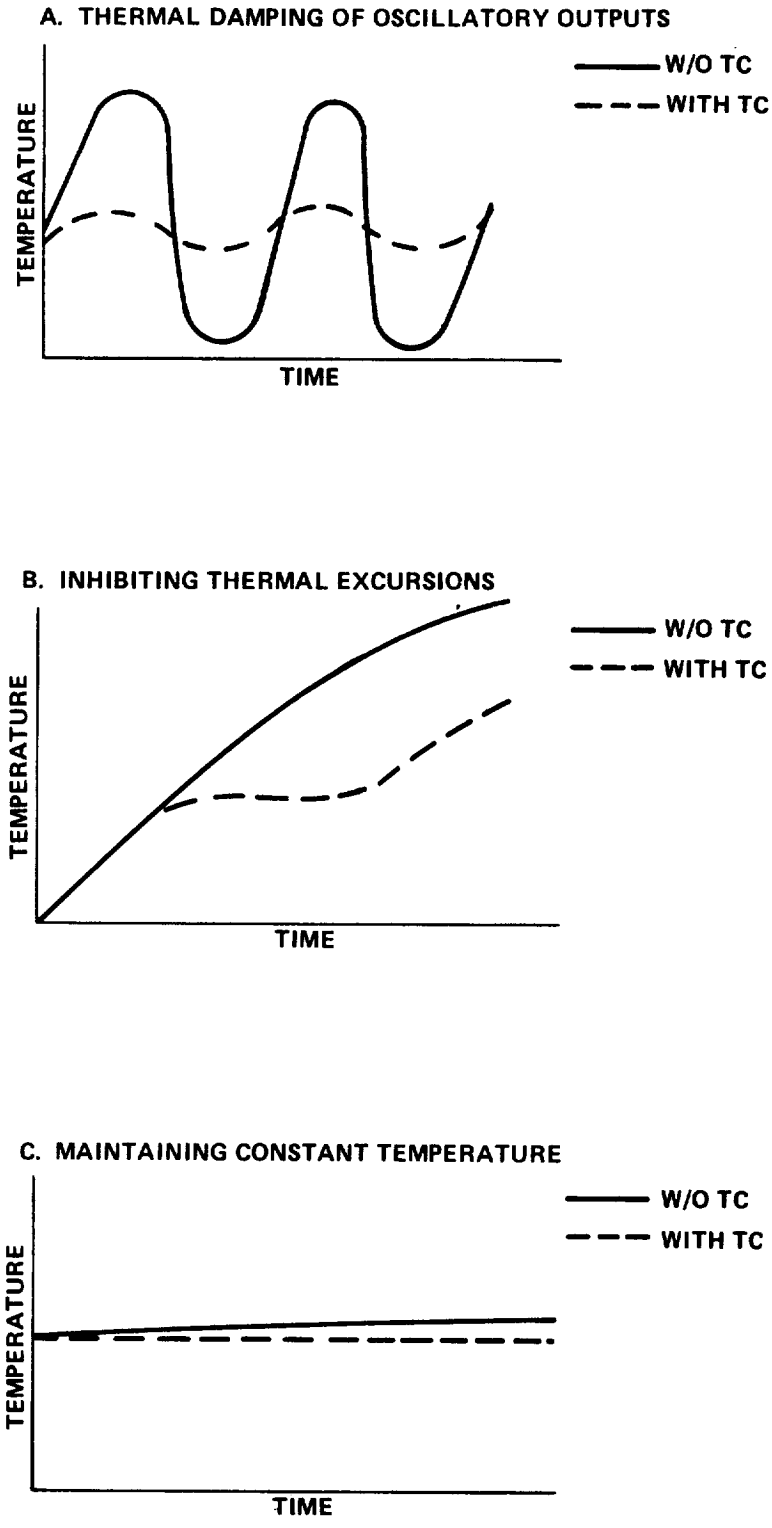

Figure 1. Responses of a Thermal Capacitor.

internally finned filler material, and the phase change material (PCM). The device being thermally controlled is excluded even though the capacitor may be an inseparable part of this device (Fig. 2). The PCM is a material which experiences transition or phase change in the regime of operating temperatures of the device (for the purpose of this study, only liquid/solid and solid/solid transitions were considered).

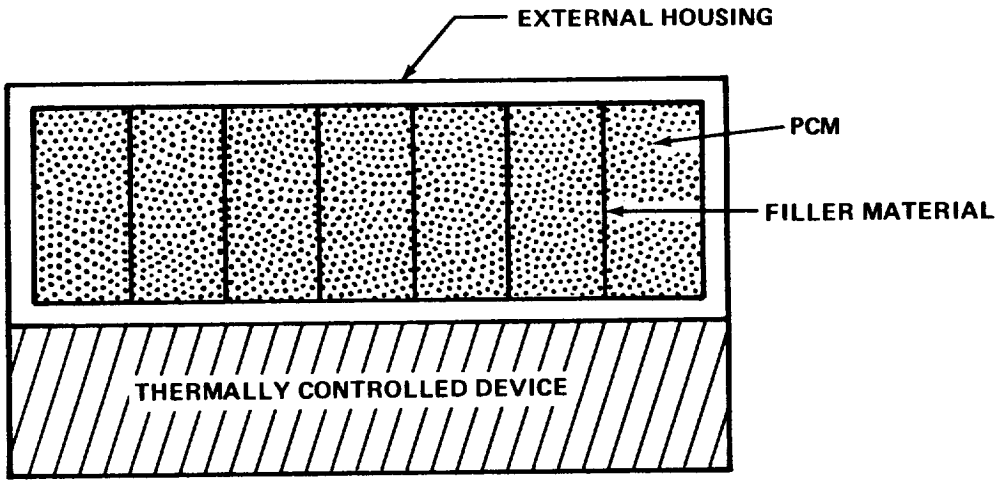

Figure 2. A thermal capacitor device.

Statement of Problem

Since the advent of manned space flight, aerospace designers have been looking for better methods of thermally controlling flight vehicle systems. In certain applications, thermal capacitors are emerging as strong competitors. The ability of thermal capacitors for either heating or cooling, or for storing thermal energy, indicates their thermal flexibility. The fact that they are passive makes them quite attractive, when compared to less reliable active

systems; such as, gas blowers, sublimators, and liquid pumped systems, to name a few. Furthermore for low and intermediate heat storage applications, the capacitor can represent a weight savings over other thermal control techniques. In addition to being an independent thermal control device, thermal capacitors can be used to supplement other devices such as, heat pipes and space radiators. Thermal capacitors have recently been used on an earth satellite, three moon vehicles, and Skylab. Possible future design applications include using capacitors on a manned space station and in future space shuttle flights.

Most designers have employed pure conduction models for design analyses, without considering convection during melting, the multidimensional effects, and the dendrite formations at the interface during freezing. As a result, significant discrepancies have existed in some cases between analytical models and one-g test data. When this occurs, the test data repeatedly indicate enhanced thermal performance, and the designer will normally use the more conservative analytical data as the design criteria. Unfortunately, this conservatism often leads to an overdesigned capacitor.

Study Approach

The objective of this work has been to investigate typical thermal capacitor performance in both earth and orbital environments. The motive was to gain insight into the processes involved in the thermal performance of a typical space vehicle phase change device. The study was directed toward accumulating experience which may assist future capacitor designers.

A survey of previous PCM studies and sources for both paraffinic and nonparaffinic materials property data has been included in this study. Techniques for estimating one-g performance are discussed, and quantitive comparison of these techniques, with possible zero-g influences, is presented. To provide additional insight into the different design techniques, a survey of past, current, and possible future applications is given. The significant problems encountered in these applications, with which the author is familiar, are outlined. In addition, physical desciptions of capacitors used in space vehicle applications are profiled.

An experimental program was conducted to study the phase change processes occurring in a typical capacitor. The test item was fabricated from transparent material to allow visual studies of the internal processes that were occurring within the PCM housing. Using thin aluminum fins, the internal PCM housing was divided into 0.635-cm (1/4-in.), 1.27-cm (1/2-in.) and 1.9-cm (3/4-in.) cells. Test data included thermocouple temperature gage outputs and motion picture film data. Temperature data of the fin and lower heat transfer surface were input into single-cell computer models to determine the phase change front position time history. The film data also was used to determine the phase change front position histories. The computed and film derived position histories were compared. Physical interpretations of film and temperature data are given and the validity of analytical models is discussed, along with possible reasons for model output discrepancies.

CHAPTER II

LITERATURE SURVEY

Introduction

The literature survey considered only those studies that related directly to the thermal design of a finned thermal capacitor. Special emphasis was placed on space vehicle applications. Information of interest pertaining to phase change materials is discussed, followed by a survey of applicable one-g and zero-g studies, and concluded with a brief description of previous experimental programs.

Analytical comments are abbreviated, as volumes of material are available pertaining to solutions of the freeze/melt problem. There was no intent in this research to cover the large body of literature relating to macroscopic and microscopic aspects of phase change. These are normally included in the materials disciplines (e.g., phase diagrams, nucleation, supercooling, superheating, etc.). For information concerning these areas, an excellent text by Chalmers [1] is available.

Phase Change Material

In general, PCMs may be catagorized into two groups: paraffinic and nonparaffinic. The paraffins are the most widely used PCM in current

aerospace applications, while the nonparaffins are being used in nonspace and future aerospace study applications. The nonparaffin group incorporate a large body of materials, including: water, hydrated salts, organics, acids, and synthetic mixtures.

Some researchers [2, 3, 4] have defined the qualities that a good PCM should exhibit, which are as follows:

1. high heat of fusion
2. proper melting point
3. high thermal diffusivity
4. high coefficient of thermal conductivity
5. non-corrosive
6. low coefficient of expansion and small volume change during phase and lattice changes
7. stable
8. high flash point
9. good wetting characteristics
10. low cost
11. minimum of void formations
12. relatively pure
13. non-toxic
14. readily available

Grodzka [2] screened a large field of nonparaffin candidate PCMs covering a range of freezing/melting points from 16.12°C (61°F) to 83.96°C (183°F). She designated a salt hydrate and three nonparaffin organics as prime PCM candidates.

Grodzka and Fan [5] also examined the limits of thermal stability and long term thermal cycling effects on certain nonparaffins considered suitable for use as PCMs. They found that long term thermal cycling can result in a buildup of impurities that may interfere with efficient operation of the PCM. They concluded that this also could cause eventual destruction of nucleation catalyst and result in stratification of impurities.

Designers have found normal paraffins to be a good PCM for space applications. Normal paraffins are hydrocarbons whose generalized chemical formula is given by C_nH_{2n+2}. A selected list of normal paraffins that are commercially available, along with their published freeze/melt points, are given in Table 1.

Paraffins with an even number of carbon atoms between 20 and 32, and those with any odd number of carbon atoms exhibit a lattice transition. The even numbered carbon atom paraffins exhibit this transition near their melting point, whereas odd numbered paraffins exhibit the transition in the solid state, as much as 16°C (30°F) below their freeze/melt temperature. Broadhurst [6] has shown that the energy associated with this transition is subtractive from the

TABLE 1. NORMAL PARAFFINS

Name	Chemical Formula	Freezing Point °F	Freezing Point °C
Undecane	$C_{11} H_{24}$	-14.1	-25.6
Dodecane	$C_{12} H_{26}$	14.7	-9.6
Tridecane	$C_{13} H_{28}$	22.3	-5.4
Tetradecane	$C_{14} H_{30}$	42.6	5.9
Pentadecane	$C_{15} H_{32}$	49.9	10.0
Hexadecane	$C_{16} H_{34}$	64.7	18.2
Heptadecane	$C_{17} H_{36}$	71.6	22.0
Octadecane	$C_{18} H_{38}$	82.8	28.2
Nonadecane	$C_{19} H_{40}$	89.4	32.1
Eicosane	$C_{20} H_{42}$	98.2	36.8
Heneicosane	$C_{21} H_{44}$	104.9	40.5
Docosane	$C_{22} H_{46}$	111.9	44.4
Tricosane	$C_{23} H_{48}$	117.7	47.6
Tetracosane	$C_{24} H_{50}$	123.6	50.9
Pentacosane	$C_{25} H_{52}$	128.7	53.2
Hexacosane	$C_{26} H_{54}$	133.5	56.4
Heptacosane	$C_{27} H_{56}$	138.2	59.0
Octacosane	$C_{28} H_{58}$	142.5	61.4
Nonacosane	$C_{29} H_{60}$	146.7	63.8
Triacontane	$C_{30} H_{62}$	150.4	65.8

normal energy absorbed or liberated due to phase change. Paraffins exhibiting this phenomena have latent heats of fusion that are 10 to 20 percent below the latent heats exhibited by their carbon atom neighbors (Fig. 3). Shlosinger and Bentilla [7] have noted that the freeze/melt point of normal paraffins increases with the number of carbon atoms (Fig. 4).

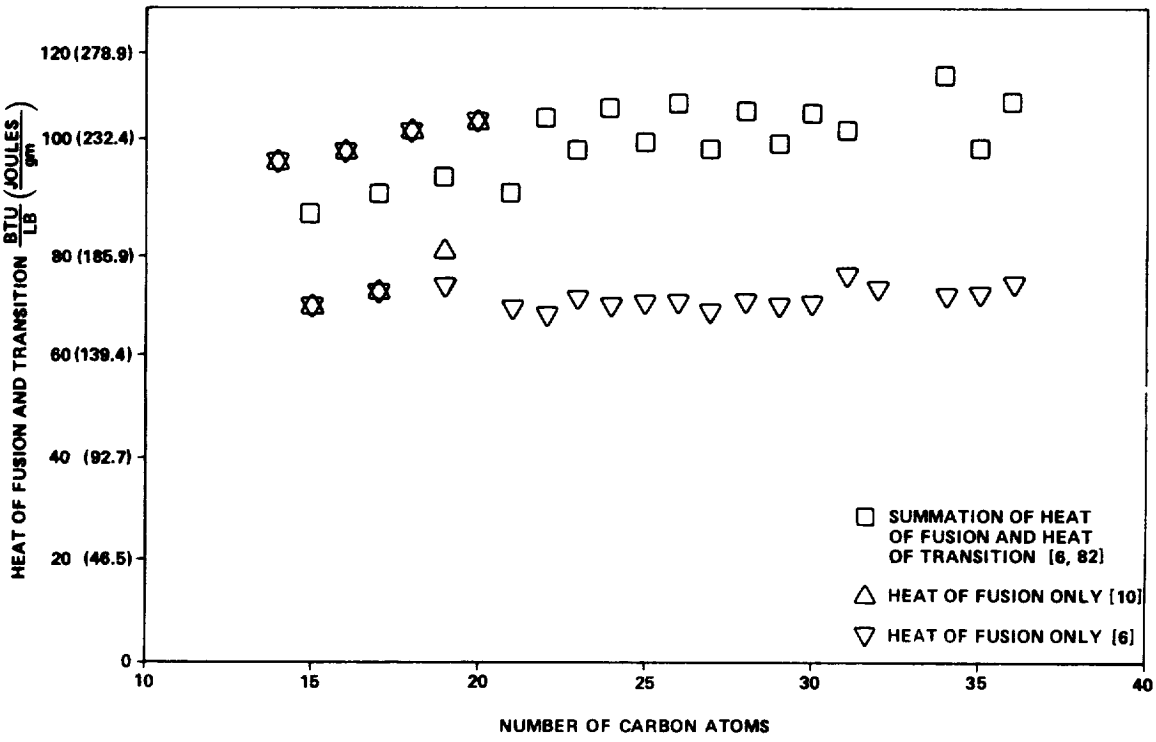

Figure 3. Energy associated with solid-liquid phase change and solid-solid transition of even-numbered and odd-numbered paraffins.

Designers have considered mixing paraffins to achieve a freezing point which is different from that of a pure material. In such cases, the question arises as to the resulting mixture's freezing point, latent heat of fusion, and other properties. Bentilla, et al., [8] constructed a two constituent phase

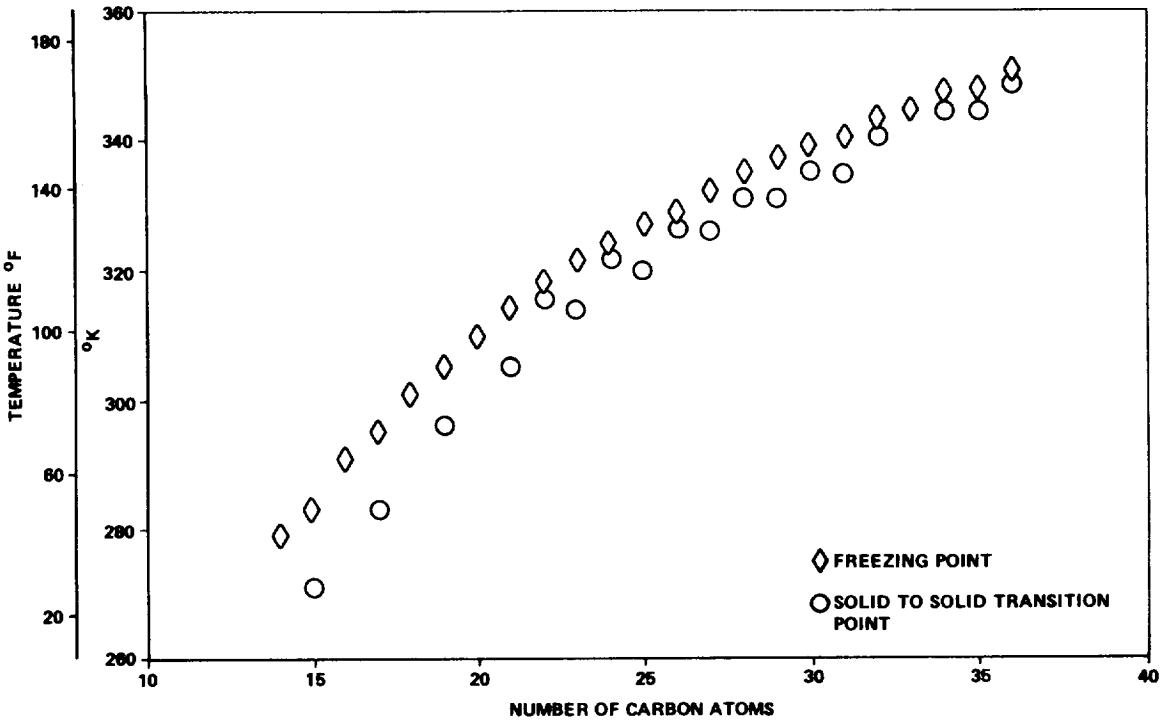

Figure 4. Temperature associated with solid-liquid phase change and solid-solid transition of even-numbered and odd-numbered paraffins.

diagram (Fig. 5) for octacosane/eicosane mixtures. These data indicate an undisturbed mixture will melt/freeze over a range of temperatures. Furthermore, additional data from this source, using the same constituents, shows that there is some selective freezing at the individual phase change temperatures of the components (Fig. 6, 7, 8). Nagel[1] and Shelpuk[2] independently produced similar results with dodecane/tridecane and eicosane/docosane mixtures,

---

[1]Nagel, R.: Unpublished Data. McDonnell Douglas Company, St. Louis, Mo. 1972.

[2]Shelpuk, B.: Thermal Design of the Lunar Communications Relay Unit. Unpublished RCA Presentation, 1971.

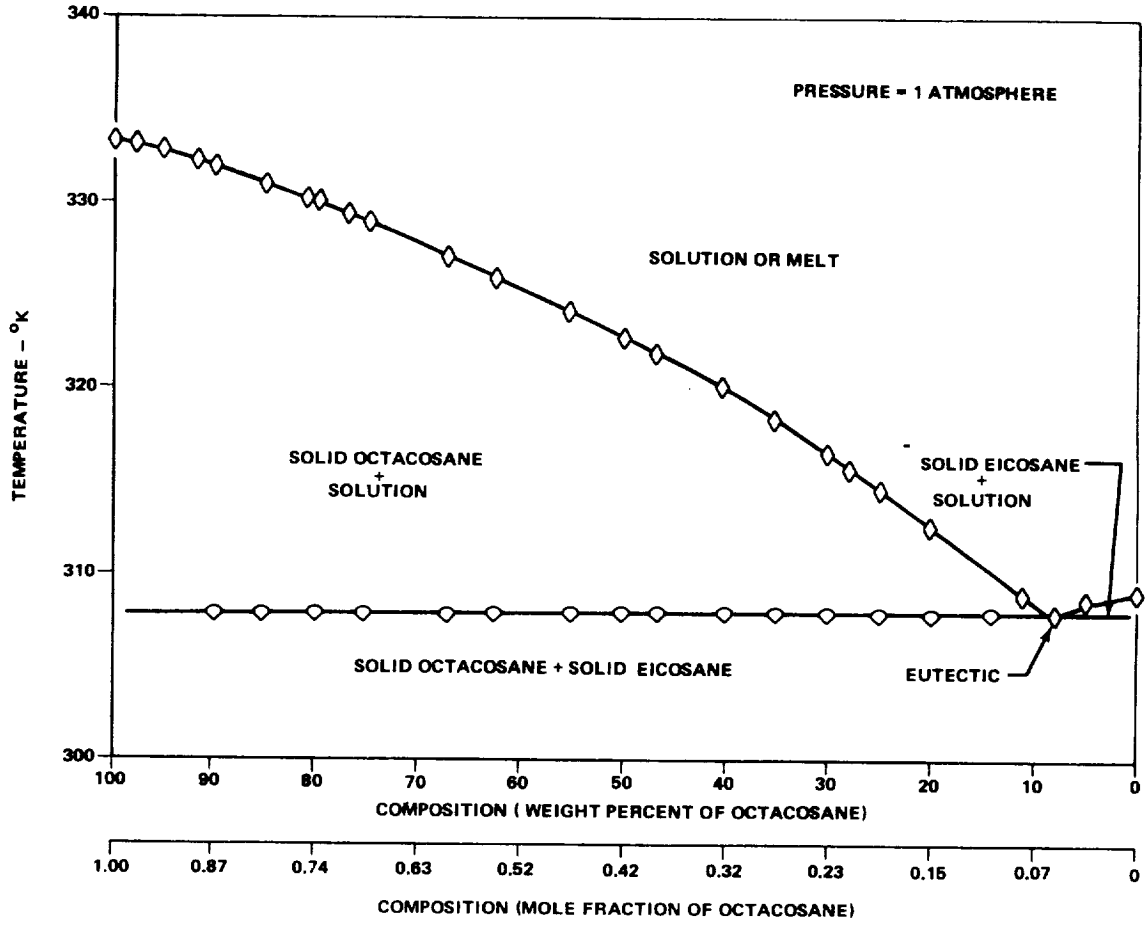

Figure 5. Temperature-composition phase diagram for the octacosane-eicosane binary system.

respectively. However, Prenger [9] has shown that a discrete phase change temperature proportional to the mass ratio of the constituents can be achieved by constant mixing of the liquid phase for a tridecane/tetradecane mixture (Fig. 9). Shelpuk has observed that on mixing eicosane and docosane (Fig. 10), both of which have latent heat of fusions of approximately 244 J/gm (105 BTU/lb), the heat of fusion of the mixture was reduced as low as 139 J/gm (60 BTU/lb). The uncertainty of a mixture melt/freeze point, added to the

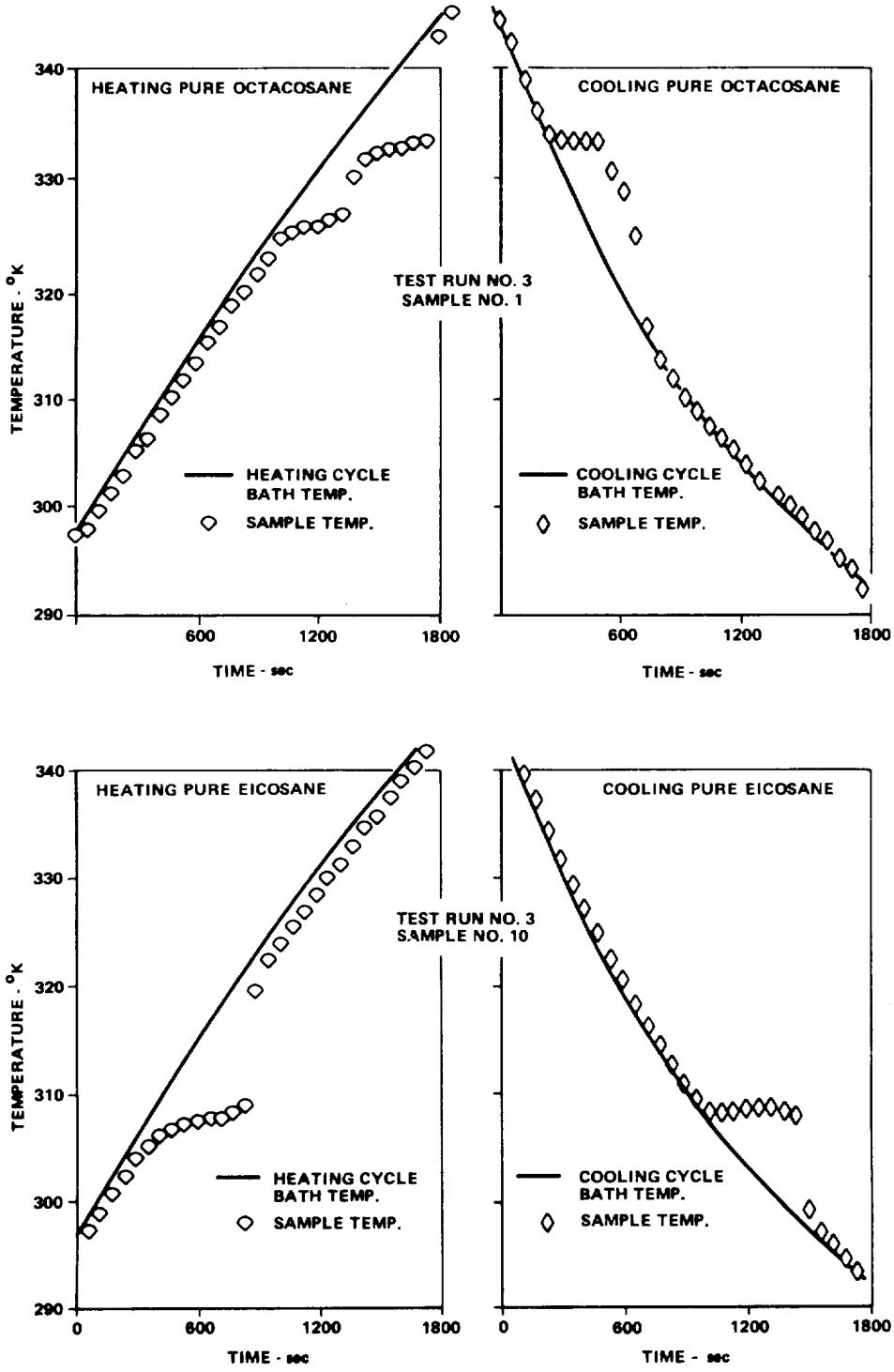

Figure 6. Heating-cooling curves for pure eicosane.

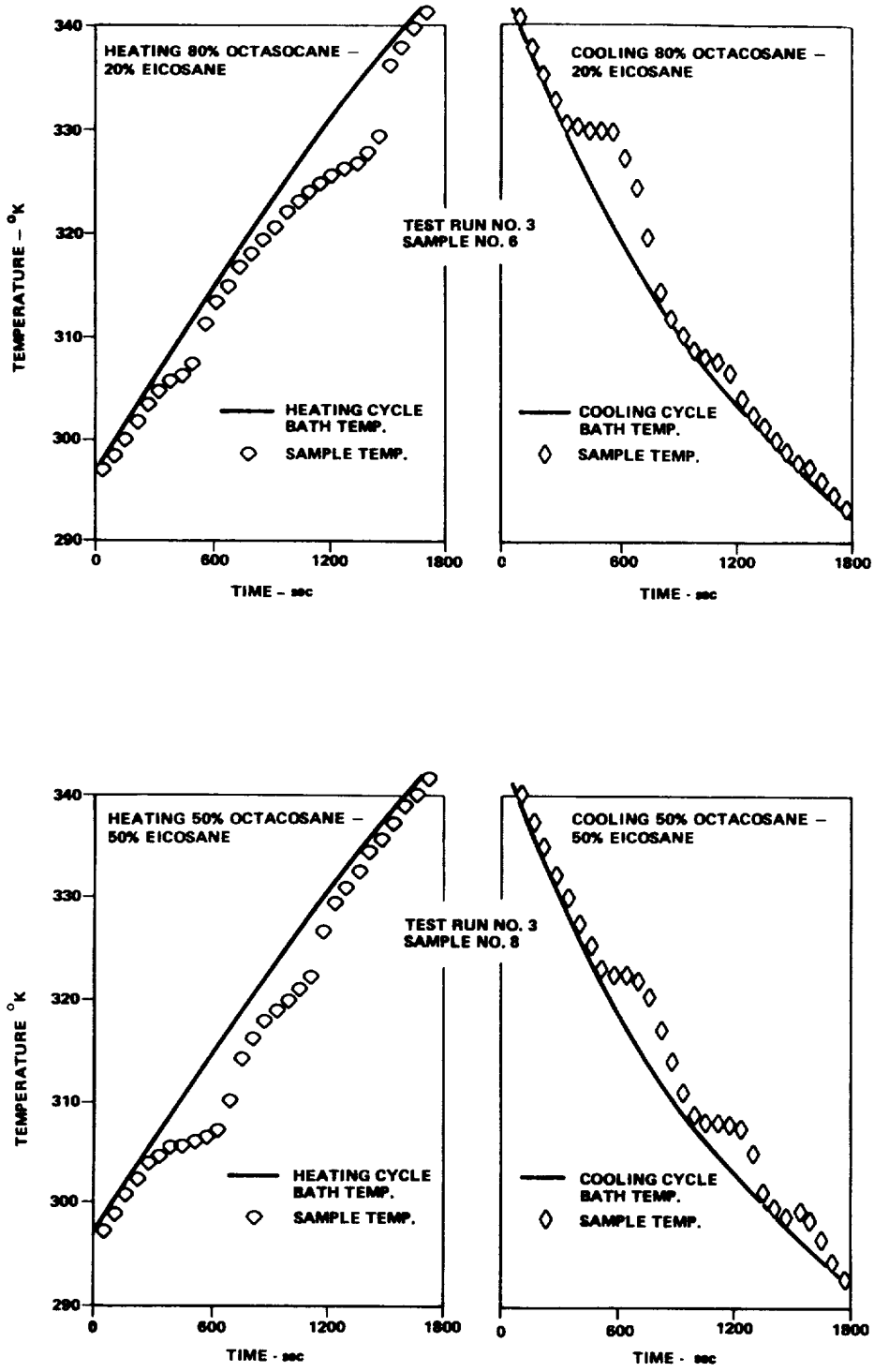

Figure 7. Heating-cooling curves for (80%-50%) octacosane - (20%-50%) eicosane binary system.

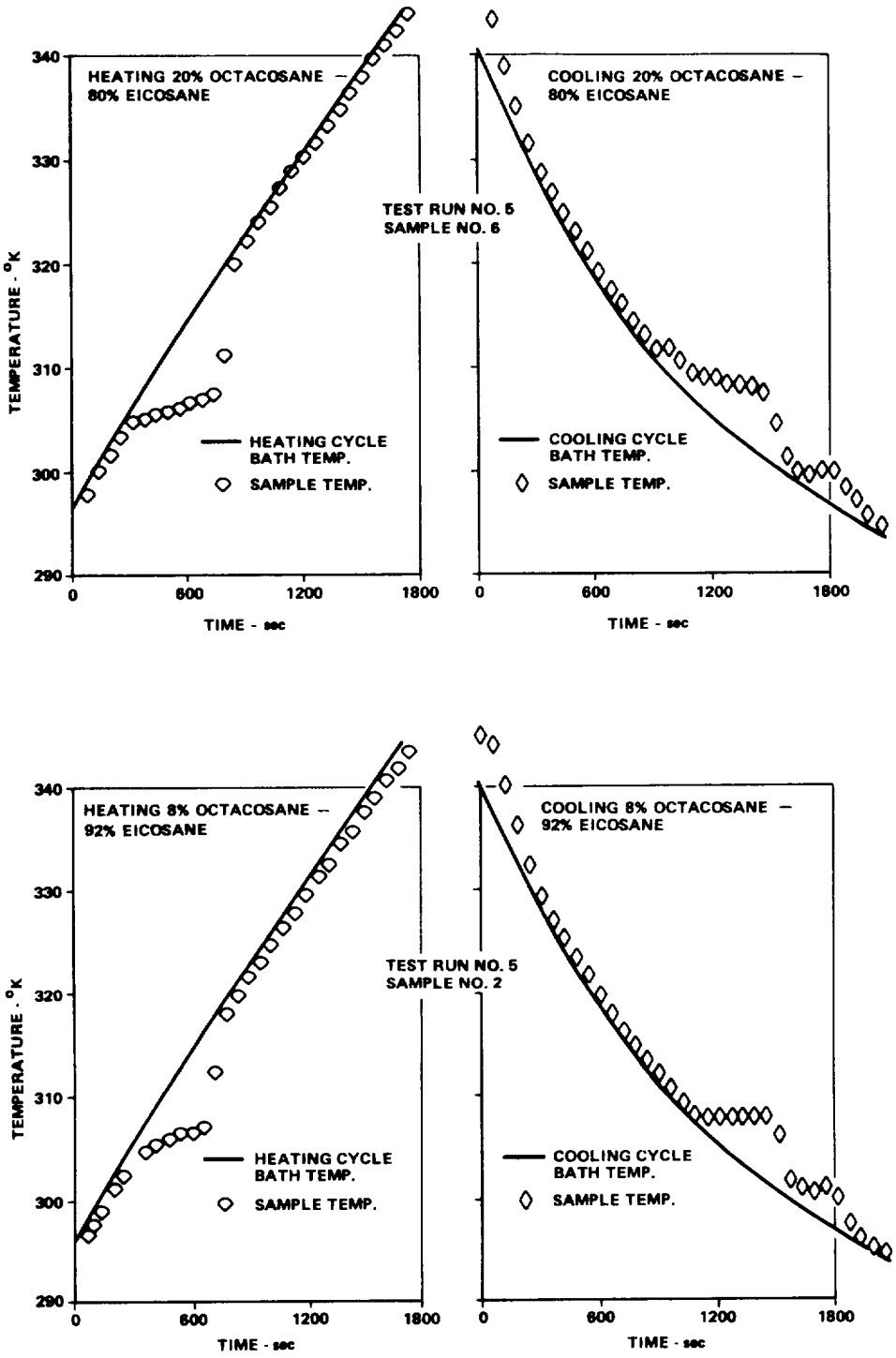

Figure 8. Heating-cooling curves for (20% -8%) octacosane - (80% -92%) eicosane binary system.

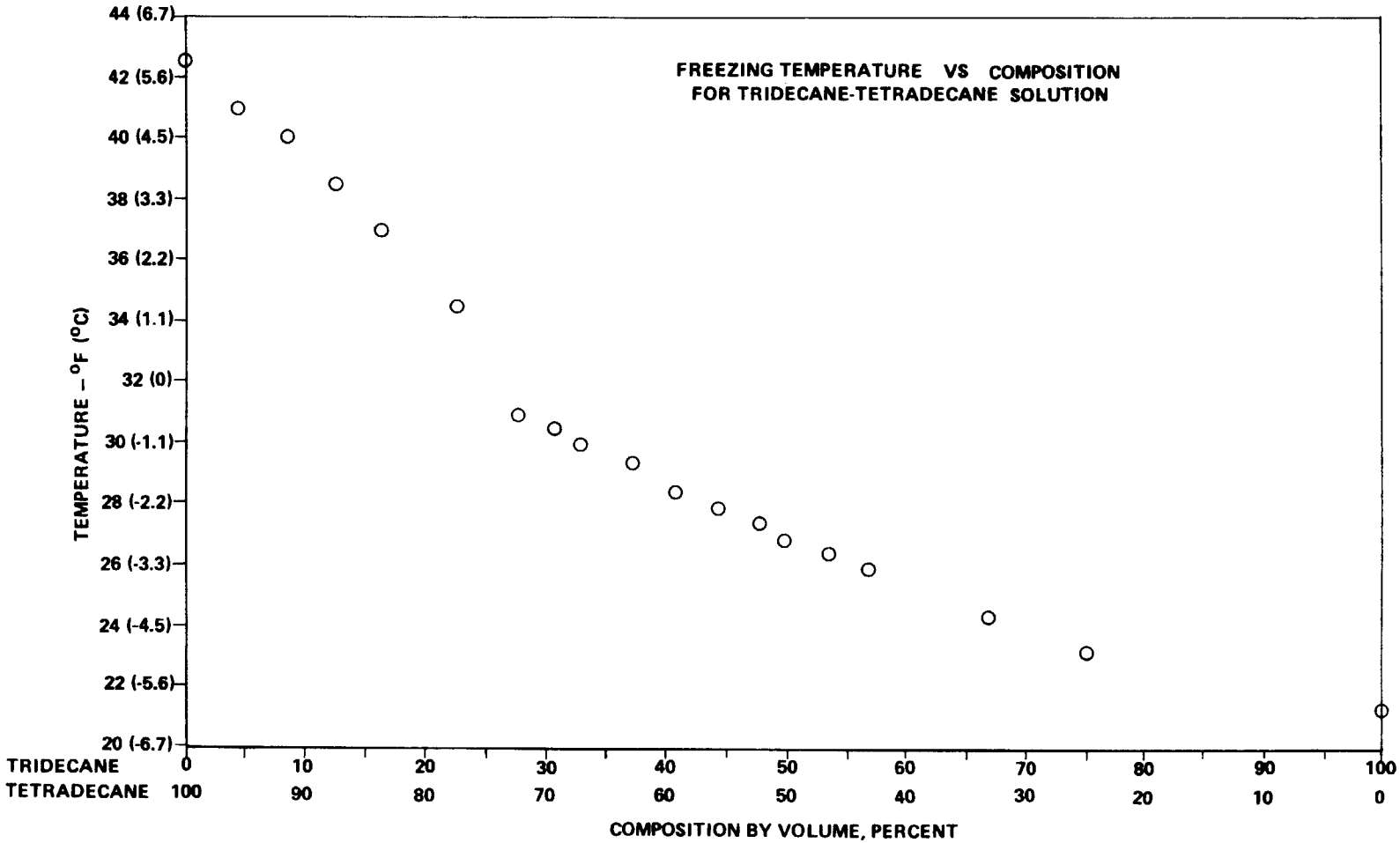

Figure 9. Freezing temperature versus composition for tridecane-tetradecane solution.

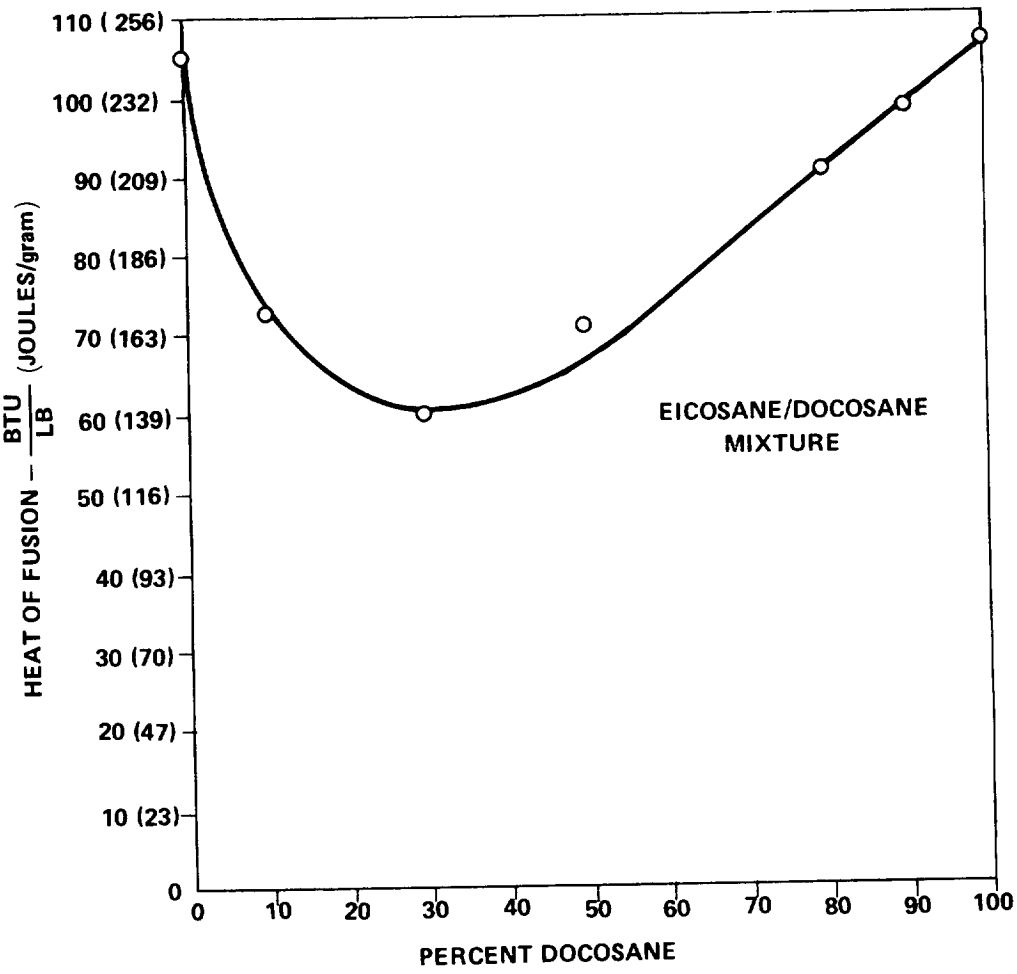

Figure 10. Heat of fusion for eicosane/docosane mixture.

reported degradation in the latent heat of fusion, couple to make paraffin mixtures unattractive from a heat transfer viewpoint. However, other considrations discussed in Chapter 3 may override thermal considerations.

Property data for PCMs can be found in various texts, most ostensibly in references 10, 11, and 12. Hale, Hoover and O'Neil [13] have tabulated some selected property values, as well as cost and compatibility information

for a group of paraffin and nonparaffin materials. The Boeing Company[3] has tabulated some thermal properties (excluding the thermal conductivity values) of paraffins for a range of temperatures. A more comprehensive property tabulation was compiled by the Phillips Petroleum Company [14]. However, certain property values do not agree with those quoted in earlier references [7, 11]. This disagreement in property value was not surprising in light of recent findings [15] which indicate that paraffin properties can vary significantly, depending on the production techniques, the levels of impurity, and the pre-treatment. It must be noted that a single paraffin may be commercially available in a number of purity levels, which are not specified in most property data. Commonly, technical grade paraffin (> 95 percent pure) is used because of its lower cost. However, more expensive laboratory grade paraffins (> 99 percent pure) are available. These higher purity paraffins offer a more predictable freezing point, as well as higher latent heat of fusions than technical grade.

The most comprehensive literature search and property measurement survey to date is given in reference 7. Unfortunately, this study considered only paraffins with freeze/melt points between 5.6°C (42°F) and 65.6°C (150°F). A comprehensive tabulation of paraffin properties excerpted from numerous documents is given in Appendix A.

[3]The Boeing Company, unpublished internal memorandum.

One-g Performance

For estimating the one-g performance of a closed cell phase change system, a determination of the relative importance of the three basic modes of heat transfer occurring internal to the capacitor must be made. Radiation for most applications at normal temperatures is negligible, leaving only conduction and convection as possible transfer modes.

Causes for convective motion in one-g could be due to:

1. buoyancy forces
2. surface tension forces
3. volume change forces
4. external forces
5. other less common effects, such as electric fields, atomic radiation, chemical reactions, etc.

Neglecting the affects of the last two, only buoyancy, surface tension, and volume change remain.

In early studies of buoyancy driven convection, Lord Rayleigh [16] relates the non-dimensional Nusselt number (Nu) to the Grashoff (Gr), Prandtl (Pr) number product. The significance and definition of these non-dimensional quantities are given by Knudsen and Katz [17] as

$$\text{Nu} = \text{dimensionless temperature ratio} = \frac{hL}{K} \qquad (1)$$

$$Gr = \frac{\text{(Bouyancy forces) (inertia forces)}}{\text{(Viscous forces)}^2} = \frac{gL\beta\ (Tw - T\infty)\ L^3}{\nu^2} \qquad (2)$$

$$Pr = \frac{\text{Molecular diffusivity of momentum}}{\text{Molecular diffusivity of heat}} = \frac{C_p \mu}{K} \qquad (3)$$

Later, the product of the Grashoff and Prandtl number became known as the Rayleigh Number (Ra).

Numerous experimenters have conducted studies that were related to hydrodynamic instability caused by buoyancy as it effects the heat transfer process, including the studies cited in references 18 through 29. Silveston and O'Toole [30] verified the Nusselt number versus Rayleigh Number correlation for a fluid confined between two parallel plates (Fig. 11). A number of authors, including Catton and Edwards [31] later showed the effect of L/D ratios for closed cells (Fig. 12), where L is the cell height and D represents the fin cell spacings.

The critical Rayleigh Number is defined as the value at which convection begins. In the region below the critical value, the heat transfer is substantially by conduction only, Nu $\cong$ 1. The critical value, which depends on the boundary conditions, is 1708 for a fluid confined between two infinite horizontal, isothermal, conducting walls; and 720 for a non-conducting walled container [29]. As shown in a bounded cell (Fig. 12a), this critical value tends to increase as the cell sides approach one another (i.e., as L/D increases), and also tends to increase as the walls become more conducting (Fig. 12b).

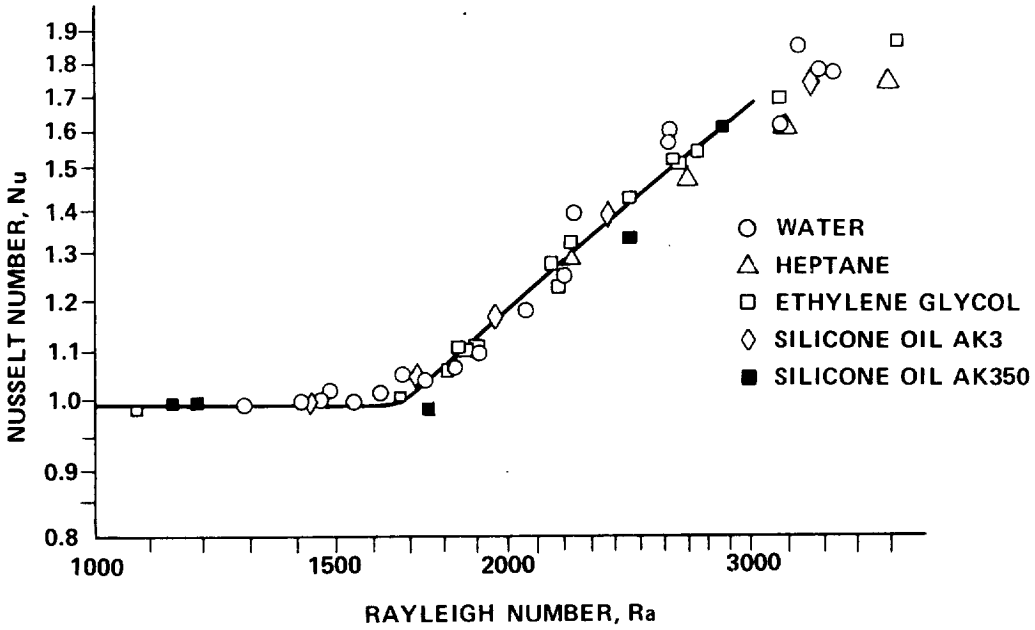

Figure 11. Silveston's experimental results in the neighborhood of instability in various liquids.

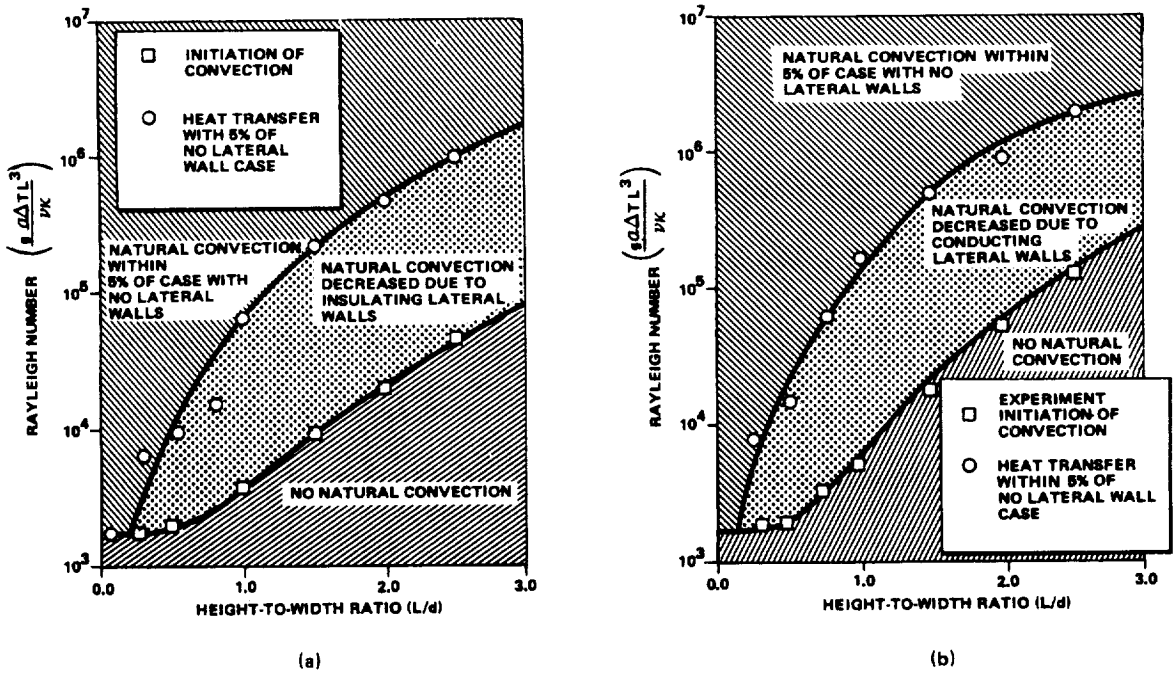

Figure 12. Region of influence of L/D on heat transfer.

Although scientists have been aware of surface tension driven convection for some time, quantitative studies of this phenomena are scarce. The flow patterns created in Bénard's classic experiment [32], which produced cellular circulation patterns in a very shallow liquid was initially attributed to buoyancy effects. However, Block [33], Pearson [34], Scriven [35], and Sternling [36], later proved that this phenomena was due to surface tension driven convection. The initial discovery of this phenomena is attributed to Marangoni [37], and the commonly used term "Marangoni Flow" was coined to name this phenomena.

The nature of the Marangoni flow, as discussed by Young, Goldstein and Block [38], is that temperature variations across a free gas/liquid interface changes the shear forces of the surface. This is due to the dependency of surface tension on temperature, which is estimated by Gambrill [39] to be linear:

$$\sigma = \sigma_o + bT \quad . \tag{4}$$

The coefficient "b" is negative, so that an increase in temperature at the surface is accompanied by a subsequent decrease in the surface tension. Hershey [40] has shown qualitatively that a depression in the surface at a local hot spot results, causing the liquid to flow away from the hot zone and toward the cold zone (Fig. 13). Subsequently, McGrew and Larkin [41] have photographed this effect for a number of configurations, producing dramatic verification of the phenomena.

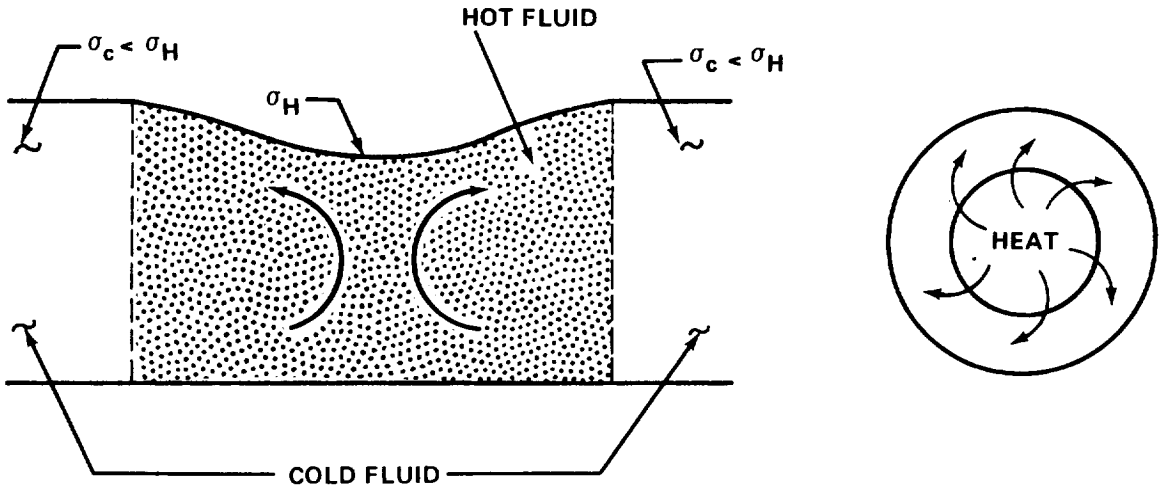

Figure 13. Surface tension convection patterns.

The level of surface tension driven convection is correlated by using the Marangoni number, Ma, which is given by:

$$\text{Ma} = \frac{\text{Surface tension forces}}{\text{Viscous forces}}$$

$$= \frac{\frac{-d\sigma}{dT}\,\frac{dT}{dy}\,L^2}{\rho\nu\alpha} \tag{5}$$

The critical Marangoni number for a fluid fixed between a rigid and free surface is given as 80.

Nields [42] has stated that the onset of convection in one-g might be better determined by correlating the Nusselt number to a normalized parameter, R, given by

$$R = \frac{Ra}{Ra_{cr}} + \frac{Ma}{Ma_{cr}} \tag{6}$$

This assumes that buoyancy and Marangoni driven convection are additive. However, Grodzka [43] noted that experimental data on buoyancy and Marangoni surface effects indicate that an additive theory does not follow. Regardless, the convective currents caused by Marangoni flow in one-g are usually small compared to those caused by buoyancy. Pearson [34] has shown that for most fluids at normal temperatures, a liquid thickness of one cm or less must be attained before Marangoni effects overshadow buoyancy effects.

For systems with small characteristic dimensions, the non-dimensional Bond number, Bo, is given by:

$$Bo = \frac{\text{gravity forces}}{\text{Surface tension forces}} = \frac{\rho g L^2}{\sigma} \qquad (7)$$

Appendix B outlines a typical calculation using nonadecane. This number is sometimes used to qualitatively evaluate the relative importances of Marangoni effects as compared to buoyancy effects. From equation (7), it follows that a low Bond number indicates a high degree of surface tension effects.

Although surface tension effects exist at all unlike interfaces, only the liquid/gas interface (as opposed to liquid/liquid and liquid/solid interfaces) is expected to produce appreciable resulting flows. However, no proof of this conjecture was noted in the literature surveyed.

Volume change driven convection can be caused by the phase change process. During freezing, the new layer of frozen material at the interface tends to contract, since the solid density is usually greater than the liquid

density. Consequently, the liquid near the front will flow toward the interface to fill the volume shrinkage caused by solidification. During melting, the liquid at the interface tends to flow away to allow for the volume created by melting. Tien and Koump [44] have stated that this effect will cause both the freezing and melting processes to be retarded. This is due to the ingress of warm fluid during freezing and the egress of warm fluid during melting (Fig. 14). However, if circulation is created in the melting processes, warm fluid could be drawn into the interface thereby augmenting the melting process.

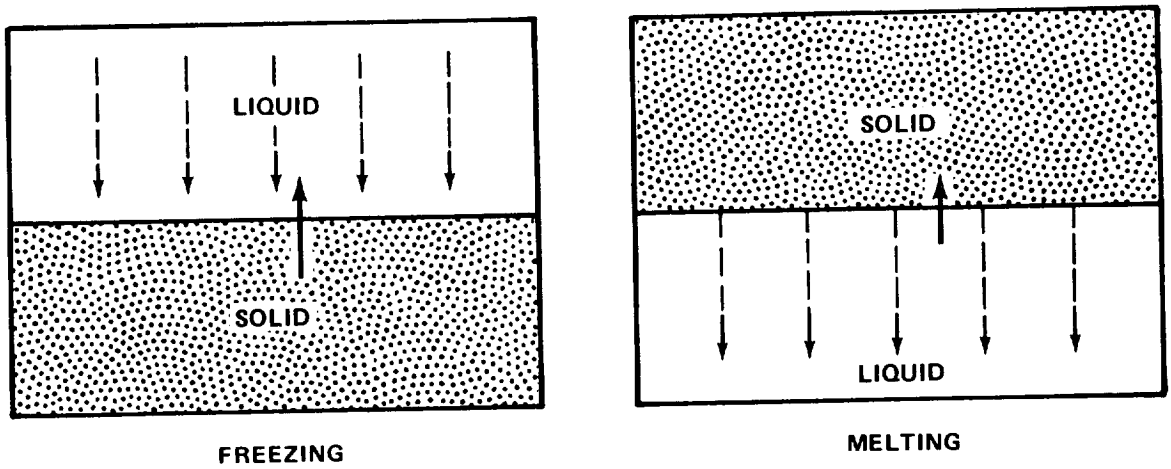

Figure 14. Volume change driven flow patterns.

Reference 44 has also shown in a computational exercise for a fictitious system where the solid density is 25 percent greater than the liquid density, that only a 10 percent reduction in the freezing rate occurs due to volume change effects. Since paraffins experience only a 5 to 10 percent volume increase on melting, it can be inferred that an even smaller effect can be expected in paraffins for similar conditions.

In summary, the only modes of heat transfer that are involved in a typical one-g static phase change process are conduction and convection. Convection is caused only by buoyancy driven currents for reasonable container sizes. Surface tension effects are negligible, except for very thin films, and volume change effects may be ignored.

Zero Gravity

When comparing environs of near earth orbital space with that of the earth, several differences are noted in the heat transfer process. In earth orbit, the reduced gravitational force is nearly balanced by the centripetal orbital force, creating an effective zero-g environment. Effects caused by reduced pressure, radiation field, meteoroid bombardment, and three-dimensional spacecraft maneuvers are also possible.

Restricting the hypothetical capacitor under consideration to be a hermetically sealed container that is isolated from exterior thermal effects by insulation and anti-penetration shields and to be aboard a non-maneuvering vehicle, then reduced gravity remains as the only important alien effect.

The primary effect of reduced gravity on the heat transfer mechanism is in the lessening or elimination of buoyancy convection. Typical measurements of the net gravitational acceleration force on a spacecraft indicates values of the order of 1×10^{-7} g. Using nonadecane paraffin properties, a typical Rayleigh number at zero-g is:

$$Ra = 0.01\ L^3\ \Delta T \tag{8}$$

Details of this calculation are given in Appendix B. From this, it is apparent that for reasonable container sizes (i.e., less than 15-cm (6-in.) cell depths), the temperature difference across the liquidus portion of the cell must be $\geqq$ 444°C (830°F) to produce buoyancy driven convection. As this temperature range is well in excess of normal operating values, buoyancy stimulated convection may be considered negligible.

At one-g, Marangoni flow driven convection is normally unimportant, however, at zero-g this is not necessarily true. As discussed earlier, liquid flow caused by surface tension at a liquid/vapor interface may occur.

A group of recent experiments, carried out during the mission of NASA's Apollo-14, revealed that the surface tension driven phenomena in zero-g is a reality and can produce significant convection [45, 46]. Using data from these experiments, Grodzka [46] has plotted the relation existing between the Marangoni number and the ratio of effective thermal conductivity to actual conductivity (Fig. 15). These data show a rapid increase in the convective level at a Marangoni number slightly greater than 300. The temperature difference in the Krytox test liquid was only 2.5°C (4.1°F) in this instance.

Close examination of this data stimulates some questions. Applying these data to nonedecane paraffin contained in a cell with a 15.24-cm (6-in.) characteristic dimension at a Marangoni number of 300, a K_{eff}/K of 12 is predicted in Figure 15. This is a very high convective level. The temperature difference across a parallel plate system required to reach this level is only

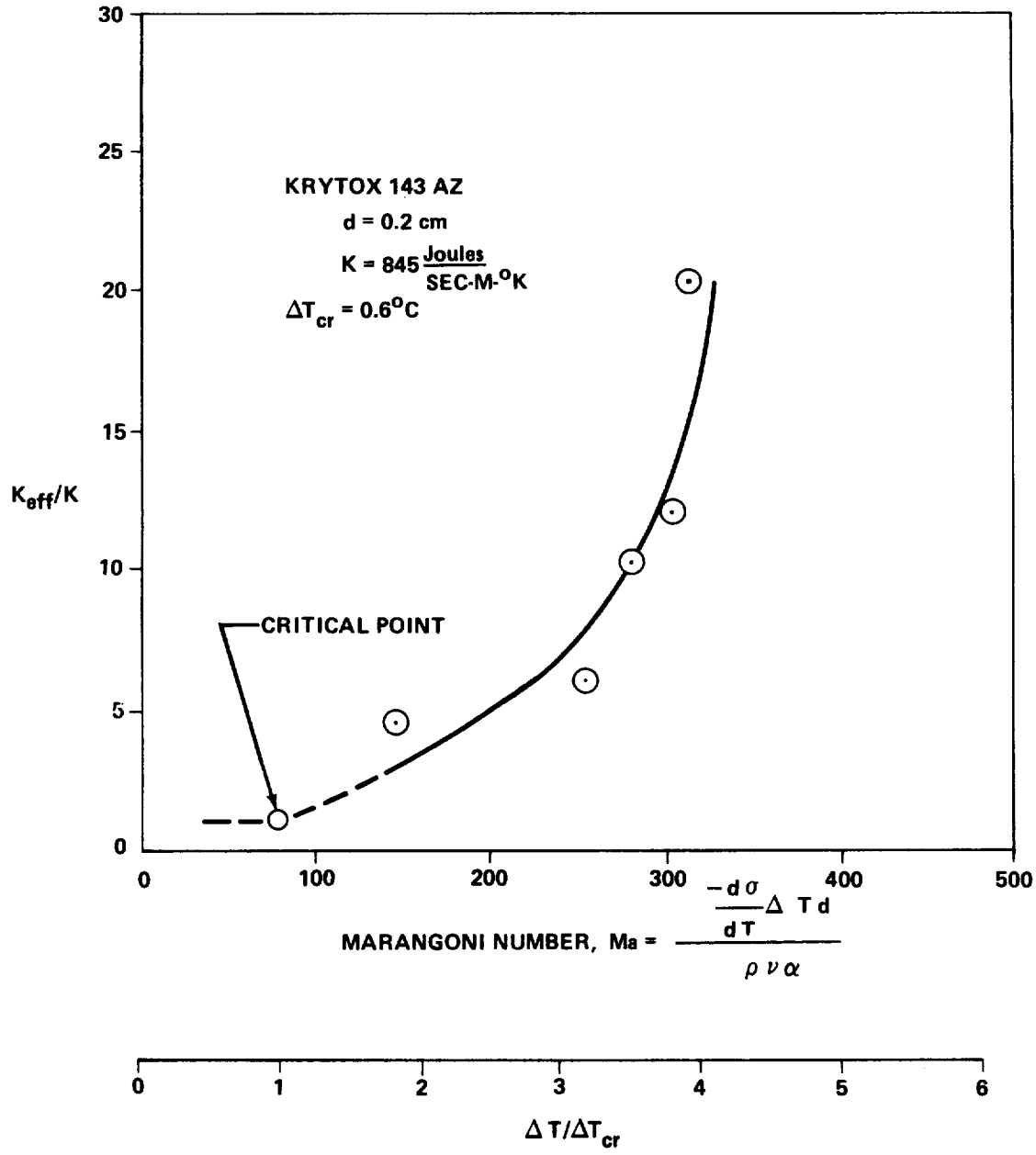

Figure 15. Heat transfer characteristics of Bénard cells.

0.0011°C (0.002°F). However, for this same system a Rayleigh number of 4.32×10^5 is predicted at one-g. From this, a K_{eff}/K of only 2.5 is indicated, which is a convective level well below that predicted by the tentative surface

tension data. This conflicts with earlier investigators, who reported that for this condition at one-g, Marangoni driven convection is unimportant. However, this could be explained, at least partially, by the fact that the Apollo-14 data is taken for a free surface, whereas the Figure 11 correlations were taken for top and bottom bounded cells.

Using nonadecane paraffin properties at the phase change temperature, the Marangoni number is given in Appendix B as

$$Ma = 2374\ \Delta TL \qquad (9)$$

This indicates that for reasonably sized capacitor cells, a temperature difference of only 0.003°K (0.006°F) is necessary for the onset of Marangoni driven convection in a paraffin filled capacitor at zero-g. This fact indicates that Marangoni convection can be appreciable at zero-g.

Since the magnitude of volume change effects discussed earlier were low for freezing (where buoyancy driven convection is negligible) as well as melting, it may be implied that the volumetric effects are negligible for pure conduction as well as convective processes. Consequently, the volumetric effects on the heat transfer process are negligible for zero-g operation. Heat transfer modes available to a thermal capacitor at zero-g are then reduced to Marangoni driven convection and pure conduction.

A secondary effect of reduced gravity which can significantly alter the heat transfer process is the ullage gas position. In a typical rectangular cell

containing ullage volume, the ullage gas may configure itself in any of a number of possible modes. A number of possible cell ullage locations are given by Reference 16, those of more importance are shown in Figure 16. When heating/cooling from the bottom, only configurations d and e (Fig. 16) would alter the normal process; however, when heating/cooling from the top or sides, configurations a, b, d, and e would all reduce the rate of heat transfer due to the insulating effect of the ullage gas. Small bubbles occurring in the liquid could induce convective currents. In a zero-g field, this motion could be caused by the Marangoni flow phenomena causing the bubbles to migrate toward warm zones. Also bubbles could be entrapped in the freezing solid (configuration d of Figure 16) decreasing the apparent thermal conductivity of the PCM. Fortunately, paraffins have the property of being good surface wetters, which in zero-g tends to force the ullage to form in the center of the cell (configuration c of Figure 16). However, insufficient quantitative data are available on these phenomena to determine affect on the heat transfer process under given conditions.

Grodzka [2] has examined effects of the space environment on the microscopic processes. She concluded that complex coupling effects between phase change kinetics and various possible modes of convective motion cannot be predicted accurately without actual flight data. She also concluded that the magnitude of magnetic and electric fields likely to be encountered in the earth's orbit are not expected to alter phase change behavior significantly from that observed on the earth. Finally, she stated that radiation fields encountered

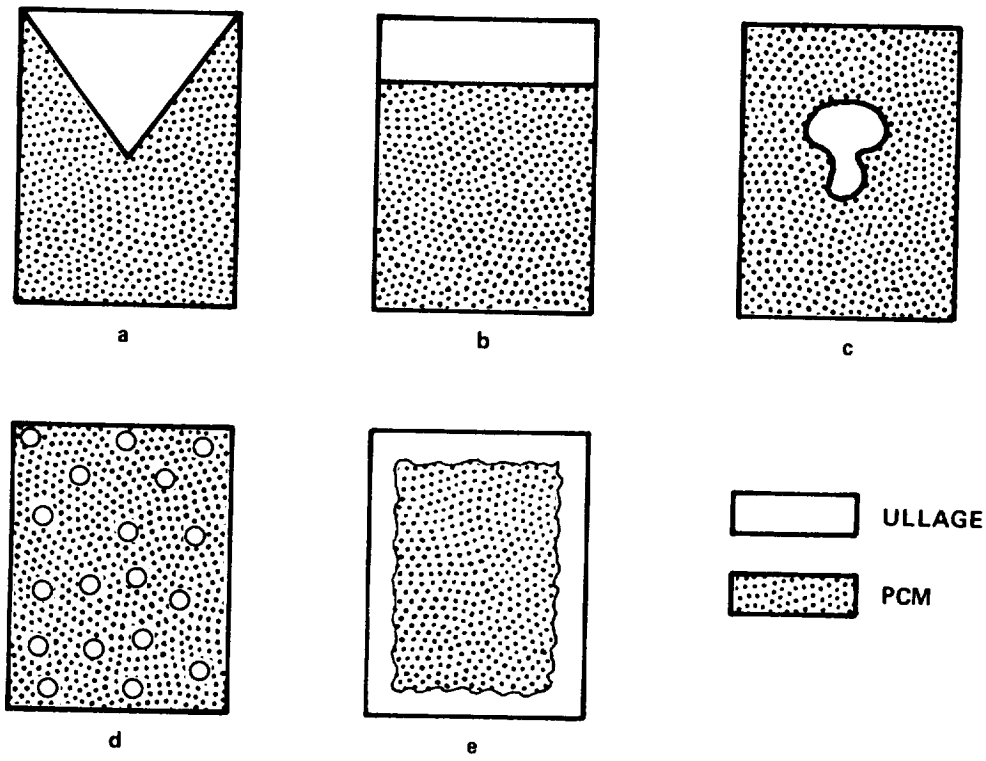

Figure 16. Zero-g ullage configurations.

in earth orbit are expected to have little effect, except perhaps in the case of organic PCM where long time exposures will result in buildup of impurity. Although the later statement applies to paraffin, no definitive information on this effect could be found in the literature surveyed.

Although insufficient reduced gravity data are available to corroborate these findings, some observations have been made as to the mechanisms of heat transfer in a thermal capacitor. When a free surface is present and thermal conditions are proper, Marangoni convection may be present. Insufficient data are currently available to determine quantatively the influence

of this phenomena. In the absence of surface tension effects, conduction is the sole process governing heat transfer. However, the conduction process may be altered by the ullage gas location. Furthermore, secondary effects of property degradation due to radiation may occur if the PCM is organic.

Experimental Investigations

The publications on experimental studies of thermal capacitors are limited. Altman, et al., [47], Fixler [3, 48], Bannister [4], and Kaye, et al., [50] experimented with various capacitor designs, proving the feasibility of the capacitor thermal control approach. The most comprehensive experimental data published were by E. Bentilla, K. Sterrett and L. Karre [8]. Using four different paraffins, they tested a variety of packaging techniques including aluminum wool, aluminum foam, copper foam and aluminum honeycomb. They concluded that the temperature rise of the paraffin container during melting was due to the insulating effects of the liquid paraffin. They also noted that the experimental data indicated a higher thermal conductivity than that specified for the property data. Freeze data indicated that the conduction model which they used to attempt to match test data, repeatedly yielded lower freeze rates. Data from melting tests, showing maximum coldplate temperature rises above the melting point temperature versus time for varying heating rates in an aluminum honeycomb system, are shown in Figure 17.

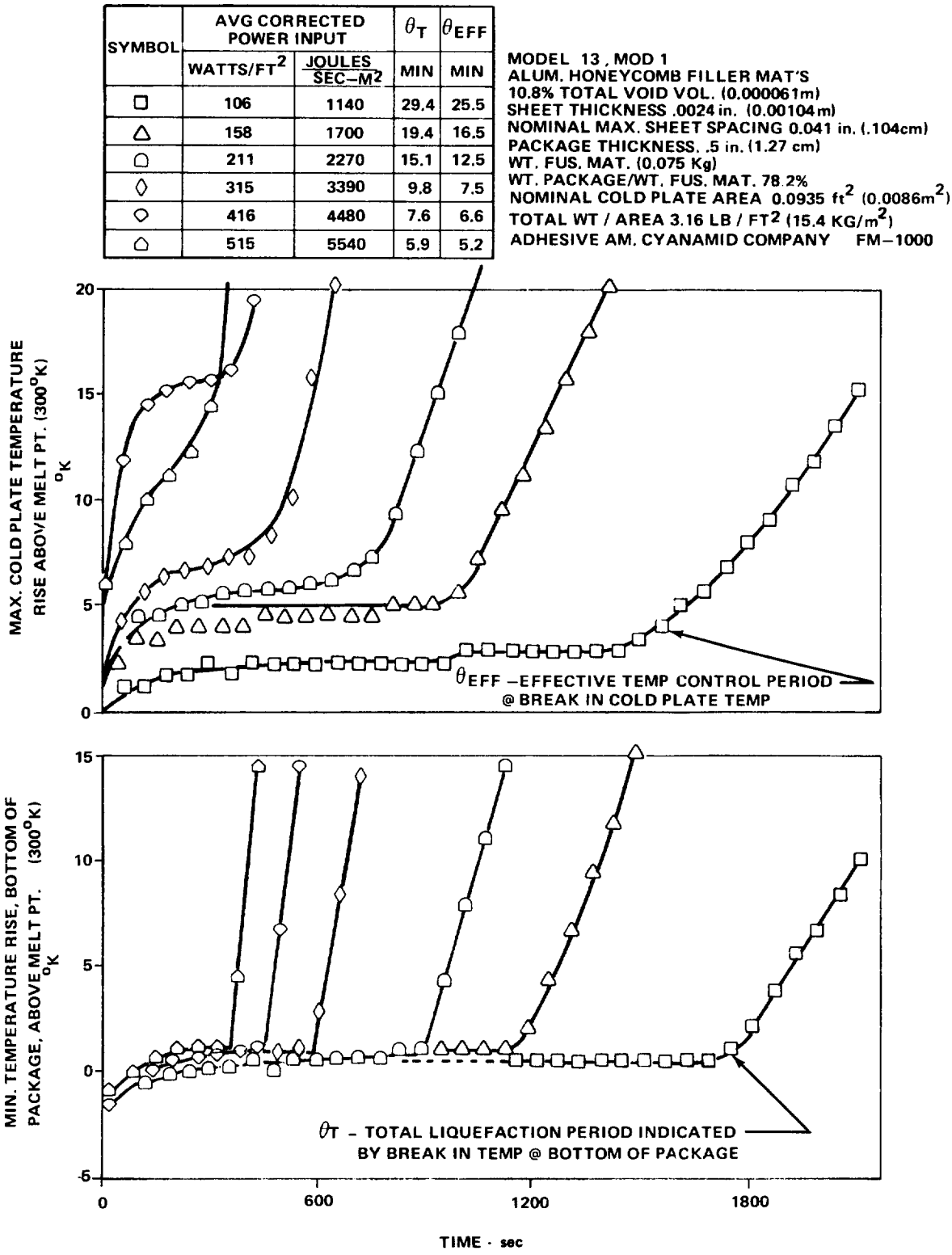

Figure 17. Adiabatic experiment test results.

Various investigators have produced microscopic photographs of the freezing interface in paraffins [51, 52, 53]. Magnification photography (175 power) by Bannister and Richard [52] shows the freeze front is composed of a multitude of dendrites of varying geometry (Figure 18). All paraffin freeze data surveyed contained references to dendrite formations. Dendrite arms appear much like cilia or fine fur to the naked eye, and they tend to grow in the direction of heat transfer. Westwater and Thomas [53], have shown that the physical shape of these dendrites are at least partially dependent on the rate of freezing. Other dependencies were not well defined, with little information available which would allow correlation of dendrite geometry to cooling rates.

Figure 18-A. Freeze front dendrite formations.

Figure 18-B. Freeze front dendrite formations.

CHAPTER 3

APPLICATIONS

Summary of Applications

The thermal capacitor design concept has a multitude of possible applications for both commercial and aerospace systems. A number of actual applications (along with problems encountered during design), as well as possible applications currently under study are discussed.

A list of these applications are given below:

A. Commercial

1. Actual

   a. children's kool aid freezer

   b. portable freezer chest

   c. thaw warning indicator

2. Possible

   a. thermal insulation for homes

   b. air conditioner supplement

   c. large solar thermal energy collector

   d. laser heat pulse absorber

   e. hospital food cart heat storage supplement

B. Military/Aerospace

1. Actual

   a. Titan transtage suction line temperature control

   b. Pegasus III temperature reference

   c. Lunar roving vehicle electronics temperature control

   d. Skylab coolant loop augmentation

   e. Skylab waste refrigeration

   f. Poseidon gimbal shipping container

2. Possible

   a. space shuttle wing leading edge temperature control

   b. space station space radiator augmentation

   c. astronaut suit cooling

   d. extra planetary probe thermal control

   e. Air Force satellite

   f. F-4 aircraft

   g. short term thermal control of army shelters

Commercial Applications

The commercial applications include a plastic container surrounded with a hollow annulus which contains a PCM. Placing the container in the freezer compartment of the refrigerator cools the PCM so that a water suspended beverage, such as kool aid, may be frozen in a slurry much like the corner store

"Koolee" or "Icee". A freezer chest is available which has a PCM liner that may be removed and refrigerator cooled, to be later used to store drinks and perishable items for long trips.

The mushroom industry commonly freeze their product for shipment. Thawing causes permanent quality degradation. As a result, a thaw warning indicator has been developed using a phase change device. A salt PCM is attached in a bag to the side of mushroom containers. The frozen salt contains a chemical additive which causes litmus paper, visible to container handlers, to change color if the PCM melts [53].

Telkes [55, 56, 57] has, for many years, conducted research on applications of PCMs to residential dwellings to minimize thermal oscillations on their heating/cooling systems. Brine and other salt solutions have been typically used in this research. Also under study are applications of PCMs to large solar collection systems, with surface dimensions upward to 10 square miles. Rapid energy conversion inherent in laser systems are prime targets for a thermal capacitor type application. Hospital carts required to store warm food for extended periods may be fitted with PCMs.

Aerospace Applications

The most widespread use of thermal capacitor techniques has been in the aerospace field. One of the earliest applications in this field was used on the Titan water jacket, applied around the engine attitude control system oxidizer

lines to limit temperature excusions below 32° F. An Eicosane PCM was used on the Pegasus III flight [58] to act as a constant temperature reference junction for a surface coating experiment.

Recently, moon flights of Apollo 15, 16, and 17 have transported thermal capacitor devices, which were mounted on various heat producing electronic components (Fig. 19) in the Lunar Roving Vehicle (LRV). The wheel drive control electronics (DCE) and the navigational signal processing unit [SPU], designed by Elliott and Paoletti [59], used paraffin filled capacitors for cooling. These two devices had sufficient masses to allow energy storage from their respective components during LRV sorties, so that component temperature excursions were kept below allowable levels. Even more unusual than the thermal capacitor applications was the thermal strap technique of transferring heat from the capacitor to a set of second-surface mirror radiators. After each sortie, the LRV was parked so that these mirror radiators were in the shade. A thermostatically controlled shutter was then opened, automatically closing after the two capacitors were refrozen.

The most significant problem reported in development of these capacitors was due to paraffin property variations. The dispersion in property data was so great that after being received, the paraffins were subjected to repeated degassings under reduced pressure to stabilize properties.

Shelpuk, designer of the LRV lunar communications relay unit (LCRU) capacitor, also noted paraffin property dispersion. He found that synthetically

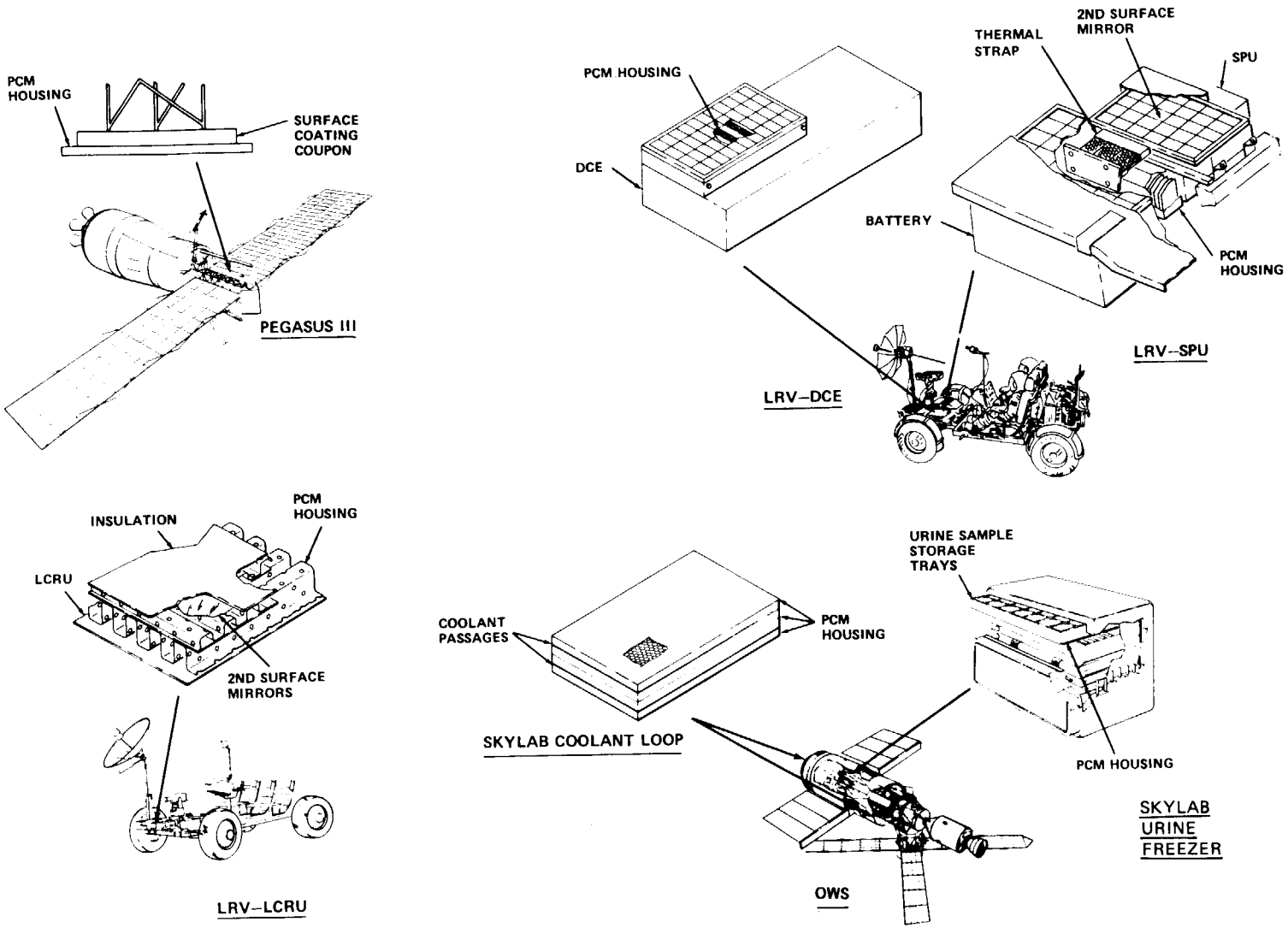

Figure 19. Space vehicle capacitor configurations.

produced paraffins had better property stability than naturally produced paraffins. He used a mixture of two paraffins in the LCRU. This allowed softening of the solid paraffin at temperatures below melting, thereby minimizing stress buildups in the capacitor cells.

One interesting aspect common to all LRV capacitors was that all were completely filled at temperatures above their maximum operating values, leaving no ullage. This technique assumes gas does not leak into the paraffin container after cooldown. This technique inherently relies on the quality of workmanship, since significant gas in-leakage could cause a large pressure buildup during subsequent heating. A strong argument for this technique is the fact that flight data telemetered back from the moon indicated that all LRV capacitors functioned properly.

There were fifteen thermal capacitors used on the first manned earth orbiting space station, Skylab. A total of five of these were located in two cooling systems, thermally controlling liquid temperatures. Two of these five capacitors were located on the primary Skylab space radiator fluid outlet, while the other three were located at the outlet of a smaller radiator used to refrigerate food and biological waste samples. Ten other capacitors were mounted in the bottom of trays used to store human waste samples while they are being transported from the Skylab Vehicle to earth.

The most significant problem encountered during development of these capacitors was the large structural stresses which occurred in the paraffin

housing during rapid melting. In the initial design, even though ullage volume was provided, stresses were sufficient to cause local buckling of the housing. This overstress conditioning was caused by the inability of the paraffin material to expand into the ullage volume. This occurred only when the capacitor was oriented in such a manner that the ullage volume migrated to a position away from the melting cells. As a result, the non-sealed corrugated fin-cell arrangement initially used was replaced with a honeycomb fin-cell arrangement. The honeycomb cells could be hermetically sealed on top and bottom, restricting ullage migration within the small honeycomb cell regardless of orientation.

This particular design by the McDonnell-Douglas Company incorporated a 20 percent ullage allowance in each cell. Although this eliminated the dependency on workmanship required in LRV capacitors, the large gas volume could interfere with the heat transfer. Additionally, this design required a heavier walled housing than was required by an evacuated concept.

A tabulation of the NASA Space Vehicle Applications is given in Table 2, itemizing the subsystem controlled and the capacitor functions. Pictorials of NASA space vehicle capacitor systems with their associated attachment arrangements are shown in Figure 19. Table 3 itemizes interesting design features of these capacitors.

The capacitor concept was used also for temperature control of the Poseidon engine gimbals during shipment. This device used a mixture of organic acids, consisting primarily of Palmitic and Stearic acids, to control the gimbals at temperatures below 55°C (131°F).

TABLE 2. NASA SPACE VEHICLE CAPACITOR APPLICATIONS

Vehicle	Subsystem Controlled	Function
Pegasus III	Surface coating contamination experiment	To provide a constant temperature reference for a thermocouple
Apollo 15 Apollo 16 Apollo 17	1) Lunar roving vehicle drive control electronics	To provide regenerable heat absorbing source
	2) Lunar roving vehicle signal processing unit electronics	To increase thermal capacitance available to signal process unit
	3) Lunar roving vehicle Lunar communications relay unit	To provide regenerable heat absorbing source
Skylab	1) Airlock coolant system	To augment space radiator performance and limit inlet temperature to downstream heat exchangers
	2) Refrigeration coolant system	Enhance space radiator performance to limit cold inlet temperature to downstream components
	3) Urine freezer	To provide temporary cooling for urine sample when being transported between Skylab and earth

TABLE 3. SPACE VEHICLE CAPACITOR DESIGN FEATURES

			Pegasus III	LRV Drive Control	LRV Signal Processing Unit	LRV Comm. Relay Unit (3 each)	Skylab Airlock (2 each)	Skylab Refrigeration (3 each)	Skylab Urine Freeze Tray
Approximate Overall Capacitor Dimensions	Length	cm	4.1 dia.	34.0	6.6		50.8	50.8	46.2
		in.	1.6 dia.	13.4	2.6		20	20	18.2
	Width	cm	-	16.5	8.9		35.6	35.6	25.4
		in.	-	6.5	3.5		14	14	10
	Height	cm	2.5	4.3	9.1		13.2	3.2	7.9
		in.	1.0	1.7	3.6		5.2	1.25	3.1
Paraffin	Type		Eicosane	Octadecane	Eicosane	Eicosane (10%) Docosane (90%)	Tridecane	Undecane	Dodecane
	Melt Temp.	°C	36.7	27.8	36.7	36.7 44.4	-5.6	-25.6	-9.6
		°F	98	82	98	98 112	22.3	-14	14.7
Total Capacitor mass/ Paraffin mass	kg/kg			2.8/1.4	1.6/0.8		16.3/9.1	8.2/4.5	2.9/1.0
	lb/lb			6.2/3.1	3.5/1.8		36/20	18/10	6.5/2.2
FIN Characteristics	Type		N/A	Rectangular	Rectangular	Rectangular	Honeycomb	Honeycomb	Corrugated
	Thickness	cm	N/A	0.13	0.13	0.015	0.015	0.015	0.015
		in.	N/A	0.05	0.05	0.006	0.006	0.006	0.006
	Spacing	cm	N/A	1.27	1.27	1.27	0.32	0.32	0.32
		in.	N/A	0.50	0.50	0.50	0.125	0.125	0.125
	Height	cm	N/A	3.81	9.14	1.27	3.20	3.20	1.90
		in.	N/A	1.5	3.6	0.5	1.25	1.25	0.75
	Bonding Technique		N/A	Machine/ Weld	Machine/ Weld	Machine/ Weld	Epoxy	Epoxy	Braze
Fill Temperature		°C	3.9	60	80		49	49	21
		°F	25	140	176		120	120	70
Percent Ullage at Fill			0	0	0	0	25	25	20

Another possible space application includes the thermal protection system for the space shuttle orbiter wing leading edge [60]. This concept utilizes a PCM which melts near 176.8°C (350°F) to limit the extreme temperature surges normally encountered on frontal areas of supersonic vehicles.

Phosphonium chloride, a high latent heat PCM, has been studied for use in Astronaut Extra Vehicle Activity (EVA) cooling equipment. Schelden and Golden [61], have studied the capacitor technique for application to thermally controlled devices in Jovian and Venusian extraplanetary space probes. The Air Force has examined this technique for classified applications to unmanned earth orbiting satellites, and as a special cooling system for modified F-4 aircraft. This technique of thermal control is also being investigated by the Russians (Vaselou, Kalisheva, and Telepin) for use on gravity measuring devices [62].

A salt hydrate type PCM has been studied for application to Army shelter refrigeration systems. This PCM material is designed to maintain a relatively constant temperature in the absence or failure of the active refrigeration system.

CHAPTER 4

EXPERIMENTAL APPARATUS

Test Item

The initial capacitor design goal was to produce a test item which closely simulated the heat transfer paths expected in a typical flight thermal capacitor while still allowing observations of the melt/freeze phenomena. Unfortunately these two goals were found to be incompatible, since the high resistance to heat transfer offered by most transparent materials disallows simulation of transfer paths normally available to an all metal capacitor. As a consequence, the final design stressed capacitor visibility, relegating geometrical simulation as a secondary goal.

The resulting design incorporated a structure fabricated almost entirely of plexiglas* with aluminum surfaces transferring heat to and from the paraffin into the coolant. The capacitor was fabricated in two parts: the fluid passage and the paraffin housing (Figures 20 and 21).

The overall fluid passage envelope dimensions were 26-cm (10.25-in.) long by 14.61-cm (5.75-in.) wide by 2.54-cm (1-in.) depth. Three 0.635-cm

*A Rohm and Haas tradename

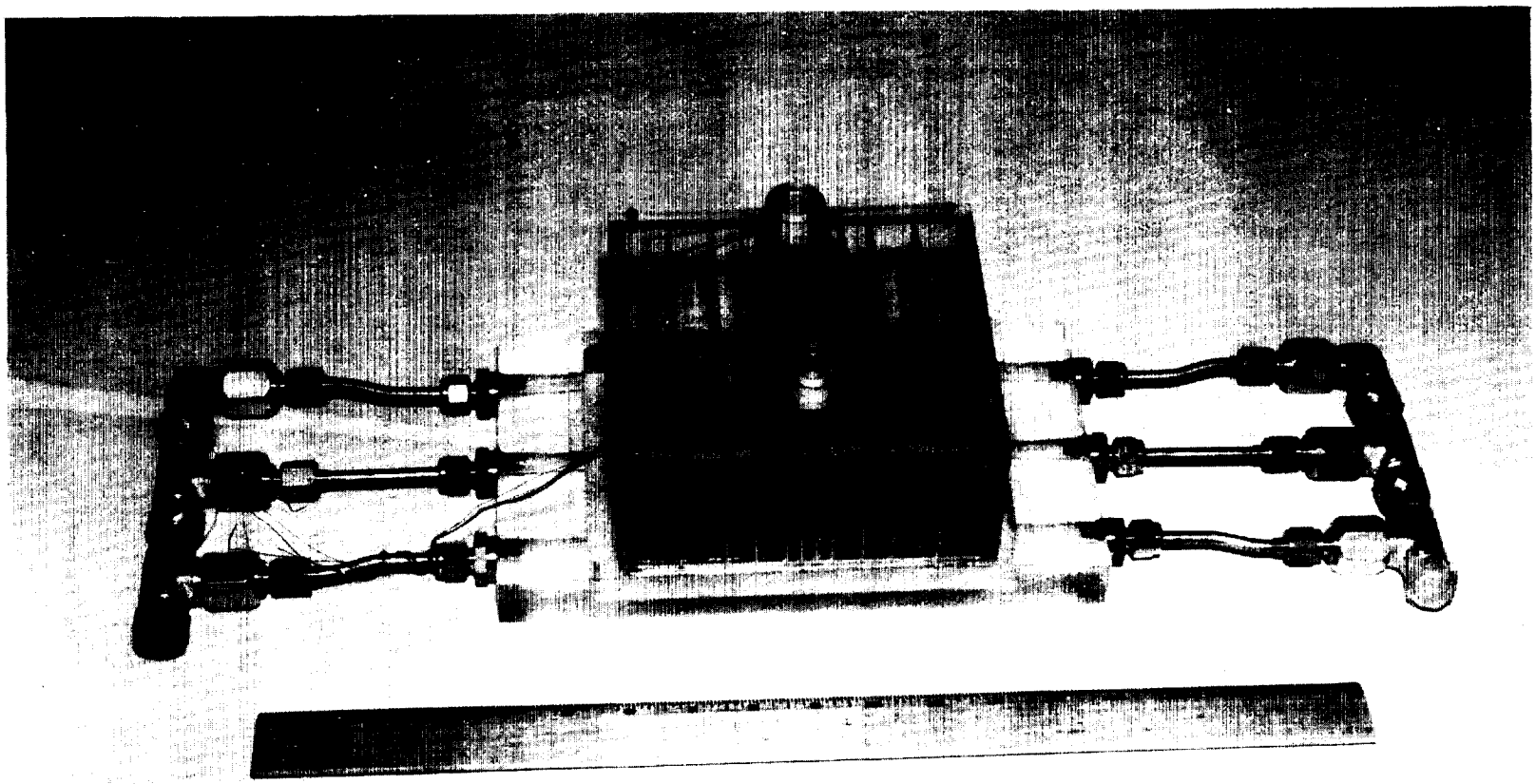

Figure 20. Thermal capacitor test item, top view.

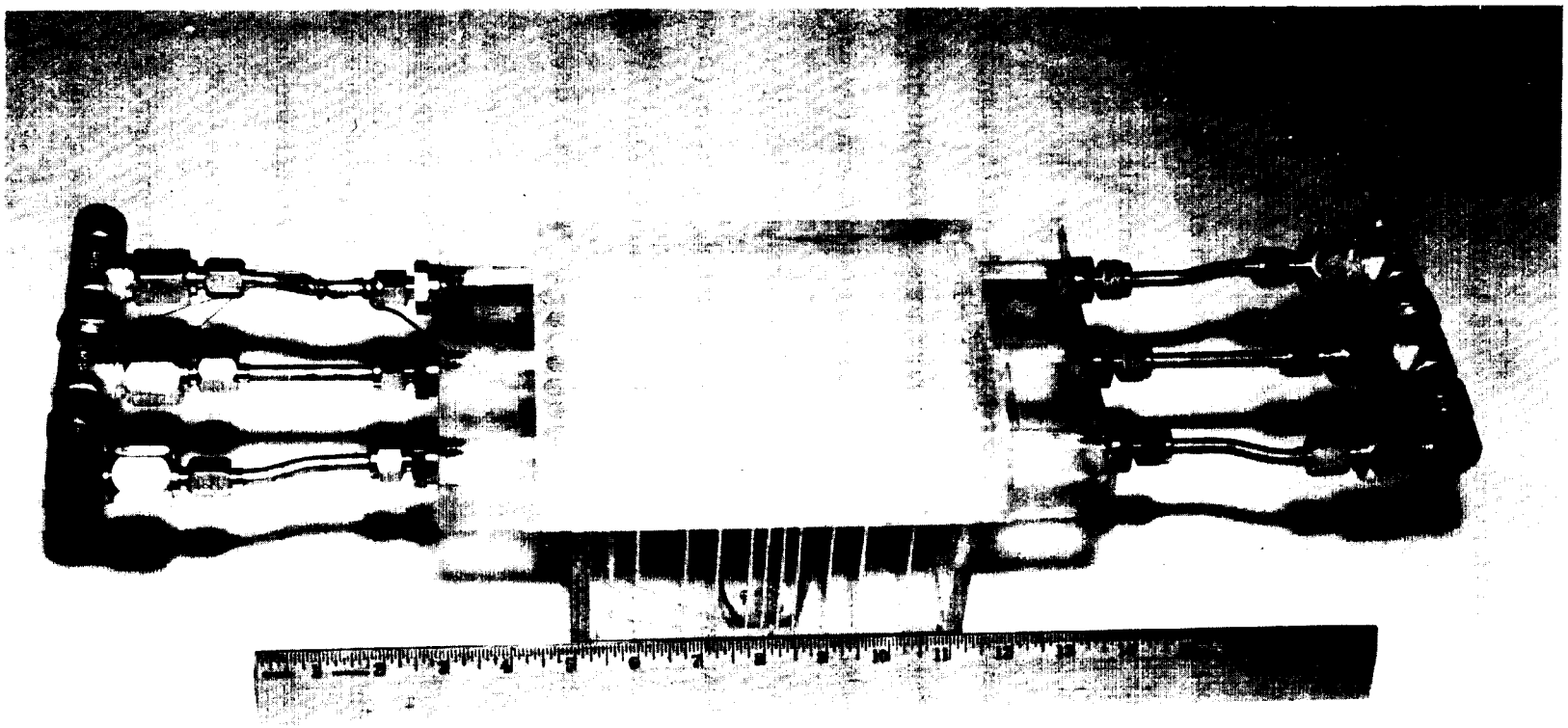

Figure 21. Thermal capacitor test item, bottom view.

(1/4-in.) diameter tapped holes were inserted parallel to the housing length (i.e., in direction of fluid flow) and into both ends of the initially solid plexiglas block. These holes extended 3.81-cm (1.5-in.) in from both ends of the housing. These three circular passages entered a 1.27-cm (1/2-in.) long by 1.91-cm (3/4-in.) deep mixing plenum, extending the width of the housing. These inlet and outlet plenums were connected by 10 fluid channels extending the remaining 15.875-cm (6.25-in.) of the housing length. The channels formed individual flow cross sections of 1.27-cm (1/2-in.) by 1.91-cm (3/4-in.), separated by 0.318-cm (1/8-in.) thick plexiglas partitions. After milling these flow passages out, a 0.635-cm (1/4-in.) thick bottom and 0.953-cm (3/8-in.) thick sides remained, with the top over the 10 fluid flow channels left open.

The upper paraffin housing was fabricated by attaching 0.02-cm (0.008-in.) thick 5052-T30 aluminum fins to a 6061-T6 aluminum bottom plate (Figure 22). The fins were 13.34-cm (5.25-in.) long and 6.35-cm (2.5-in.) deep, notched at both ends to accommodate 0.48-cm (0.188-in.) deep grooves cut in the plexiglas sides. The fins were vertically mounted on the bottom plate by first soldering a 0.24-cm (3/32-in.) long base along the length of each fin. Three 0.08-cm (1/32-in.) diameter rivets were then driven through the fin foot into the bottom plate, while being sealed at the same time by an epoxy filler with a silver matrix* coating between the foot and the bottom plate.

Four 1.9-cm (3/4-in.), four 1.27-cm (1/2-in.) and three 0.635-cm (1/4-in.) fin spacings were used in the paraffin housing. The spacings were

*Emerson and Cummings Co., Ecco Bond 56C

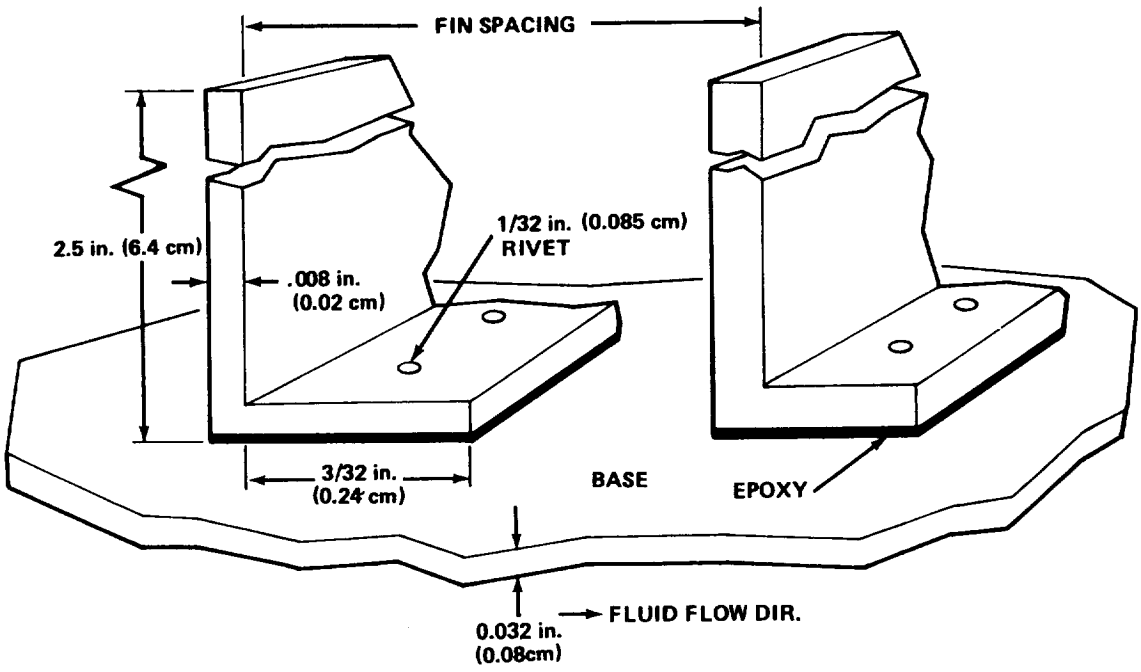

Figure 22. Typical fin mounting arrangement.

symmetrically arranged with two 1.91-cm (3/4-in.) spacing on each of the outer ends, two 1.27-cm (1/2-in.) spacing following these, and three 0.635-cm (1/4-in.) spacing at the housing center section.

Then 0.95-cm (3/8-in.) grooved sides and 0.635-cm (1/4-in.) thick ends were bonded together and attached to the bottom plate, using epoxy.* Finally, the bottom plate of the paraffin container section was epoxied to the open top of the fluid housing (i.e., on edges and top of partitions) so that the fin lengths were perpendicular to the direction of fluid flow.

The top of the housing for paraffin was fabricated of 0.635-cm (1/4-in.) thick plexiglas, with two 0.95-cm (3/8-in.) diameter paraffin fill bosses, and

---

*NARMCO 7343 was used for all plexiglas bonding

was mounted on top of the paraffin housing with epoxy. Screws 0.32 cm (1/8 in.) in diameter were used to secure the paraffin housing top, being installed into tapped holes which extended through the top into the vertical sides. At each corner underneath the fluid housing 2.54-cm (1-in.) cubical plexiglas standoffs were bonded to minimize heat transfer from the supporting surface.

After fabrication and instrumentation, two calibrated strips with 0.318-cm (1/8-in.) indexing were attached to the face of the paraffin housing (as viewed by the camera). A vertical strip was attached to the fluid outlet end, extending the full 6.50-cm (2.56-in.) height of the PCM housing. Along with the length of the housing, in the fluid flow direction and at the top, a 15.24-cm (6-in.) calibrated strip was also attached. These strips provided visual dimensional reference for filmed data.

Instrumentation

At various times during the experimental program, the system was instrumented with as many as 40 temperature probes, 6 differential temperature probes, an RPM counter (pump flow rate controller), a flow meter, and a pressure transducer. All thermocouple temperature transducers were fabricated from 0.025-cm (0.01-in.) diameter (No. 30 gage) chromel constantan wire with 0.08-cm (0.031-in.) diameter thermocouple beads. Both resistance temperature bulb* (RTB) and chromel-constantan type probes were used for

*Rosemont platinum resistance bulb

differential temperature measurements. The flowmeter was a Potter 0.954-cm (0.375-in.) turbine type which provided flow measurements over the range of zero to 1.26×10^{-4} m^3/sec (2 gal/min). The pressure transducer was a Statham strain gage type.

The test item was instrumented with 27 thermocouples, as shown in Figure 23. Three paraffin cells were instrumented, two 1.9-cm (3/4-in.) width cells and one 0.625-cm (1/4-in.) width cell. The 1-9-cm (3/4-in.) width cells are located on each side of the capacitor, adjacent to the outermost cells. Each of these had one thermocouple attached to the paraffin/fluid separator plate, three thermocouples attached to the surface of the interior fin, and four thermocouples suspended into the paraffin. The 0.625-cm (1/4-in.) cell was located in the mid-section of the capacitor and had three thermocouples attached to the upstream-side fin surface and three thermocouples were suspended into the paraffin.

After the first series of tests, three externally mounted thermocouples were additionally attached. These thermocouples were centrally mounted on the outer paraffin housing width and height, located at the capacitor inlet/outlet and the capacitor center top. These measurements were used to determine the sensible heat absorbed/rejected by the plastic structure.

In addition to the 27 thermocouples mounted on the capacitor, four thermocouples and two RTB's were installed in the fluid inlets and outlets.

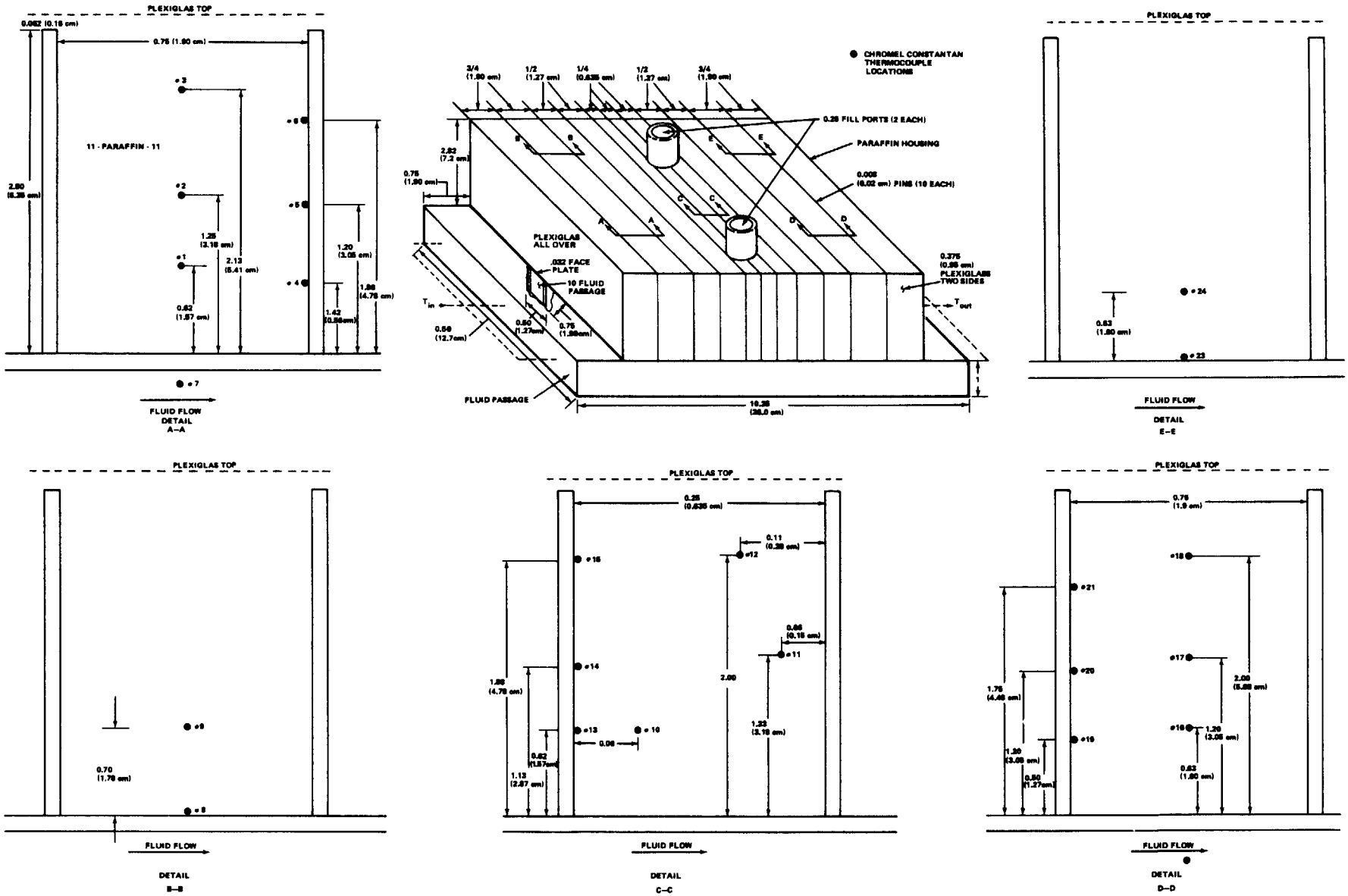

Figure 23. Diagram of thermal capacitor instrumentation.

Differential temperature readings were taken on these thermocouples between the inlet and outlet fluid. The flowmeter recorded the fluid volumetric flow-rate while a thermocouple mounted in the fluid at position adjacent to it recorded the fluid temperature. All other measurements were used to monitor facility input parameters for control purposes and were not used for data reduction.

All thermocouples which were suspended in the paraffin were covered with 0.24-cm (3/32-in.) diameter ceramic sheaths to rigidize them in their locations. The lower end of the sheaths were stripped away to allow a 0.32-cm (1/8-in.) length of the thermocouple to extend out of the sheath. Figure 24 shows a typical paraffin suspended thermocouple arrangement.

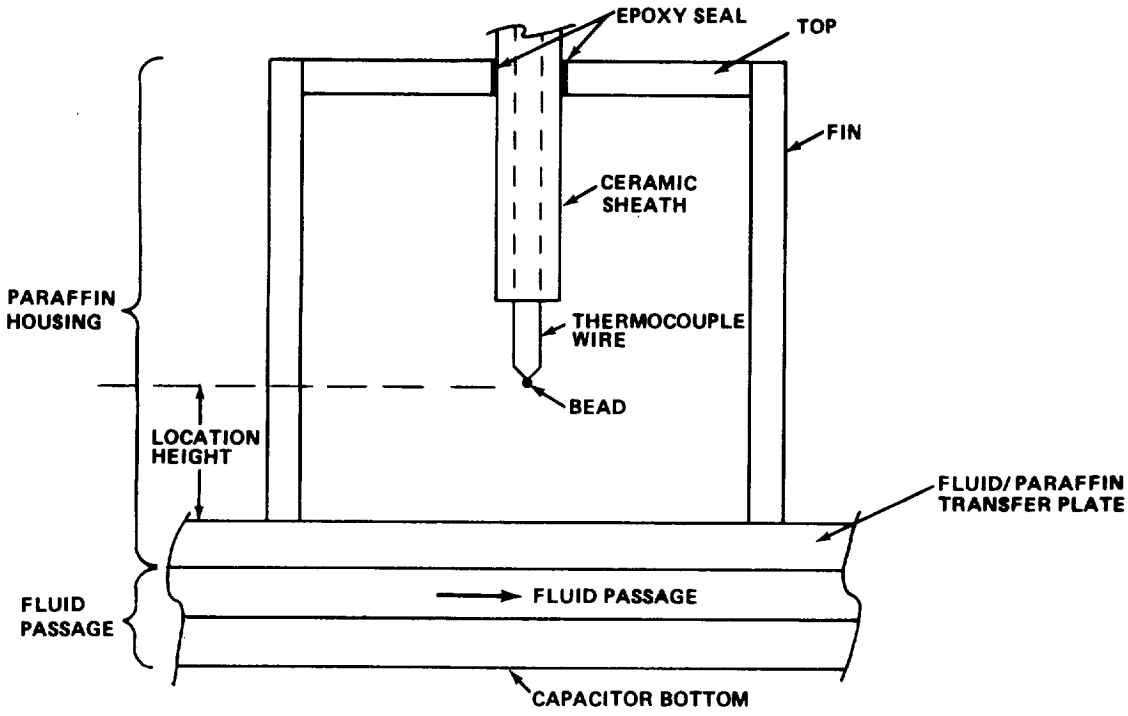

Figure 24. Typical thermocouple instrumentation.

All surface and fin mounted thermocouples were attached with epoxy. The fin surfaces were thoroughly cleaned and lightly roughened with sand paper before application. The thermocouple beads were then flattened and pressed to the surface, using 1-mil. thick 0.954-cm (3/8-in.) by 0.954-cm aluminum tape patches. Epoxy was then applied over the entire patch/thermocouple installation. Figure 25 shows a typical fin mounting scheme.

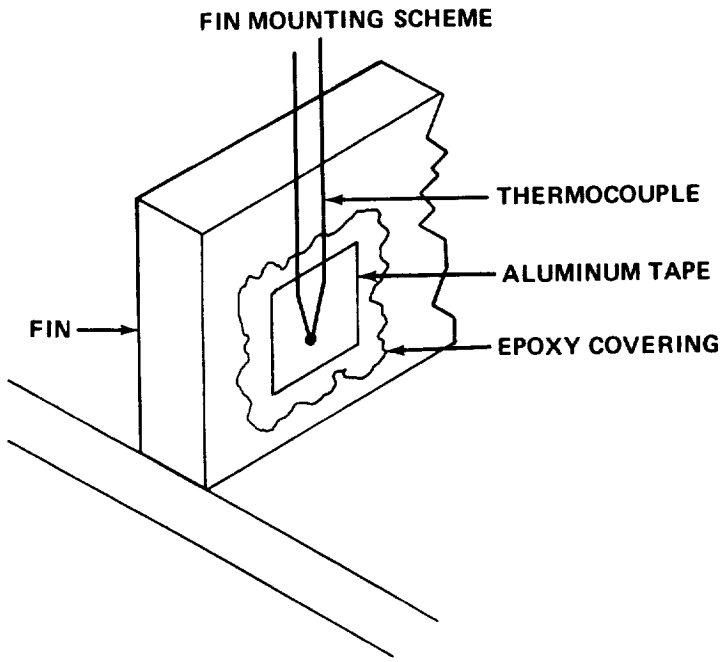

Figure 25. Typical fin thermocouple mounting arrangement.

The circuitry for all thermocouple installations inside of the paraffin housing were routed through the capacitor top using epoxy to seal the penetrations. The circuitry for thermocouple measurements of fluid temperature were routed through the bottom of the fluid passage and sealed with epoxy.

A chromel-constantan thermocouple accuracy study, performed by the Marshall Space Flight Center Test Instrumentation Group, indicates an absolute accuracy of 0.4° C (0.8° F) or better. RTB's were more accurate, but exhibited poorer response. RTB measurements were not used for evaluating data because of the transient nature of these tests. Thin wire chromel-constantan thermocouples were selected because it minimized heat leak into the paraffin housing, thereby maximizing temperature response, to give the largest possible voltage output per unit temperature rise (Fig. 26).

An extensive study was conducted to minimize error in reading the differential fluid temperature across the capacitor. However, due to the low temperature difference 0.9°C (1.5°F), the accuracy of this measurement never reached an acceptable level to allow correlation of the differential temperature data.

The raw data was routed to the digital computer for interpretation on the basis of calibration curves that had been programmed into the computer system. Tabulated printouts of data was available immediately during and after each test. After the first 15 tests, the computer program was reconstructed to allow computerized plotting of the temperature versus time test data.

Test System

During all testing, the test item and support hardware were located in a thermostatically controlled room. As a consequence, the external environment for all tests was at temperatures between 21.2 and 23.9°C (70 and 75°F).

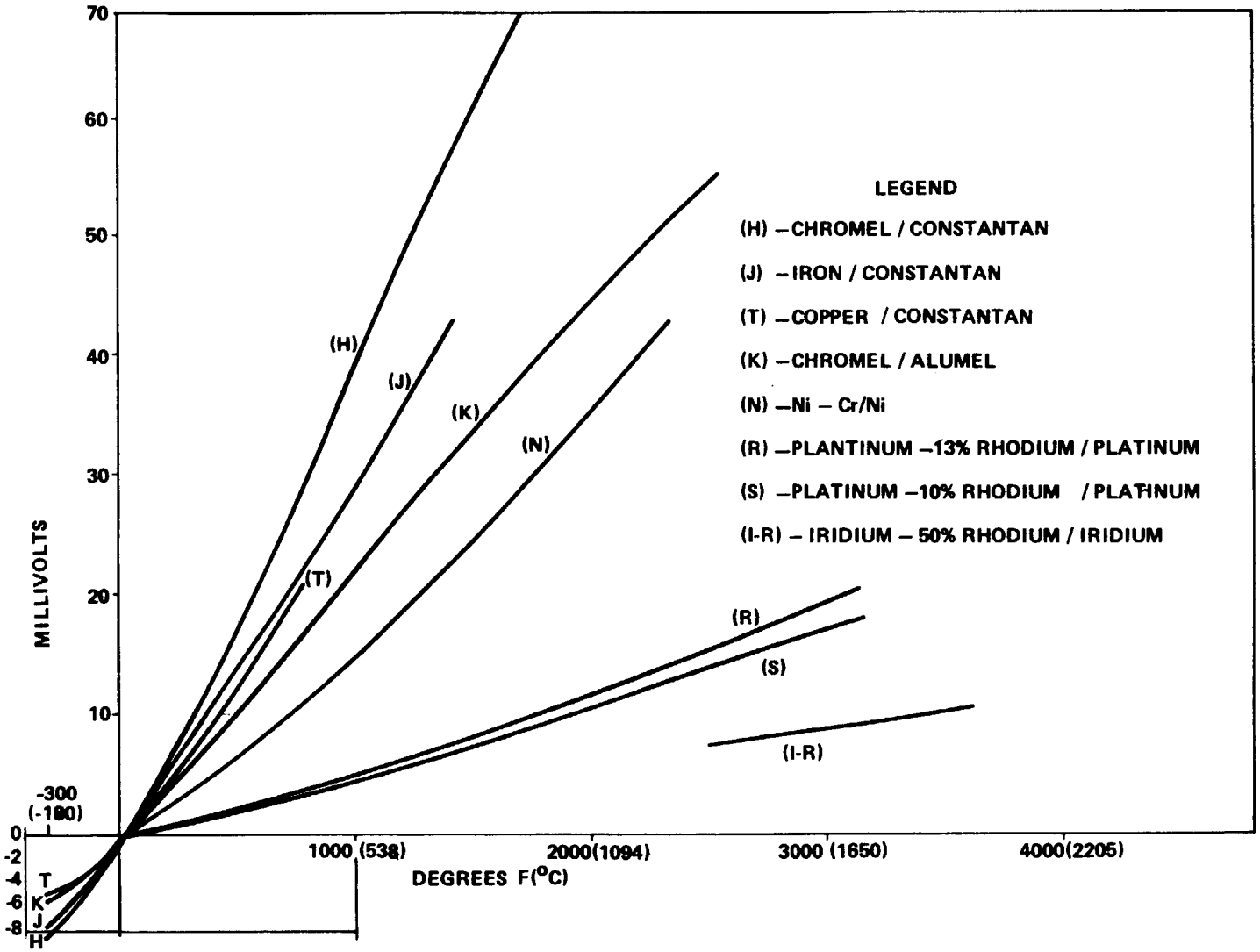

Figure 26. Temperature-millivolt graph for thermocouples.

Nonadecane, normal paraffin was used as the PCM during all tests. The nonadecane was procurred from the Phillips Petroleum Company in the technical grade.

The plexiglas test item was mounted in a closed fluid flow loop (Fig. 27). This allowed circulation of cold and hot fluid through the fluid passage at varying fluid flowrates. A motion picture camera was mounted in a position whereby paraffin phase change position with respect to time could be viewed and recorded (Fig. 28).

The coolant flow system consisted of hot and cold heat exchangers, a small-fluid pump, and appropriate valves and tubing (Fig. 27). The fluid was Monsanto coolanol-15, a silicate ester, used because of its frequent application to space vehicle coolant loops. The pump was a Viking 2.5 $m^3/sec \times 10^{-4}$ to 3.8 $m^3/sec \times 10^{-3}$ (4 to 60 gal/hr) variable speed constant volumetric flow device. The pump speed was electrically controlled so that a constant non-varying mass flowrate could be set as desired.

The coolant temperature was controlled by routing the thermal capacitor test item outlet fluid to a parallel bank of a hot and cold "tube-in-shell" heat exchangers. The hot heat exchanger contained water which was heated with a 3000 joule/sec (3 kW) chromalox calrod unit mounted internally to the heat exchanger shell. This unit was thermostatically controlled to maintain the heat exchanger shell fluid at a maximum of 82.3°C (180°F). The other leg of

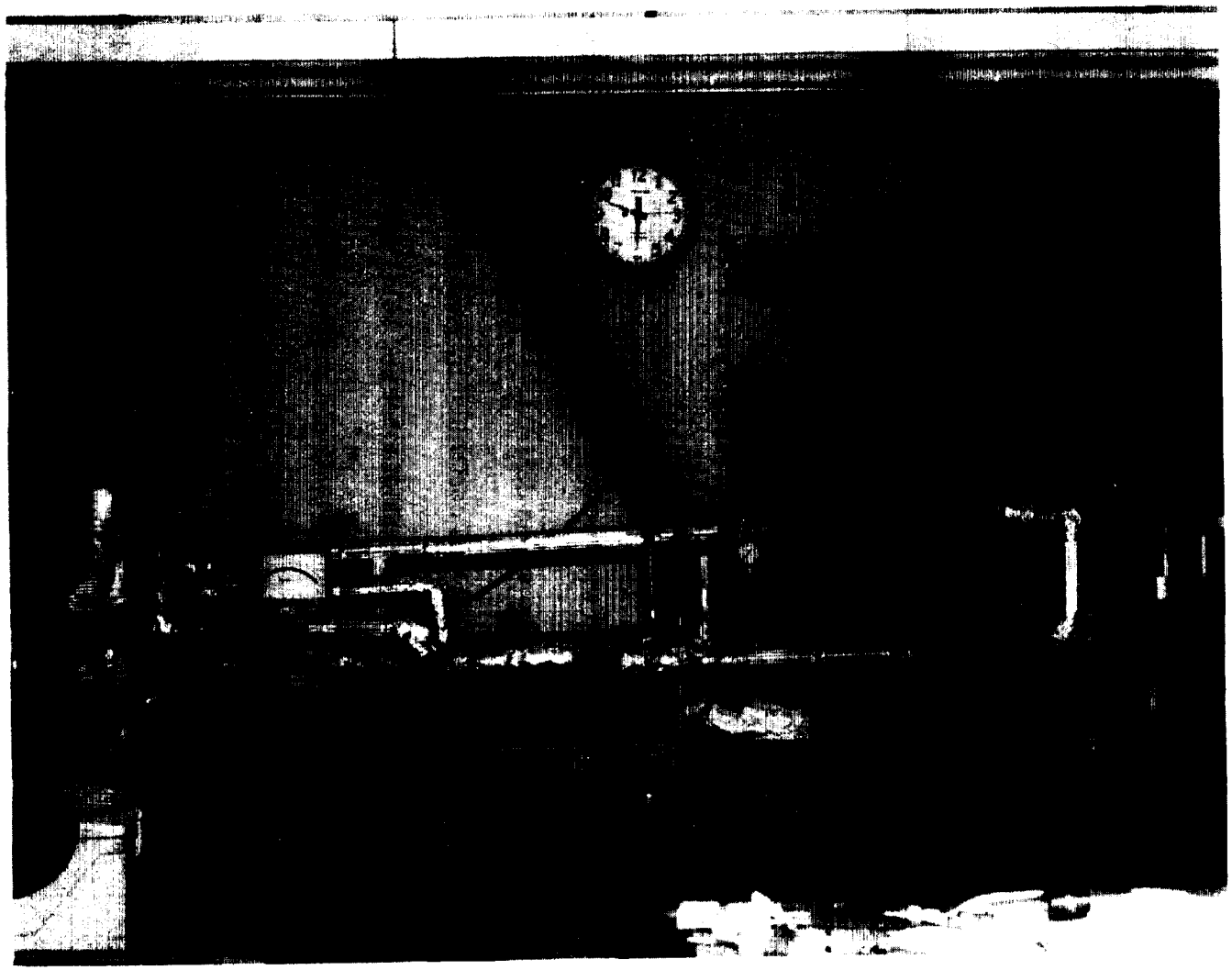

Figure 27. Thermal capacitor test facility.

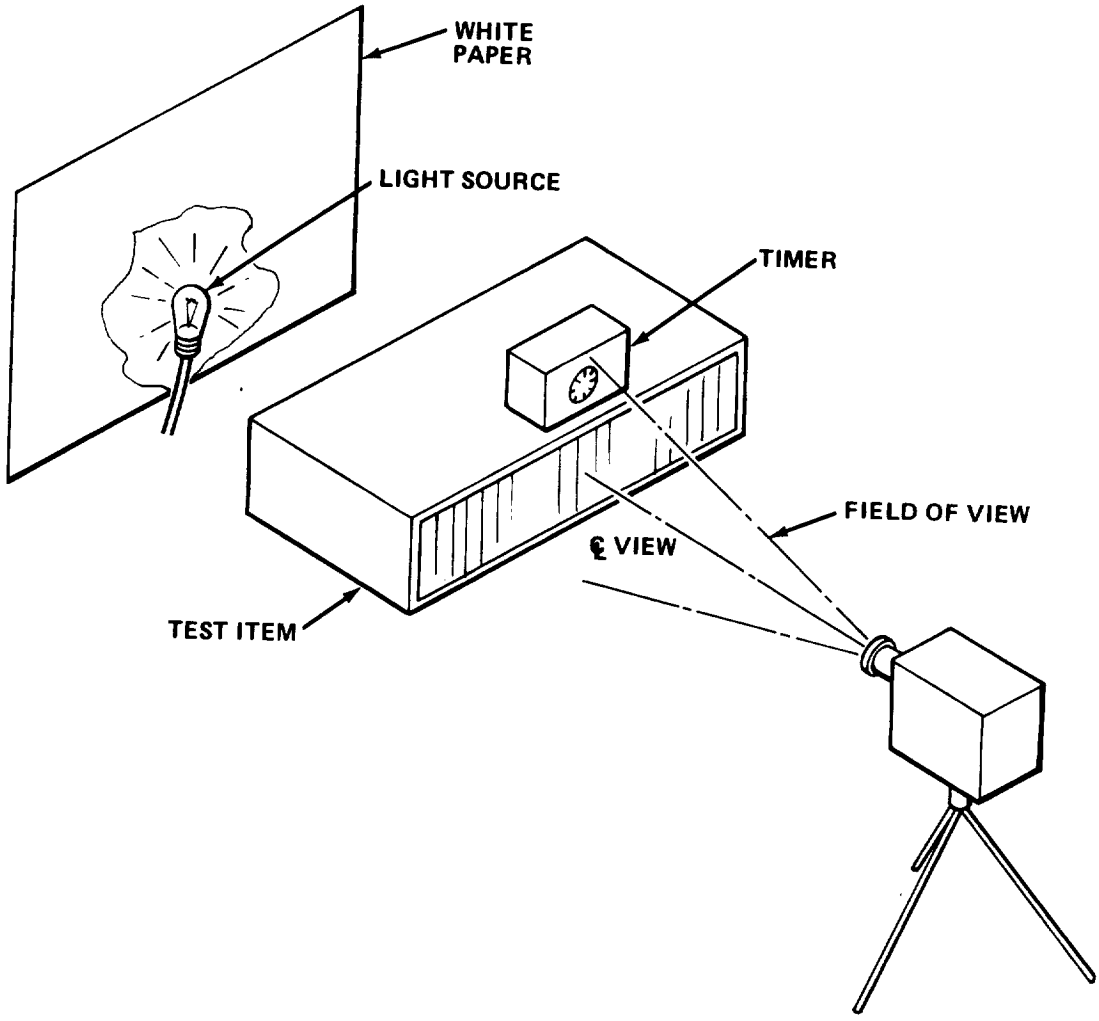

Figure 28. Motion picture camera arrangement.

the parallel bank was routed through the cold heat exchanger, containing a coolanol-15/dry ice slurry. The shell fluid temperature stayed at a relatively constant -79°C (-110°F).

Hand valves were mounted on the heat exchanger outlets to control the ratio of hot to cold fluid mixed. Downstream of these valves, the tubing was joined. From this point, a common line was routed back to the thermal capacitor inlet.

All line routings were fabricated from 1.27-cm (1/2-in.) stainless steel tubing of 0.127-cm (0.049-in.) wall thickness. The three 0.635-cm (1/4-in.) ports on the thermal capacitor inlet and outlet were manifolded together before the inlet and outlet tubing was connected. Prior to testing, flow checks were made to assure an even flow split between the three fluid connections.

The output of a thermocouple mounted at the test item inlet was transmitted to a visual output meter. Using this output, hand valves were adjusted to maintain the desired fluid inlet temperature.

The capacitor was insulated on both top and bottom with 5.08-cm (2-in.) thick fiberglas bating. The interconnecting tubing was insulated with 2.54-cm (1-in.) fiberglas wrap.

A motion picture camera was mounted so that it viewed the capacitor paraffin housing from the sides where the majority of the instrumentation was located. The camera was situated so that its field of view included the entire capacitor plus a digital timer (Fig. 28). During initial testing, the timer was located on the fluid outlet side of the capacitor. In later tests, it was relocated to the top of the paraffin housing.

The camera used during initial testing was a Mitchell, which filmed real time at variable speeds between 6 and 24 frames per second. Due to the voluminous amount of data which was accumulated, with a real-time output, the camera was intermittently switched on and off. Later, a Cine Special

camera with a variable framing rate of 0.25 to 1 frame per second was used for intermittent filming. This allowed compact filming without compromising data acquisition. During all runs, color film was used to optimize film definition.

The timer was a Cramer Controls Corporation device. The digital readout contained five digits: four whole digits and one decimal second digit.

During initial testing, the capacitor was illuminated from the camera side of the test system. However, the lighting was later moved to the opposite side of the capacitor for better film definition.

Testing

Prior to starting the tests, the capacitor was filled with nonadecane by heating the paraffin and the capacitor separately to a temperature of 71.7°C (160°F). The housing was filled by simply pouring the hot paraffin into one of the two fill ports, while allowing the other to vent.

The initial weight of the nonadecane required to fill the paraffin housing was 1.95 lbs. The paraffin weight was determined by using a specially constructed load cell weighing arrangement. The paraffin weight was determined by weighing the full paraffin container plus the paraffin prior to fill; then weighing the container plus the remaining paraffin after fill.

$$Wt_f = Wt_{c+pf} - Wt_c \qquad (10)$$

The inlet and outlet fluid temperatures, along with the test item structural temperature measurements, were used to determine the heat lost or gained from the fluid during paraffin phase change. This was compared to the heat received by the paraffin during phase change plus the sensible heat change of the test item, assuming heat loss to be negligible.

Nonadecane was selected because its melting point is slightly above normal room temperature, its physical properties were known, and the literature search had showed that none of the previous experimenters had used this particular PCM.

The band of inlet fluid temperatures was arbitrarily established over a range of ± 21.1°C (70°F) which centered on the published nominal freezing point temperature. This required an inlet temperature range from -6.7 to 71.1°C (20 to 160°F). The mass flowrate range from 12.6 to 37.8 g/sec (100 to 300 lb/hr) was used because it represented space vehicle typical coolant flowrates.

Based on information given in Reference 70, the need for a guard vacuum around the capacitor to assure an adiabatic system was not considered necessary. This is primarily because of the good insulating qualities of the plexiglas walls [K = 0.16 J/m sec °K (0.09 BTU/hr ft°R)]. However, all surfaces except those requiring exposure were well insulated during all runs. One test was conducted to verify the adiabatic assumption. During this run the entire capacitor was enveloped in insulating material. These test data were

compared to data obtained from a previous uninsulated test which was performed with identical input conditions. This comparison confirmed the adiabatic test item assumption.

A typical test procedure is itemized in Table 4. The designation used for all thermal capacitor tests by the testing group was with the prefix 230. The total number of tests performed in conjunction with this study was 60 tests, 230-1 through 230-60. However, of these runs, a large number of facility checkout tests were performed, during which unacceptable data was obtained. As a result, only 20 of these tests are reported herein. Of these, 9 were melt tests and 11 were freeze tests. A summary of the test designation, along with pertinent input parameters for those tests deemed acceptable, is given in Table 5. Appendix D presents all pertinent raw test data.

The primary problem associated with operation of the test apparatus lay in the control of the fluid inlet temperature. Using hand operated valving, the inlet temperature could be maintained no closer than 2.8°C (5°F), with short excursions reaching a variation of 5.6°C (10°F) from the nominal target value. These excursions stemmed from the inherent time lag that existed from the time that hot and cold fluid was introduced into the system, until the time when the temperature sensor began to pick up the perturbation. For example, when the operator received a low temperature reading on the inlet sensor, he would increase the flow with the hot side valve. There would be a time interval before the hot pulse could be detected by the sensor,

TABLE 4. TYPICAL TEST PROCEDURE

Test Time Reference	Procedure		
	Freeze Test Only	Common	Melt Test Only
Pretest	• heat paraffin to a uniform temperature above melt point, i.e., 35 to 48.9°C (95°F to 120°F)		• Allow the paraffin temperature to stabilize at room temperature, i.e., 21.1 to 23.9°C (70 to 75°F)
Pretest		• Using the pump speed control establish the desired constant mass flow rate	
Pretest		• by causing the fluid to bypass the capacitor establish the fluid inlet temperature	
T = 0		• Simultaneously, open the capac- inlet valve and • turn on the mo- picture camera and • initiate instrumentation data sampling	
During entire test		• maintain a constant inlet fluid temperature to capacitor	
Test end		• deactivate motion picture camera data sampling, and turn off pump	

TABLE 5. SUMMARY OF TEST INPUTS

Test Designation	Type Test	Nominal Fluid Inlet Temperature		Nominal Fluid Flowrate	
		° F	° C	lb/hr.	kg/sec
230-5	Melt	160	71.2	300	0.038
230-6	Melt	130	54.7	300	0.038
230-7	Freeze	20	-6.7	300	0.038
230-8	Melt	110	43.4	300	0.038
230-9	Melt	150	65.6	300	0.038
230-10	Freeze	50	10.0	300	0.038
230-11	Freeze	70	21.1	300	0.038
230-15	Freeze	30	-1.1	300	0.038
230-49	Melt	150	65.6	100	0.013
230-50	Melt	130	54.7	100	0.013
230-51	Freeze	20	-6.7	100	0.013
230-52	Freeze	30	-1.1	30	0.0038
230-53	Freeze	50	10.0	200	0.025
230-54	Freeze	70	21.1	100	0.013
230-55	Freeze	70	21.1	100	0.013
230-56	Freeze	30	-1.1	100	0.013
230-57	Melt	160	71.2	200	0.025
230-58	Freeze	30	-1.1	200	0.025
230-59	Melt	110	43.4	200	0.025
230-60	Melt	130	54.7	300	0.038

probably due to slow fluid velocity, poor mixing, and the large sensible mass of the system. As a result, if the operator reacted too quickly or overacted to a temperature pertubation, it would induce a cyclic temperature, with a large excursion band. This was magnified by the control band placed on the thermostat control in the hot heat exchanger, which was quite large

CHAPTER 5

ANALYTICAL TECHNIQUES

Introduction

The energy equations which must be solved in order to determine such values as interface position and temperature profile variation with time are formulated in this section. The techniques used to solve these equations and the equation input values are discussed.

General

The first law of thermodynamics for a system may be written in differential form as

$$\frac{de}{dt} = \frac{dq}{dt} - \frac{dw}{dt} \tag{11}$$

For an open, unsteady system (neglecting radiation, nuclear, and electromagnetic contributions), Bird, Stewart, and Lightfoot [63] have expressed the first law as the following energy balance:

$$\left(\begin{array}{c}\text{Rate of}\\ \text{accumulation}\\ \text{of internal}\\ \text{and kinetic}\\ \text{energy}\end{array}\right) + \left(\begin{array}{c}\text{Rate of}\\ \text{internal and}\\ \text{kinetic energy}\\ \text{out by}\\ \text{convection}\end{array}\right) - \left(\begin{array}{c}\text{Rate of}\\ \text{internal and}\\ \text{kinetic energy}\\ \text{in by}\\ \text{convection}\end{array}\right) = \left(\begin{array}{c}\text{net rate}\\ \text{of heat}\\ \text{addition by}\\ \text{conduction}\end{array}\right) - \left(\begin{array}{c}\text{net rate of}\\ \text{work done by}\\ \text{the system}\\ \text{on}\\ \text{surroundings}\end{array}\right)$$

for a fluid, this reduces to a vector tensor form:

$$\underset{(a)}{\frac{\partial}{\partial t}\left[\rho\left(\hat{u}+\tfrac{1}{2}V^2\right)\right]}+\underset{(b)}{\left[\vec{\nabla}\cdot\rho\vec{V}\left(\hat{u}+\tfrac{1}{2}V^2\right)\right]}$$

$$=\underset{(c)}{-\left(\vec{\nabla}\cdot\vec{Q}\right)}+\underset{(d)}{\rho(\vec{V}\cdot\vec{g})}\underset{(e)}{-\left(\vec{\nabla}\cdot P\vec{V}\right)}\underset{(f)}{-\left[\vec{\nabla}\cdot\left(\vec{\tau}\cdot\vec{V}\right)\right]} \quad . \qquad (12)$$

where:

(a) is the rate of gain of energy per unit volume

(b) is the rate of energy input, per unit volume, by convection

(c) is the rate of energy input, per unit volume, by conduction

(d) is the rate of work done on the fluid, per unit volume, by gravity forces

(e) is the rate of work done on the fluid, per unit volume, by pressure forces

(f) is the rate of work done on the fluid, per unit volume, by viscous forces

For a typical cell undergoing phase change, the kinetic and potential energy contributions are small, eliminating the last term in a and b and the whole of d. Assuming the pressure forces are not allowed to build up appreciably, e may be neglected. The limited fluid velocities encountered for normal melting processes eliminates f. Thus equation (12) reduces to:

$$\frac{\partial}{\partial t}\left(\rho\hat{u}\right)=-\left[\vec{\nabla}\cdot\left(\rho\vec{V}\hat{u}\right)\right]-\left(\vec{\nabla}\cdot\vec{Q}\right) \quad , \qquad (13)$$

For a fluid at constant pressure, the internal energy differential is given by:

$$d\hat{u} = -pdv + cpdT \tag{14}$$

Neglecting viscous dissipation and assuming constant properties and an incompressible fluid, equation (13) may be written:

$$\rho c_p \frac{\partial T}{\partial t} = -\rho c_p (\vec{\nabla} \cdot \vec{V}T) - (\vec{\nabla} \cdot \vec{Q}) \tag{15}$$

Since $\vec{\nabla} \cdot \vec{Q} = -K\nabla^2 T$, then from equation (15):

$$\frac{\partial T}{\partial t} = \frac{K}{\rho c_p} \nabla^2 T - (\vec{\nabla} \cdot \vec{V}T) \tag{16}$$

for the fluid phase. For the solid phase, the convective term does not exist and (16) reduces to the familiar Fourier Conduction equation

$$\frac{\partial T}{\partial t} = \alpha \nabla^2 T \tag{17}$$

Using equation (17), a formulation of a one-dimensional phase change problem may be constructed (Fig. 29). Consider the liquid phase to be at a constant temperature, T_o at time $t = 0$, and the surface temperature at $x = 0$ to be step changed from $T = T_o$ to 0 and maintained there for all $t > 0$. For a pure conduction process, differential equation (17) for each zone is

$$\frac{\partial T_s}{\partial t} = \alpha_s \frac{\partial^2 T_s}{\partial x^2}$$

and

$$\frac{\partial T_L}{\partial t} = \alpha_L \frac{\partial^2 T_L}{\partial x^2} \tag{18}$$

with initial conditions:

$$T_L = T_o = T_s \text{ at } t = 0 \tag{19}$$

and

$$T_s = 0 \text{ at } x = 0 \text{ (for all t)} \tag{20}$$

If $\rho_L = \rho_s = \rho$, then

$$K_s \frac{\partial T_s}{\partial x} = K_L \frac{\sigma T_L}{\partial x} + \rho \Delta H \frac{dS}{dt} \quad , \tag{21}$$

at $x = S(t)$; therefore,

$$T_L = T_s = T_{Fr} \tag{22}$$

and

$$T_L = T_o \text{ as } x \rightarrow \infty \quad . \tag{23}$$

The first published discussion of this classical problem was by Stefan [64], and the first solution attributed to Neumann [65]. These solutions were discussed by Carslaw and Jaeger [65].

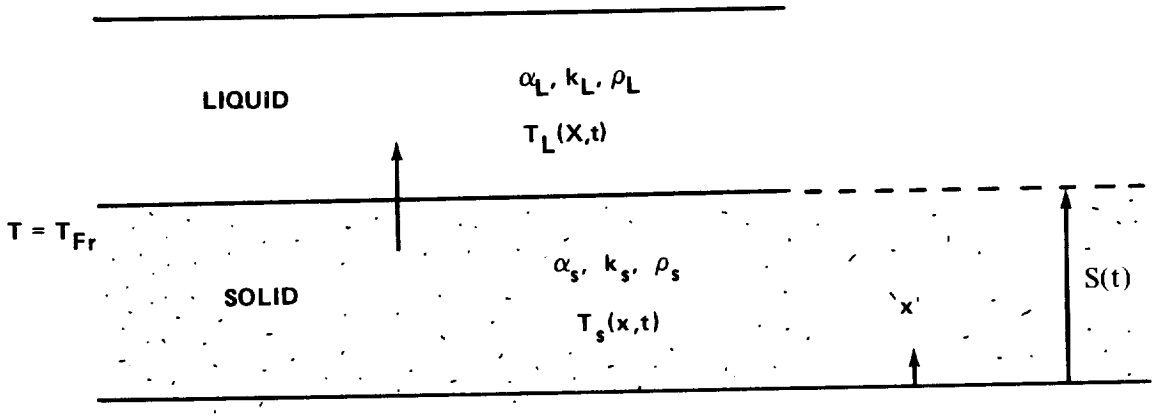

Figure 29. One-dimensional freezing.

Numerous other solutions for various boundary and initial conditions, for pure conduction and convection processes are available in technical publications. Sunderland and Muehlbaur, [67], gave an excellent bibliography of techniques used to solve the phase change problem through 1965. Additional work has been done since then on specific conduction problems, some of the more notable being cited in References 62, 68, and 69. The more important convection problems are cited in References 49 and 70. The work on freezing and melting done under the tutelage of Golden at the Colorado School of mines is worthy of mention [51, 71, 72, 73, 74]. These studies attempt to solve the fluid motion equations in conjunction with the energy equation by using a numerical scheme. Although this technique is commendable, as yet, it has not proven to be sufficiently flexible to allow application to a broad bank of real physical geometries. This is because the flow pattern must be known before a solution can be obtained.

The typical capacitor cell presents problems which are considerably more complicated than those formulated in previous studies. In a typical cell (Fig. 30), the problem is two-dimensional, involving convection and conduction in the one-g case, with varying boundary conditions on a minimum of three sides; where $T_F = T(y, t)$, $T_B = T(t)$, and $y = S(x, t)$ constitute the phase change position occurring on the moving boundary.

Assuming again a pure conduction process, the differential equations for the liquid phase are:

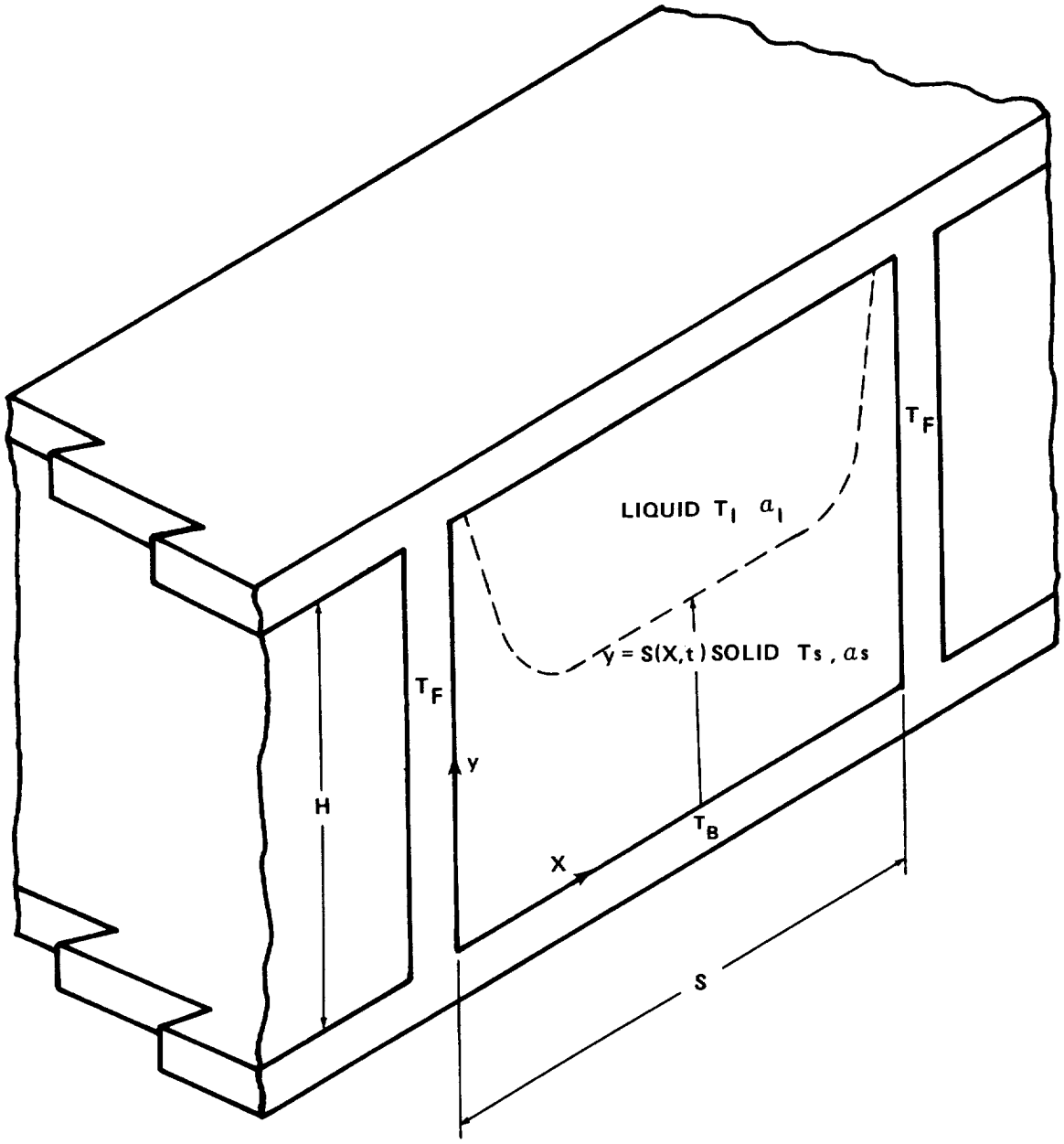

Figure 30. Two-dimensional freezing.

$$\frac{\partial T_L}{\partial t} = \alpha_L \left(\frac{\partial^2 T_L}{\partial x^2} + \frac{\partial^2 T_L}{\partial y^2} \right)$$

for $0 < x < S,\ S(x, t) < y < H$. (24)

The equations for the solid phase are:

$$\frac{\partial T_S}{\partial t} = \alpha_S \left(\frac{\partial^2 T_S}{\partial x^2} + \frac{\partial^2 T_S}{\partial y^2} \right) ,$$

for $0 < x < S,\ S(x, t) < y < H$. (25)

The initial conditions are given by

$$T_S = T_B = T_F \text{ at } t = 0 \tag{26}$$

and

$$T_L = T_B = T_F \text{ at } t = 0 , \tag{27}$$

and the boundary conditions are:

$$T_B = T_S, \text{ at } y = 0 ; \tag{28}$$

$$T_L = T_S, \text{ at } y = S(x, t) ;$$

and

$$\frac{\partial T_L}{\partial y} = 0, \text{ at } y = H \tag{29}$$

From Rathgen and Jiji [75], the second boundary condition at the interface is given by

$$\left(K_S \frac{\partial T_S}{\partial y} - K_L \frac{\partial T_L}{\partial y} \right) \left[1 + \left(\frac{\partial S}{\partial x} \right)^2 \right] = \rho \Delta H \frac{\partial S}{\partial t} . \tag{30}$$

(See Appendix E for the derivation of this boundary condition).

Due to the complexity of this problem it has not been solved in a closed form. In non-idealized problems, such as this, a numerical technique is typically utilized.

Single Cell Description

After analyzing film data (see Chapters 6 and 7) and a report from a previous study [76], it was concluded that proper selection of the cells in the capacitor housing allow the cells to be considered thermally independent. However, since this adiabatic assumption could have introduced error, the cells were also isolated from each other by specifying fin and plate temperatures as boundary conditions. Computer models of the 1/4 inch and 3/4 inch cells were constructed. These single cell models were used to predict variations in temperatures and interfacial positions with time.

The model used an explicit forward finite differencing routine. Programs were initially written in a simplified computer language known as CINDA (Chrysler Improved Numerical Differencing Analyzer [77]). Later, a more specific Fortran program was written which allowed operational convenience in varying the parameters of the phase change study. Using identical inputs, the programs were compared and found to have nearly identical outputs. As a result, these two programs were used interchangeably to analyze test results. A description of these programs is given in Appendix C.

Initial computer runs used to prove the CINDA and Fortran models were made on an IBM 230 computer. All other runs were made on the Univac 1108 and IBM 7094 high speed computers. Run times varied from 15 minutes to 1 hour, depending largely on the time step required for stability and the duration of the experimental test. During most computer runs, a time step of 0.0001 hours sufficed.

For analytical purposes the cells were subdivided into the nodal arrangement shown in Figure 31. The general calculation flow chart scheme is shown in Figure 32 and the notation used in the Fortran program is shown in Figure 33.

The computational procedure started with specification of initial temperatures for all nodes and calculation of all physical and thermal characteristics. Typically the following properties were used in all runs.

Paraffin properties:

ρ = 47.2 lb/ft^3 (755.7 kg/m^3)

K = 0.087 BTU/Hr ft °R (0.149 J/m sec °K)

C_p = 0.5 BTU/lb°R (2092 J/kg-°C)

ΔH = 73.4 BTU/lb (1.70×10^5 J/kg)

ΔH_T = 22.11 BTU/lb (5.14×10^4 J/kg)

β = 0.00045 1/R^O (0.00081 1/°C)

μ = 14.3 Lbm/Hr-ft (5.9×10^{-3} Newton sec/m^2)

$C_{P_L} = C_{P_S}$

$K_L = K_S$

$T_T = 73.04°F\ (22.81°C)$

$T_{Fr} = 89.8°F\ (32.13°C)$

Metal properties:

$\rho = 171\ lb/ft^3\ (2.736 \times 10^3\ kg/m^3)$

$K = 93\ BTU/Hr\ ft°\ R\ (159.2\ J/m\text{-}sec°K)$

$C_p = 0.22\ BTU/lb°R\ (919.9\ J/kg°C)$

Plexiglas properties:

$\rho = 72.5\ lb/ft^3\ (0.94 \times 10^3\ kg/m^3)$

$K = 0.09\ BTU/Hr\ ft°R\ (0.154\ J/m\text{-}sec\text{-}°K)$

$C_p = 0.33\ BTU/lb°R\ (1380.7\ J/kg\text{-}°C)$

In addition to the above property data, cell geometry data and initial temperature data were input. Although the model had the capability of using temperature dependent properties, constant values were used. An initial study had proven that the variation in temperature and distance outputs was not highly sensitive to small variations in ρ, C_p and K. Moreover, the accuracy of available property data was questionable. Therefore, the additional computer time required to incorporate a varible property routine and to change a forward/backward finite differencing approach was considered unnecessary.

Node positions were located as close as possible to the fin and plate experimental points of measurement, and the measured values of temperature,

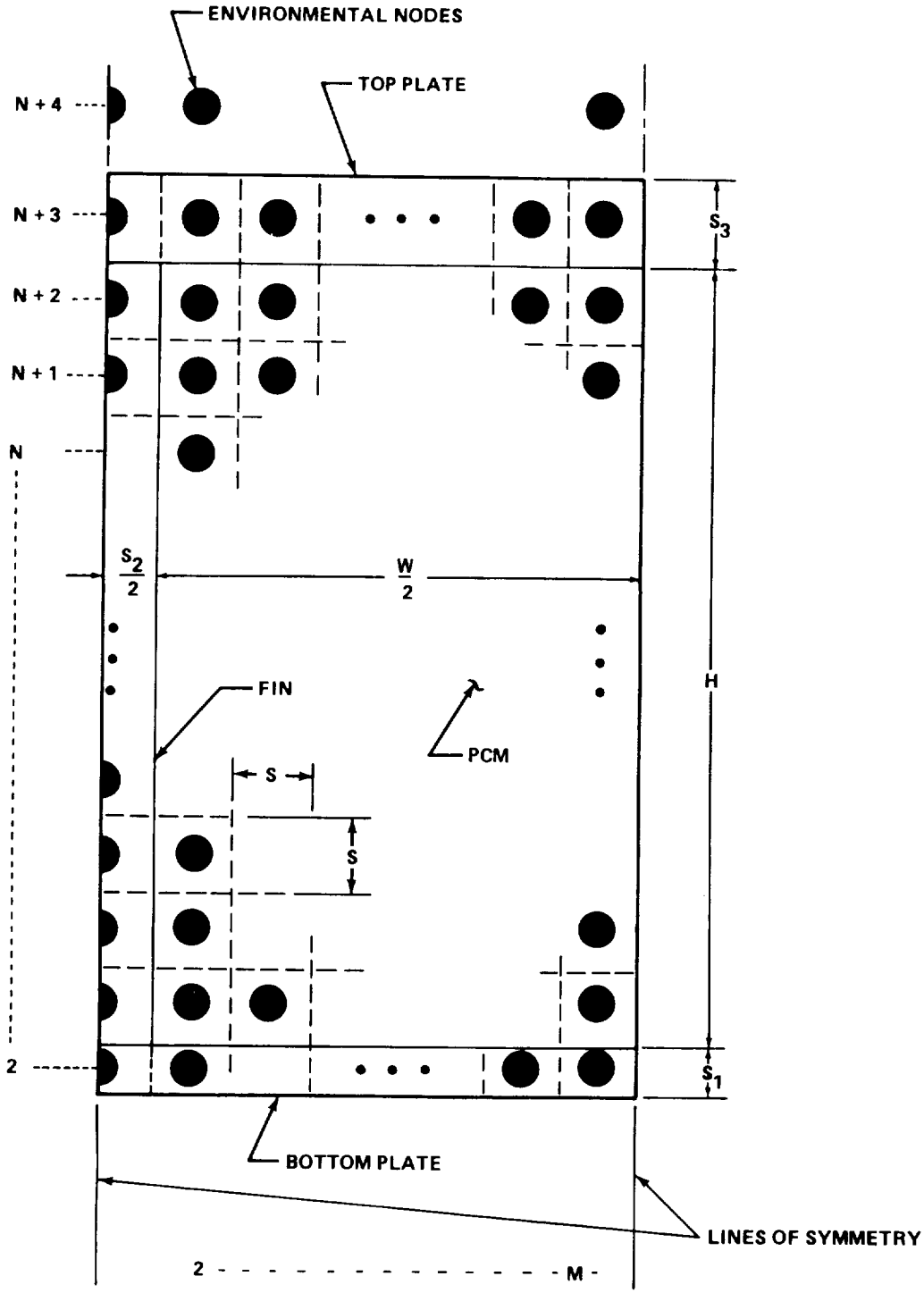

Figure 31. Symmetrical section of nodal arrangement.

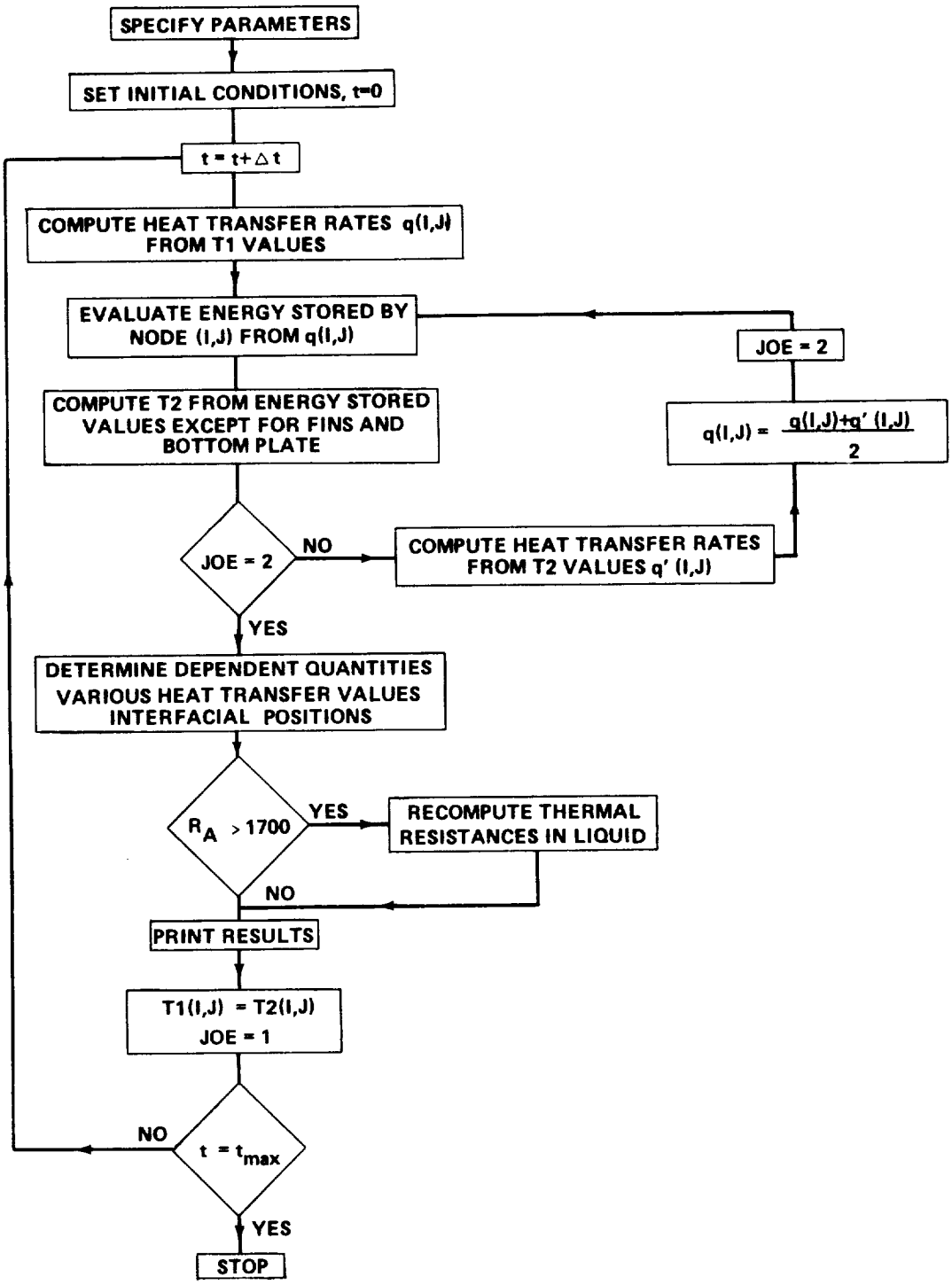

Figure 32. Computer model flow chart.

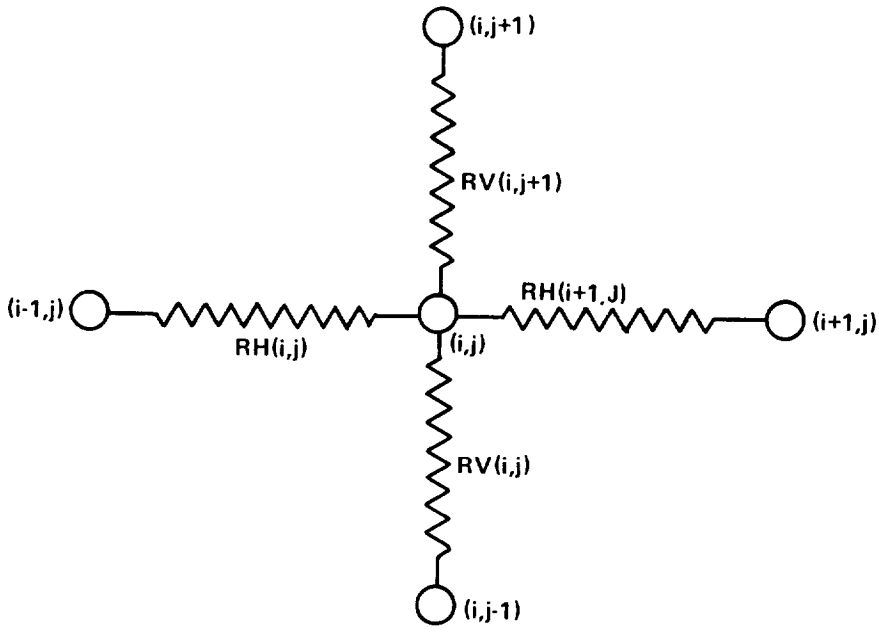

Figure 33. Typical node arrangement.

as a function of time, were input for these nodes. This technique precluded error in the side walls, due to the adiabatic cell assumption. Due to the small capacitance and the resulting small computer time step required to achieve stability, when using a transient for analyses of the thin fins, the steady state Laplace equation was used to solve for the fin temperatures. Also the nodes were arranged in two dimensions, assuring no heat transfer down the cell. During most tests, this assumption was verified by the fact the interface height remained relatively constant across the test unit's width.

The heat transfer rate of each paraffin node was computed by using the following two dimensional numerical approximating technique:

$$q(i,j) = \frac{T(i-1,j) - T(i,j)}{RH(i,j)} + \frac{T(i+i,j) - T(i,j)}{RH(i+1,j)}$$

$$+ \frac{T(i,j-1) - T(i,j)}{RV(i,j)} + \frac{T(i,j\ 1) - T(i,j)}{RV(i,j+1)} \qquad (31)$$

This rate was stored and used in subsequent calculations. The temperature of the node at the next time increment, $t+\Delta t$, was found by

$$T'(i,j) = T(i,j) + \frac{q(i,j)}{C(i,j)}\ \Delta t \qquad (32)$$

The computation was then iterated by computing $q'(i,j)$ using equation (31) and the new temperature found using equation (32). The average of $q(i,j)$ and $q'(i,j)$ was then used in equation (31) to predict a more accurate $T'(i,j)$ value. This procedure was repeated at each time step.

Appropriate modification to equations (31) and (32) were made for nodes located on or near a boundary. Since the boundary condition at the interface changes due to the absorption or rejection of the latent and transitional heats, a special technique had to be used at the phase change and transitional temperatures. The method used herein forced the temperature to be constant until sufficient heat had been absorbed or rejected by the node to change phase (Fig. 34). This was accomplished by monitoring the total energy stored in each node so that when the nodal temperature reached the transition or fusion temperature, it was maintained at this value until sufficient energy was absorbed or rejected to balance the transitional or latent heat of fusion for the node. The fraction of the node melted or frozen was determined at each

time step based on the energy accumulation in the node. From this, the melt height was determined for each column of nodes.

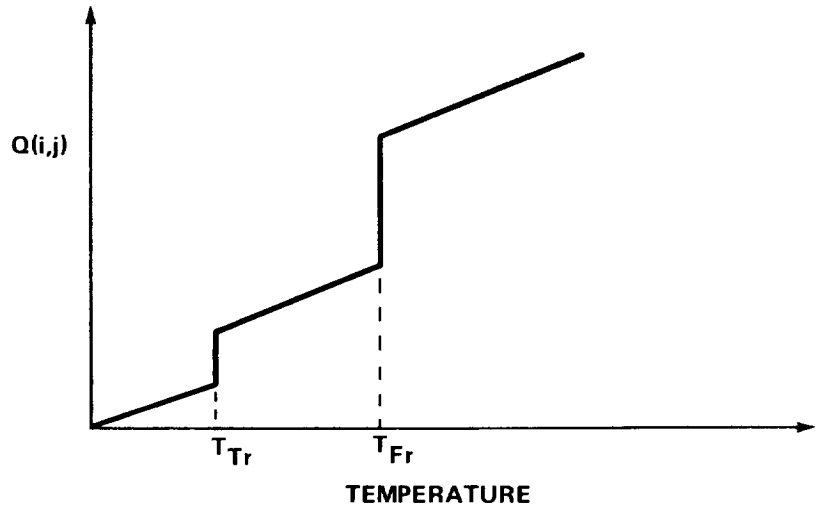

Figure 34. Heat stored versus temperature.

After initial runs, the basic conduction model was modified for melt analysis. During melting, the thermal conductivity values were modified in the liquid region to account for convection. The method used was to determine the Rayleigh number by using an average melt height, given by

$$\bar{x} = \sum_{i=1}^{m} x_i \Big/ m \tag{33}$$

The driving temperature difference was the absolute difference between the melting temperature and the lower plate temperature.

$$\Delta T = T_B - T_{Fr} \tag{34}$$

Using these variable quantities along with appropriate physical properties, the Rayleigh number was determined at each time step.

Initially the bounded cell Nusselt number versus Rayleigh number correlations of Catton and Edwards [31] were considered; however, since the initial point at which the melt layer exceeds the critical Rayleigh number is extremely small, the infinite flat plate correlations of Silveston and O'Toole [30] were used instead. These correlations are given for the four Rayleigh number regimes, as

Regime I	$Ra < 1700$	$K_{eff}/K = 1$
Regime II	$3,500 \geq Ra \geq 1700$	$K_{eff}/K = 0.00238\ Ra^{0.816}$
Regime III	$1 \times 10^5 \geq Ra \geq 3500$	$K_{eff}/K = 0.229\ Ra^{0.252}$
Regime IV	$Ra > 1 \times 10^5$	$K_{eff}/K = 0/104\ Ra^{0.305}Pr^{0.084}$

Although correlations are actually for Nusselt number, the K_{eff}/K ratio is the same since, $K_{eff} = hL$.

Node Sensitivity Study

To avoid excessive computer time usage without compromising modeling accuracy, a study was made to determine optimum node spacing. Although the study included both the modified and unmodified conduction models, no significant differences were noted.

Half of a 1.9-cm (3/4-in.) cell was modeled. The cell was assumed to be isothermal along its width, so that heat was allowed to transfer only in the cell height and length directions. The nodes were arranged in square patterns. The node sizes examined ranged from 0.16-cm (1/16-in.) to 0.95-cm (3/8-in.). The melt front position versus time data was used for comparison.

Figure 37 shows the convective model runs. From this data, it can be seen that there was a significant difference in data output when comparing 0.48-cm (3/16-in.) node data with 0.32-cm (1/8-in.) node data. However, when the 0.16-cm node data was run, the interface position matched that of the 0.32-cm node model, within one percent for the range of values run. Stability runs using the sensitivity model also showed that a stable time step of 0.001 hours was required to avoid unstable data outputs.

As a result, all runs were made with nodes arranged in 0.32-cm square patterns, requiring 21 vertical nodes for the single cell model. In the case of the half model of the 1.9-cm cell, the node matrix was 3-by-21, and for the 0.64-cm (1/4-in.) cell it was 1-by-21.

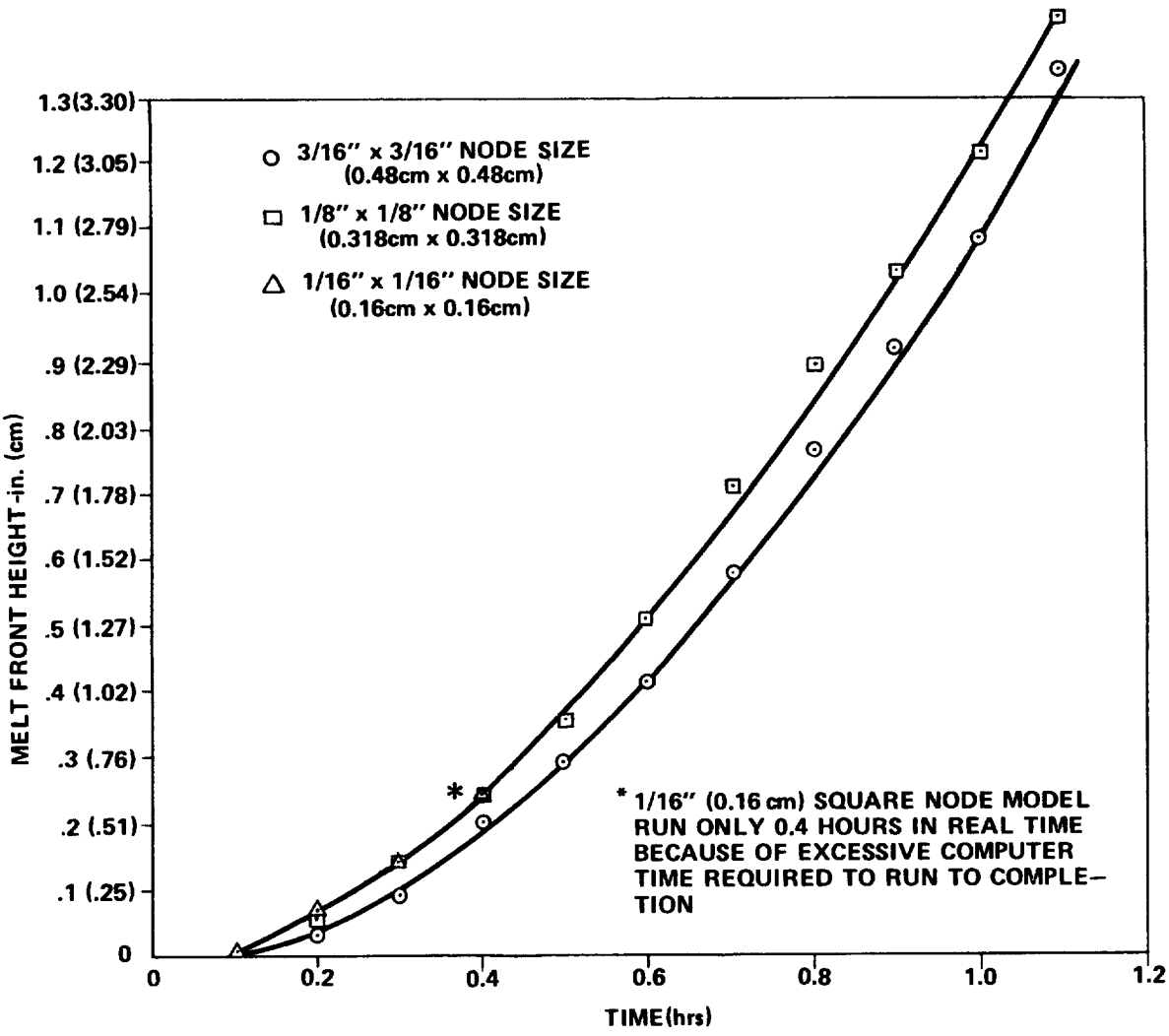

Figure 35. Node sensitivity study.

CHAPTER 6

DATA REDUCTION

Film Data Reduction

All motion pictures were screened on a Data Instruments Film Analyzer. The apparent phase change position versus time was recorded for the center of paraffin cells and at the innermost fins of the three representative cells. Early tests demonstrated that the plate which separated the coolant fluid and paraffin acted as an isothermal surface. For this reason, the melting of the 1.98-cm (3/4-in.) and 1.27-cm (1/2-in.) paraffin cells were nearly symmetric from inlet to outlet sides of the capacitor. Some edge effects were noted on the outer 1.9-cm cells, so that only the visual data from the innermost 1.9-cm cell on the fluid outlet was used for data reduction. The innermost 1.27-cm cell on the fluid outlet side of the capacitor and the center 0.64-cm cell were also used in visual data reduction (Fig. 36).

The film analyzer projects an enlarged image of each film frame on the moveable grid surfaces of the film analyzer (Fig. 37). Two grids allow sensing of both horizontal and vertical positions. These grids are electrically integrated with the interpreter section of the analyzer so that it automatically senses these positions. Each cell image is calibrated in the analyzer as the ratio of the known height, H, of the cell to the image height. The moveable

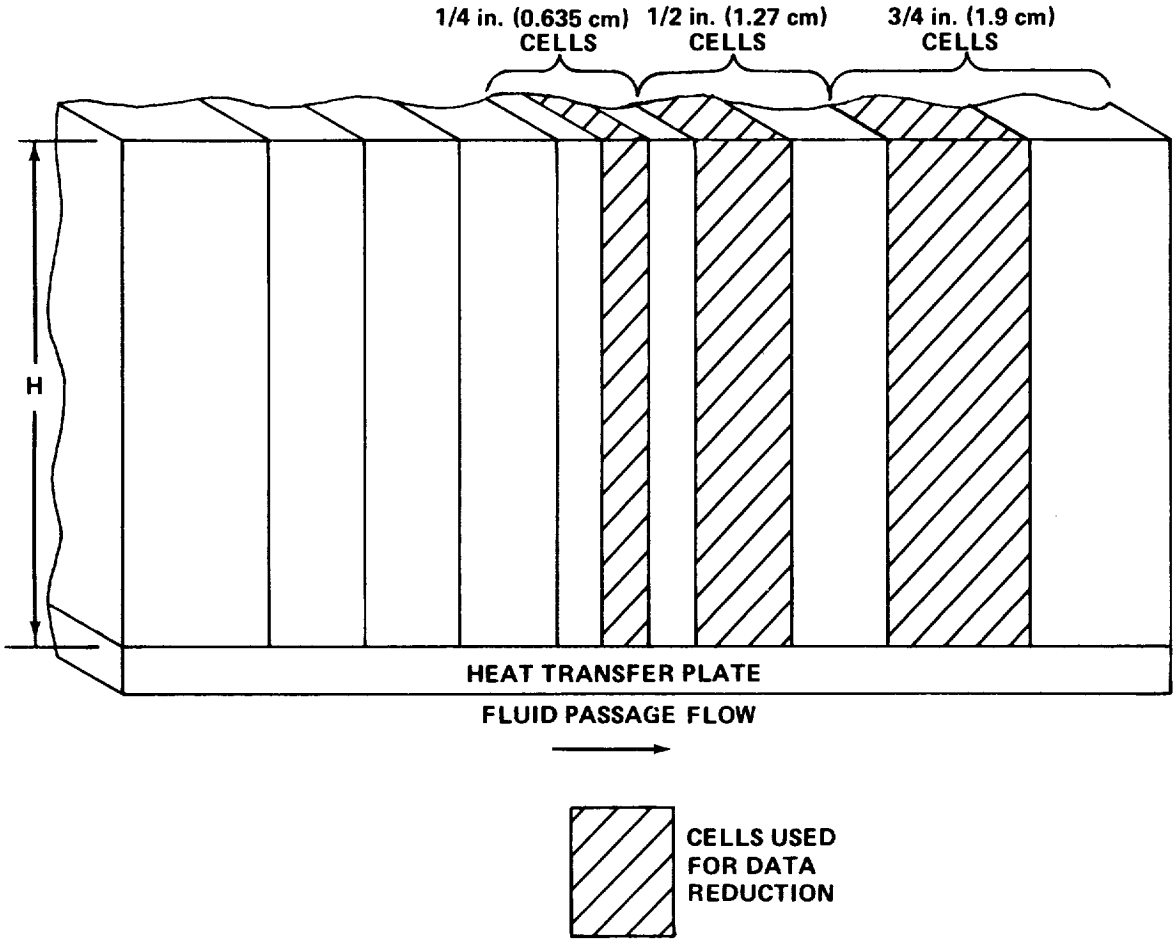

Figure 36. Visual data reduction cells.

horizontal grid was positioned over the phase change vertical position and the height was recorded by the interpreting electronics. These values, along with corresponding timer readings from the film, were fed in by the operator forming a bivariant height/time array. These data were automatically key-punched on computer cards for later use.

During melt tests, the phase change front position was obvious because of the well defined liquid/solid interface. However during freezing, a dark

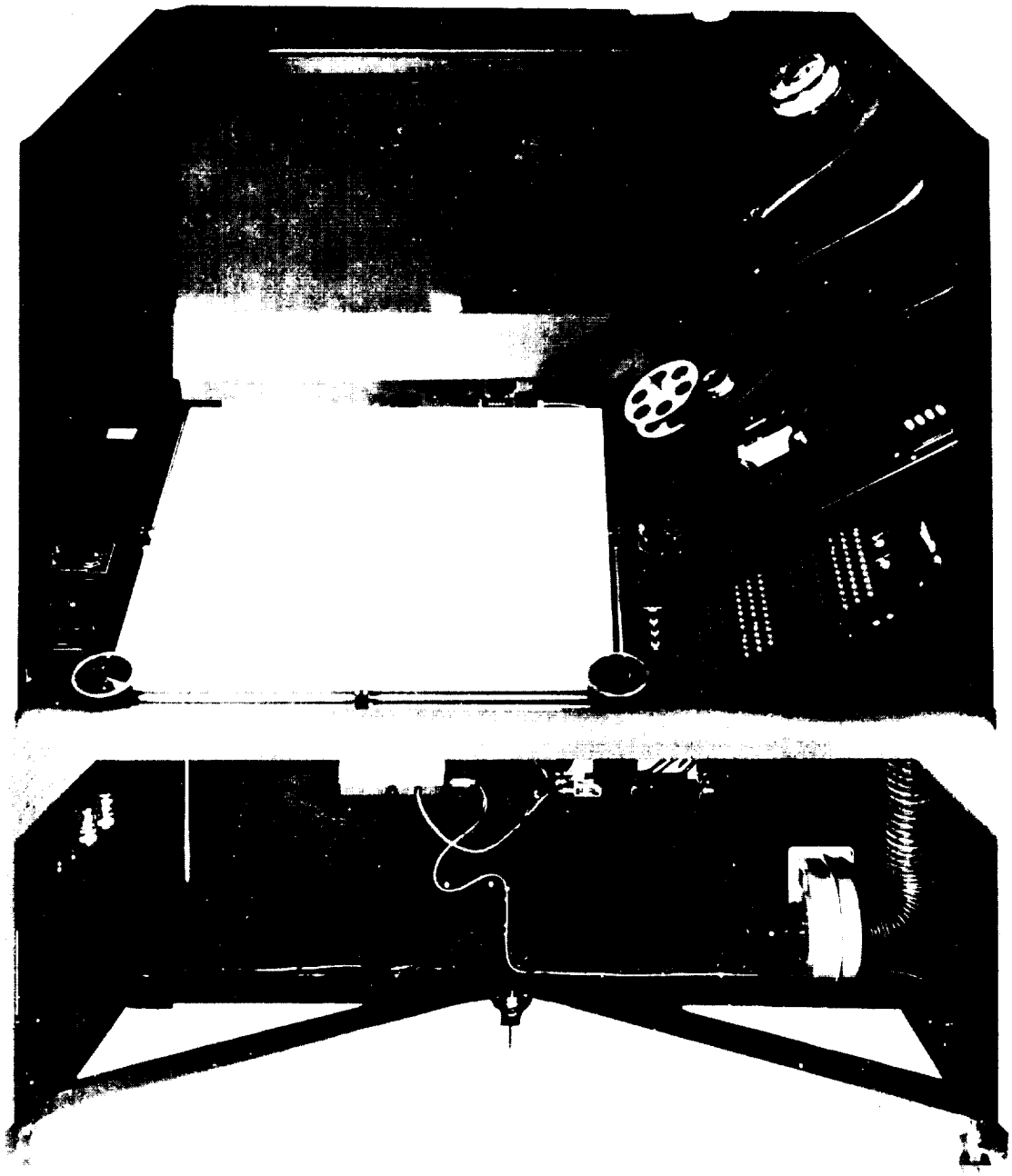

Figure 37. Data instruments film analyzer.

liquid/solid dendritic front progressed into the liquid phase, followed by a completely solid region characterized by a chalky appearance. Since the dendrite front progressed well in advance of the chalky region, some confusion as to the actual phase change front position resulted. As a result, a study was made to determine what line defined the front. The results of the study, discussed in Chapter 7, indicated the forward most dendrite penetration represents the phase change front. This definition is shown pictorially in Figure 38.

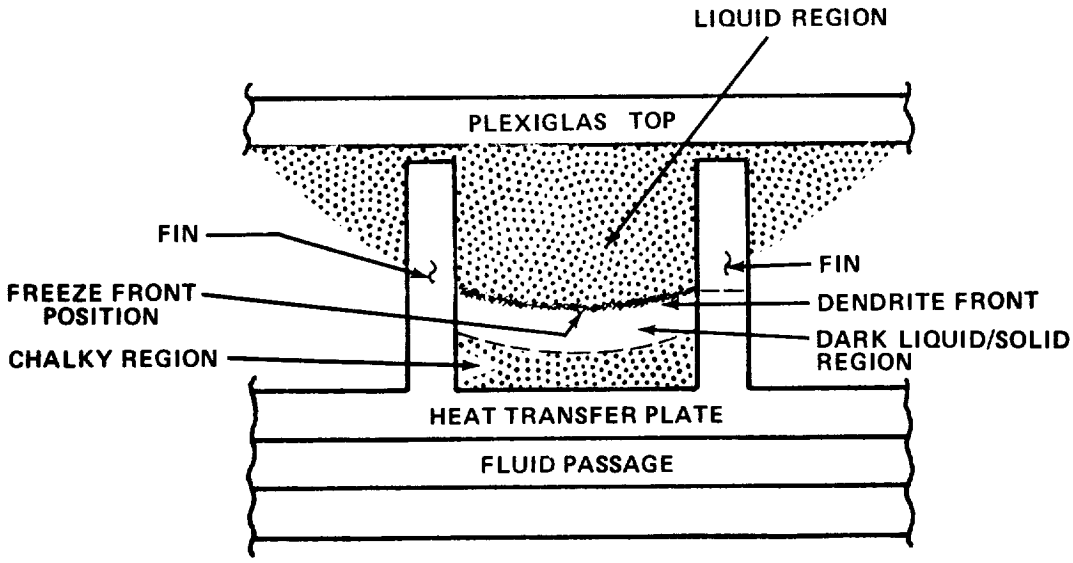

Figure 38. Freeze front definition.

Although only one individual transcribed most of the film data, two different individuals were used to take readings on selected runs to determine the possible reader error. Comparisons of the independent melt height readings showed that paired data varied no more than 0.127 cm (0.05 in.). However for the freeze test, the variations were as large as 0.38 cm (0.15 in.).

These paired readings were compared only for melt heights above 0.51 cm (0.2 in.) because the epoxy used to seal the paraffin housing to the fluid passage partially obscured readings below this level.

The data points on the computer cards output from the film analyzer were programmed, using an existing root mean square smoothing routine. Another routine was used to make linear approximation of the phase change front velocity by first fitting the smoothed height versus time data to a first degree polynominal, $x = a + bt$, and then differentiating this to get a constant velocity approximation $\frac{dx}{dt} = b$. This was justified by the fact that in most cases the height-versus-time data could be approximated by a straight line, with little error.

Freezing Temperature Data

The temperature probe profiles during all freeze runs were similar. A typical profile of temperature variation of the paraffin probes with time is shown in Figure 39 for a 1.9-cm (3/4-in.) inch cell, with numerical designations of significant events. Event number one designates the point at which the entire cell was at a uniform temperature. This point also coincides with incipent freezing at the cell bottom, which indicates that during freezing tests the initial cooling was devoted almost entirely to removing sensible heat from the liquid mass, cooling the entire cell to the paraffin freeze point. The temperature did not then drop significantly until the freeze front had passed through

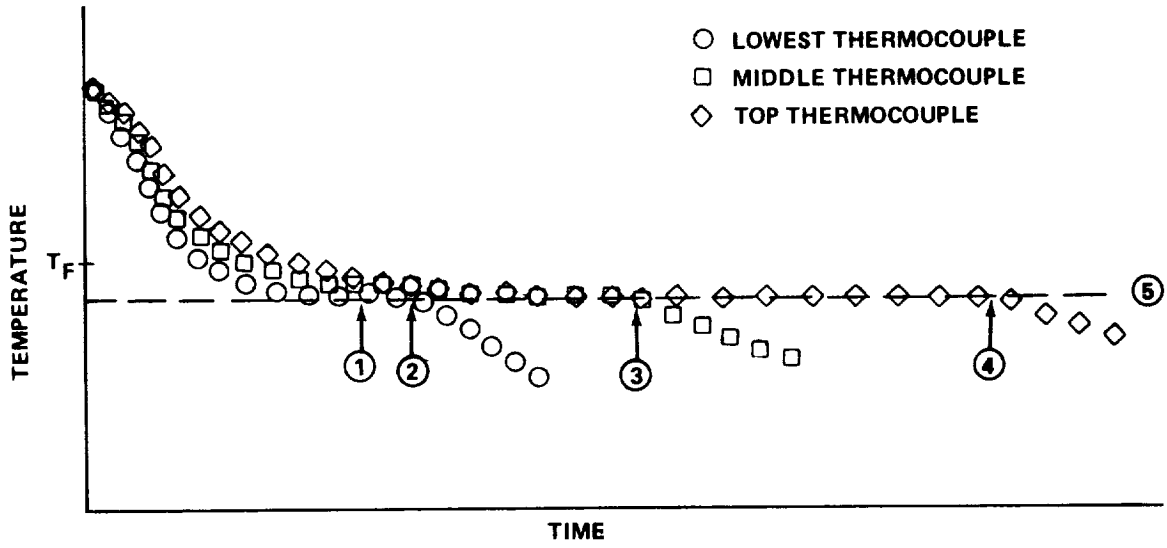

Figure 39. Typical 1.9-cm (3/4-in.) cell freezing temperature history.

the thermocouple positions which are designated as events two, three and four. From visual data, it was apparent that the dendrite front passed by the thermocouples just before their temperature started to drop from the plateau. The plateau temperature ranged from 29.5°C (85°F) to 32.3°C (90°F). In early tests, the plateaus occurred at temperatures near 90°F, however the plateau tended to occur at lower temperature during later tests.

A typical 0.635-cm (1/4-in.) cell temperature profile during freezing is given in Figure 40. In contrast to the 1.9-cm (3/4-in.) cells, in which all thermocouples reached the freeze plateau simultaneously (Fig. 39), the 0.635-cm cell freeze front passed consecutively through each respective thermocouple location (Fig. 40). This indicates that sensible heat was still being removed from the upper cell liquid while the lower cell had already frozen. This shows

fins to be the dominant cooling path in the small cells, whereas the lower plate is dominant at wider spacings. This effect was partially caused by the higher cooling rates due to the closer fin spacing in the smaller cells. Events one, three and five in Figure 39 represents the time at which the liquid had dropped into freeze temperature zone. Events two, four and six represents the freeze front passing the respective thermocouple positions. Point seven is at the freeze plateau level. The freeze plateau exhibited by the two cells were approximately equal.

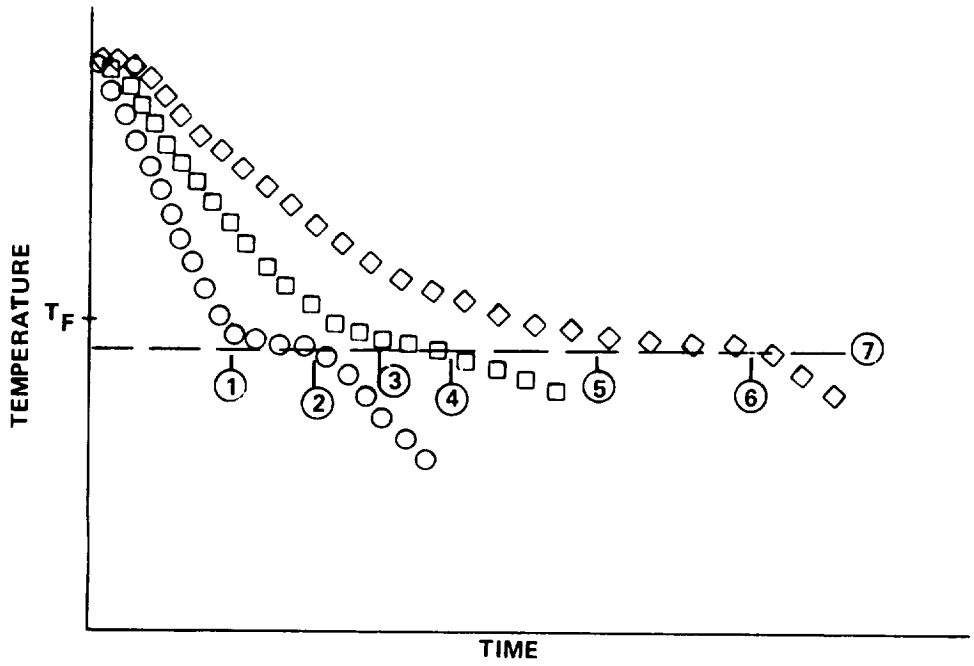

Figure 40. Typical 0.635-cm (1/4-in.) cell freezing temperature history.

Interpretation of Melting Temperature Data

A melting history comparison is shown in Figure 41, comparing the characteristics of melting front progression for low and high heating rates. Although the 1.9-cm (3/4-in.) cell melting temperature profiles were similar, there were differences, depending on the heating rates. Point one corresponds to a temperature level at which a marked increase in the rate of temperature rise begins. From observations, the melt front appeared to pass the thermocouple locations just after the temperature rise occurred and well before point two was reached, at temperatures slightly below the published melting point. Point two corresponds to a characteristic overshoot, followed either by a temperature leveling at point three or a slight drop. After maintaining a plateau (represented by point four) for a period of time, the fluid temperatures dropped to a level represented by point five, prior to the cell being completely melted. Also prior to complete melting, temperatures recorded in the liquid exhibited unstable oscillations between points two and six levels. At six, the cell was completely melted and all thermocouples rose above the pseudo plateau level.

For the low heating rate experiments, the temperature rise which had occurred in the high heating rate cases was either greatly diminished or completely absent. The temperatures slowly rose to a plateau at point seven only slightly above the published melting point, with the phase change occurring at point eight as each thermocouple reaches the plateau temperature. Again

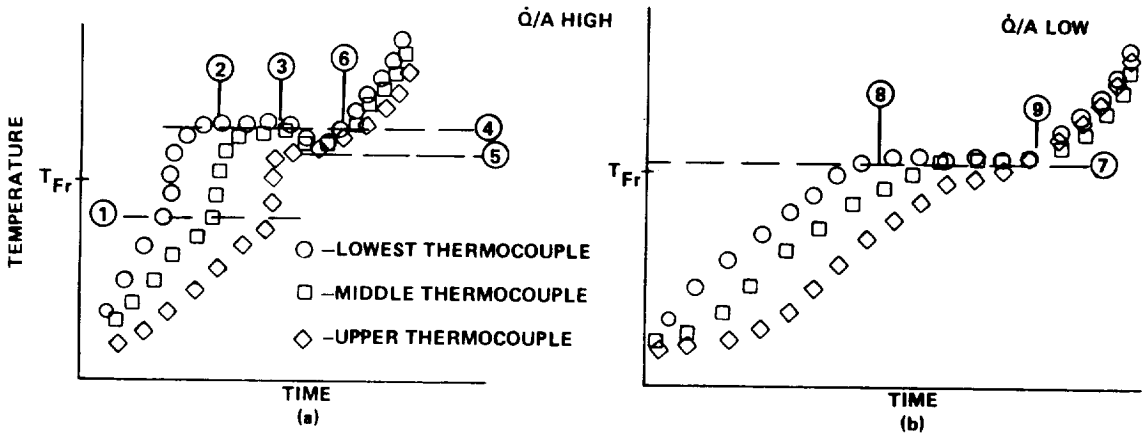

Figure 41. Typical 1.9-cm (3/4-in.) cell melting temperature history.

after the cell was completely melted, all liquid temperatures started to rise sharply, as indicated by point nine. Although unstable temperature oscillations were present between eight and nine, they were diminished and of a higher frequency than for the high heating rate cases.

The 0.635-cm (1/4-in.) cell data is not worthy of separate discussion since the primary difference as compared to the 1.9-cm (3/4-in.) cell data, was the delay time at the plateau temperature. In the case of the 0.635-cm cell, the plateau consisted only of a slight curve inflection near the values of the 1.9-cm (3/4-in.) cell plateau. In the fast melt cases, the 0.635-cm (1/4-in.) cell melted so rapidly, that in some cases temperatures in these cells reached a second higher plateau corresponding to the liquid equilibrium value.

Test Observation

Figures 42 through 49 show views of the thermal capacitor cells during the phase change process for four arbitrarily selected times. Low and

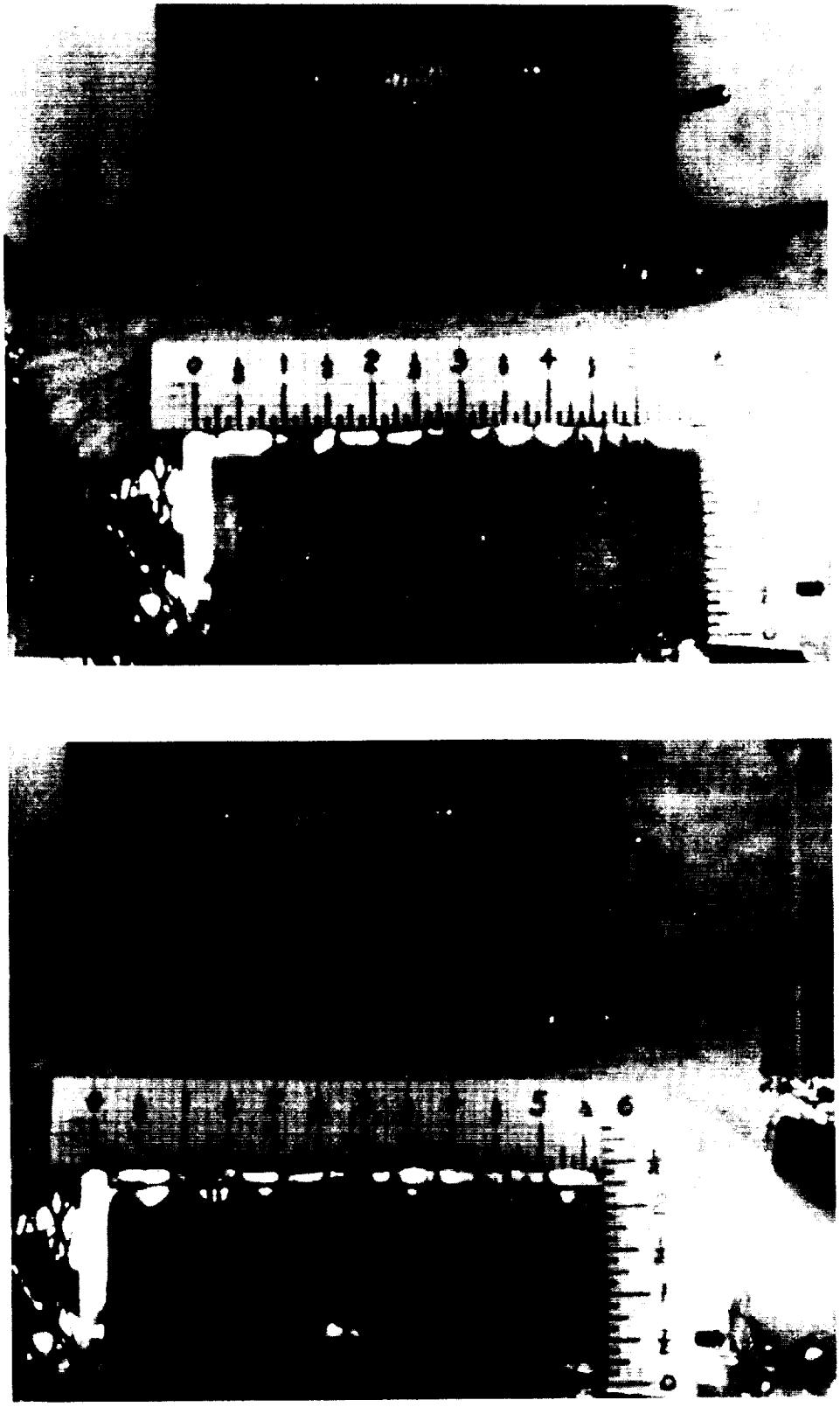

Figure 42. Initial stages of slow melt phase change process.

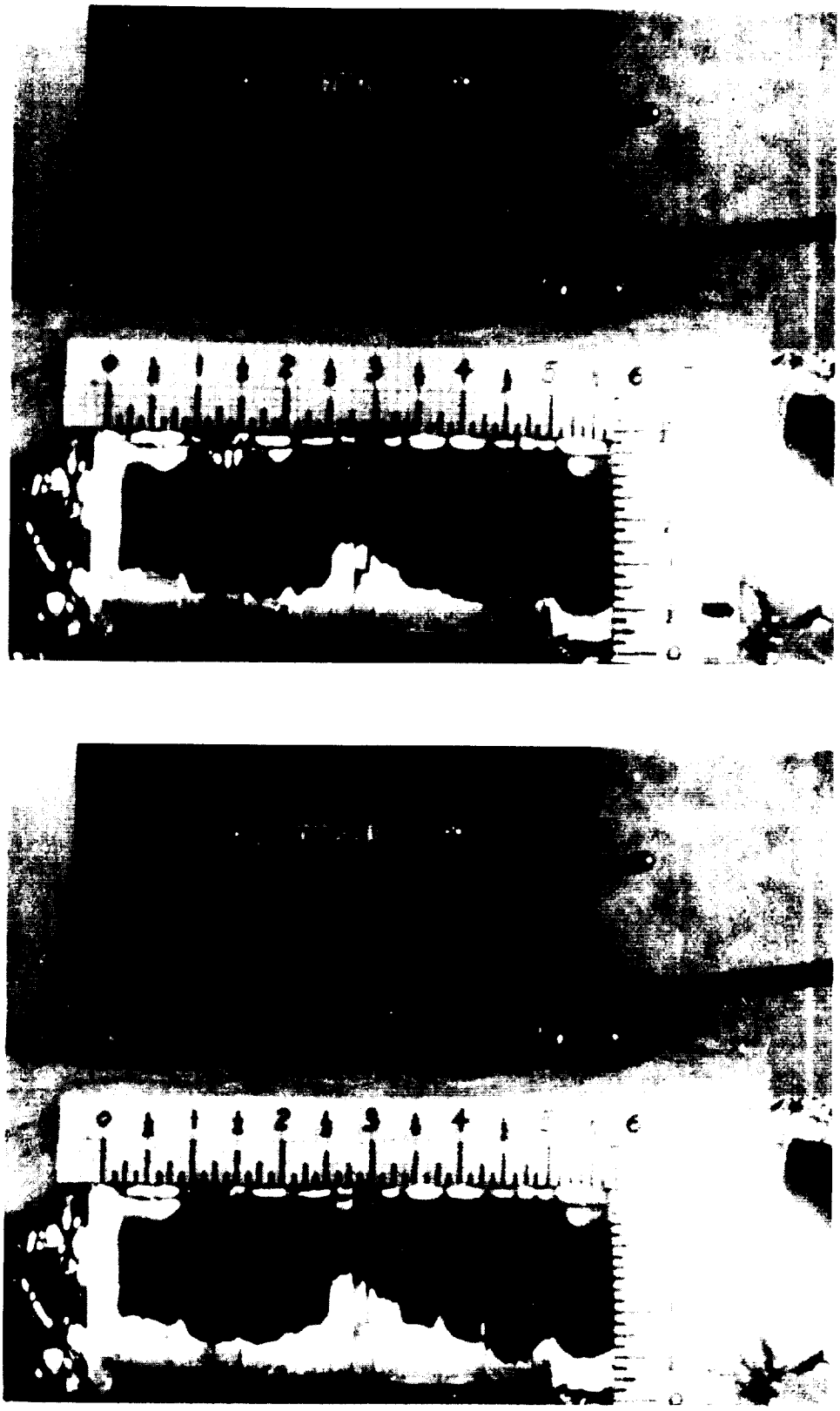

Figure 43. Final stages of slow melt phase change process.

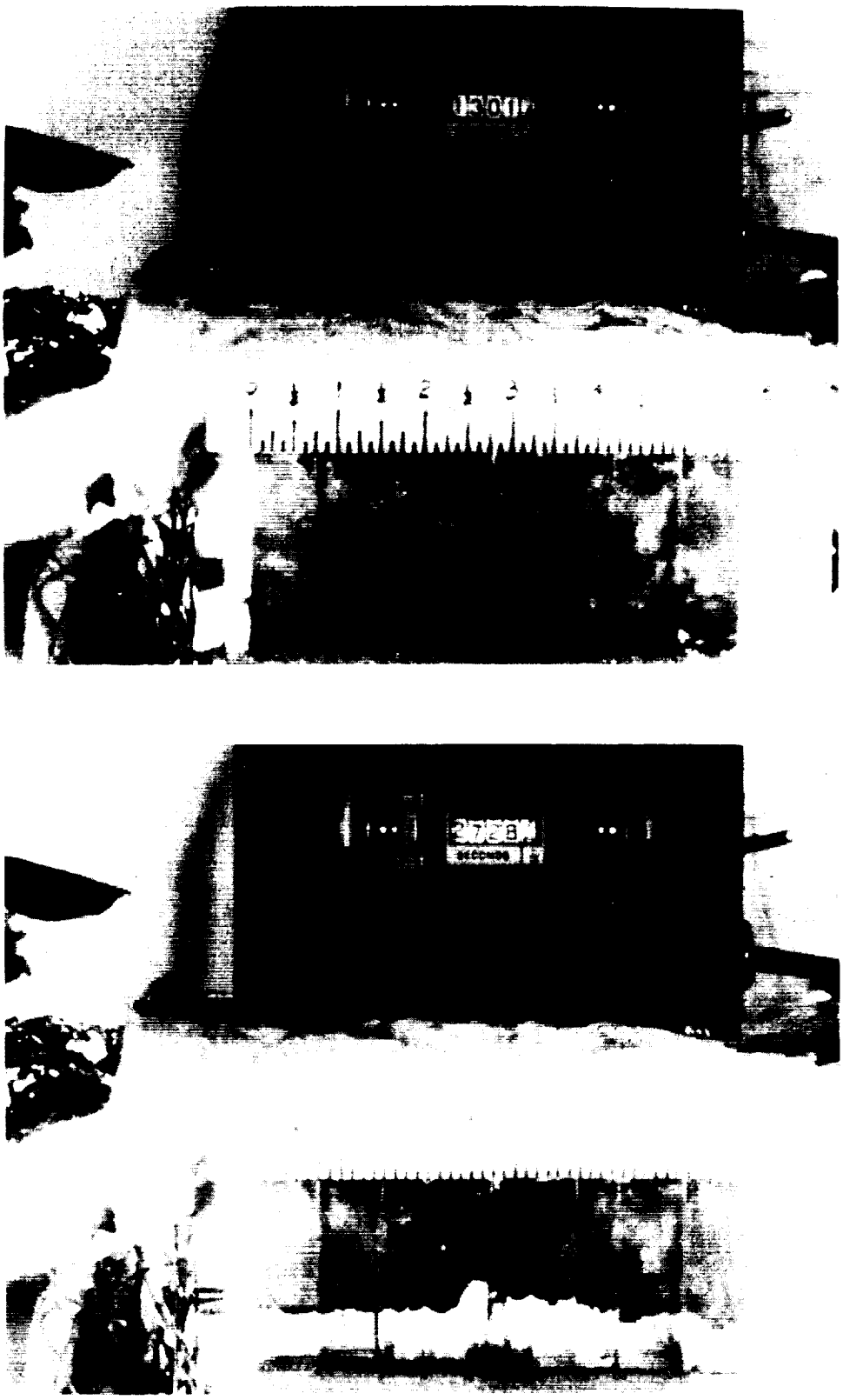

Figure 44. Initial stages of fast melt phase change process.

Figure 45. Final stages of fast melt phase change process.

Figure 46. Initial stages of slow freeze phase change process.

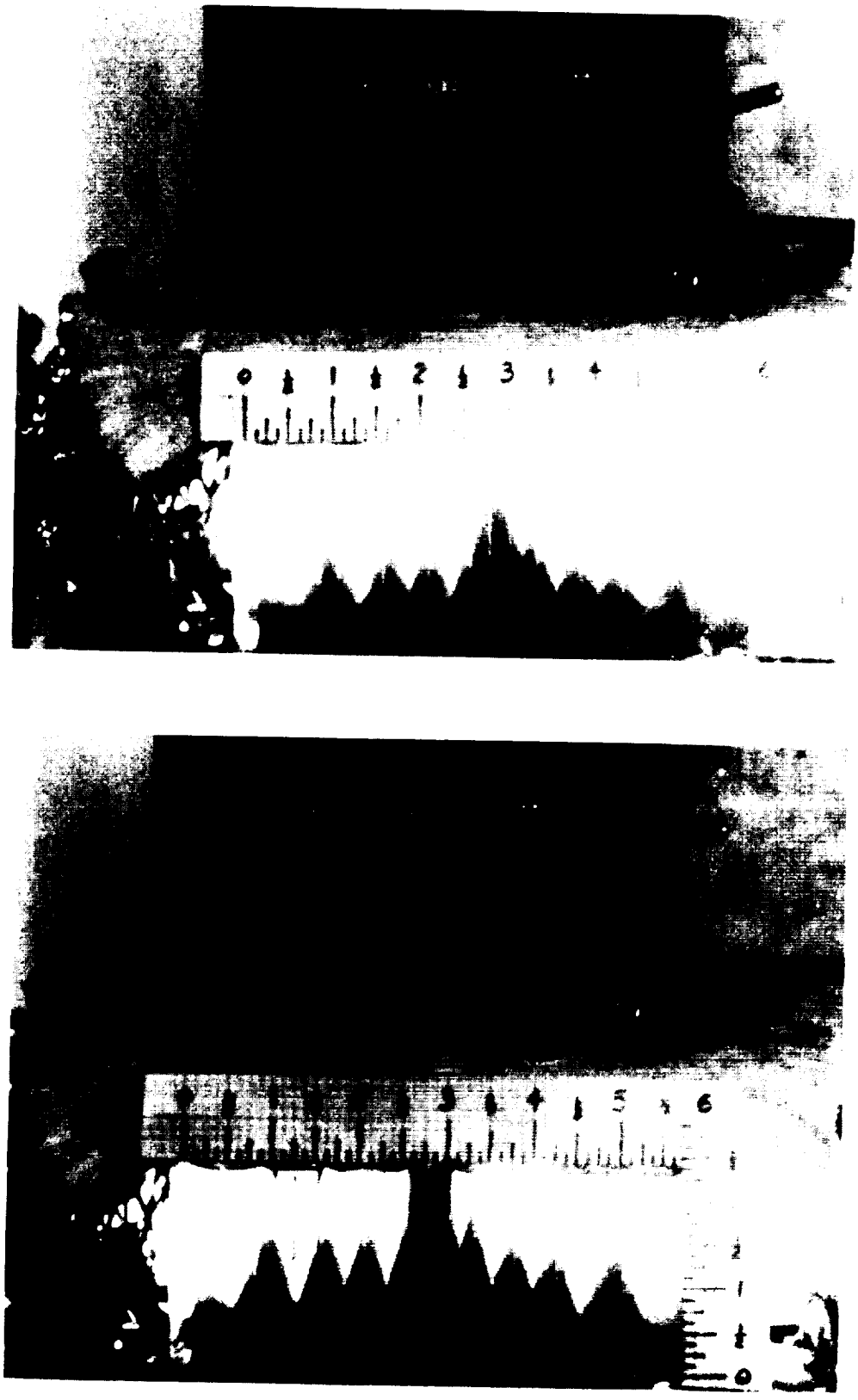

Figure 47. Final stages of slow freeze phase change process.

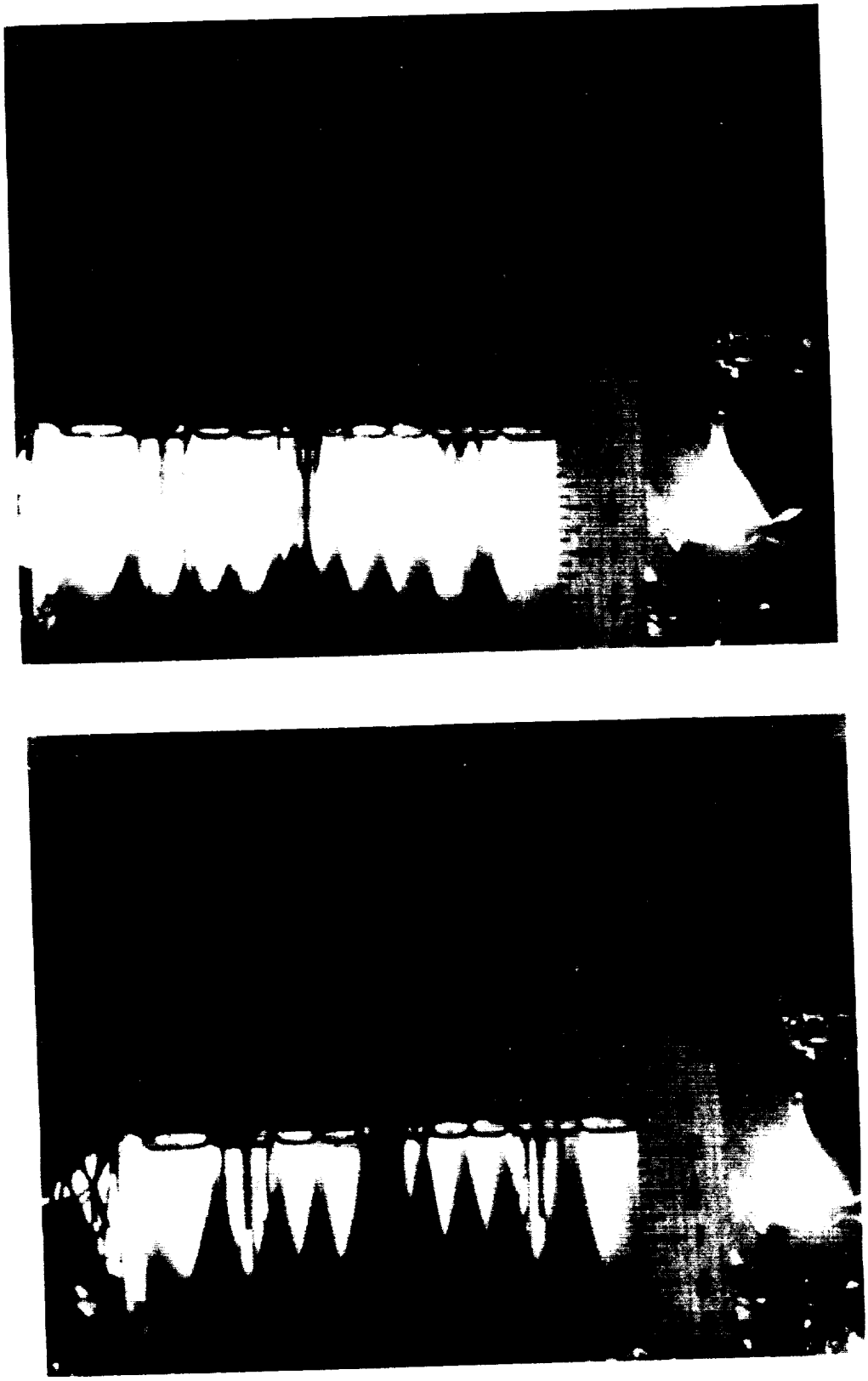

Figure 48. Initial stages of fast freeze phase change process.

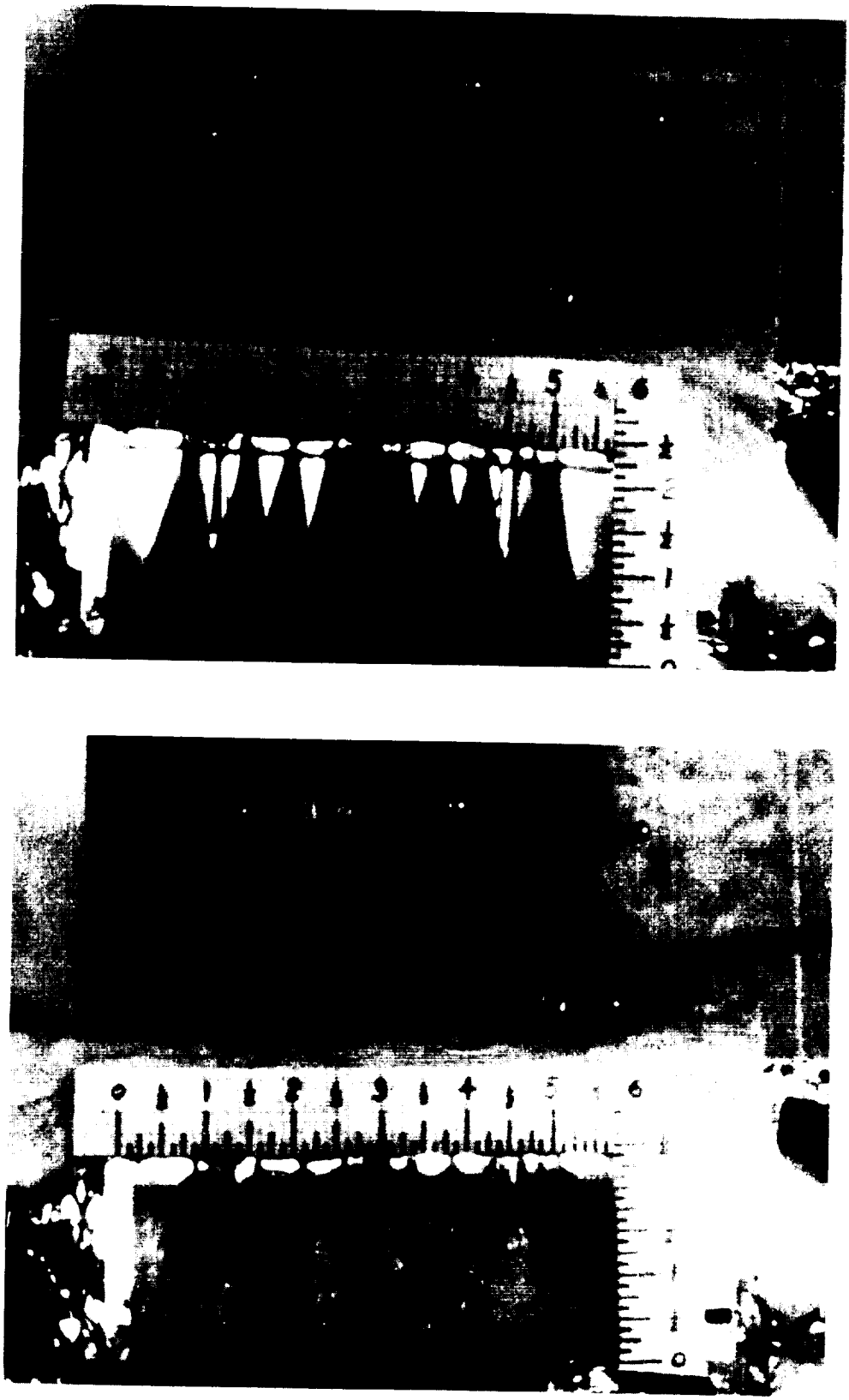

Figure 49. Final stages of fast freeze phase change process.

and high heating rate tests (230-59 and 230-49) and low and high cooling rate tests (230-54 and 230-58) are presented, respectively. It appears from these photographs that the zero point on the vertical scale is below the plate level. However, as discussed earlier, the bottom of the cells are obscured by an epoxy coating used to seal the bottom plate to the coolant passage. The rear epoxy line appears as a lighter horizontal line in these photographs. The irregular dark vertical lines appearing in the 1.9-cm (3/4-in.) and 0.635-cm (1/4-in.) cells are thermocouple wires of which the wider ones are the freely suspended sheathed wires and the narrower ones are the wires leading to plate and fin thermocouples.

The absence of photographs of elevated phase change interface heights near the top of the cells was caused by two limitations. The first was due to the prohibitive length of time required to run a complete capacitor phase change cycle, especially in low heat flux tests. The second, which occurred in the case of melting only, is the fact that when the cells had melted to within 1.27 cm (1/2 in.) of the top, the unmelted solid tended to slide down into the liquidus region. Either of these reasons was sufficient to terminate a test.

In the case of melting (Figures 42 through 45) some disparity is seen between the melt heights of the 1.9-cm (3/4-in.) cells on the right and left sides of the capacitor. This disparity occurred only in a few tests and was discernable in these photographs. The nebulous appearance is due to fur-like dendrite formations at the interface, shown magnified in Figure 18A.

Also the nearly planar front evident in the melting photographs gives way to a sharp saw tooth freeze front profile. The saw tooth profile is less pronounced for the closer fin spacing because the freeze front moving up the fins and the cell center are merged.

Comparison of the meniscus formed in the upper portion of each frame, between the ullage and the liquid, indicates a decreasing level with time. This decrease is caused by freezing contraction occurring in the paraffin, and was most pronounced in slow melting tests as shown by comparison to the fast melting and freezing photographs. Since the melting heights were repeatedly higher on the coolant inlet side (i.e., left side in photographs), the bottom plate was apparently not exactly isothermal, but sustained a temperature gradient, increasing from inlet to outlet sides.

In both rapid and slow cases it is obvious that the 1.9-cm (3/4-in.) and 1.27-cm (1/2-in.) cell melting rates are nearly equal. However, a much faster rate is seen in the 0.635-cm cell.

In Figures 46 through 49 (representing slow and fast freezing), the liquid/solid interface, which was well defined in melting, appears nebulous. Although not well defined in the photographs, the rough dendrite interface is visible as a dark region. For those frames in which the freezing of the cell is nearly complete, the chalky zones are visible.

It is obvious that the freeze rates are much slower than the melt rates. This is caused by loss of convection in the freezing modes.

CHAPTER 7

DISCUSSION OF EXPERIMENTAL AND ANALYTICAL RESULTS

Phase Change Temperature

Because the apparent temperature plateau achieved during melting tests did not correspond to the phase change temperatures exhibited during freezing, only freeze tests were used to estimate variations in the phase change temperature. From discussions to be given later, it will be apparent that the phase change temperature was not constant. Figure 50 shows a plot of the measured freeze temperature as a function of time. It can be seen from this Figure that the apparent freeze temperature decreased with time. This was accompanied by a "yellowing" of the solid paraffin, which had been initially chalky white in the solid state.

To account for this apparent change in the freeze temperature in the numerical work, the phase change temperature used in the numerical computations was altered to agree with experimental freeze data. However, since numerous investigators have reported that deviations between freezing and melting temperatures are common, referred to as phase change hysteresis, the phase change temperature was not altered for numerical predictions corresponding to the melt tests. However, for a single melt test, computer runs were made with varying phase change temperatures to illustrate the effect

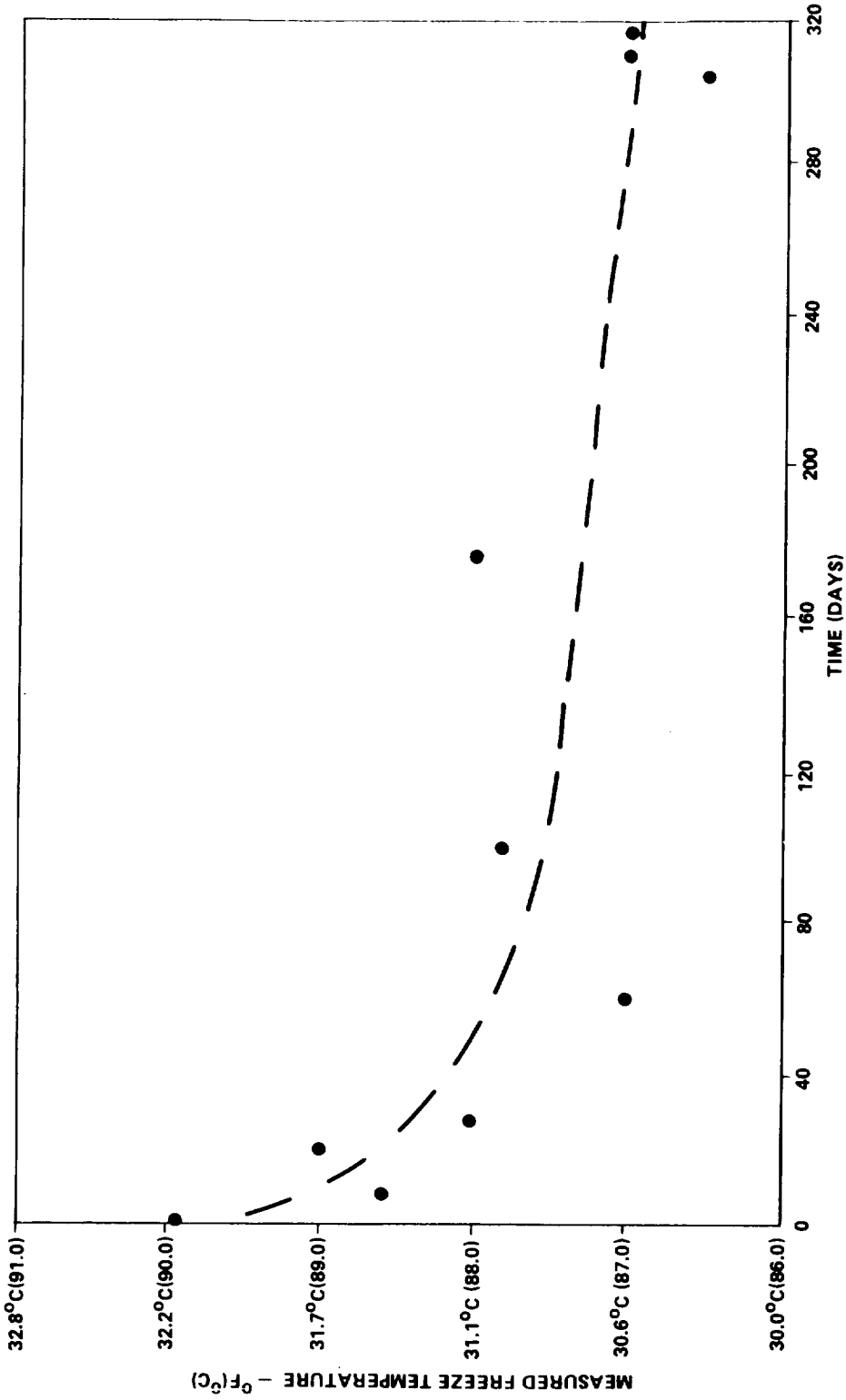

Figure 50. Measured freeze temperature variation.

of altering this property. The influence of changing the fusion temperature on numerical predictions for the selected melt runs is illustrated in Figure 51.

From this Figure it can be seen that small changes in the melting temperature drastically alter the predicted melt height velocity. As this temperature is depressed, the onset of increased interface velocity occurs earlier. This is explained by the fact that for the same boundary temperature in both cases the temperature difference in the Rayleigh Number expression is proportionately higher for the case with lower melting temperature. This reduces the height at which the onset of convection occurs and thereby causes the melting velocity to increase at an earlier time. No such drastic differences were noted for the predictions for freeze runs since contributions due to convection were absent and accordingly omitted from the numerical model.

Apparent Heating/Cooling Rates

The apparent experimental heating/cooling rates for tests were determined by using appropriate paraffin property data along with the interface velocity information discussed in Chapter 6.

Since the 1.9-cm (3/4-in.) cell freeze and melt fronts approached a planar front, a uniform horizontal front was assumed. Even though the front was not exactly planar, especially in the freezing case, this is an acceptable approximation since the phase change front velocity, which was used to determine the experimental heating/cooling rates, did not alter shape with time.

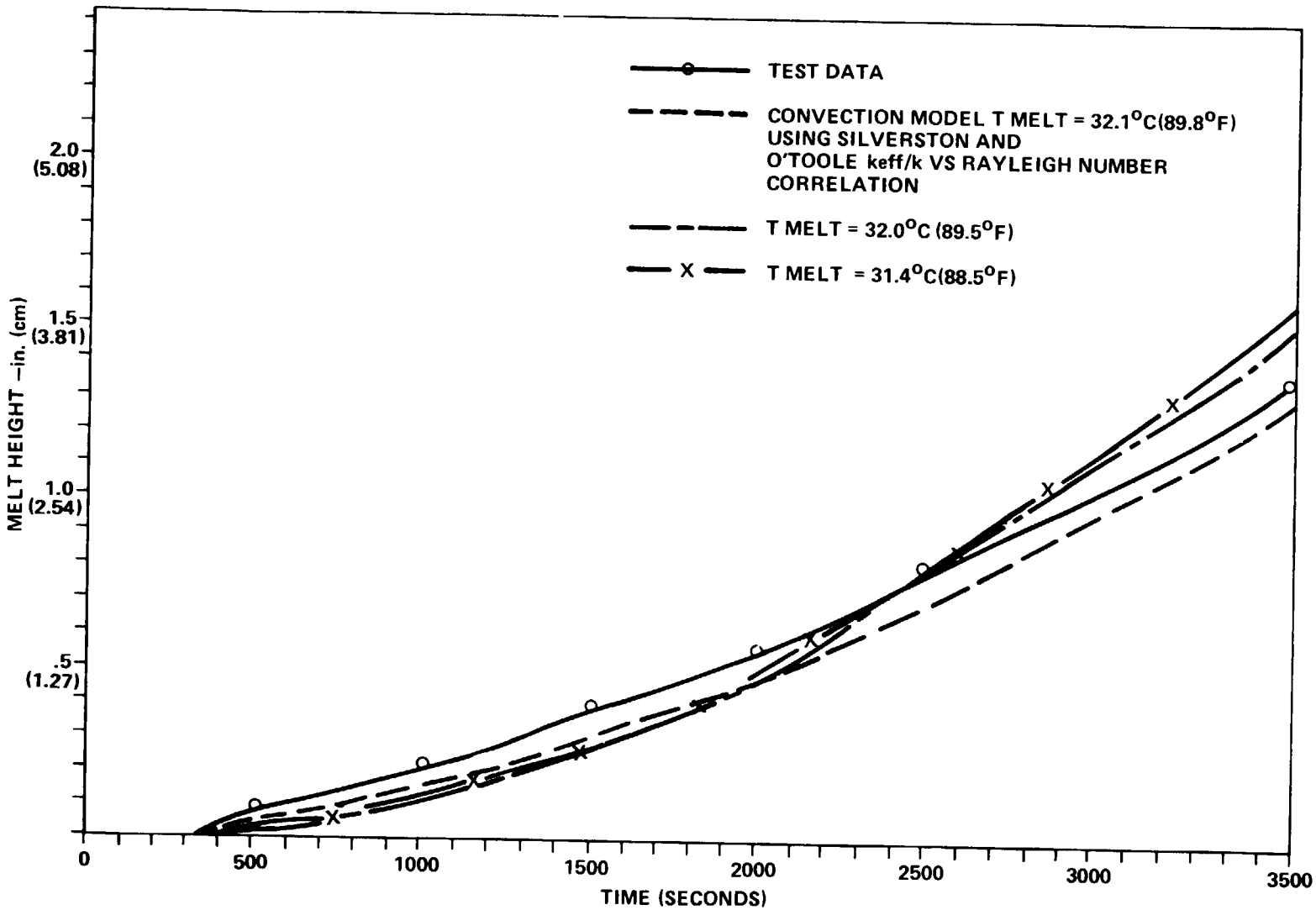

Figure 51. Comparison of test data to predicted data.

Also, since the sensible heat absorbed/rejected by the paraffin and its housing were small compared to the heat absorbed/rejected by the phase front, all of the energy transfer was considered to produce phase change. Finally, to express the heating/cooling rates on a unit area basis, the lower plate was considered to be the base area through which the heat was transferred. Visual data revealed that the assumption of a planar interface was not valid for 0.635-cm cells. As a result, heating and cooling rates and fluxes are given only for 1.9-cm (3/4-in.) cells.

Using the approximations outlined above, the following equations were used to generate experimentally determined heating/cooling rates,

$$\dot{Q}ap = \rho \frac{ds}{dt} V \Delta H$$

and

$$(\dot{Q}/A)ap = \dot{Q}_{ap}/A_{bp}$$

These values are given in Tables 6 and 7.

Comparison of Experimental and Analytical Data

The experimental data were compared to analytically generated interfacial positions at varying times. Although the analytically predicted temperature profiles with respect to time and distance are discussed, it should be emphasized that the primary objective in formulating the numerical model was to match the interface position data, and consequently the rate and flux data. It was realized that the artificial manner in which convective effects were incorporated into the numerical model would not provide accurate predictions of the temperature field in the liquid region.

TABLE 6. 1.9-CM (3/4-INCH) CELL COOLING RATES AND FLUXES

Test	Freeze Front Velocity		$\dot{Q}_{A.P.}$		$(Q/A)_{A.P.}$	
	(cm/sec × 10^{-4})	(in./sec × 10^{-4})	(J/sec)	(Btu/hr)	(J/m^2-sec)	(Btu/hr-ft^2)
230-7	4.83	1.90	1.42	4.86	568.0	180
230-10	4.32	1.70	1.27	4.35	508.0	161
230-11	2.54	1.00	0.76	2.60	303.0	96
230-15	2.18	0.86	0.64	2.20	258.5	82
230-51	4.27	1.68	1.26	4.30	501.2	159
230-52	3.30	1.30	0.96	3.28	384.6	122
230-53	2.11	0.83	0.62	2.12	249.2	79
230-54	1.34	0.53	0.43	1.46	170.2	54
230-55	1.04	0.41	0.31	1.05	122.9	39
230-56	1.02	1.40	1.05	3.58	419.3	133
230-58	4.75	1.87	1.40	4.79	561.1	178

TABLE 7. 1.9-CM (3/4-INCH) CELL HEATING RATES AND FLUXES

Test	Melt Front Velocity		$\dot{Q}_{A.P.}$		$(Q/A)_{A.P.}$	
	(cm/sec × 10^{-4})	(in./sec × 10^{-4})	(J/sec)	(Btu/hr)	(J/m^2-sec)	(Btu/hr-ft^2)
230-5	9.4	3.7	2.77	9.47	1106.5	351
230-6	4.6	1.8	1.35	4.61	539.1	171
230-8	2.3	0.9	0.67	2.30	268.0	85
230-9	9.1	3.6	2.70	9.22	1075.0	341
230-49	8.4	3.3	2.48	8.45	986.7	313
230-50	5.6	2.2	1.65	5.63	662.0	210
230-57	8.1	3.2	2.40	8.19	955.2	303
230-59	1.8	0.7	0.47	1.79	208.1	66
230-60	4.1	1.6	1.17	4.0	472.9	150

Freeze Temperature Profiles

In the case of freezing, the analytically produced temperature profiles versus time and distance matched quite well with experimental results. Typical comparisons are shown in Figures 52 and 53.

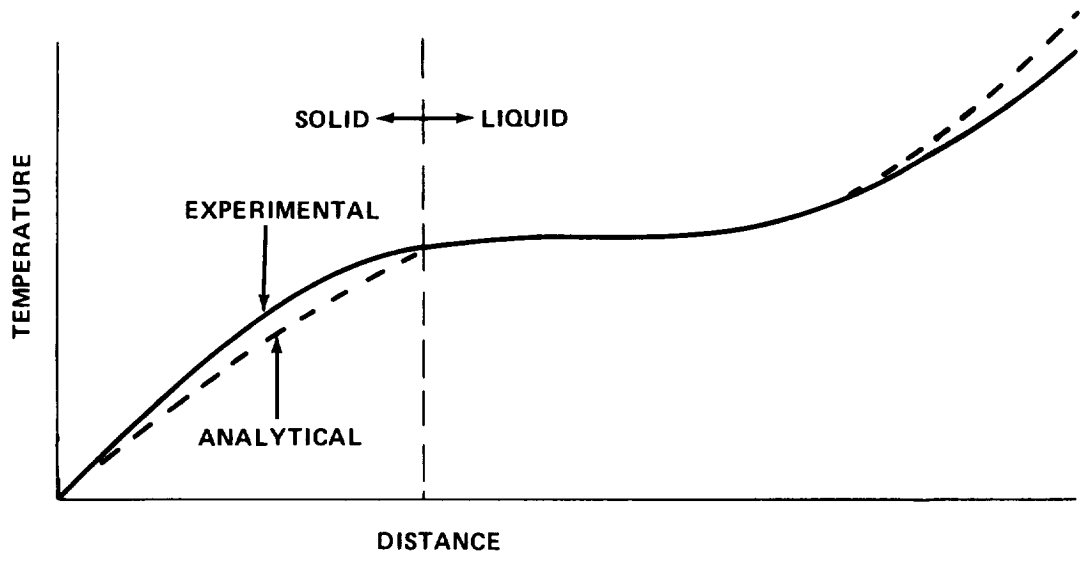

Figure 52. Freeze test temperature versus distance.

From Figures 52 and 53, it is apparent that the largest discrepancy is in the solid region. This is due to the method by which the heat transfer surface area was artificially increased for all nodes to account for the augmented interface velocities, thereby causing an apparent increase in the thermal conductivity of the paraffin. In the liquid region, the temperature profile tended to yield a better match for the experimental data with augmented transfer area, indicating the thermal diffusivity properties used for the liquid were either low or that some convection was occurring in the liquid during

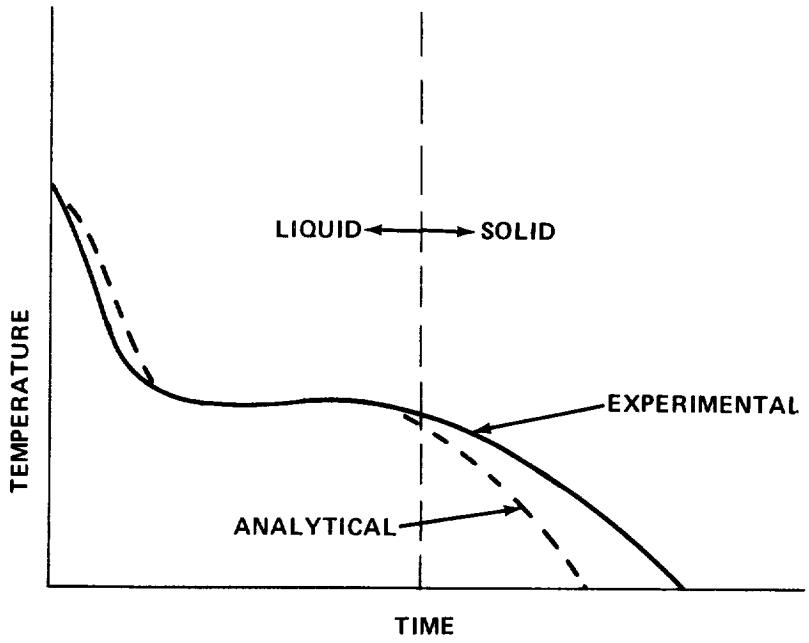

Figure 53. Freeze test temperature versus time.

freezing. This was possible, to a degree, since the fins were typically cooler than the paraffin in the center of the cell, giving rise to a doublet with flow from the fins toward the center, see Figure 54.

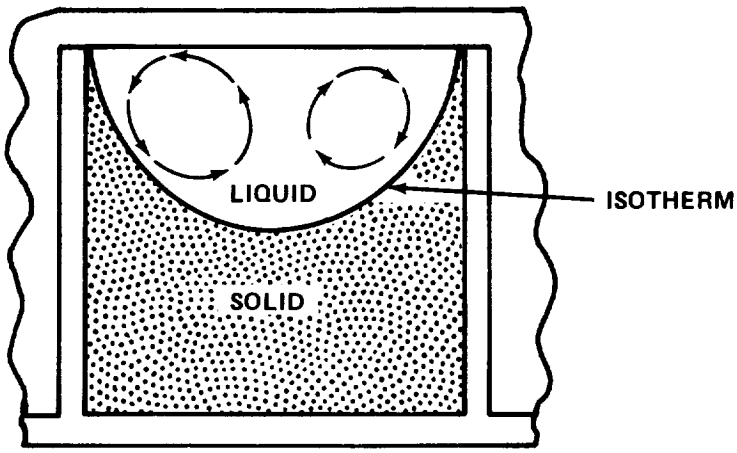

Figure 54. Possible doublet flow during freezing.

The temperature plateau in the liquid portion of the cell formed quickly and was maintained as the freeze front passed through the entire cell. This indicated that most sensible heat was removed from the paraffin before latent heat removal started. The plateau apparently was caused by the liquid region being surrounded by a nearly isothermal freeze boundary. Although not apparent on filmed data, visual inspections and the freeze models indicated a thin freeze film occurred on the fin and plate wall almost immediately. This is consistent with the rapid drop in fin and plate temperature. On reaching the freezing temperature, the fin temperatures leveled out until the freeze front had passed through the vicinity.

As noted earlier, the plateau temperature decreased below the published phase change temperature with time. From inspection of the test data, it was apparent that this depressed plateau was the temperature level at which phase change was actually occurring. Since most freeze tests were slow, it could be easily determined that the liquid dendrite front had passed the thermocouple at about the same time the thermocouple indicated a "decline" from the plateau. Since phase change had to be occurring on the dendrite zone or the chalky zone, and the chalky zone passed through at temperatures well below plateau values, the freeze front was taken to be the line of demarcation between the liquids and dendrite zones and the corresponding plateau was then considered to be the freeze temperature.

Apparently the depression which occurred in the measured fusion temperature could be a result of contaminants ingested during testing, or already present in the newly procured paraffin. The cause for this freezing point depression was not investigated.

Melt Temperature Profiles

The predicted and experimental results for melt tests exhibit more of a discrepancy in temperature versus time and distance data, see Figures 55 and 56. The primary reason for this is the artificial way in which the effective thermal conductivity of the liquid was used to account for convective effects. The analytical predictions, based on a pure conduction model with the thermal conductivities modified in the liquid, do not reveal a constant temperature plateau. The experimental data, although exhibiting some oscillations, remains relatively constant at a plateau value for a period of time inversely proportional to the heating rate.

The plateauing is immediately preceded by a temperature jump. This jump may be due to the film coefficient which occurs at the liquid/solid interface as a result of convection in the liquidus region. The convection is a result of buoyancy induced convection in the fluid cell. In the case of melting, the mixing action of the convective currents caused the pseudo-plateau, as opposed to the isothermal boundary causing the plateau in the freezing case. The unsteady oscillations in the liquidus plateau region are caused by these

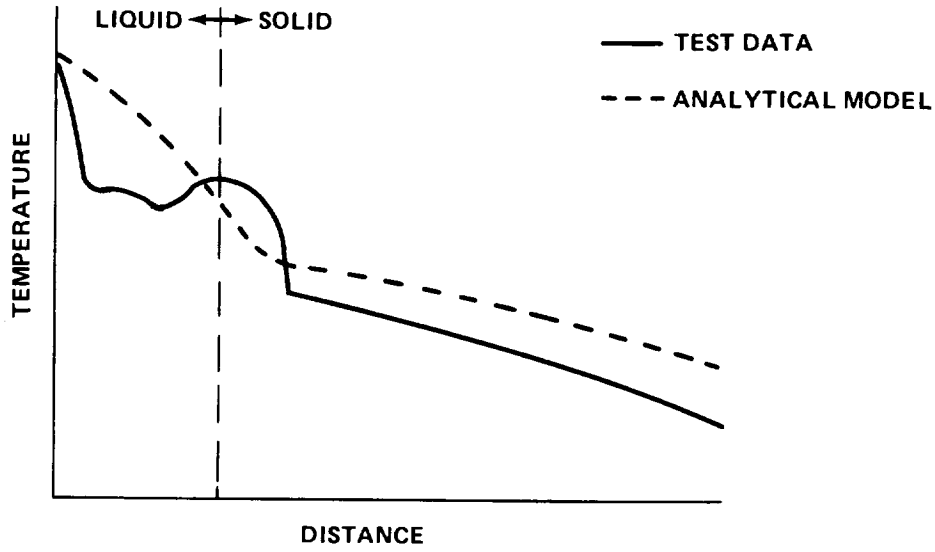

Figure 55. Melt test temperature versus distance.

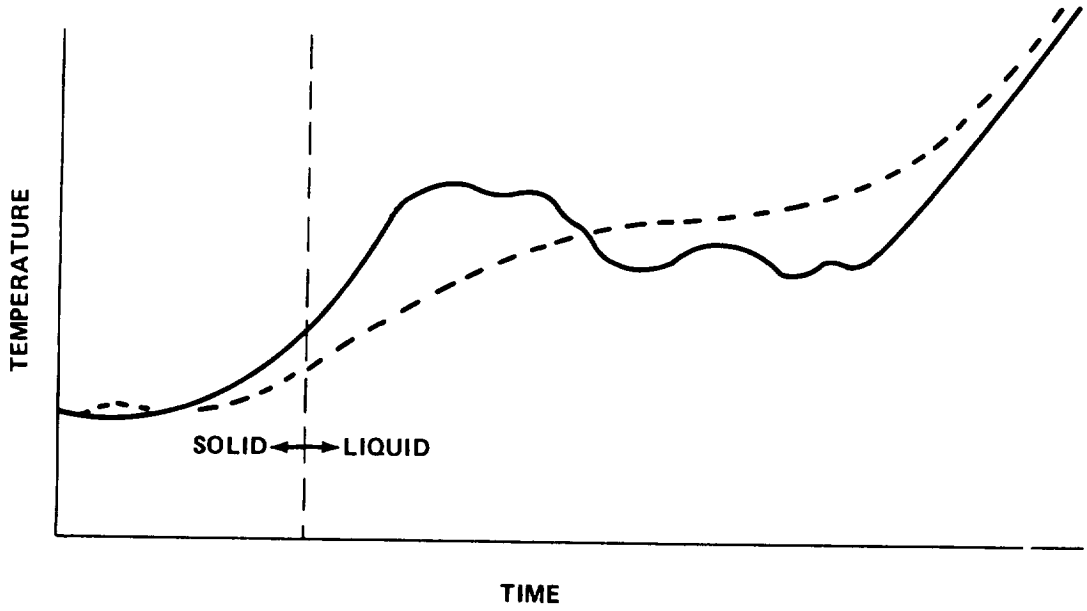

Figure 56. Melt test temperature versus time.

convective currents. Since these tests were run, Griggs [78] has run tests on individual cells which verify the occurrence of these oscillations. The plateau level is dependent upon the mean temperature between the melt temperature value at the solid/liquid interface and the plate temperature. Typically a simple averaging of these two values at any time approximated the plateau level. The plateau level is maintained in the cell until the entire cell is melted, which is followed by a rapid rise in all measured liquid temperatures. A second plateau is reached in some cases. This plateau is the limiting temperature of the cell, slightly lower than the plate temperature.

As the heating rates were increased and for narrow fin spacings, the plateau became less pronounced, tending to disappear with very high heating rates in the 0.635-cm (1/4-in.) cells. Reference 77 verifies these findings, showing that the plateau duration in time and absolute level is a function of cell wall material as well as heating rates.

Freeze Front Position

Comparison of measured transient freeze front position histories with corresponding numerical predictions are shown in Figures 57 and 58 for slow and fast cooling rates, respectively. From these figures it is apparent that a pure conduction modeling technique under-predicts the transient freeze interface position as well as the freeze front velocity.

A literature research reveals this disparity has also been noted in References 8 and 74. Reference 8 gave no explanation for this underprediction.

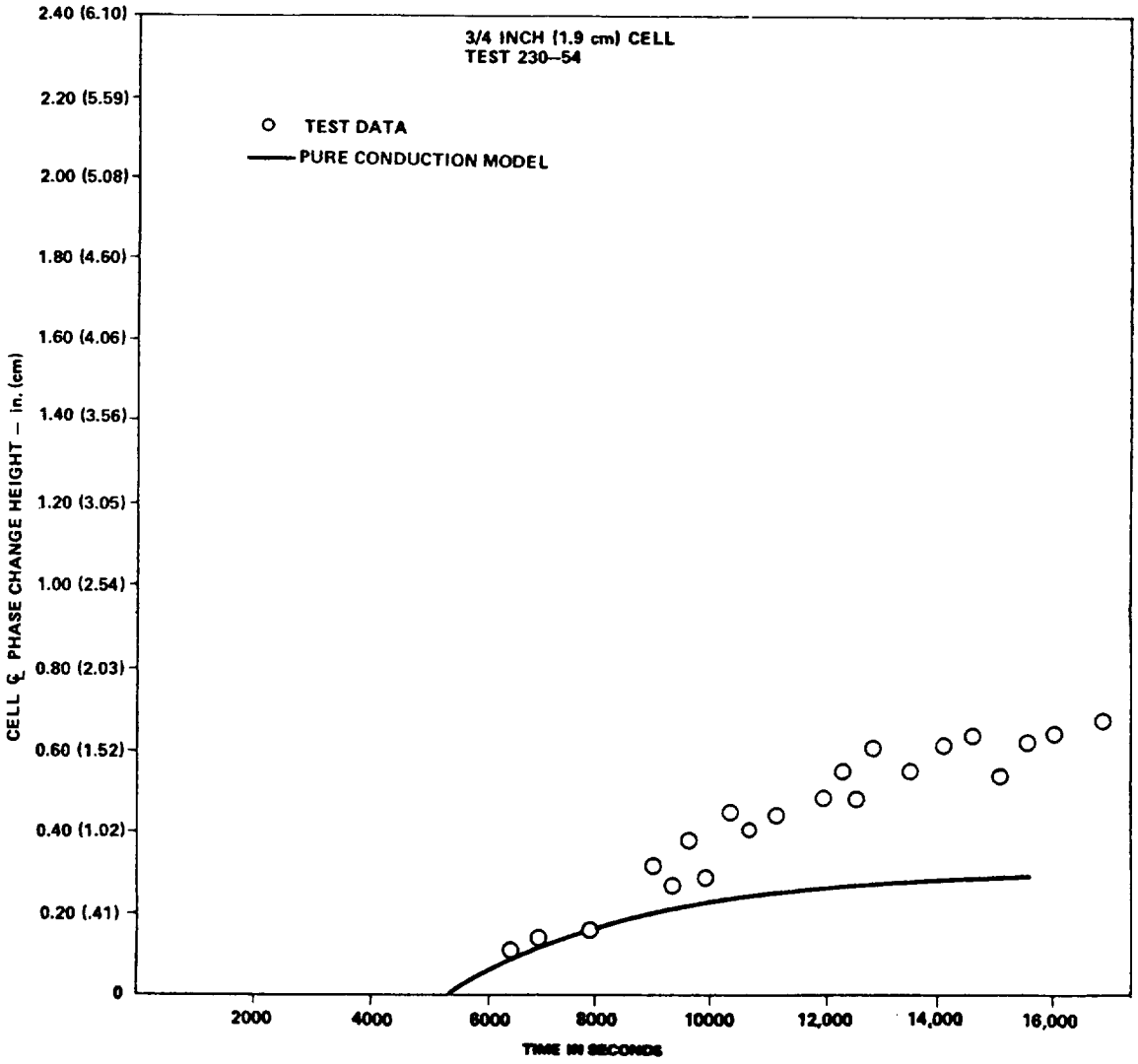

Figure 57. Comparison of freeze front position test data and predicted data for a slow cooling rate.

Although Golden [74] attributed this disparity to erroneous property data, evidence shows this not to be the case in this instance.

Possible causes of underprediction are liquid phase convection, anisotropic or erroneous property data resulting in higher thermal diffusivities or

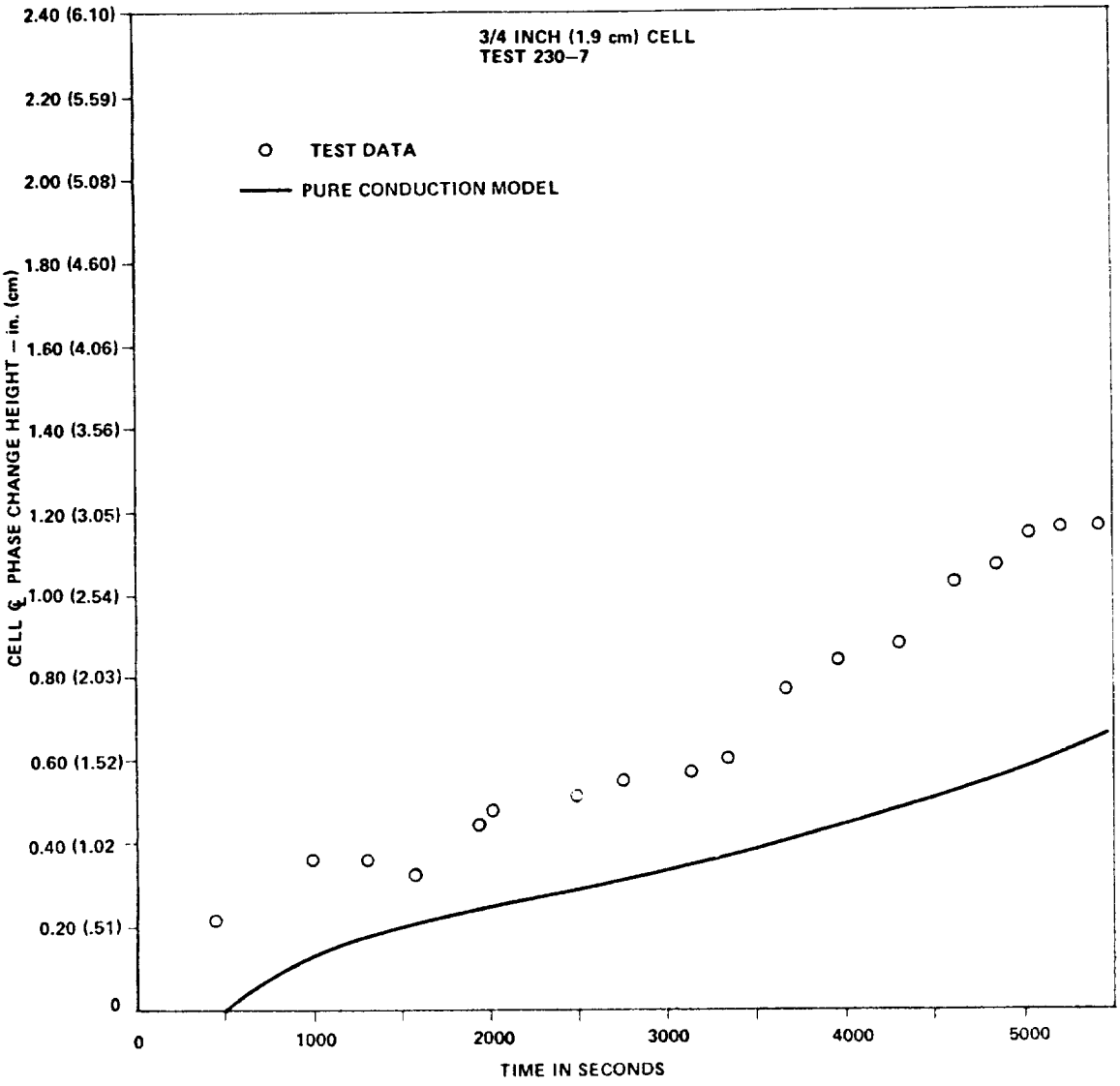

Figure 58. Comparison of freeze front position test data and predicted data for a fast cooling rate.

latent heat values than used in the model, and augmented heat transfer surface area at the interface due to dendrite formation. Bailey* has shown however,

*Verbal communication between the author and Dr. Bailey of N.C. State University.

that the deviation in latent heat of fusion of the paraffin used in these tests from the values quoted in the literature is negligible.

Convection in the bulk liquid or local interdendrite convection could produce this underprediction. However, since freezing is from below the former is not expected to be a large effect, and the latter effect produced by the volume change phenomena has been shown in Chapter 2 to be negligible.

To examine the approximate level of paraffin thermal conductivity change required to match test data, a highly simplified technique was used. The vertical conductors (i.e. $KA/\Delta X$ values) in the conduction model were artifically increased by applying multiplying factors to the conductors in the liquid and solid phases. These factors were varied until a good interface position match was attained.

Plots of fast and slow cooling rate tests showing the effect of the optimum match are shown in Figures 59 and 60, respectively. Applying this technique to a number of tests, multiplying factors ranging from 4 to 10 resulted. Although the technique used to reproduce test data is highly simplified, it serves to show the magnitude of thermal conductivity coefficient augmentation required is much greater than any expected increase due to anisotropic effects or property measurement inaccuracies.

Using the author's data, Griggs [77] has shown that by altering the vertical conductors at the interface only, good approximations of test results can also be achieved (Fig. 61). Extrapolation of these data indicates multiplication factors on the order of 100 to 200 are required for best results.

Examination of microscopic photographs indicates these magnitudes are not inconsistent with the dendrite geometry at the interface.

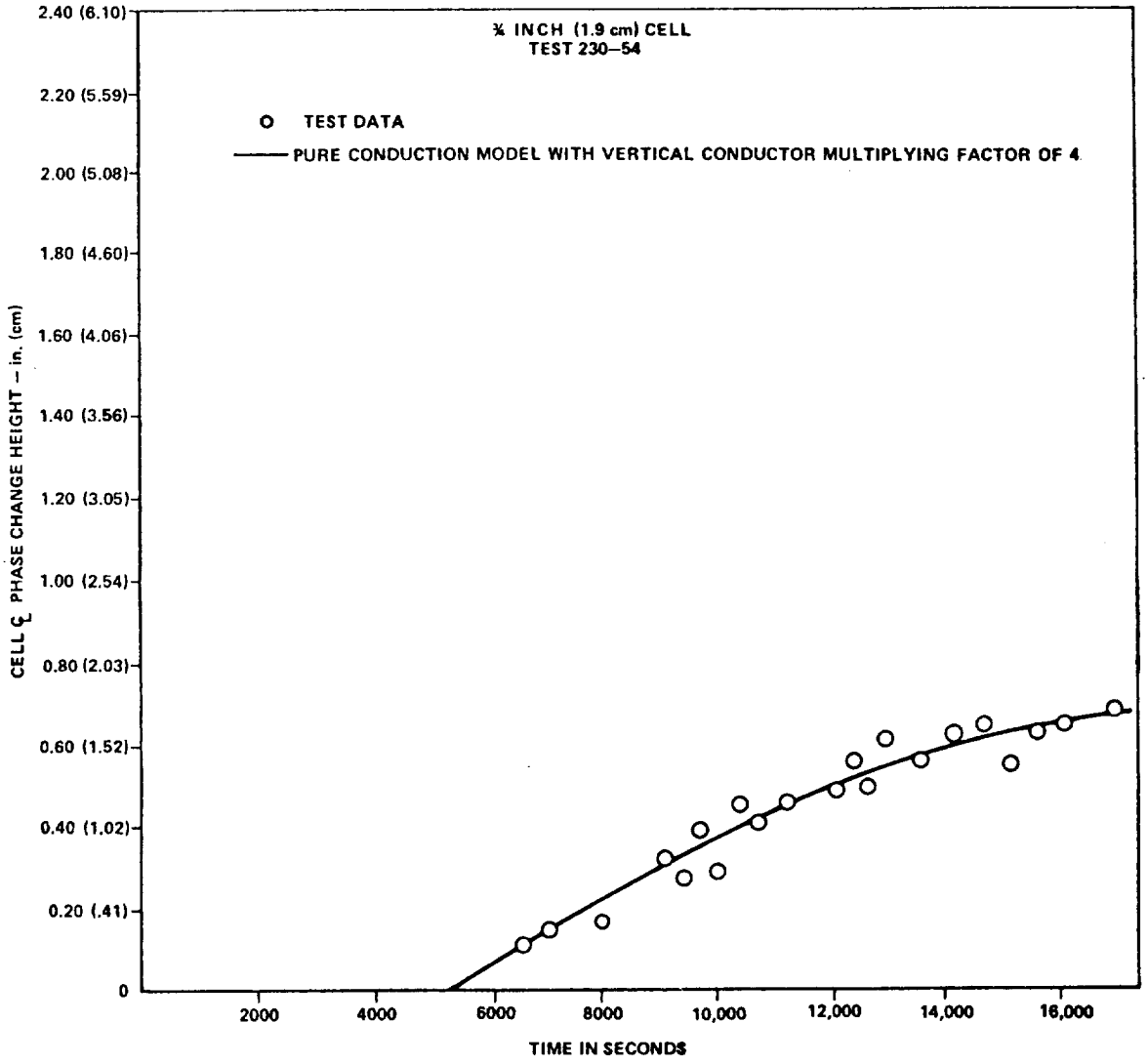

Figure 59. Comparison of freeze front position test data and predicted data for fast cooling rate.

From the foregoing discussion it can be concluded the exclusion of the heat transfer surface area augmentation at the interface is the most probable cause of underprediction. However, combination effects of augmentation with other effects discussed is also a possibility.

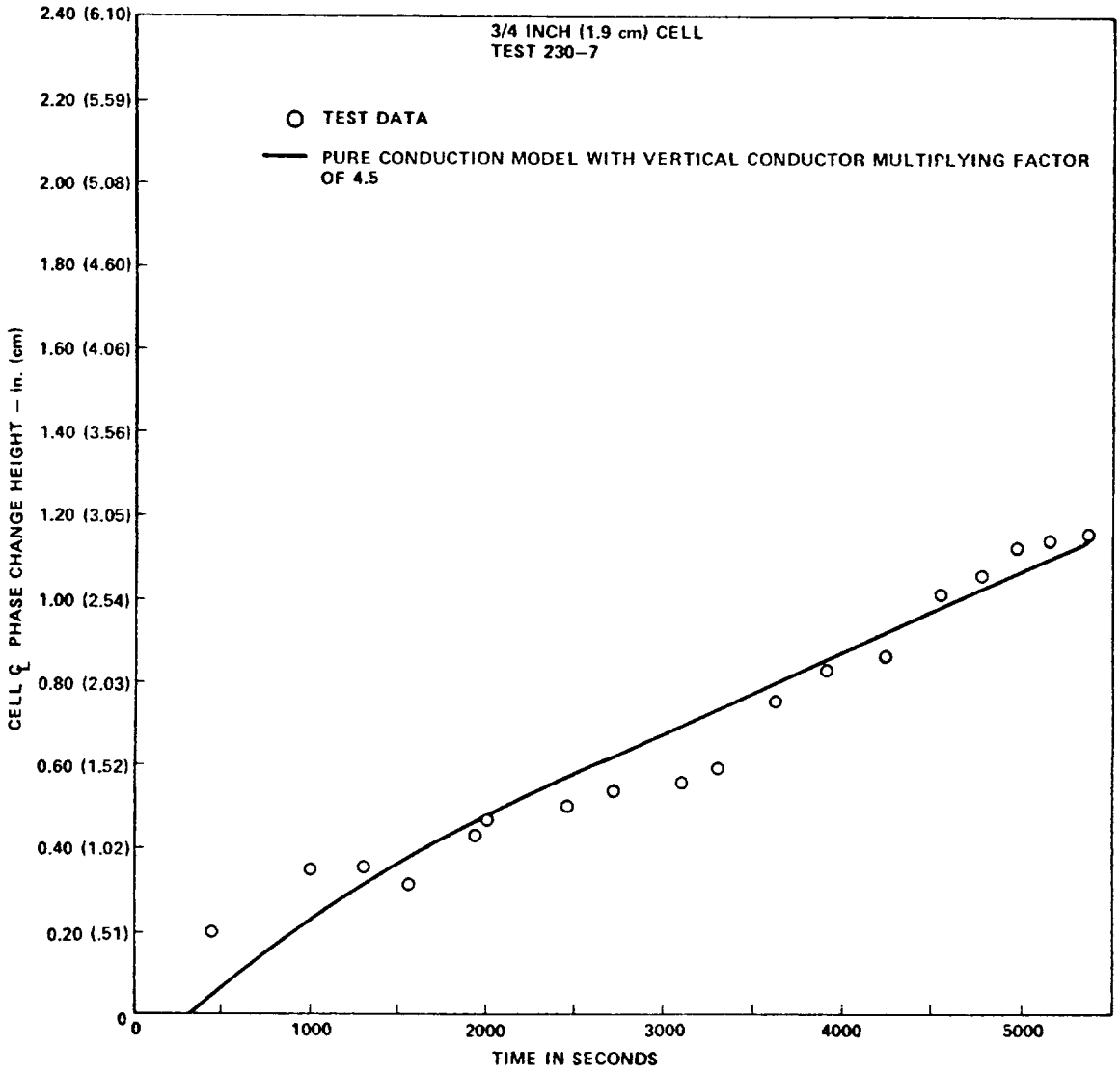

Figure 60. Comparison of freeze front position data and predicted data for slow cooling rate.

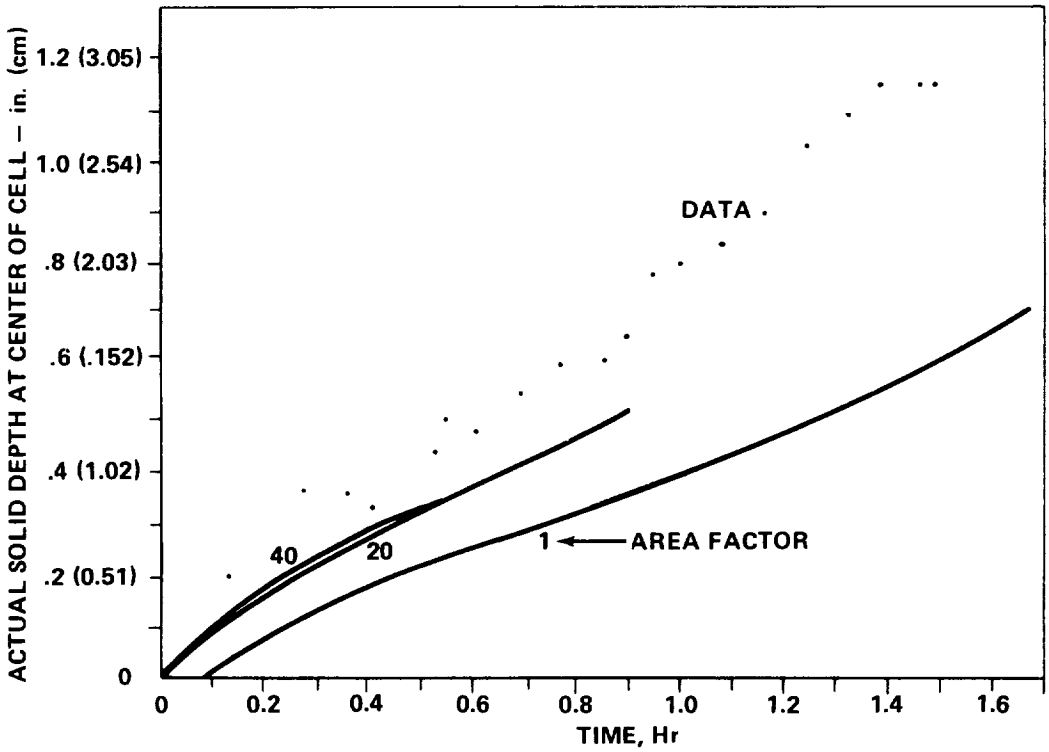

Figure 61. Comparisons of predicted interfacial positions at center of cell for MSFC in-house run 230-7.

Melt Front Position

The pure conduction model did not predict the melt front position with any degree of accuracy (Fig. 62). Estimations of natural convective levels, clearly indicated that this was due to the augmentation created by the convective currents. As a result, the basic conduction program was modified, as discussed earlier, to provide an estimate of convective enhancement. An estimating approach was taken rather than try to solve the convection problem, because of the complicated nature of the problem when the energy is coupled

with the momentum equations. No attempt was made to form convection coefficient conductors because insufficient film coefficient data were available to estimate these coefficients at a melting solid/liquid interface.

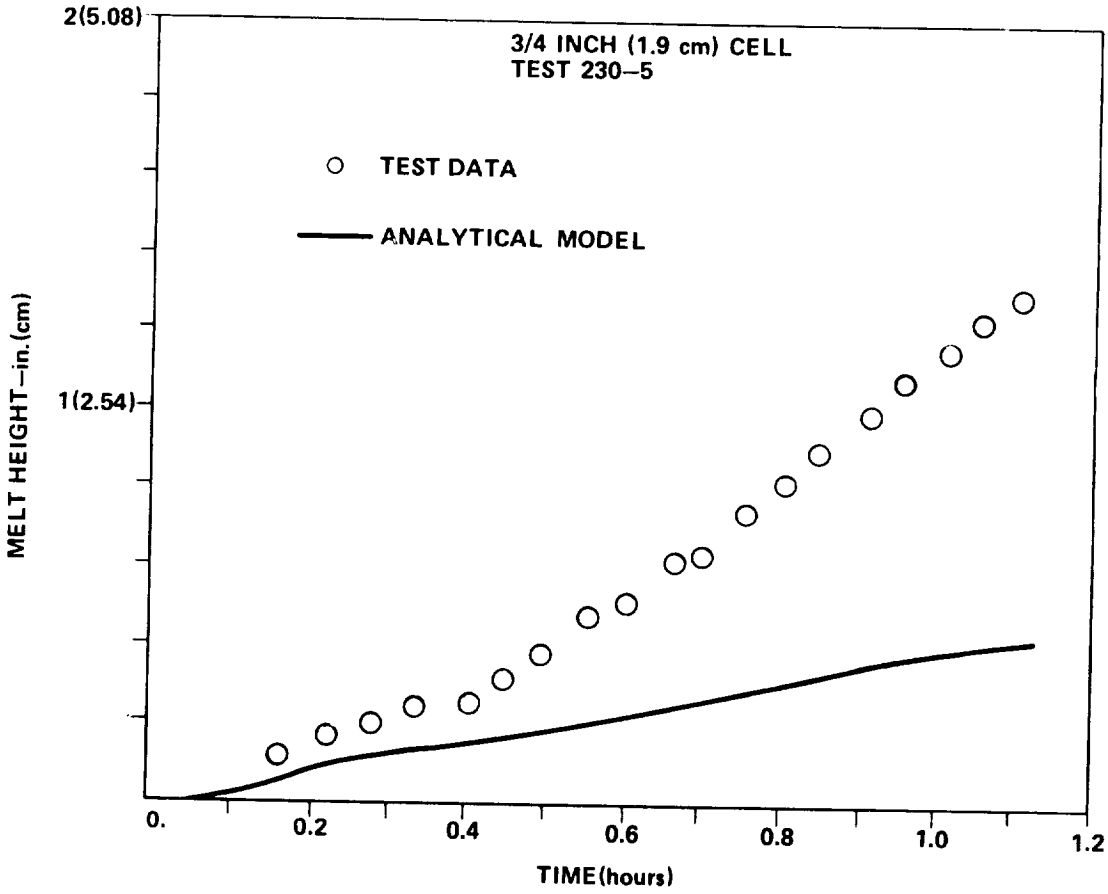

Figure 62. Conduction mode sensitivity for 1.9-cm (3/4-in.) cell.

Comparison plots of experimental data with analytical data are shown in Figures 63 through 71 for 1.9-cm (3/4-in.) cells and in Figures 72 through 76 for 0.635-cm (1/4-in.) cells. From these plots, it is obvious that in most cases the modified model satisfactorily represents melting rates and consequently the heating rates. The analytical data in most cases slightly underpredicts the experimental results, although the lag is only slight.

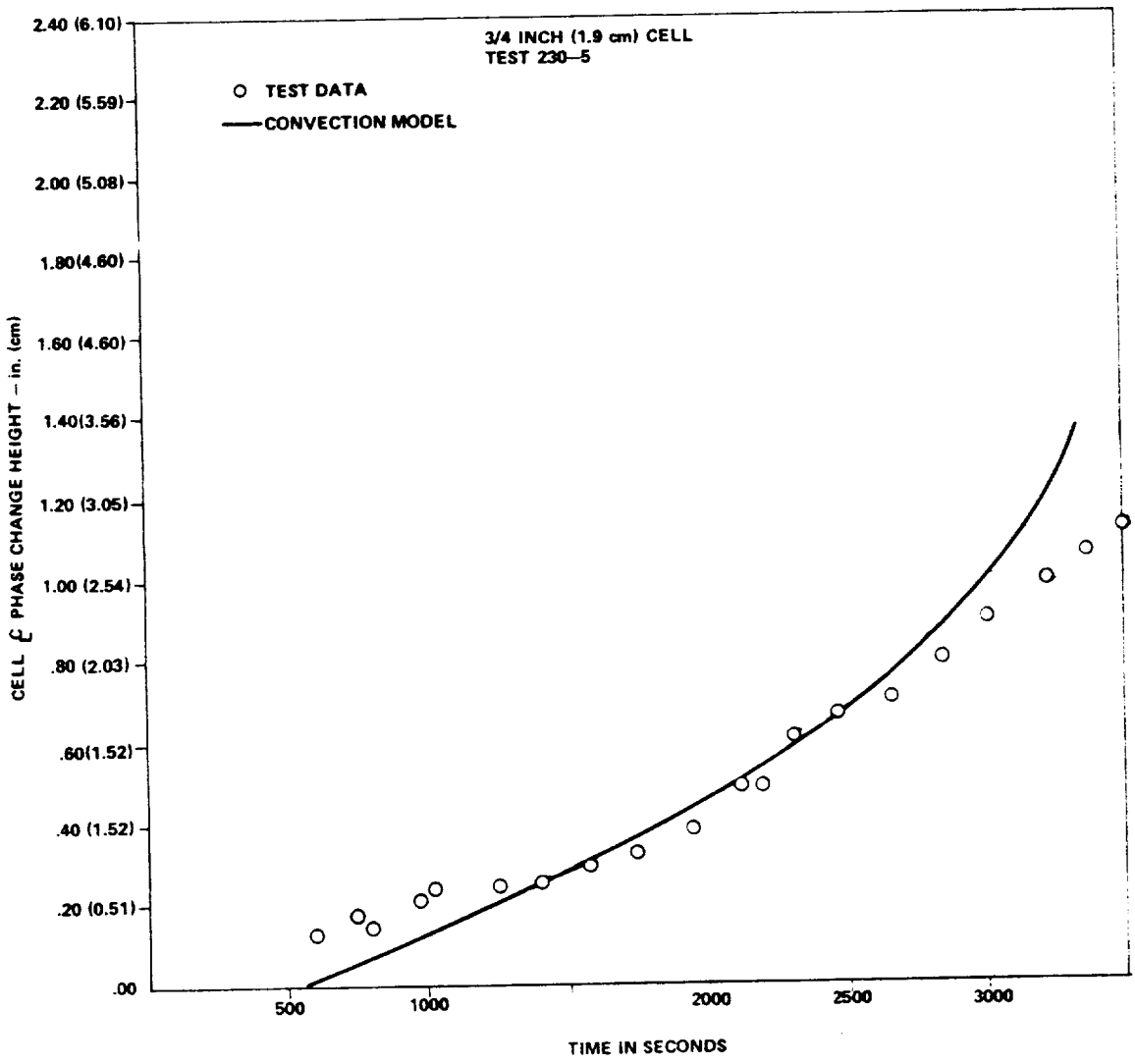

Figure 63. A comparison of experimental and analytical data for test 230-5.

A constant melt temperature of 89.8°F was used in the model for all computer sums. The experimental results of freezing tests indicated that phase change temperature appeared to decrease with time. The later predictions could have been improved by decreasing the model melt temperature to the experimental level.

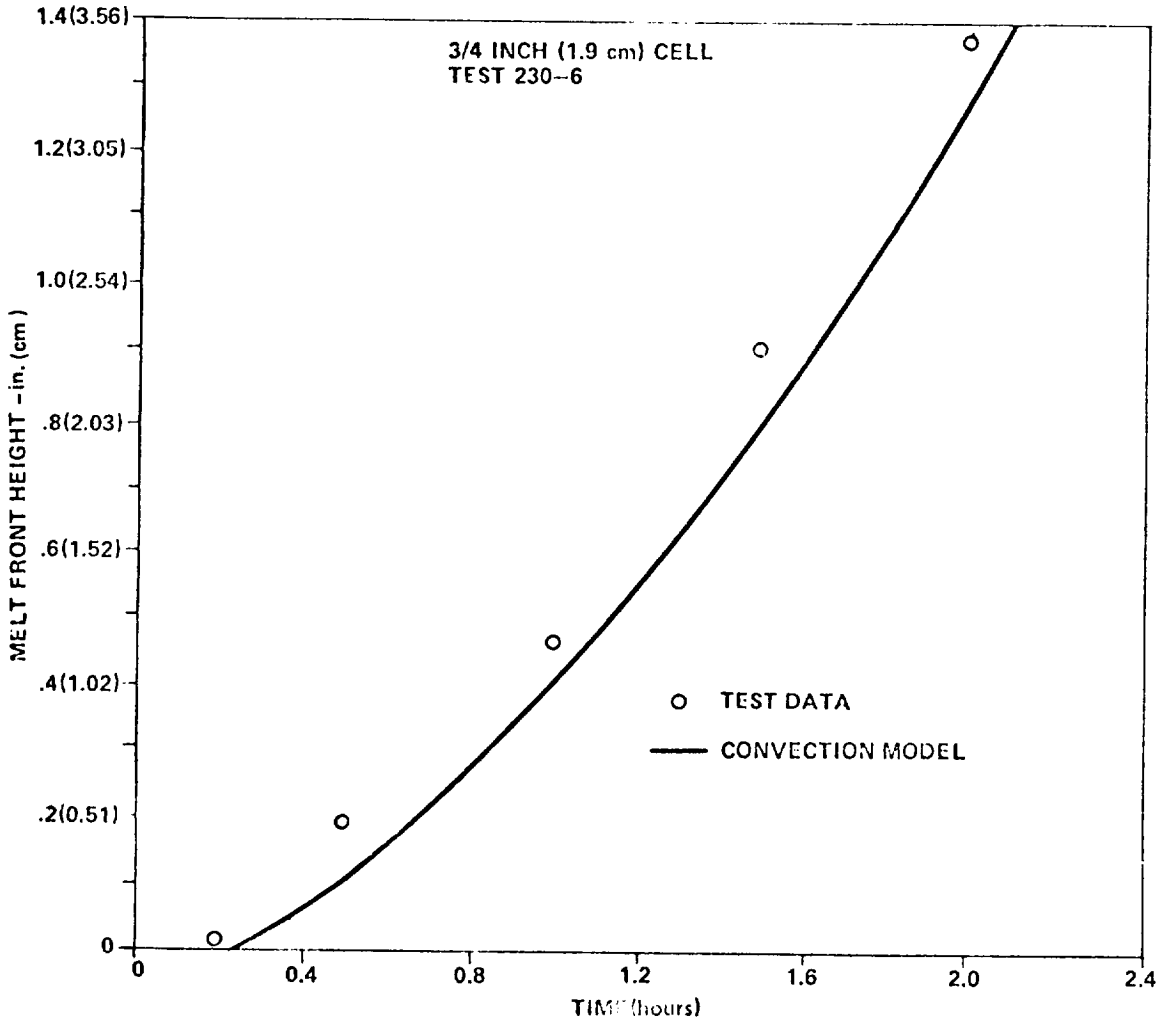

Figure 64. A comparison of experimental and analytical data for test 230-6.

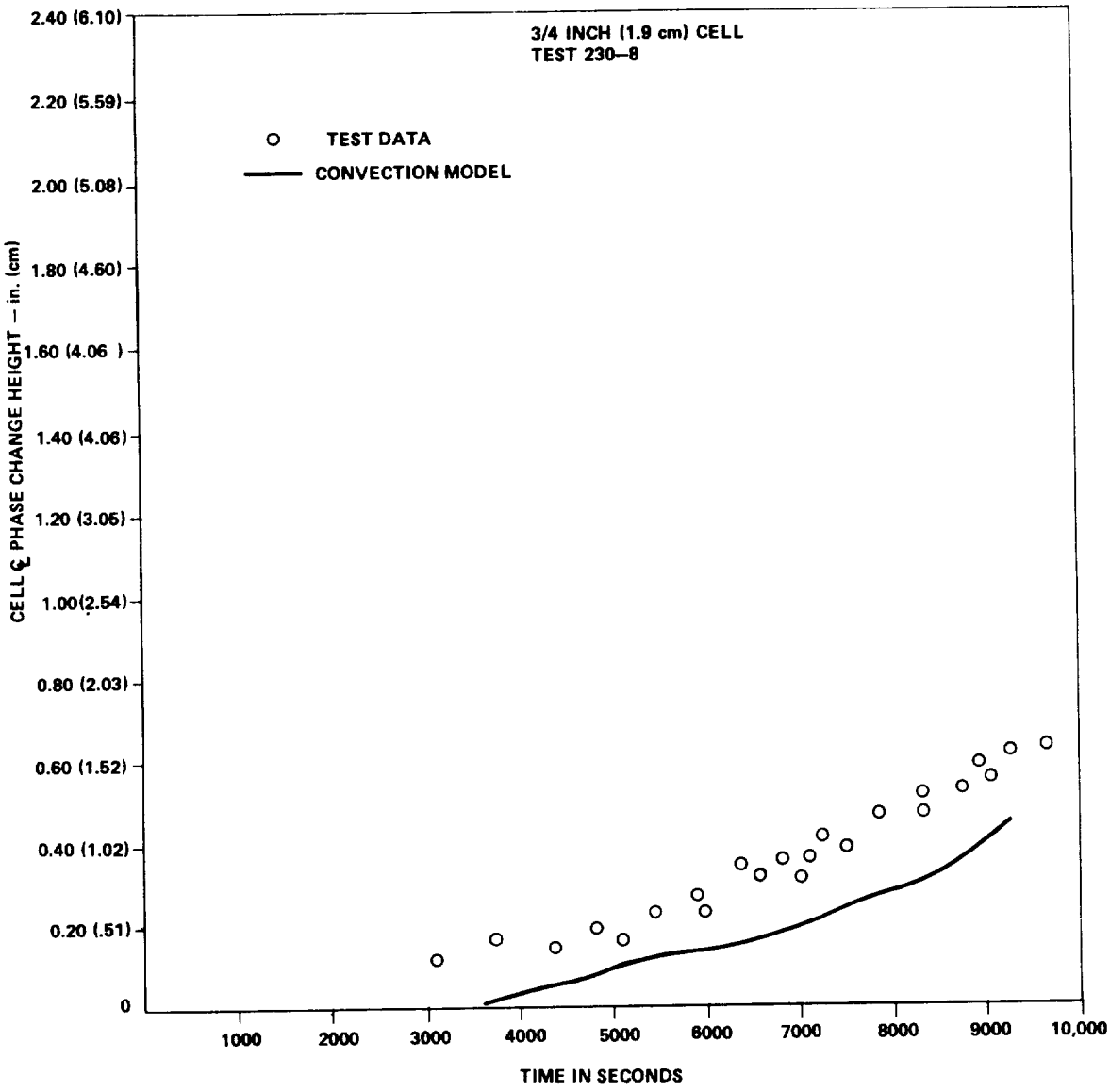

Figure 65. A comparison of experimental and analytical data for test 230-8.

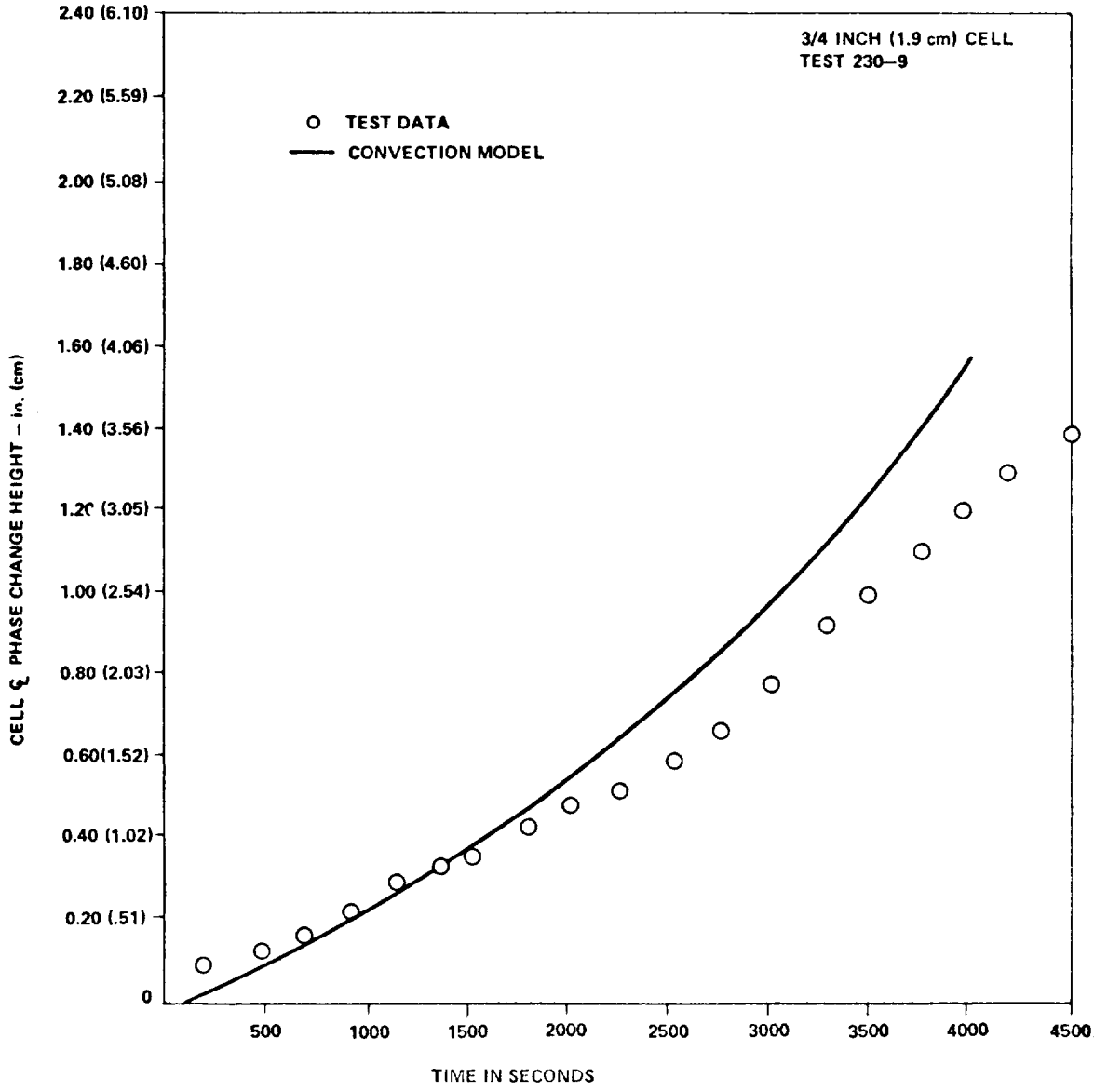

Figure 66. A comparison of experimental and analytical data for test 230-9.

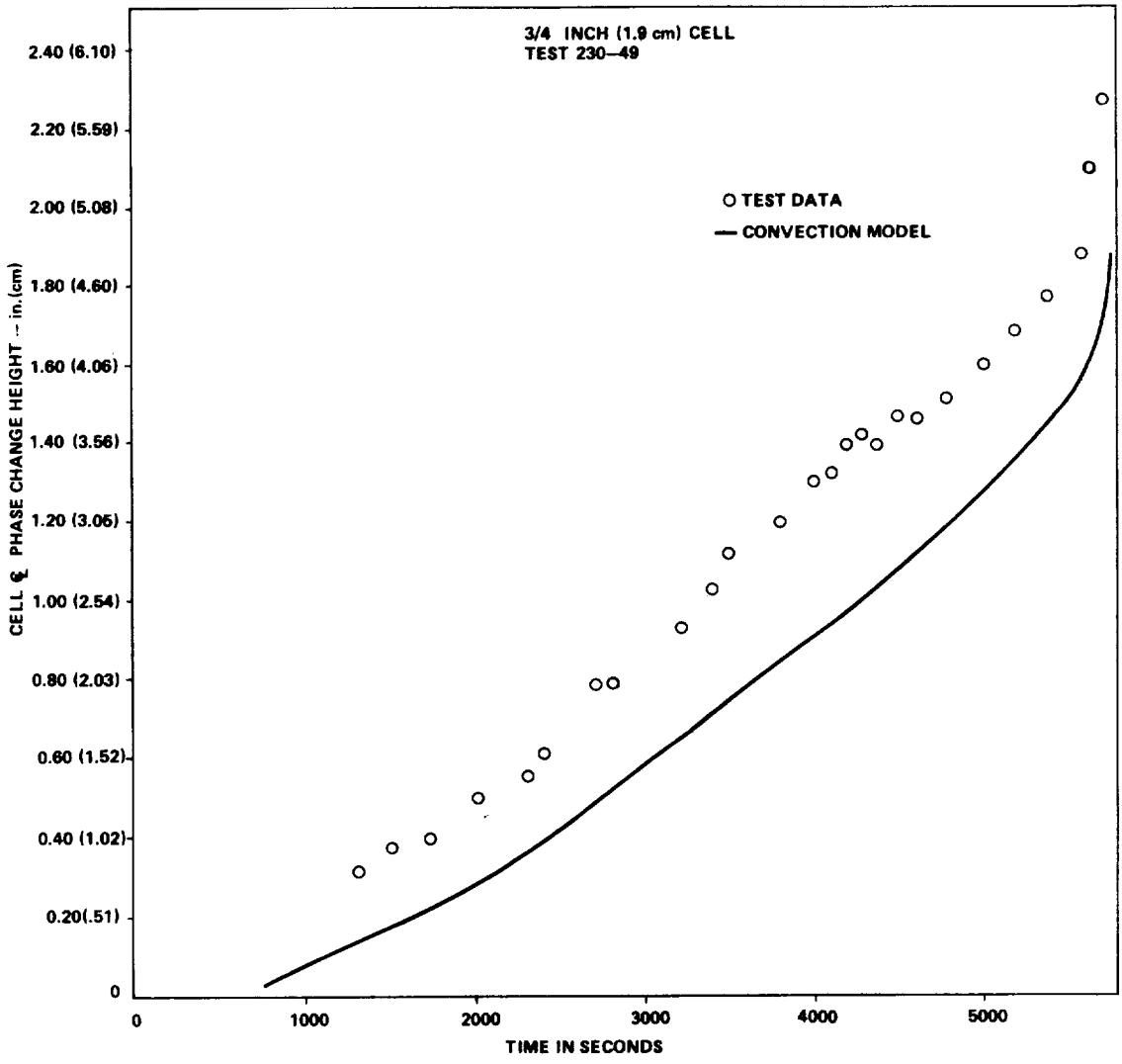

Figure 67. A comparison of experimental and analytical data for test 230-49.

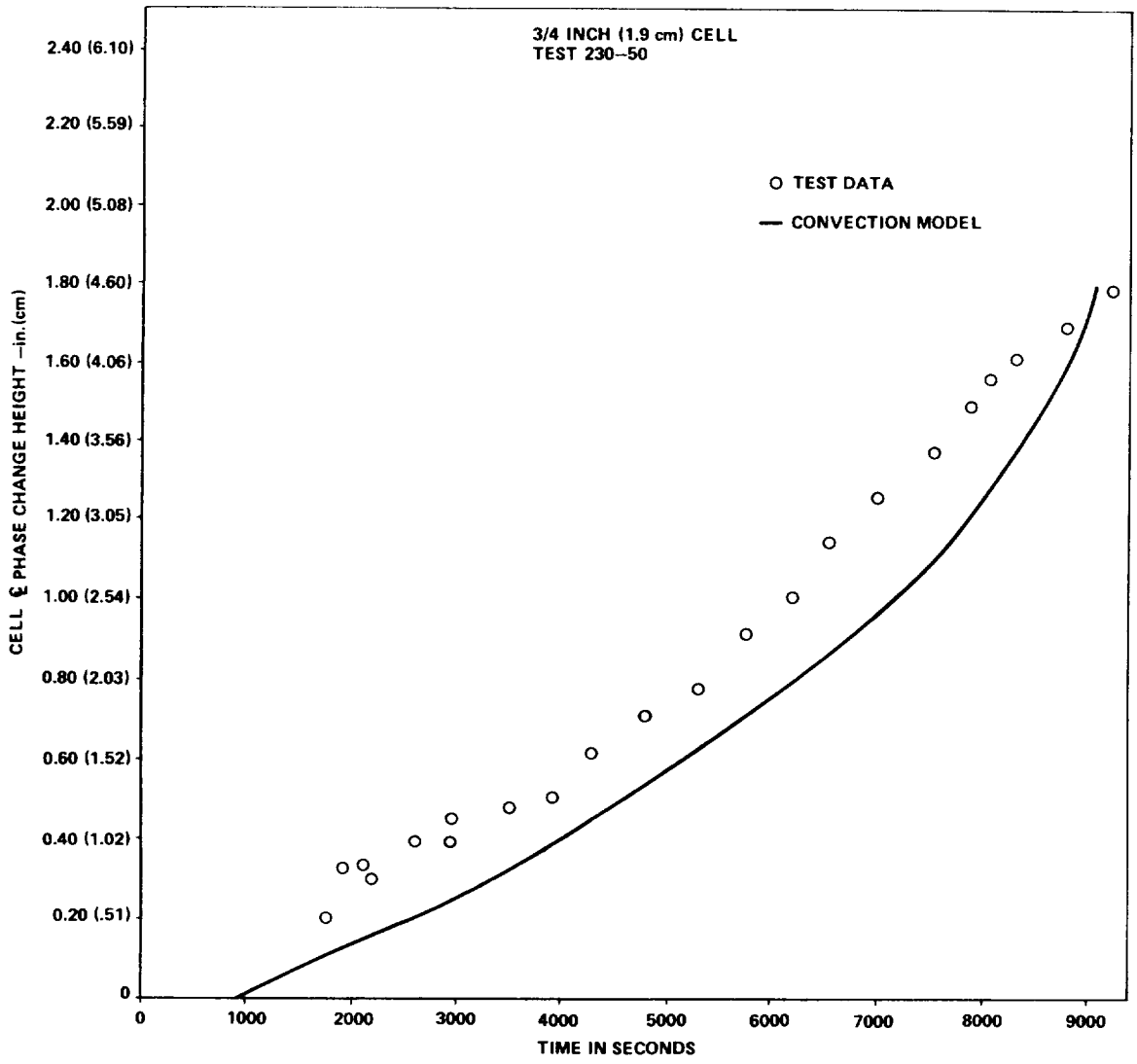

Figure 68. A comparison of experimental and analytical data for test 230-50.

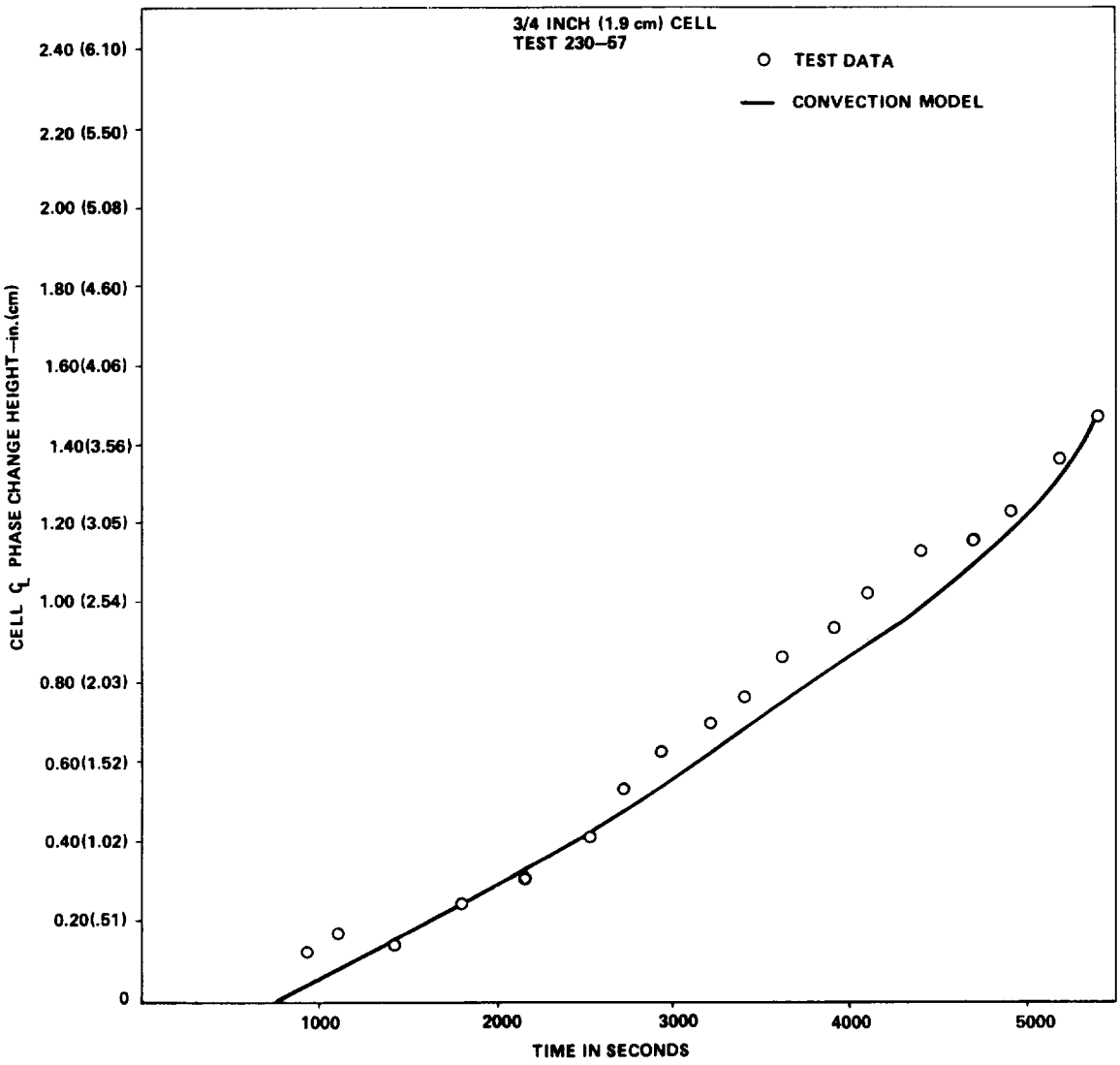

Figure 69. A comparison of experimental and analytical data for test 230-57.

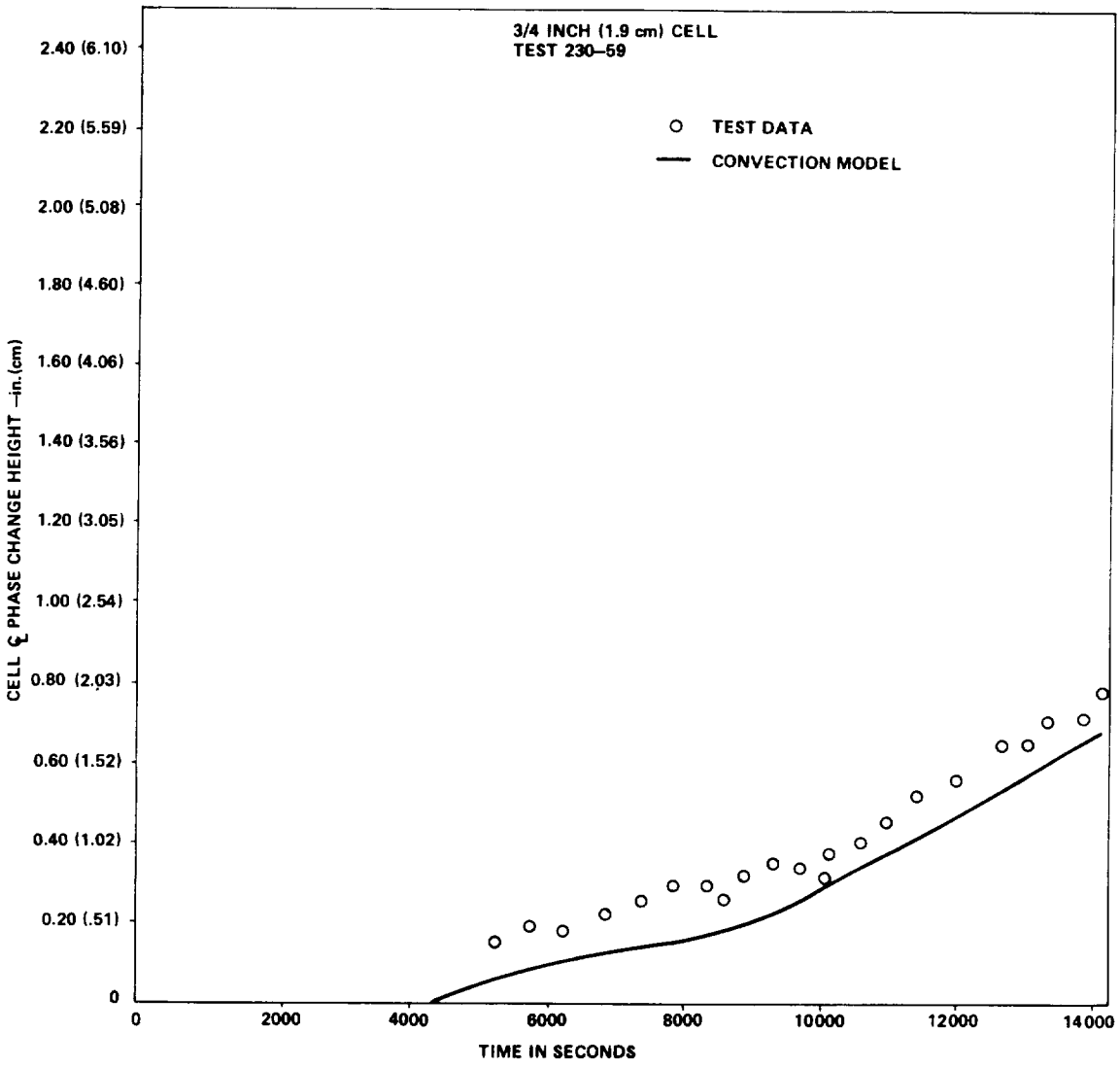

Figure 70. A comparison of experimental and analytical data for test 230-59.

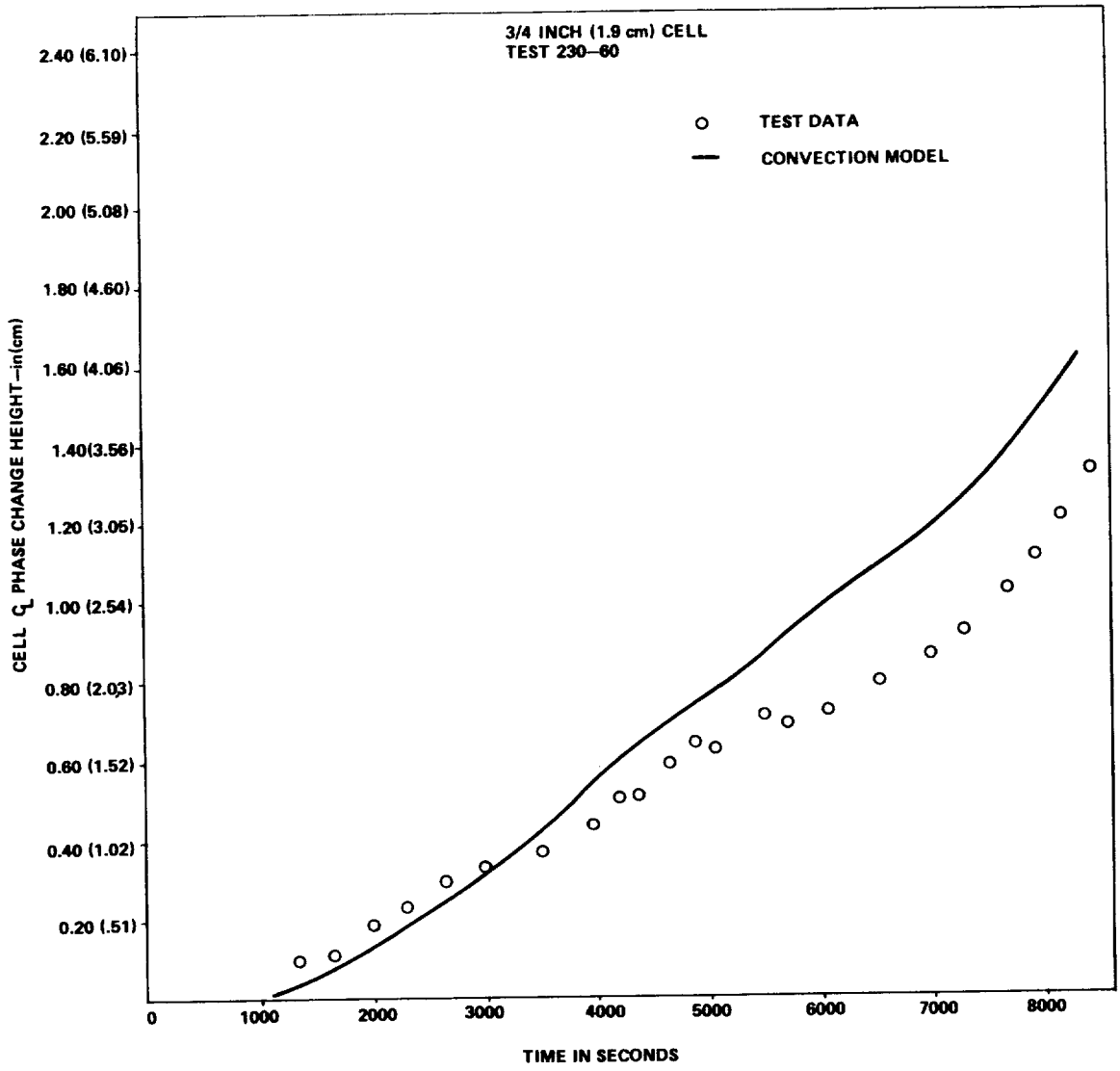

Figure 71. A comparison of experimental and analytical data for test 230-60.

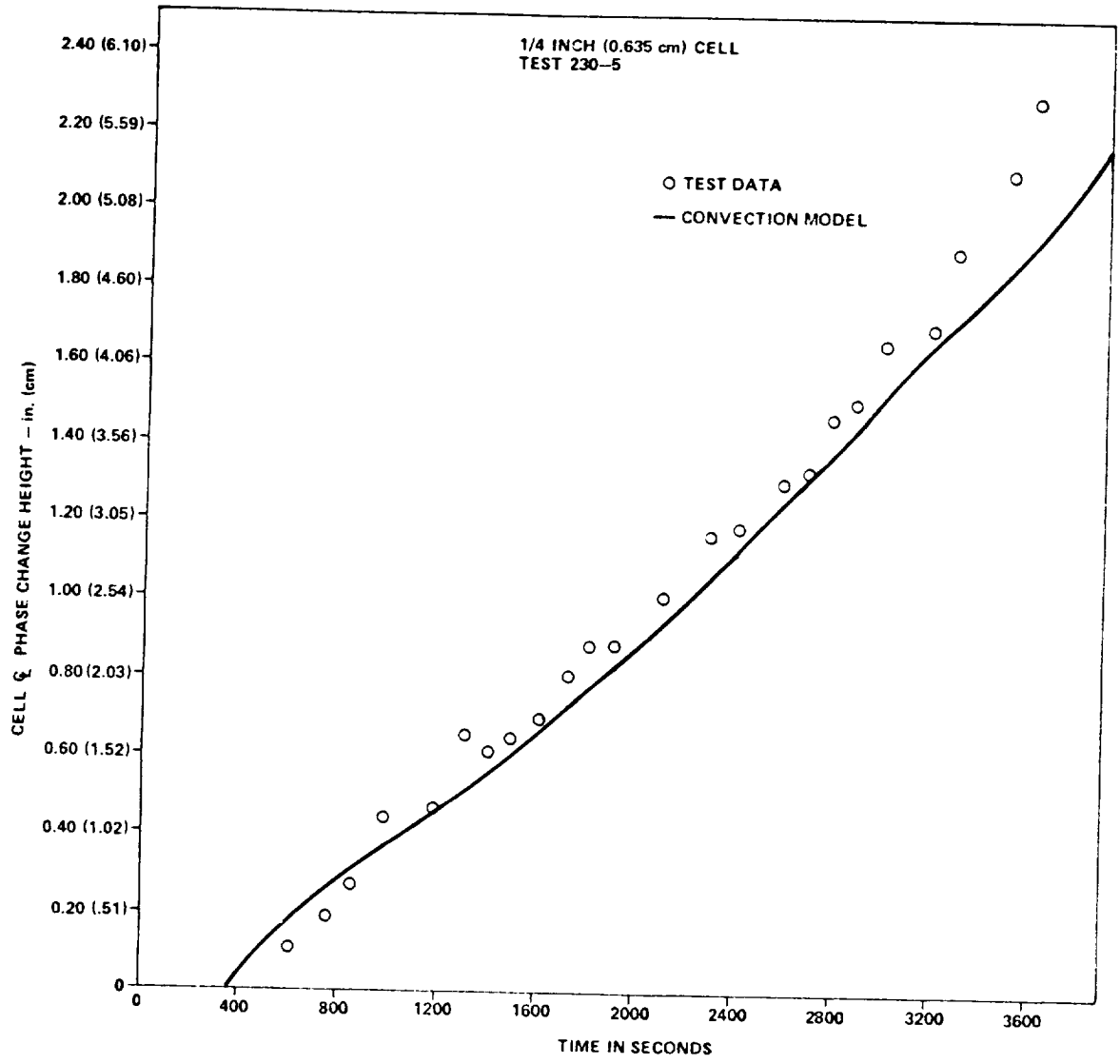

Figure 72. A comparison of experimental and analytical data for test 230-5.

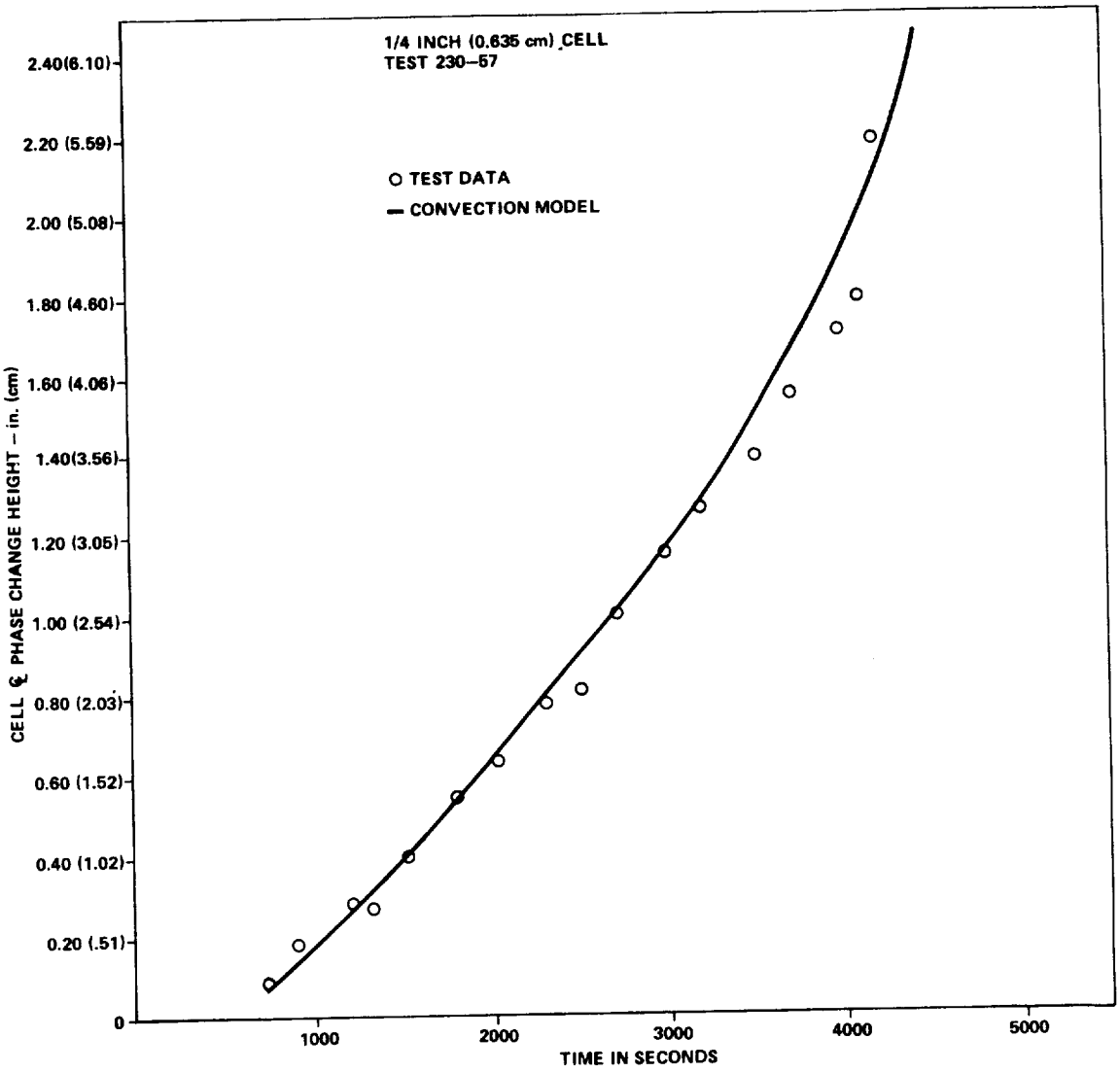

Figure 73. A comparison of experimental and analytical data for test 230-57.

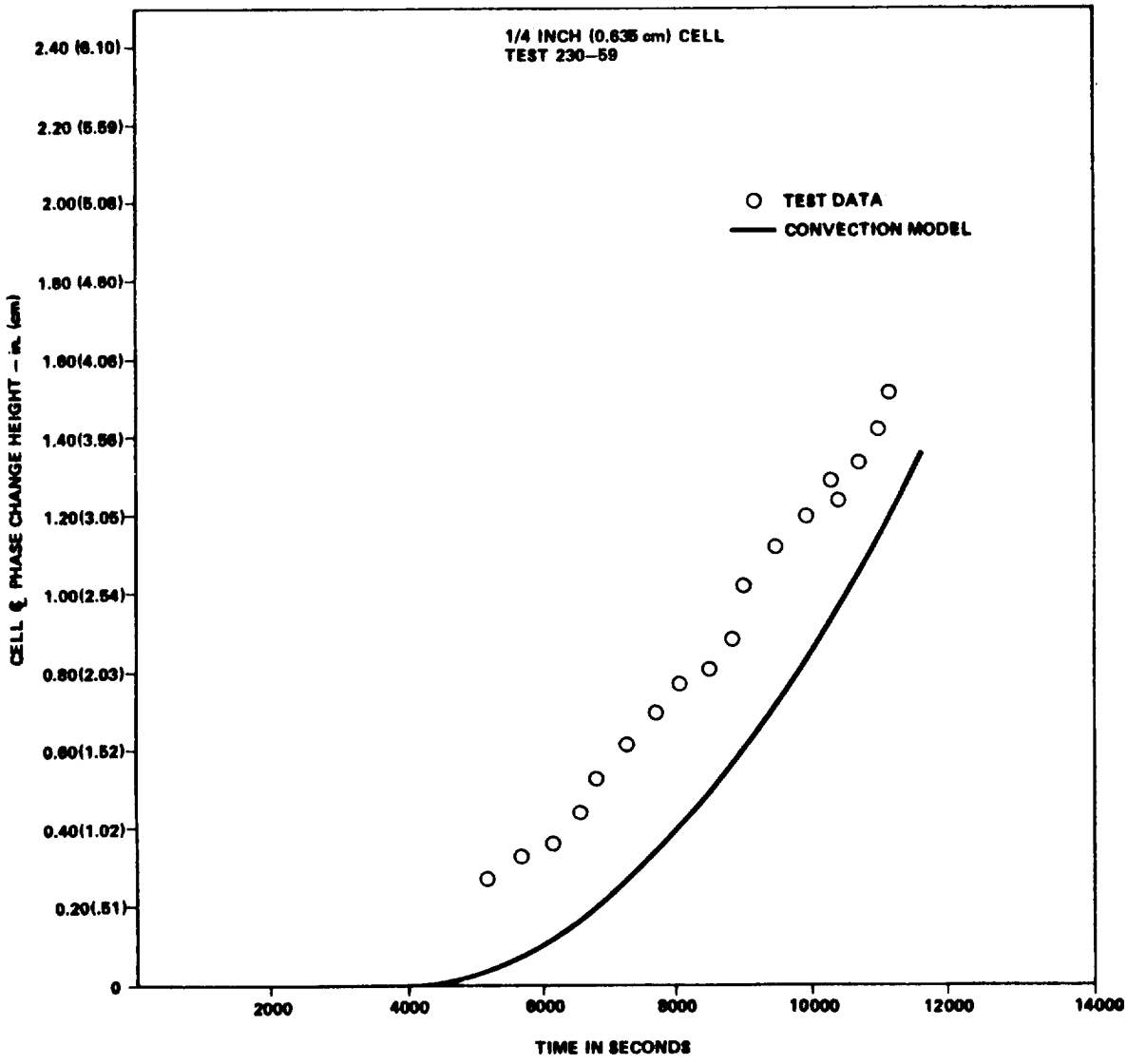

Figure 74. A comparison of experimental and analytical data for test 230-59.

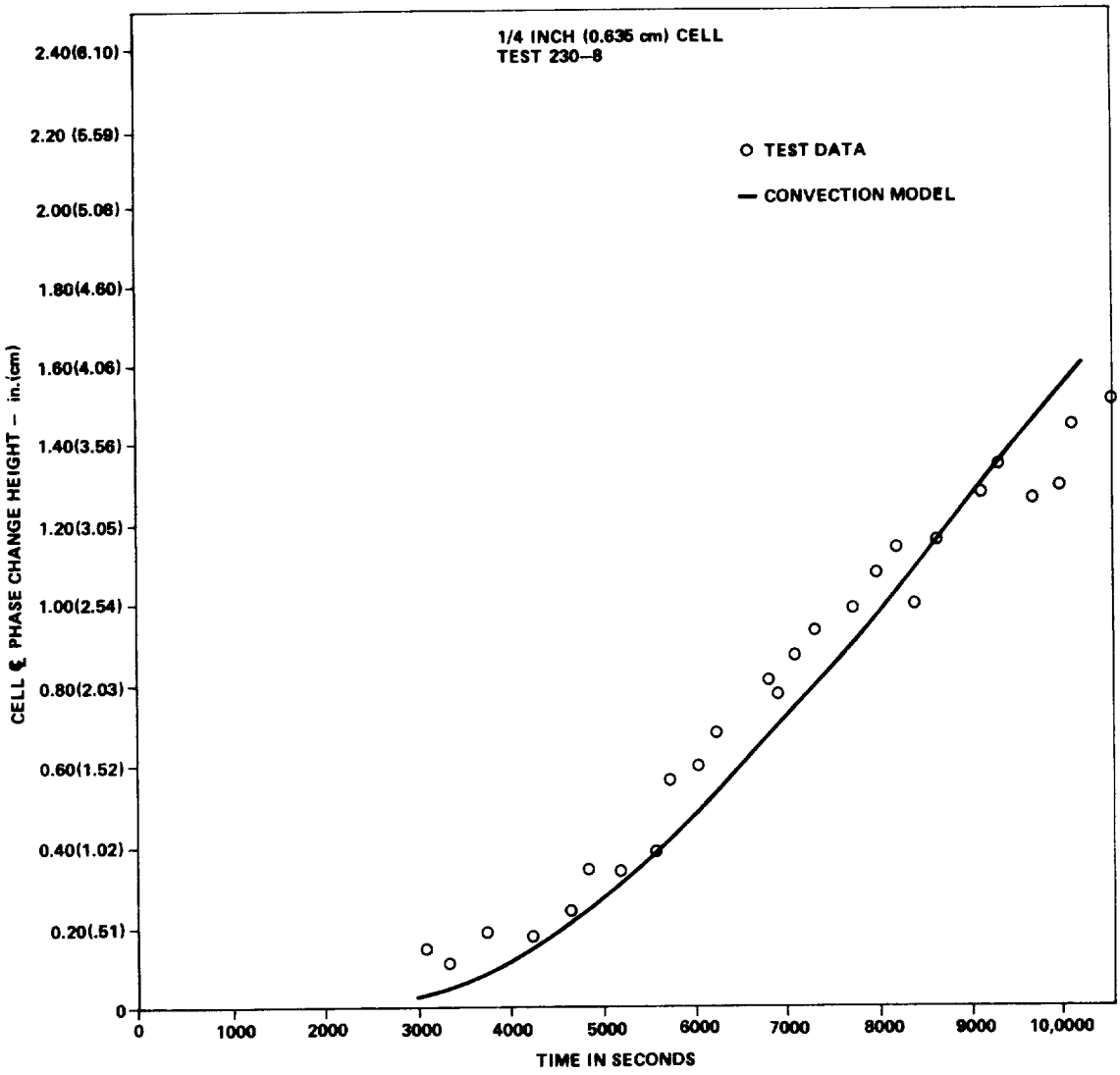

Figure 75. A comparison of experimental and analytical data for test 230-8.

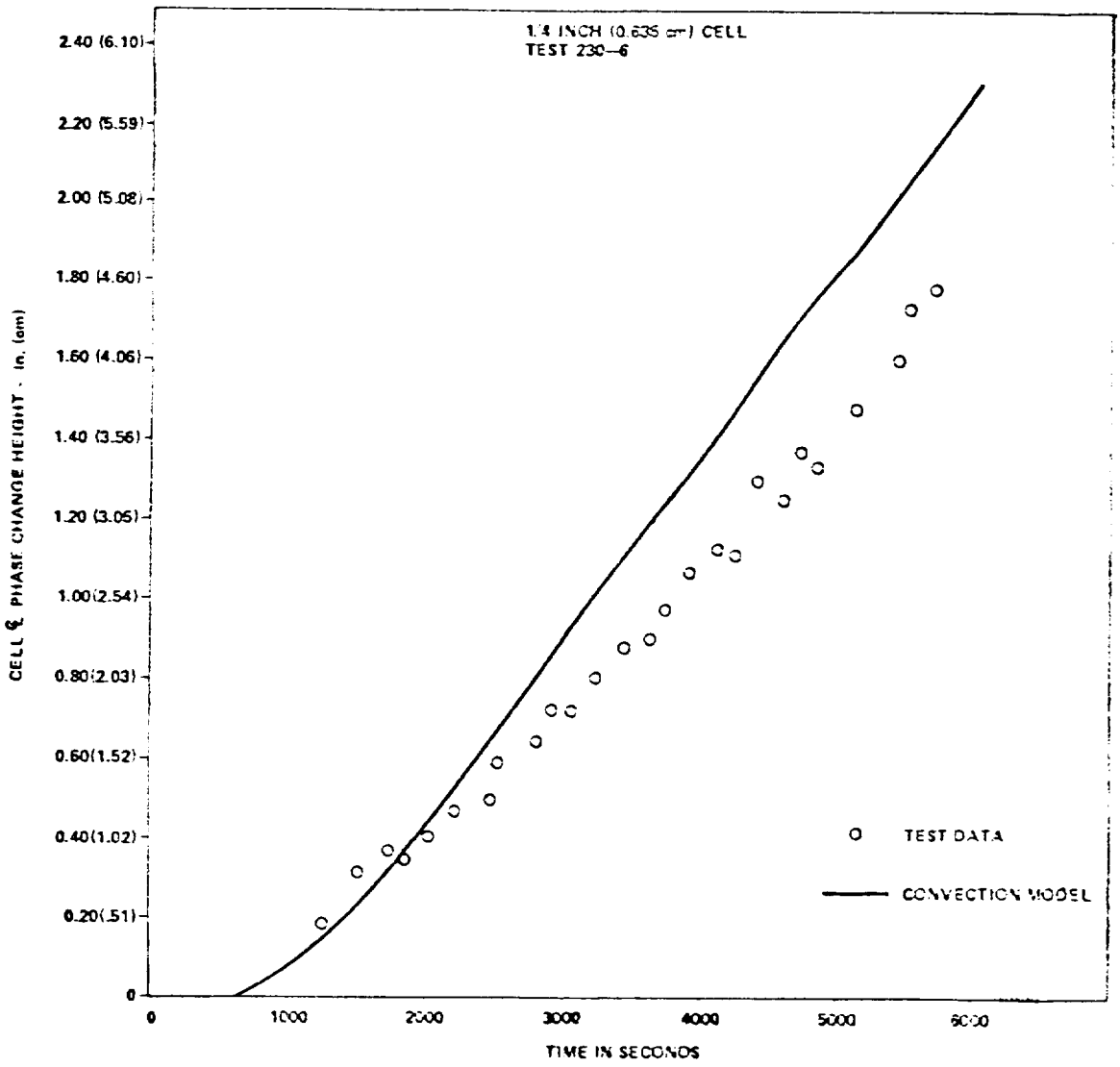

Figure 76. A comparison of experimental and analytical data for test 230-56.

From the data is it obvious that the phase change position versus time for melting runs can be approximated by a straight line. This phenomena can be justified analytically. In Appendix B the Rayleigh Number is given as

$$Ra = 1.68 \times 10^8 \, L^3 \, \Delta T$$

For these tests the range of temperature differences in the liquid region was

$$2.8°C \ (5°F) < \Delta T < 13.9°C \ (25°F)$$

Using these limits with the above equation and the Rayleigh Number regimes defined by Silveston and O'Toole [30], a plot of Rayleigh Number versus melt height may be generated. (See Figure 77).

From this figure, it is apparent that most of the cell is operating in regime 4. Although this is basically a transient problem, a steady-state approximation of the velocity profile may be made. Noting that the Nusselt Number is given by

$$Nu = \frac{hL}{K}$$

and combining this with the regime 4 Nusselt Number expression, the heat transfer coefficient may be approximated by

$$h = \frac{K}{L} (0.104) \, Ra^{0.305} \, Pr^{0.084}$$

Again assuming constant properties and a constant temperature difference, the following relation holds

$$h = C_1 \, L^{-0.085}$$

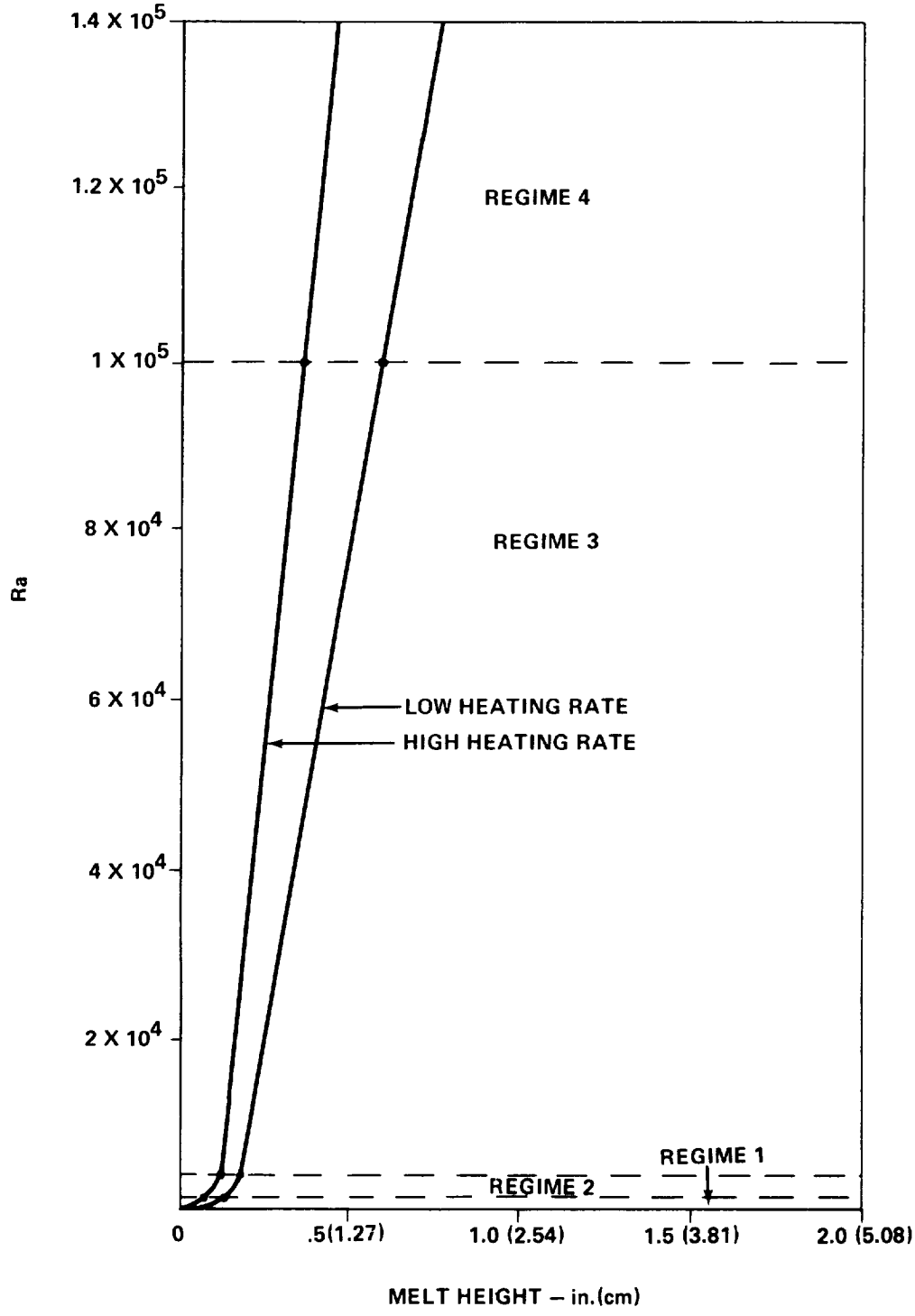

Figure 77. Rayleigh number versus melt height.

neglecting sensible heat and an energy balance on the melt interface yields

$$h\Delta T = \Delta H \rho V$$

or

$$V = C_2 L^{-0.085} \quad .$$

This indicates that velocity is relatively constant, only weakly dependent on the melt height.

CHAPTER 8

SUMMARY AND CONCLUSIONS

1. In a one-g environment, a pure conduction model cannot be used to determine freeze or melt front position accurately in paraffin. The freeze and melt front positions are both underpredicted. In the case of melting, the actual rate is faster because of the augmenting effect of natural convection. For freezing, the inability to reproduce experimental results is thought to be due to the influence of dendrites. However, this suggestion is not proven herein.

2. A convection model accurately predicted experimental results for melting. However, a notable fallacy is that this model cannot accurately reproduce temperature profiles in the liquid phase. This model utilizes an effective thermal conductivity variation with Rayleigh Number to simulate conductive effects. Although the model has been demonstrated to give good results for only the geometry and heat flux ranges discussed in the text, the model is expected to apply to larger cell sizes and for lower and higher heat fluxes up to nucleate boiling initiation. Because of the reversal trend predicted by Jones and Smith [79], for cell sizes below 0.635-cm (1/4-in.) (Figure 78) alterations are necessary. These alterations require the Silveston and O'Toole correlations be replaced by the Catton and Edwards closed cell correlations.

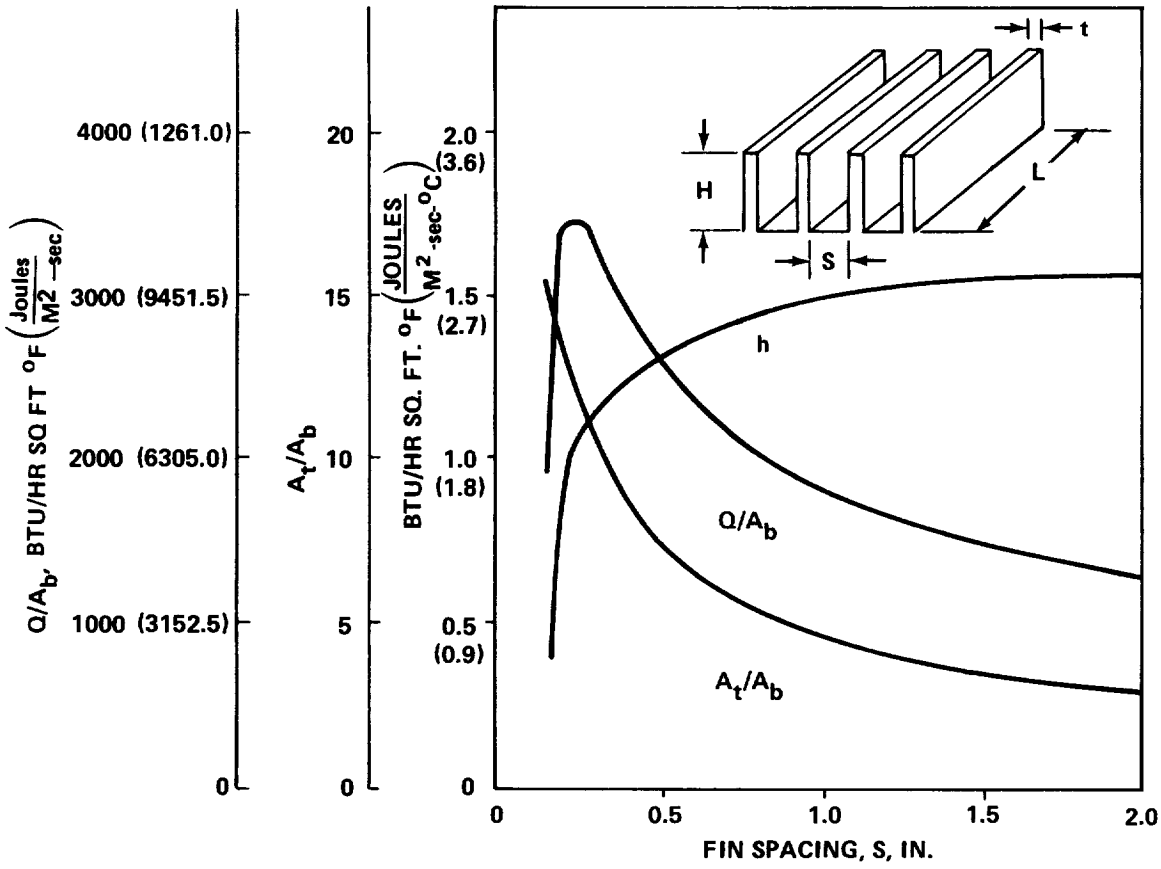

Figure 78. Typical effects on fin spacing on average heat-transfer coefficients.

3. During freezing of paraffins the phase change boundary is made up of numerous dendritic arms. This phenomena is not present in melting. Although this effect is well known in material sciences, it was not considered by a number of authors investigating heat transfer during solidification.

4. The freeze front position cannot be matched without making unverified assumptions. It is apparent that dendrite formations augment the surface area available for heat transfer at the interface during freezing. Augmentation of this area will improve conduction model data matching. It is hypothesized that

failure to include this augmented area effect is the major cause of the reported underprediction. Further study of these effects is needed before positive conclusions may be reached.

5. Insufficient information is available to determine if the unexpectedly rapid freeze front progression noted in one-g will also occur in zero-g. However, assuming the augmented rate is due to dendrite formations, as hypothesized, the paraffin freeze rate should again be underpredicted by a pure conduction model. This is true since there is no evidence in the literature that dendrite formations are affected by the gravity level.

6. In a zero-g environment, conduction modeling techniques are expected to be applicable to determining melt front positions and temperature profiles unless significant surface tension driven convection is present. However, there are insufficient zero-g data to corroborate this finding.

7. From the literature, surface tension driven convection can be appreciable for normal paraffin capacitors in zero-g only in systems containing adjacent liquid/gas phases. Insufficient data are currently available to allow quantitative estimates of convective levels created by this phenomena.

8. Excluding convection due to orbital maneuvers, the only other affect expected to be important during phase change is that of ullage bubble location. The ullage location, in the case of paraffins, will be favorable for maximum heat transfer from metal surface, because of good wetting characteristics of paraffins.

APPENDIX A

PARAFFIN PROPERTIES

Introduction

A tabulation of paraffin property data is given in Table A-1. These data were compiled from the authors listed below in references A-1 through A-10. Items A-25 through A-59 give a list of property references compiled by the Thermophysical Properties Research Center at Purdue University. These authors in-turn referenced those items listed for A-11 through A-24. In most cases the authors did not specify the paraffin grade, however, it is assumed that all data was acquired by using pure or research grade paraffin. Only those data considered reliable are presented herein.

Data for twenty normal paraffins with carbon atom chains ranging from eleven to thirty are presented. These paraffins cover a freezing point temperature range from -25.6°C (-14°F) to 65.6°C (150°F), encompassing the normal interest of the thermal capacitor designer.

The reader is referred to references A-4, and A-5, for more specific information of property variations with temperature.

Available paraffin cost data is given in Table A-2.

Item	Name	Chemical Formula	Molecular Weight	Phase Change Temperature		Transition Temperature	
				°F	°C	°F	°C
1	Undecane	$C_{11}H_{24}$	156.302	-14.1	-25.6	-32.8	-36.0
2	Dodecane	$C_{12}H_{26}$	170.328	14.7	-9.6	none	none
3	Tridecane	$C_{13}H_{28}$	184.354	22.3	-5.4	-0.4	-18.0
4	Tetradecane	$C_{14}H_{30}$	178.380	42.6	5.9	none	none
5	Pentadecane	$C_{15}H_{32}$	212.406	49.9	10.0	27.9	-2.3
6	Hexadecane	$C_{16}H_{34}$	226.432	64.7	18.2	none	none
7	Heptadecane	$C_{17}H_{36}$	240.458	71.6	22.0	50.9	10.5
8	Octadecane	$C_{18}H_{38}$	254.484	82.8	28.2	none	none
9	Nonadecane	$C_{19}H_{40}$	268.510	89.4	32.1	73.0	22.8
10	Eicosane	$C_{20}H_{42}$	282.536	98.2	36.8	97.2	36.3
11	Heneicosane	$C_{21}H_{44}$	296.562	104.9	40.5	90.5	32.5
12	Docosane	$C_{22}H_{46}$	310.588	111.9	44.4	109.4	43.0
13	Tricosane	$C_{23}H_{48}$	324.614	117.7	47.6	104.9	40.5
14	Tetracosane	$C_{24}H_{50}$	338.640	123.6	50.9	118.6	48.1
15	Pentacosane	$C_{25}H_{52}$	352.666	128.7	53.8	117.6	47.6
16	Hexacosane	$C_{26}H_{54}$	366.692	133.5	56.4	127.9	53.3
17	Heptacosane	$C_{27}H_{56}$	380.713	138.2	59.0	127.4	53.0
18	Octacosane	$C_{28}H_{58}$	394.744	142.5	61.4	137.4	58.6
19	Nonacosane	$C_{29}H_{60}$	408.770	146.7	63.8	136.8	58.3
20	Triacontane	$C_{30}H_{62}$	422.796	150.4	65.8	143.6	62.0

*Values taken at 158°F (70°C)

**Values taken at 107°F (41.7°C)

Latent Heat of Fusion		Heat of Transition		Total Heat		Density at Phase Change Temperature				Specific Heat at Phase Change Temperature	
						Liquid		Solid			
Btu/lb	J/g	Btu/lb	J/g	Btu/lb	J/g	lb/ft^3	Kg/m^3	lb/ft^3	Kg/m^3	Btu/lb-°R	J/Kg-°K
57.9	134.6	18.4	42.7	76.3	177.3	-	-	-	-	-	-
93.0	216.1	none	none	93.0	216.1	-	-	-	-	-	-
66.5	154.5	17.9	41.6	84.4	196.1	-	-	-	-	-	-
97.7	227.1	none	none	97.7	227.1	48.4	774.4	50.8	812.8	0.50	2092
70.5	163.8	18.6	43.2	89.1	207.0	-	-	-	-	-	-
101.3	235.4	none	none	101.3	235.4	48.4	774.4	52.1	833.6	0.51	2134
72.4	168.3	19.6	45.6	92.0	213.9	-	-	-	-	-	-
104.7	243.3	none	none	104.7	243.3	48.5	776.0	53.3	852.8	0.52	2176
73.4	170.6	22.1	51.4	95.5	222.0	48.2	771.2	52.4	838.4	-	-
107.0	248.7	none	none	107.0	248.7	48.6	777.6	51.2	819.2	0.53	2218
69.1	160.6	22.4	52.1	91.5	212.7	47.4*	758.4*	-	-	-	-
69.1	160.6	39.6	92.0	108.7	252.6	47.6*	761.6*	-	-	-	-
71.5	166.2	28.8	66.9	100.3	233.1	47.7*	763.2*	-	-	-	-
69.7	162.0	39.7	92.3	109.4	254.3	48.02*	768.3*	-	-	-	-
76.7	178.3	31.8	73.9	108.5	252.2	48.01*	768.3*	-	-	0.52	2176
69.8	162.2	37.8	87.8	107.6	250.0	48.2	771.2*	-	-	-	-
68.2	158.5	32.7	76.0	100.9	234.5	48.7	779.2	-	-	-	-
70.4	162.8	38.6	89.7	109.0	252.5	48.4*	774.4*	-	-	-	-
69.5	161.5	31.2	72.5	100.7	234.0	-	-	-	-	-	-
108.0	251.0	none	none	108.0	251.0	-	-	-	-	-	-

TABLE A-1. PARAFFIN PROPERTY DATA

Coefficient of Thermal Conductivity at Phase Change Temperature		Boiling Point at 14.7 psia		Heat of Vaporization at 14.7 psia and Boiling Point		Vapor Pressure			Coefficient of Expansion at 60°F (15.6°C) and 14.7 psia (1.013×10^5 N/m^2)	
Btu/hr-ft-°F	J/sec-m-°K	°F	°C	Btu/lb	J/g	Psia	@°F	@°C	1/°F	1/°C
-	-	384.60	196.05	114.2	265.4	41.6	220	104.5	0.00056	0.00101
-	-	421.30	216.45	110.2	256.1	-	-		0.00055	0.00099
-	-	455.79	235.63	106.3	247.0	41.5	139	59.5	0.00052	0.00094
0.087	0.149	483.43	251.00	103.4	240.3	1.03	166	74.5	0.00051	0.00092
-	-	519.13	270.84	100.0	232.4	-	-	-	0.00050	0.00090
0.087	0.149	548.23	287.07	97.7	227.0	1.03	222	105.6	-	-
-	-	575.28	302.06	95.0	220.8	-	-	-	-	-
0.087	0.149	601.02	316.38	92.6	215.2	1.03	347	175.1	-	-
-	-	625.5	329.99	90.5	210.3	-	-	-	-	-
0.087	0.149	648.9	343.00	87.8	204.0	1.03	388	197.9	0.00047	0.00085
-	-	671.2	355.39	-	-	-	-	-	-	-
-	-	692.6	367.29	-	-	-	-	-	-	-
-	-	712.9	378.58	-	-	-	-	-	-	-
-	-	732.6	369.53	-	-	-	-	-	-	-
-	-	751.5	400.04	-	-	-	-	-	-	-
-	-	769.5	410.05	-	-	-	-	-	-	-
-	-	786.9	418.61	-	-	-	-	-	-	-
-	-	803.7	429.07	-	-	-	-	-	-	-
-	-	819.9	439.07	-	-	-	-	-	-	-
-	-	835.5	446.74	-	-	-	-	-	-	-

Volume Change on Freezing/ Melting	Surface Tension at 14.7 psia (1.013×10^5 N/m^2)	Absolute Viscosity of Liquid at 68°F (20°C) and 14.7 psia (1.013×10^5 N/m^2)		Refractive Index of Liquid at 68°F (20°C) and 14.7 psia (1.013×10^5 N/m^2)	Heat of Formation of Gas at °R	
Percent	dynes/cm	Centipoise	N-sec/m^2		Btu/lb-mole	J/gm-mole
-	24.7	1.185	0.001185	1.4173	-88434	-2.05×10^5
-	25.4	1.503	0.001503	1.4216	-94986	-2.20×10^5
-	25.9	1.880	0.00188	1.4756	-101556	-2.36×10^5
4.8	26.6	2.335	0.002335	1.4289	-108176	-2.51×10^5
-	27.1	2.863	0.002863	1.4355	-114678	-2.67×10^5
7.4	27.6	3.474	0.003474	1.4368	-121230	-2.82×10^5
-	27.9	4.196	0.004196	1.4389	-127782	-2.97×10^5
9.6	28.3	-	-	1.4408	-134352	-3.12×10^5
-	28.6	-	-	1.4425	-140886	-3.27×10^5
5.2/3.0	28.9	4.29**	0.00429**	1.4420	-147456	-3.43×10^5
-	-	-	-	1.4247	-	-
-	-	-	-	1.4260	-	-
-	-	-	-	1.4276	-	-
-	-	-	-	1.4286	-	-
-	-	-	-	1.4302	-	-
-	-	-	-	1.4310	-	-
-	-	-	-	1.4321	-	-
-	-	-	-	1.4330	-	-
-	-	-	-	1.4340	-	-
-	-	-	-	1.4348	-	-

Net Heat of Combustion at 77°F (25°C) and 14.7 psia (1.013×10^5 N/m^2)		Flash Point		CRITICAL CONSTANTS					
				Pressure		Temperature		Specific Volume	
Btu/lb-mole	J/gm-mole	°F	°C	Psia	N/m^2	°F	°C	ft^3/lb	m^3/Kg
2968.2	6898.1	149	65	282	1.94×10^6	694	368	0.0676	0.0042
3230.3	7507.2	160	71	262	1.81×10^6	728	387	0.0676	0.0042
3492.6	8116.8	175	79	250	1.72×10^6	761	405	0.0667	0.0042
3754.7	8725.9	250	121	235	1.62×10^6	791	422	0.0667	0.0042
4016.8	9335.8	-	-	220	1.52×10^6	818	417	0.0667	0.0042
4278.9	9944.2	-	-	206	1.42×10^6	844	451	0.0667	0.0042
4541.0	10553.3	-	-	191	1.32×10^6	869	465	0.0667	0.0042
4803.5	11163.3	-	-	176	1.21×10^6	890	477	0.0667	0.0042
5065.4	11265.5	-	-	162	1.12×10^6	912	489	0.0667	0.0042
5327.8	12381.8	-	-	162	1.12×10^6	932	500	0.0667	0.0042
-	-	-	-	-	-	-	-	-	-
-	-	-	-	-	-	-	-	-	-
-	-	-	-	-	-	-	-	-	-
-	-	-	-	-	-	-	-	-	-
-	-	-	-	-	-	-	-	-	-
-	-	-	-	-	-	-	-	-	-
-	-	-	-	-	-	-	-	-	-
-	-	-	-	-	-	-	-	-	-
-	-	-	-	-	-	-	-	-	-
-	-	-	-	-	-	-	-	-	-

Property Data References

A-1 Phillips Petroleum Company: Reference Data for Hydrocarbons and Petro-Sulfur Compounds. Special Products Div., Bartlesville, Okla. 1962.

A-2 Maxwell, J.B.: Data Book on Hydrocarbons. van Nostrand Co., 1950.

A-3 Trimmerans, J., Physico-Chemical Constants of Pure Organic Compounds, Vol. 2, Elsevier Publishing Co., New York, N.Y., 1965.

A-4 Phillips Petroleum Company: Phillips 66 Hydrocarbon and Petro-Sulfur Compounds. Bulletin 522, sixth edition, Bartlesville, Okla., 1964.

A-5 Bentilla, E.W.; Sterrett, K.F.; and Karre, L.E.: Research and Development Study on the Thermal Control by Use of Fusible Materials. NASA Report NSL 65-16-1, April 1966.

A-6 Shlosinger, A.P.; and Bentilla, E.W.: Research and Development Study on Thermal Control by Use of Fusible Materials. NASA Report 65-16, February 1965.

A-7 Hale, D.V.; Hoover, M.J.; and O'Neill, M.J.: Phase Change Materials Handbook, NASA CR-61363, September 1971.

A-8 Foti, J.J.; Nisbit, J.L.; and Neati, J.D.: Evolution of Eicosane as a Heat of Fusion — Heat Sink. Vitro Laboratories, TN 04800.29903-1, May 1964.

A-9 Rossini, F.D., et al: Selected Values of Physical and Thermodynamics Properties of Hydro-Carbons and Related Compounds. American Petroleum Institution of Research, Project 44.

A-10 The Boeing Company: Unpublished Tabulation of Physical Properties.

A-11 International Critical Tables of Numerical Data, Physics and Technology. McGraw-Hill Book Co., Inc., New York, 1933.

A-12 Hodgman, C.D.: Handbook of Chemistry and Physics. 42nd ed., The Chemical Rubber Publishing Co., Cleveland, Ohio, 1960-61.

A-13 Broadhurst, M.G., Jr.: An Analysis of the Solid Phase Behavior of the Normal Paraffins. Jour. of Research of the NBS, vol 66A, No. 3, May-June, 1962.

A-14 Schaerer, A.A.; Basso, C.J.; Smith, A.E.; and Skinner, L.B.: Properties of Pure Normal Alkanes in the C_{17} to C_{36} Range, Chemical Society 77, 1955.

A-15 Sakiadis, B.C.; and Coates, J.: Studies of Thermal Conductivity of Liquids. Part III, A.I.ch.E. Jour., vol. 3, 1957.

A-16 Lange, N.A.; Handbook of Chemistry. 8th ed., Handbook Publishers, Inc., Sandusky, Ohio, 1952.

A-17 Schiessler, R.W.; and Whitmore, F.C.: Properties of High Molecular Weight Hydrocarbons. Industrial and Engineering Chem. Vol. 47, No. 8, 1955.

A-18 Sakiadis; and Coates, J.: Prediction of Specific Heat of Organic Liquids. A.I.ch.E. Jour, March 1956.

A-19 Watson, K.M.: Correlation of the Physical Properties of Petroleum. The Science of Petroleum, vol 2, Oxford Univ. Press, London, 1938.

A-20 Powell, R.W.; and Challar, A.R.: Thermal Conductivity of n-Octadecane. Ind. Eng. Chem., 53, 581, 1961.

A-21 Sutherland, R.D.; Davis, R.S.; and Seyer, W.F.: Heat-Transfer Effects Molecular Orientation of Octadecane. Ind. Eng. Chem. 51, 585, 1959.

A-22 Zeibland, H.; and Patient, J.E.: Thermal Conductivity of Octadecane. Jour. of Chem. Enging., Data 7, Part I, 530-1, 1962.

A-23 Watson, K.M.; and Nelson, E.F.: Improved Methods of Approximating Critical and Thermal Properties of Petroleum Fractions. 85th Meeting of the Am. Chem. Soc., Washington, D.C., March 26-31, 1933.

A-24 Cecil, A.B.; and Munch, R.H.; Thermal Conductivity of Some Organic Liquids. Ind. Eng. Chem., vol 48, no. 3, March, 1956.

A-25 Burd, D. Jr.: An Analytical Method for Predicting Hydrocarbon Ideal Gas Thermodynamic Properties. M.S. Thesis, Penn State Univ. 1966.

A-26 Klaus, E.E.; Tewksbury, E.J.; Fenske, et al.: Fluids, Lubricants, Fuels and Related Materials. AFML-TR-67-107, part I, 1967.

A-27 Tolsma, J.: The Thermal Conductivity of Liquids. M.S. Thesis Newark College of Engineering, 1965.

A-28 Agishev, A. Sh.: Investigation of Brownian Rotation of NonSpherical Liquid Molecules by Nuclear Paramagnetic Resonance. English Trans. of Zh. Eksperim. i Teor. Fis., 46, 3-9, Soviet physivs-jetp, 19, 1964.

A-29 Askwith T.C.; Cameron, A.; Crouch, R.F.: Chain Length of Additives in Relation to Lubricants in Their Film and Boundary Lubrications. Proc. Roy. Soc. (London), 292A, 500-19, 1966.

A-30 Jobst, W.; Measurement of Thermal Conductivities of Organic Aliphatic Liquids by an Absolute Unsteady-State Method. International Jour., Heat Mass Transfer (Great Britain), vol. 7, no. 7, 725-32, July 1964.

A-31 Bidlack, D.C.; and Anderson, D.K.: Mutual Diffusion in Nonideal, Nonassociating Liquid Systems. J. Phys. Chem. 68, (12),3790-4, 1964.

A-32 Appeldoorn, J.K.; Campion, R.J.; and Tao, F.F.: Lubricity Properties of High Temperature Jet Fuels. Esso Research and Engineering Co., AF APC TR-66-89, Part I, August 1966.

A-33 Heric, E.L.; and Brewer, J.G.: Viscosity of Some Binary Liquid Nonelectrolyte Mixtures. Jour. of Chem. Eng., Data 12, 574-83, 1967.

A-34 Hogenboom, D.L.: Viscosity-Pressure-Temperature Behavior of Three Normal Paraffins. M.S. Thesis, Penn State Univ., 1961.

A-35 Joliet, J.F.; and Chatard-Moulin, M.: Surface Tension of the Monohalogenated Derivatives $C_nH_{2n+1}X$ and Vander Waals Radii of Halogens. Coll. Sci. Univ. Arsonval, Limoges, France, Compt. Rend., Ser. C263 (1), 13-16, 1966.

A-36 Courtsey, B.M.; Heric, E.L.: Viscosity of Some Binary Systems of Hexadecane and Normal Chloroalkanes. Joun. of Chem. Eng. Data., 14(4), 426-30, 1969.

A-37 Abas-zade, A.K.; and Akhmedov, A.G.: Calculations of the Heat Capacities of Liquid n-alkanes. Russian Jour. of Phys. Chem. (English Trans.), 40(6), 673-4, 1966.

A-38 Permutt, G.: Absolute Viscosity of the N-Paraffin Liquids. M.S. Thesis, Newark College of Engr., 1960.

A-39 Gill, S.J.; and West E.M.: The Indirect Determination of Heat Capacity, C_p, of a Liquid. Jour. of Chem. Education, 43 (10), 557-9, 1966.

A-40 Hogenboom, D.L.; Webb, W.; and Dixon, J.A.: Viscosity of Several Liquid Hydrocarbons as a Function of Temperature. Pressure and Free Volume. Jour. of Chem. Phys., 46(7), 2586-98, 1967.

A-41 Gross, P.H.; and Zimmerman, H.K.: Properties of the Liquid State. Description of Viscosity Over the Entire Liquid Range. Rheol. Acta 3(4), 290-4, 1964.

A-42 Abas-zade, A.K.; and Guseinov, K.D.: The Thermal Conductivity of Saturated Hydrocarbons at High Temperatures and Pressures. Khim. i Tekhnologiya Topliv i Masel (USSR) (English Trans.) 11 (2), 54-7, 1966.

A-43 Porter, R.S.; and Johnson, J.F.: Viscosity Measurements Near a Million Seconds. Trans. soc. Rheol, 9(2), 49-55, 1965.

A-44 Messerly, J.F.; Guthrie, G.B.; Todd, S.S.; and Finke, H.L.: Low Temperature Thermal Data for Pentane, n-Heptadecane and n-octadecane. Jour. of Chem. Eng. data, 12(3), 338-46, 1967.

A-45 Shieh, J.J.: Transport Properties in Linear Alkanes. Dissertation, Yale Univ., 1967.

A-46 Gillap, W.R.; Weiner, N.D.; and Gibaldi, M.: Interfacial Properties of Hydrocarbons. Jour. of Amer. Oil and Chem. Soc., 44(2), 71-3, 1967.

A-47 Shieh, J.C.; and Lyons, P.A.: Transport Properties of Liquid n-Alkanes. Jour. of Physics Chem., 73, (10), 3258-64, 1969.

A-48 Jhon, M.S.; Klotz, W.L.; and Eyring, H.: Theoretical Calculations of the Pressure Dependence of Liquid Hydrocarbon Viscosities. Jour. Chem. Phys. 51(9), 3692-4, 1969.

A-49 Tamplin, W.S.; and Zuzic, D.A.: Specific Heat of Organic Hydrocarbons. Hydrocarbon Process. 46(8), 145-6, 1967.

A-50 Travicek, E.A.: Measurement of Binary Diffusion Coefficients of Five Systems of Liquid Hydrocarbons by a Microinterferometric Technique, at 25°C. PHD Thesis, Kansas State Univ., 1968.

A-51 Aveyard, R.: Adsorption from Some n-Alkane Mixtures of the Liquid/Vapor, Liquid/Water, and Liquid/Solid Interfaces. Trans. Faraday Soc. 63 (11), 2778-88, 1967.

A-52 Mukhamedzyanov, G. Kh.; and Usmanov, A.G.: Thermal Conductivity of Higher Saturated Hydrocarbons. Eng. Trans. of Izv. Vyssh. Ucheb. Zaved., Netfgaz (Russian:, 10(4), 76-80, 1967.

A-53 Mukhamedzyanov, G. Kh.; and Usmanov, A.G.: Thermal Conductivity Liquid Saturation Hydrocarbons (C_6H_{44}-$C_{17}H_{36}$) and Normal Alcohols $C_4H_{10}O$-$C_{18}H_{39}O$). English trans. (Russian) Teplo Massoperenos, 7, 135-45, 1966.

A-54 Jagannathan, T.K.; Viswanath, D.S.; and Kuloor, N.R.: Predict Organic Liquid Viscosity. Hydrocarbon Process., 47(2), 133-6, 1968.

A-55 Tarzimanov, A.A.; and Mashirov, V.E.: Experimental Investigation of the Thermal Conductivity of Vapours of Normal Saturated Hydrocarbons at Temperatures up to 450°C. Thermal Engineering, 14(12), 96-100, 1967.

A-56 Mustafaev, R.A.: Temperature Dependence of Some Thermophysical Values of Liquids n-Alkanes at Atmospheric Pressure. English trans. IZV. vyssh. Ucheb, Zaved., (Russian), Neft gaz, 11(6), 75-8, 1968.

A-57 Reyburn, A.K.: Viscosity and Ultrasonic Velocity in Nonassociated Hydrocarbon Liquid Mixtures. Dissertation, Oklahoma State Univ., 1968.

A-58 Pigal Skaya, L.A.: Temperature Fields and Effective Thermal Conductivity in a Cylindrical Layer of an Absorbing Medium. Eng. trans, Teplofiz. vys. temperatur, 7(4), 687-93, 1969.

A-59 Sewell, J.H.: Calculation of Critical Surface Tensions of Polymers and Surface Tensions of Liquids from Chemical Structure Only. Report no. RAE-TR-69211, Royal Aircraft Establishment, Farnborough, England, Oct. 1969.

TABLE A-2. PARAFFIN COST DATA*

	Paraffin	Cost/lb > 90% Pure	Technical Grade Cost/lb > 95% Pure	Pure Grade Cost/lb > 99% Pure	Research Grade ** Cost/lb > 99.8% Pure
1	Undecane	-	$ 6.40	$ 11.30	$ 86.40
2	Dodecane	-	5.75	.08	107.30
3	Tridecane	-	10.10	20.00	106.40
4	Tetradecane	-	8.60	9.20	-
5	Pentadecane	-	13.60	20.00	-
6	Hexadecane	-	14.30	8.40	-
7	Heptadecane	-	13.60	22.00	-
8	Octadecane	-	13.60	9.30	-
9	Nonadecane	-	12.70	24.00	-
10	Eicosane	$13.70	1.60	1.30	-
11	Heneicosane	-	-	-	-
12	Docosane	-	-	30.00	-
13	Tricosane	-	-	-	-
14	Tetracosane	-	-	30.00	-
15	Pentacosane	-	-	-	-
16	Hexacosane	-	-	-	-
17	Heptacosane	-	-	-	-
18	Octacosane	-	-	30.00	-
19	Nonacosane	-	-	-	-
20	Triacontane	-	-	-	-

* Lowest 1972 prices from Eastman (Kodak) Organic Chemicals, Rochester, N. Y.; Humphrey Chemicals, North Haven, Conn.: and Phillips Petroleum Co., Bartlesville, Okla. - based on quoted quantity prices nearest one pound.

** > 99.9 percent purity sold for ~$ 90 per 5 ML sample.

APPENDIX B

NON-DIMENSIONAL NUMBERS

Introduction

When estimating thermal performance in zero-g and one-g environments, the Rayleigh Number, Marangoni Number and Bond Numbers often appear. The Rayleigh Number can be used to estimate the convective level due to natural buoyancy in a one-g field. The Maragoni Number may be used to correlate the Nusselt Number at zero-g. Finally, the Bond Number may be used to assess the relative magnitude between buoyancy driven and surface tension or capillary driven convection.

Rayleigh Number

The Rayleigh Number is given by

$$Ra = GrPr = \frac{g\beta L^3}{\nu\alpha} (T_S - T_E) \quad ,$$

where

$$\alpha = \frac{k}{\rho cp} \quad ,$$

g = gravitational constant = 32.2 ft/sec^2 (9.8 m/sec),

β = coefficient of Volumetric expansion,

L = characteristic fluid dimension — in this case L is taken to be the average height of the fluid phase in a cell,

T_S = boundary temperature of the hot fluid temperature at the transfer plate,

T_E = is the equilibrium temperature at the phase front = T_{Fr},

ν = $\frac{\mu}{\rho}$ the kinetic viscosity,

k = the coefficient of thermal conductivity in the liquid phase,

ρ = the average liquid phase density,

Cp = the specific heat of the liquid phase, and

μ = the absolute viscosity of the liquid phase.

Assuming the following constant values for these properties, the one-g Rayleigh number for melting may be found in terms of the fluid temperature difference and characteristic dimension:

β = 0.00045 (1/°R) [0.00081 (1/°C)],

k = 0.087 BTU/HR-FT-°R (0.149 J/sec-m-°K),

ρ = 47.2 lb/ft^3 (755.2 kg/m^3),

C_p = 0.5 BTU/lb m-°F (2092 J/kg-°K),

μ = 14.3 lbm/hr-ft (0.0059 n j/m^2), and

giving for one-g

$$Ra = 1.68 \times 10^8 \, L^3 \, \Delta T;$$

where

$$\Delta T = T_S - T_E$$

For a zero-g determination, the Rayleigh Number is zero because of the gravity term. For the case where the net equivalent gravity acting on the melting cell is reduced to 1×10^{-7} g, the zero-g Rayleigh Number is given by

$$Ra = 16.8\ L^3\ \Delta T \quad .$$

Marangoni Number

In the case of paraffins the diminution of surface tension as temperature increases is approximately linear over a large temperature range [39]. The variation of surface tension with temperature is given by Eotvos, Ramsey and Shield equation [80] as

$$\sigma\left(\frac{M}{\rho}\right)^{2/3} = a\ (T_c - T - 6) \quad . \tag{B-1}$$

where σ is the surface tension in dynes/cm, M is the molecular weight, T_c is the critical temperature and a is an arbitrary constant. Since a, M and T_c are constant, and ρ varies only weakly with temperature over the range of interest, differentiating equation (B-1) with respect to temperature yields the surface tension-temperature gradient,

$$\frac{d\sigma}{dT} = -\frac{a}{\left(\frac{M}{\rho}\right)^{2/3}} \quad , \tag{B-2}$$

a constant. Rearranging equation (B-1), an expression for a results in

$$a = \frac{\sigma}{(T_c - T - 6)}\left(\frac{M}{\rho}\right)^{2/3} \quad . \tag{B-3}$$

Substituting a surface tension value of 28.7 dynes/cm at 20°C (68°F), a critical temperature of 490°C, a density of 0.79 gm/cm^3 and a molecular weight of 268.51 for nonadecane [14], the value of a is found to be 3.0.

Now using equation (B-3), we have

$$\frac{d\sigma}{dT} = -0.062 \frac{\text{dynes}}{\text{cm-°C}} \quad , \tag{B-4}$$

so that the Marangoni Number may now be determined by using

$$Ma = \frac{\left(\frac{-d\sigma}{dT}\right)\left(\frac{dT}{dL}\right) L^2}{\rho \nu \alpha} \quad . \tag{B-5}$$

Assuming a linear temperature profile, the $\frac{dT}{dL}$, L^2 product becomes ΔTL. Substituting the liquid properties for nonadecane given earlier, the gravity independent Marangoni Number relationship is found to be

$$Ma = 1684\ \Delta TL \tag{B-6a}$$

for ΔT in °C and L in centimeters, and

$$Ma = 2374\ \Delta TL \tag{B-6b}$$

for ΔT in °F and L in inches.

Bond Number

The Bond Number is given by

$$Bo = \frac{\rho g L^2}{\sigma} \tag{B-7}$$

Again using the nonadecane liquid properties given earlier, the one-g Bond Number is given by

$$Bo = 26.6\ L^2 \tag{B-8a}$$

where L is in centimeters, and

$$Bo = 171.6\ L^2 \tag{B-8b}$$

where L is in inches.

Reynolds, et al., [81] have shown by a graphic representation similar to Figure B-1, the hydrostatic regimes for typical liquids. The gravity dominated regime being above the paraffin diagonal in this Figure and the capillary or surface tension dominated regime being below. Operating points falling in a near proximity of the diagonal are not clearly dominated by either phenomena.

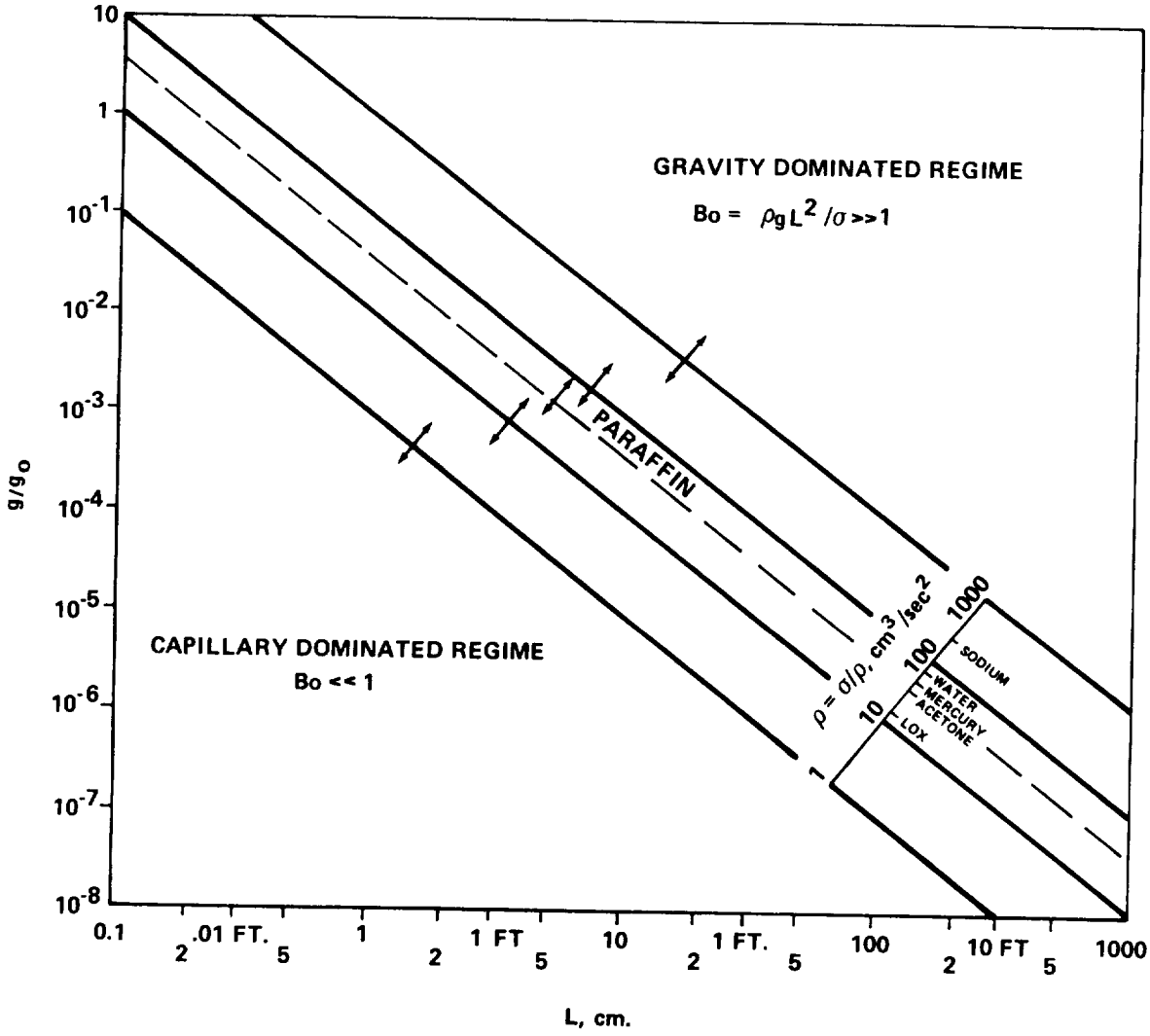

Figure B-1. Hydrostatic regimes for typical liquids.

APPENDIX C

COMPUTER PROGRAMS

Introduction

The computer programs used in the foregoing study are detailed in this Appendix. Some of the information given herein is excerpted from Reference 78. Copies of the FORTRAN programs for a typical melting run with inclusion of convective effects (Table C-1), a typical freezing run, written in FORTRAN (Table C-3), and a CINDA freezing run (Table C-4) are given, along with the corresponding notations. The details of each step is discussed for the melting FORTRAN model in Table C-2. All programs, excluding the CINDA program, are written in FORTRAN V. Programs utilize explicit forward finite differencing techniques.

Since the CINDA model uses techniques similar to those employed in the FORTRAN model no explanation is given and the reader is referred to Reference 77 for explanations of listed sub routines. A skeleton flow chart for the melting model is given in Figure C-1.

It was later discovered that the FORTRAN program for melting would not run for the case of $m = 1$. The statements causing this incompatibility are indicated in the melting program listing by an arrow placed at the left of the appropriate statement. The FORTRAN freezing program incorporates the changes necessary to allow runs for $m = 1$.

NOMENCLATURE

AJ	J-3, used in computing interface location
AM	value of integer M converted to floating point
B	length of section, ft.
BETA	volume expansivity of wax, R^{-1}
BJ	J-2, used in computing interface location
C(I,J)	thermal capacitance of node (I,J), Btu/F
CL	constant pressure specific heat of wax, Btu/lbmF
CP	constant pressure specific heat of wax, Btu/lbmF
CP1	constant pressure specific heat of bottom plate, Btu/lbmF
CP2	constant pressure specific heat of fin, Btu/lbmF
CP3	constant pressure specific heat of top plate, Btu/lbmF
DAVG	average height of liquid based on amount melted, in.
DDOT	interfacial velocity for nodes adjacent to centerline (I=MM), in/hr.
DELT	absolute value of temperature difference between bottom plate and interface, F.
DEN	wax density, lbm/ft^3
DEN1	bottom plate density, lbm/ft
DEN2	fin density, lbm/ft^3
DEN3	top plate density, lbm/ft^3
DFLO[1]	approximate interfacial location for nodes adjacent to fin (I=2) based on amount melted being equal to F2JM, in.
DFIN	interfacial position for nodes adjacent to fin (I=2) based on any amount being melted, in.
DIF	temperature difference used in comparing new and old temperatures during iteration when solving steady state equations for unspecified fin temperatures, °F.
DMID	interfacial position for node adjacent to centerline, in.

NOMENCLATURE (Continued)

DMO	DMID evaluated at previous time, in.
DT	time increment, hr.
EPS	arbitrarily set small number used as a comparator
ERROR	percent error in computed energy balance based on transfer rates, percent.
F(I,J)	mass fraction of node (I,J) which has undergone phase change since start of process
FAC	time ratio used in linearly interpolating specified fin temperatures at a particular time in terms of bracketed data values.
F2JM	fraction of S which corresponds to 1/32 inch (arbitrary)
G	acceleration of gravity, ft/hr^2
H	PCM section height (See Figure 31), ft.
HBOT[2]	heat transfer coefficient between external fluid and bottom plate, $Btu/hr\text{-}ft^2\text{-}F$
HMELT	heat of fusion, Btu/lbm
HTOP[3]	heat transfer coefficient between external fluid and top plate, $Btu/hr\text{-}ft^2\text{-}F$
HTR	heat of transition, Btu/lbm.
I	integer designation of vertical column in which a mode is located (See Figure 31)
J	integer designation of horizontal row in which a mode is located (See Figure 31)
JOE	counter used in refining the heat transfer computation before progressing in time
KCHK	integer used to control printing of results at desired times (See definition of KCOUNT)
KCOUNT	integer counter used to print our results at times when KCOUNT = KCHK
M	number of wax nodes in a horizontal row
MCOUNT	counter used in determining unspecified fin temperatures
MFIN	maximum value of MCOUNT which when exceeded causes program to stop
MM	M+1 (See Figure 31)

NOMENCLATURE (Continued)

N	number of wax nodes in a vertical column
ND	number of data points for measured fin temperatures
NDP	ND-1
NI	N+4
NJ	N+3
NN	N+2
PR	Prandtl number
Q(I,J)	unnecessary variable - replaced where needed by QS(I,J)
QBT	instantaneous heat transfer rate through bottom, Btu/hr
QBW	instantaneous heat transfer rate through bottom to wax only, Btu/hr
QFTR	instantaneous rate of heat transfer to fin, Btu/hr.
QMELT	energy which acounts for amount of wax melted at any time, Btu.
QRAT(I,J)	the instantaneous net rate of heat transfer to node I,J, Btu/hr.
QS(I,J)	the energy stored by node I,J above TREF for wax and above 0 for metal nodes, Btu
QSIN	the energy stored by node I,J above TREF corresponding to initial temperature throughout network, Btu.
QSW	instantaneous heat transfer rate from fin to wax, Btu/hr.
QTOP	instantaneous heat transfer rate out of top of section, Btu/hr.
QTTR	instantaneous rate of heat transfer to top plate, Btu/hr.
QTW	instantaneous heat transfer rate from top plate to wax, Btu/hr
QWAX	net energy transfer to wax since start, Btu.
Q1	energy stored by wax node above TREF corresponding to start of phase transition, Btu.
Q2	energy stored by wax node above TREF corresponding to end of phase transition, Btu.
Q3	energy stored by wax node above TREF corresponding to start of melting, Btu.
Q4	energy stored by wax node above TREF corresponding to end of melting, Btu.

NOMENCLATURE (Continued)

QRA2(I,J)	instantaneous rate of heat transfer to node I,J based on temperatures obtained from QRAT(I,J) and then used to correct temperature predictions, Btu/hr
RA	Rayleigh number for liquid wax
RATIO	ratio of instantaneous heat transfer rate from fin to wax to that from bottom plate to wax
RH(I,J)	horizontal thermal resistance between node I-1,J and node I,J, hr-F/Btu
RV(I,J)	vertical thermal resistance between node I,J and I,J-1, Hr-F/Btu
S	wax node width, ft.
S1	bottom plate thickness, ft.
S2	fin thickness, ft.
S3	top plate thickness, ft.
TAMB	temperature of environment external to top plate, °F
TAU	limiting time value to stop program, Hr.
TIME	instantaneous value of time, Hr.
TIN	initial temperature of all nodes, °F
TK	wax thermal conductivity (artificially allowed to vary in liquid to account for convection), Btu/hr-ft-F
TKL	thermal conductivity of liquid, Btu/hr-ft-F
TKR	ratio of effective thermal conductivity to thermal conductivity
TMELT	fusion temperature of wax, °F
TREF	arbitrary reference temperature (should be less than TIN), °F
TTR	transition temperature, °F
T1(I,J)	temperature of node I,J at time t, °F
T2(I,J)	temperature of node I,J at time t+Δt, °F
T3(I,J)	temperature of node I,J in fin at beginning of each iteration step used in finding steady state solution, °F
TAU2	arbitrarily defined time value used in print-out control, Hr.

NOMENCLATURE (Concluded)

TK1	thermal conductivity of bottom plate, Btu/hr-ft-F
TK2	thermal conductivity of fin, Btu/hr-ft-F
TK3	thermal conductivity of top plate, Btu/hr-ft-F
TIM(L)	time value corresponding to input data of measured fin temperatures, hr.
TM1(L)	measured bottom plate temperature (input data), °F
TM2(L)	first measured fin temperature (input data), °F
TM3(L)	second measured fin temperature (input data), °F
TM4(L)	third measured fin temperature (input data), °F
VIS	viscosity of liquid, lbm/hr-ft
V1	volume of wax melted at time t, ft^3
V2	volume of wax melted at time $t+\Delta t$, ft^3
W	width of wax cell, ft

---

[1] This assumes that some finite thickness must have melted before it would be detectable on the film. The number DFIN is the height corresponding to a node with any amount melted.

[2] This was included to be general but has not been used to date as bottom plate temperatures were specified as input data.

[3] This has been included but set at a small value to essentially correspond to the top being insulated.

TABLE C-1. FORTRAN COMPUTER PROGRAM FOR MELTING

```
      DIMENSION  RV(5,31) , RH(5,31) , C(5,31) , QS(5,31), T1(5,31)
      DIMENSION T2(5,31) , F(5,31) , Q(5,31) , QRAT(5,31), T3(1,31)
      DIMENSION TM1(9), TM2(9), TM3(9), TM4(9), TIM(9)
      DIMENSION QRA2(5, 31)
  COMPUTATIONAL PARAMETERS
      N=27
      M=4
      AM=M
      MM=M+1
      NN=N+2
      NJ=N+3
      NI=N+4
      ND=9
      NDP=8
      TAU=1.1
      KCOUNT=1
      MCOUNT=1
      MFIN=500
      EPS=1.E-06
      KCHK=1000
      JOE=1
      DT=1.0E-04
      TAU2=(10.*DT)+(DT/3.)
  PHYSICAL PROPERTIES
      TAMB=80.
      TIN=73.5
      HTOP=1.E-08
      HBOT=5.0
      G=(32.2*3600.*3600.)
    WAX
      DEN=47.2
      TK=0.087
      CP=0.5
      TTR=73.04
      HTR=22.108
      TMELT=89.8
      HMELT=73.357
      TREF=50.0
      BETA=0.00045
      VIS=14.3
      CL=CP
      TKL=TK
   BOTTOM PLATE DENOTED BY 1
      DEN1=171.0
      TK1=93.0
      CP1=0.22
   FIN DENOTED BY 2
      DEN2=171.0
      TK2=93.0
      CP2=0.22
   TOP PLATE DENOTED BY 3
      DEN3=72.5
      TK3=0.09
      CP3=0.33
```

TABLE C-1. (Continued)

```
55     GEOMETRY PARAMETERS
56         W=0.75/12.0
57         H=2.625/12.0
58         B=5.0/12.0
59         S=W/(2.0*AM)
60         S1=0.032/12.0
61         S2=0.008/12.0
62         S3=0.25/12.0
63         F2JM=1.0/(32.0*S*12.0)
64       VERTICAL RESISTANCES
65         RV(1,2)=(S1/(TK1*S2*B))+(2./(HBOT*S2*B))
66         DO 10 I=2,MM
67      10 RV(I,2)=(S1/(2.*TK1*S*B))+(1./(HBOT*S*B))
68         RV(1,3)=(S/(TK2*S2*B))+(S1/(TK1*S2*B))
69         DO 20 I=2,MM
70      20 RV(I,3)=(1./(2.*TK*B))+(S1/(2.*TK1*S*B))
71         DO 30 J=4,NN
72      30 RV(1,J)=((2.*S)/(TK2*S2*B))
73         DO 40 J=4,NN
74         DO 40 I=2,MM
75      40 RV(I,J)=(1./(TK*B))
76         RV(1,N+3)=(S3/(TK3*S2*B))+(S/(TK2*S2*B))
77         DO 50 I=2,MM
78      50 RV(I,N+3)=(S3/(2.*TK3*S*B))+(1./(2.*TK*B))
79         RV(1,N+4)=(S3/(TK3*S2*B))+(2./(HTOP*S2*B))
80         RV(2,N+4)=(S3/(2.*TK3*B*(S+(S2/2.))))+(1./(HTOP*B*(S+(S2/2.))))
81 ------> DO 60 I=3,MM
82      60 RV(I,N+4)=(S3/(2.*TK3*S*B))+(1./(HTOP*S*B))
83       HORIZONTAL RESISTANCES
84         RH(2,N+3)=((S2+S)/(2.*TK3*S3*B))
85 ------> DO 70 I=3,MM
86      70 RH(I,N+3)=(S/(TK3*S3*B))
87         DO 80 J=3,NN
88      80 RH(2,J)=(S2/(2.*TK2*S*B))+(1./(2.*TK*B))
89         DO 90 J=3,NN
90 ------> DO 90 I=3,MM
91      90 RH(I,J)=(1./(TK*B))
92         RH(2,2)=((S2+S)/(2.*TK1*S1*B))
93 ------> DO 100 I=3,MM
94     100 RH(I,2)=(S/(TK1*S1*B))
95         RH(2,N+3)=RH(2,N+3)+RV(1,N+3)
96     NODAL CAPACITANCES
97         C(1,2)=((DEN1*S1*S2*B*CP1)/2.)
98         DO 110 I=2,MM
99     110 C(I,2)=(DEN1*S1*S*B*CP1)
100        DO 120 J=3,NN
101    120 C(1,J)=((DEN2*S2*S*B*CP2)/2.)
102        C(1,N+3)=((DEN3*S2*S3*B*CP3)/2.)
103        C(2,N+3)=(S3*B*(S+(S2/2.))*DEN3*CP3)
104 -----> DO 130 I=3,MM
105    130 C(I,N+3)=(DEN3*S3*S*B*CP3)
106        DO 140 J=3,NN
107        DO 140 I=2,MM
108    140 C(I,J)=(DEN*(S**2)*B*CP)
109 -----> Q1=(C(3,4)*(TTR-TREF))
110        Q2=Q1+((DEN*(S**2)*B*HTR))
```

TABLE C-1. (Continued)

```
      Q3=Q2+((C(3,4))*(TMELT-TTR))
      Q4=Q3+((DEN*(S**2)*B*HMELT))
C  INITIALIZATION OF PERTINENT QUANTITIES
      TIME=0.0
      QWAX=0.0
      QBW=0.0
      QSW=0.0
      QTW=0.0
      QTOP=0.0
      QFTR=0.0
      QTTR=0.0
      V1=0.0
      V2=0.0
      DMO=0.0
      DO 150 J=2,NJ
      DO 150 I=1,MM
  150 T1(I,J)=TIN
      IF(TIN.LT.TTR)QSIN=(C(3,4)*(TIN-TREF))
      IF(TIN.GT.TTR.AND.TIN.LT.TMELT) QSIN=Q2+((C(3,4))*(TIN-TTR))
      IF(TIN.GT.TMELT)QSIN=Q4+((C(3,4))*(TIN-TMELT))
      DO 160 I=1,MM
  160 T1(I,N+4)=TAMB
      DO 170 J=3,NN
      DO 170 I=2,MM
  170 QS(I,J)=QSIN
      DO 180 I=1,MM
      Q(I,2)=0.0
  180 Q(I,N+3)=0.0
      DO 190 J=3,NN
  190 Q(1,J)=0.0
      DO 199 J=2,NI
      DO 199 I=1,MM
      F(I,J)=0.0
  199 QRAT(I,J)=0.0
      READ(5,11) (TM1(I), I=1,ND)
      READ(5,11) (TM2(I), I=1,ND)
      READ(5,11) (TM3(I), I=1,ND)
      READ(5,11) (TM4(I), I=1,ND)
      READ(5,11) (TIM(I), I=1,ND
   11 FORMAT(8F10.0)
      WRITE(6,22) TIME,W,H,N,M
   22 FORMAT(1X,5HTIME=,E15.8,10X,2HW=,E15.8,10X,2HH=,E15.8,10X,2HN=,I2,
     15X,2HM=,I2)
      WRITE(6,33)Q1,Q2,Q3,Q4
   33 FORMAT(1X,3HQ1=,E15.8,10X,3HQ2=,E15.8,10X,3HQ3=,E15.8,10X,3HQ4=,E1
     5.8)
      WRITE(6,44)
   44 FORMAT(2X,4HI J,5X,19HVERTICAL RESISTANCE,6X,21HHORIZONTAL RESIST
     ANCE,6X,17HNODAL CAPACITANCE,6X,11HTEMPERATURE,5X,7HQS(I,J))
      DO 200 J=2,NI
      DO 200 I=1,MM
      IF(J.EQ.N+4) GO TO 1
      GO TO 2
    1 QS(1,J)=0.0
      RH(I,J)=1.E08
      C(I,J)=0.0
```

TABLE C-1. (Continued)

```
      2 IF(I.EQ.1)RH(I,J)=1.E08
        IF(J.EQ.2.OR.J.EQ.N+3)QS(I,J)=0.0
        IF(I.EQ.1)QS(I,J)=0.0
        WRITE(6,55)I,J,RV(I,J),RH(I,J),C(I,J),T1(I,J),QS(I,J)
     55 FORMAT(1X,I2,1X,I2,5X,E15.8,10X,E15.8,10X,E15.8,6X,E16.8,4X,E15.8)
    200 CONTINUE
        DO 889 J=3,NN
    889 T3(1,J)=T1(1,J)
    COMPUTATION SECTION  COMPUTATION SECTION COMPUTATION SECTION
      3 TIME=TIME+DT
        DO 210 J=3,NJ
        QRAT(1,J)=((T1(2,J)-T1(1,J))/RH(2,J))+((T1(1,J-1)-T1(1,J))/RV(1,J)
        +((T1(1,J+1)-T1(1,J))/RV(1,J+1))
        QRAT(MM,J)=((T1(M,J)-T1(MM,J))/RH(MM,J))+((T1(MM,J-1)-T1(MM,J))/RV
        (MM,J))+((T1(MM,J+1)-T1(MM,J))/RV(MM,J+1))
    210 CONTINUE
        DO 211 J=3,NJ
        DO 211 I=2,M
        QRAT(I,J)=((T1(I-1,J)-T1(I,J))/RH(I,J))+((T1(I+1,J)-T1(I,J))/RH(I+
        1,J))+((T1(I,J-1)-T1(I,J))/RV(I,J))+((T1(I,J+1)-T1(I,J))/RV(I,J+1)
        )
    211 CONTINUE
    212 DO 220 J=3,NJ
        DO 220 I=1,MM
    220 QS(I,J)=QS(I,J)+(QRAT(I,J)*DT)
        DO 240 I=2,MM
    240 T2(I,N+3)=T1(I,N+3)+((QRAT(I,N+3)*DT)/C(I,N+3))
        T2(1,N+3)=T2(2,N+3)
        DO 250 J=3,NN
        DO 250 I=2,MM
        IF(QS(I,J).LT.Q1)T2(I,J)=TREF+(QS(I,J)/C(I,J))
        IF(QS(I,J).GE.Q1.AND.QS(I,J).LE.Q2) T2(I,J)=TTR
        IF(QS(I,J).GT.Q2.AND.QS(I,J).LT.Q3) T2(I,J)=TTR+((QS(I,J)-Q2)/C(I,
        J))
        IF(QS(I,J).GE.Q3.AND.QS(I,J).LE.Q4) T2(I,J)=TMELT
     WHEN GOING FROM MELT TO FREEZE OR VICE-VERSA CHANGE THE FOLLOWING CARD
        IF(QS(I,J).GT.Q3.AND.QS(I,J).LT.Q4) F(I,J)=(QS(I,J)-Q3)/(DEN*(S**2
        )*B*HMELT)
        IF(QS(I,J)GT.Q4)  T2(I,J)=TMELT+((QS(I,J)-Q4)/C(I,J))
     WHEN GOING FROM MELT TO FREEZE OR VICE-VERSA CHANGE THE FOLLOWING CARD
        IF(QS(I,J).GE.Q4)F(I,J)=1.0
        IF(QS(I,J).LE.Q3) F(I,J)=0.0
    250 CONTINUE
    SPECIFICATION AND/OR DETERMINATION OF FIN TEMPERATURES
              THE FOLLOWING DO LOOP ASSUMES FIN TEMPERATURES FOR ITERATION
        DO 255 J=3,NN
    255 T2(1,J)=T3(1,J)
        DO 260 L=1,NDP
        IF(TIME.GE.TIM(L).AND.TIME.LE.TIM(L+1)) GO TO 4
    260 CONTINUE
      4 FAC=(TIME-TIM(L))/(TIM(L+1)-TIM(L))
        T2(1,2)=TM1(L)+((TM1(L+1)-TM1(L))*FAC)
        T2(1,8)=TM2(L)+((TM2(L+1)-TM2(L))*FAC)
        T2(1,15)=TM3(L)+((TM3(L+1)-TM3(L))*FAC)
        T2(1,21)=TM4(L)+((TM4(L+1)-TM4(L))*FAC)
        DO 270 I=1,MM
```

TABLE C-1. (Continued)

```
222   270 T2(I,2)=T2(1,2)
223   UNSPECIFIED FIN TEMPERATURES DETERMINED BY STEADY STATE EQUATIONS
224   256 MCOUNT=MCOUNT+1
225       DO 280 J=3,NN
226       T3(1,J)=T2(1,J)
227       IF(J.EQ.8.OR.J.EQ.15) GO TO 5
228       IF(J.EQ.21) GO TO 5
229       T2(1,J)=((T2(1,J-1)/RV(1,J))+(T2(2,J)/RH(2,J))+(T2(1,J+1)/RV(1,J+1
230       )))/((1./RV(1,J))+(1./RH(2,J))+(1./RV(1,J+1)))
231     5 CONTINUE
232   280 CONTINUE
233       IF(MCOUNT.GT.MFIN) GO TO 8
234       DO 281 J=3,NN
235       DIF=T2(1,J)-T3(1,J)
236       IF(ABS(DIF).GT.EPS) GO TO 256
237   281 CONTINUE
238       IF(JOE.EQ.2) GO TO 285
239       JOE=JOE+1
240       DO 888 J=3,NJ
241       DO 888 I=1,MM
242   888 QS(I,J)=QS(I,J)-(QRAT(I,J)*DT)
243       DO 282 J=3,NJ
244       QRA2(1,J)=((T2(2,J)-T2(1,J))/RH(2,J))+((T2(1,J-1)-T2(1,J))/RV(1,J)
245       )+((T2(1,J+1)-T2(1,J))/RV(1,J+1))
246       QRA2(MM,J)=((T2(M,J)-T2(MM,J))/RH(MM,J))+((T2(MM,J-1)-T2(MM,J))/RV
247       (MM,J))+((T2(MM,J+1)-T2(MM,J))/RV(MM,J+1))
248   282 CONTINUE
249       DO 283 J=3,NJ
250       DO 283 I=2,M
251       QRA2(I,J)=((T2(I-1,J)-T2(I,J))/RH(I,J))+((T2(I+1,J)-T2(I,J))/RH(I+
252       1,J))+((T2(I,J-1)-T2(I,J))/RV(I,J))+((T2(I,J+1)-T2(I,J))/RV(I,J+1)
253       )
254   283 CONTINUE
255       DO 284 J=3,NJ
256       DO 284 I=1,MM
257   284 QRAT(I,J)=(QRAT(I,J)+QRA2(I,J))/2.0
258       GO TO 212
259   285 MCOUNT=1
260       DO 286 I=1,MM
261   286 QRAT(I,2)=((T2(I,2)-T1(I,2))*C(I,2)/DT)
262       DO 287 I=1,MM
263   287 QS(I,2)=QS(I,2)+(C(I,2)*(T2(I,2)-T1(I,2)))
264       DO 290 I=2,MM
265       QBW=(T2(I,2)-T2(I,3))/RV(I,3)+QBW
266   290 QTW=(T2(I,N+3)-T2(I,N+2))/RV(I,N+3)+QTW
267       QBT=QBW+((T2(1,2)-T2(1,3))/RV(1,3))
268       DO 300 J=3,NN
269   300 QSW=QSW+((T2(1,J)-T2(2,J))/RH(2,J))
270       DO 310 I=1,MM
271   310 QTOP=((T2(I,N+3)-TAMB)/RV(I,N+4))+QTOP
272       DO 311 J=3,NN
273   311 QFTR=QFTR+QRAT(1,J)
274       DO 312 I=1,MM
275   312 QTTR=QTTR+QRAT(1,NJ)
276       QWAX=(QBW+QTW+QSW)*DT+(QWAX)
277       RATIO=QSW/QBW
```

TABLE C-1. (Continued)

```
      ERROR=((QBT-(QBW+QSW+QTW+QTOP+QFTR+QTTR))*100.0)/QBT
      DO 930 J=3,NN
      DO 930 I=2,MM
      V2=V2+(F(I,J)*(S**2)*B)
  930 CONTINUE
      DAVG=((2.0*V2)/(W*B))*12.0
      QMELT=((V2-V1)*DEN*HMELT)/DT
      V1=V2
      V2=0.0
      DELT=ABS(T2(1,2)-TMELT)
      PR=(VIS*CL)/TKL
      RA=((DEN**2)*G*CL*BETA*DELT*(DAVG**3))/(VIS*TKL*1728.0)
      IF(T2(1,2).LE.TMELT) RA=0.0
      IF(RA.GT.1.E05)TK=(TKL*0.104*(RA**0.305)*(PR**0.084))
      IF(RA.GE.3500.0.AND.RA.LE.1.E05) TK=(TKL*0.229*(RA**0.252))
      IF(RA.GE.1700.0.AND.RA.LT.3500.0) TK=(TKL*0.00238*(RA**0.816)
      TKR=TK/TKL
      DO 945 I=2,MM
      IF(F(I,3).LT.0.25) GO TO 945
      RV(I,3)=(1./(2.*TK*B))+(S1/(2.*TK1*S*B))
  945 CONTINUE
      DO 946 J=4,NN
      DO 946 I=2,MM
      IF(F(I,J).LT.EPS) GO TO 946
      RV(I,J)=(1./(TK*B))
  946 CONTINUE
      DO 947 I=2,MM
      IF(F(I,NN).LT.0.75) GO TO 947
      RV(I,N+3)=(S3/(2.*TK3*S*B))+(1./(2.*TK*B))
  947 CONTINUE
      DO 950 J=3,NN
      IF(F(2,J).LT.0.25) GO TO 949
      RH(2,J)=(S2/(2.*TK2*S*B))+(1./(2.*TK*B))
  949 CONTINUE
      DO 950 I=3,MM
      IF(F(I,J).LT.EPS) GO TO 950
      RH(I,J)=(1./(TK*B))
  950 CONTINUE
      IF(KCOUNT.EQ.KCHK) GO TO 6
      KCOUNT=KCOUNT+1
      GO TO 7
    6 WRITE(6,66) TIME, QWAX, ERROR
   66 FORMAT(1X,5HTIME=,E15.8,10X,5HQWAX=,E15.8,10X,6HERROR=,E15.8)
      DO 313 J=3,NN
      AJ=J-3
      BJ=J-2
      IF(F(2,J).GT.F2JM) DFLO=(BJ*S*12.0)
      DFIN=(AJ*S*12.0)
      IF(F(2,J).LT.EPS) GO TO 314
  313 CONTINUE
  314 DO 315 J=3,NN
      AJ=J-3
      IF(F(MM,J).LT.1.0) DMID=((AJ*S)+(F(MM,J)*S))*12.0
      IF(F(MM,J).LT.1.0) GO TO 316
  315 CONTINUE
  316 WRITE(6,67) DFIN, DFLO, DAVG, DMID
```

TABLE C-1. (Concluded)

```
334    67 FORMAT(1X,5HDFIN=,E15.8,10X,5HDFLO=,E15.8,10X,5HDAVG=,E15.8,10X,5H
335       DMID=,E15.8)
336       DDOT=(DMID-DMO)/DT
337       DMO=DMID
338       WRITE(6,68) RA, TKR, QMELT, DDOT
339    68 FORMAT(1X,3HRA=,E15.8,10X,4HTKR=,E15.8,10X,6HQMELT=,E15.8,10X,5HDD
340       OT=,E15.8)
341       WRITE(6,77) QBW, QSW, QTW, QBT, RATIO
342    77 FORMAT(1X,4HQBW=,E15.8,3X,4HQSW=,E15.8,3X,4HQTW=,E15.8,3X,4HQBT=,E
343       15.8,3X,6HRATIO=,E15.8)
344       WRITE(6,88)
345    88 FORMAT(2X,1HI,2X,1HJ,10X,11HTEMPERATURE,10X,15HFRACTION MELTED,10X
346       ,11HENERGY RATE,10X,13HENERGY STORED)
347       DO 320 J=2,NJ
348       DO 320 I=1,MM
349       WRITE(6,99)I,J,T2(I,J),F(I,J),QRAT(I,J),QS(I,J)
350    99 FORMAT(1X,I2,1X,I2,8X,E15.8,8X,E15.8,8X,E15.8,8X,E15.8)
351   320 CONTINUE
352       KCOUNT=1
353     7 QBW=0.0
354       QSW=0.0
355       QTW=0.0
356       QTOP=0.0
357       QTTR=0.0
358       QFTR=0.0
359       DO 330 J=2,NJ
360       DO 330 I=1,MM
361   330 T1(I,J)=T2(I,J)
362       JOE=1
363       IF(TIME.LT.TAU) GO TO 3
364     8 WRITE(6,111) MCOUNT
365   111 FORMAT(1X,I3)
366       STOP
367       END
```

TABLE C-2. DISCUSSION OF COMPUTER PROGRAM FOR MELTING

In the following discussion, references are made to line numbers corresponding to those designated on the copy of the program.

LINES	DISCUSSION
1 - 4	required dimension statements for subscripted variables; values should be (MM, NI) for all double subscripted variables except T3 for which they should be (1, NJ); values should be ND for single subscripted variables; NOTE: Q(MM,NI) is superfluous and can be omitted with lines 136 - 140.
5 - 23	specification of computational parameters
24 - 54	specification of physical properties
55 - 63	specification of geometry parameters
64 - 82	computation of all vertical thermal resistance values RV (I,J)
83 - 95	computation of all horizontal thermal resistance values RH(I,J); note that line 95 is a special definition which amounts to bypassing node (1,N+3) which was done to overcome stability criterion required by this small corner node
96 - 108	computation of all nodal capacitance values C(I,J)
109 - 112	computation of energy stored by a wax node relative to TREF for the start and end of phase transition and the start and end of fusion, respectively
113 - 144	initialization of pertinent quantities; the initial value of the stored energy depends on the relationship of the initial temperature to the reference temperature TREF; note that lines 136 - 140 are superfluous and can be omitted; some initialization of certain parameters is done in the DO loop between lines 160 and 172 which are set primarily to avoid random print-out and are not essential to the computation done in the heart of the program
145 - 150	input data values for measured fin and bottom plate temperatures and corresponding time values

TABLE C-2. (Continued)

151 - 172	print out of initial values for checking purposes and print out of certain computed quantities for informational purposes
173 - 174	initially defines T3(1,J) for all fin nodes and sets these equal to the initial temperatures T1(1,J)
175	beginning of main computation scheme
176	time is stepped forward by Δt
177 - 188	loops which compute and store the net rate of heat transfer to nodes (I,J) based on old temperatures T1(I,J); the rate of heat transfer to node (I,J) is given by $$\dot{q}(I,J) = \frac{T(I-1,J)-T(I,J)}{RH(I,J)} + \frac{T(I+1,J)-T(I,J)}{RH(I,J)} + \frac{T(I,J-1)-T(I,J)}{RV(I,J)} + \frac{T(I,J+1)-T(I,J)}{RV(I,J+1)}$$ this expression must be modified accordingly for nodes near a boundary which are not surrounded by four neighbors
189 - 191	computation of total energy stored by node (I,J) since the start which is given by $$Q_{stored} = \sum_{time} \dot{q}\Delta t$$
192 - 193	computation of new top plate temperatures T2(I,N+3) from the expression $$T2(I,J) = T1(I,J) + \frac{\dot{q}(I,J)\Delta t}{C(I,J)}$$
194	sets the corner top plate node (1,N+3) temperature equal to that of the second node (2,N+3); omission of the corner node in the computation scheme was done to avoid stability problems due to its small size
195 - 208	computation of new wax node temperatures from the energy stored by the nodes and their capacity and/or phase change enthalpy values; when the stored energy lies between Q1 and Q2 the new temperature is forced to be the transition temperature and when it lies between Q3 and Q4 the new temperature; is forced to be the fusion temperature; also the fraction of the node which has undergone

TABLE C-2. (Continued)

	phase change is calculated from the relationship of the stored energy to Q3 and Q4; note that certain designated cards need to be changed when running the program for freezing as contrasted to melting
209 - 210	beginning of determination of fin temperatures
211 - 212	all new fin temperatures are set to T3(1,J) which simply represents an assumed value always corresponding to the previously computed value except at the very beginning at which time it is set as the initial temperature
213 - 220	interpolation scheme which assigns new temperatures to the three nodes on the fin and one on the bottom plate corresponding to positions where temperature measurements were made; the new temperatures are linearly interpolated from the input data
221 - 222	assigns all nodes along the bottom plate the same value of new temperature
223	beginning of iteration process to determine unspecified fin temperatures from steady state equation; fin nodes were not treated as transient cases due to their extremely small capacitances that would impose a severe stability criterion
224 - 237	iteration process used to determine unspecified fin temperatures; in each iteration, T2(1,J) is computed from steady state equations and then compared with T3(1,J) which corresponds to the calculated temperatures during the previous iterative step; the iteration is continued until the differences between computed fin temperatures and their corresponding values for the previous iterative step are all acceptably small; should the iteration exceed MFIN counts the program is directed to stop
238	when counter JOE equals 2, the new temperatures at all nodes are considered to be the solution at the particular time and the program advances to line 259
239	increase of counter JOE to 2
240 - 242	the energy stored at each node (I,J) is reset back to its original value; this is to allow for an improved computation of the net heat transfer rate to each node to be made and then a recomputation of the stored energy and the corresponding new temperatures
243 - 254	computation of net heat transfer rate to each node using new temperatures T2

TABLE C-2. (Continued)

255 - 257	calculation of net heat transfer rate to each node as the average of that based on old temperatures T1 and new temperatures T2
258	return to line 189 which consists of redirecting the computation through that of computing improved new temperatures, energy storage values, and fractional melted values by using the improved (averaged) heat transfer rate (Lines 255 - 257); this corrective technique is only employed once
259 - 278	computation of various heat transfer quantities from the new temperatures obtained at time $t+\Delta t$
279 - 282	computation of volume of melted wax
283	computation of average liquid depth from the volume melted
284	computation of energy required to melt the wax which has melted
285 - 286	resetting of V1 and V2 for next time step
287	determination of absolute value of temperature difference between bottom plate and the fusion temperature
288	computation of the Prandtl number
289 - 290	computation of the Rayleigh number
291 - 293	determination of effective liquid conductivity due to convection by using correlations of O'Toole and Silveston
294	computation of ratio of effective liquid conductivity to actual value
295 - 315	recomputation of thermal resistances in the liquid by using the effective thermal conductivity rather than the actual value
316	counter check which controls printing out of desired results as well as computation of interfacial position
317	counter advance
318	by-pass of printing results except when line 316 is executed

TABLE C-2. (Concluded)

319 - 320	write statement for printing results
321 - 332	computation of interface position for columns next to fin and next to centerline
333 - 335	write statement for printing results
336 - 337	calculation of interfacial velocity and renaming interfacial position to provide for determining its change at the next time step
338 - 351	write statements and corresponding formats for printing results
352 - 358	reinitialization of pertinent quantities for next time step.
359 - 361	setting new temperatures for current time step to be old temperatures for the next time step
362	reinitialization of counter
363	comparison of time to upper limit value which when exceeded results in stopping the program
364 - 365	printing out of value of counter used in fin temperature iteration
366	STOP
367	END

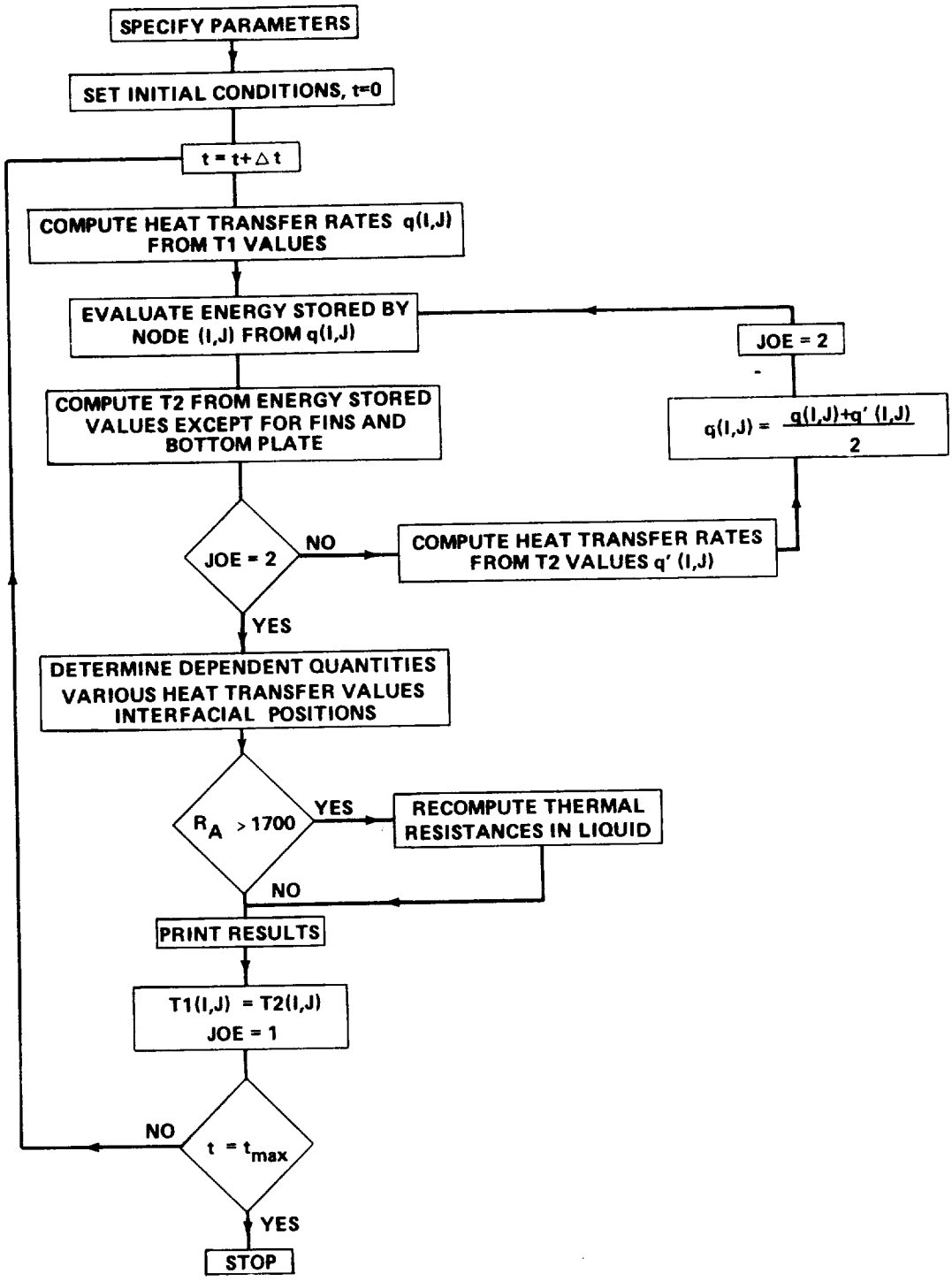

Figure C-1. Skeleton flow chart.

TABLE C-3. FORTRAN COMPUTER PROGRAM FOR SOLIDIFICATION

```
C      TEST 230-45 FREEZE TEST 3/4 INCH CELL
       DIMENSION RV(5,31), RH(5,31), C(5,31), QS(5,31), T1(5
      1,31)
       DIMENSION T2(5,31), F(5,31), QRAT(5,31), T3(1,31),QRA2
      1(5,31)
       DIMENSION TM1(25), TM2(25), TM3(25), TM4(25), TIM(25)
       DIMENSION VR(5,31), HR(5,31)
C COMPUTATIONAL PARAMETERS
       N=27
       M=4
       AM=M
       MM=M+1
       NN=N+2
       NJ=N+3
       NI=N+4
       ND=23
       NDP=22
       TAU=1.5
       KCOUNT=1
       MCOUNT=1
       MFIN=500
       EPS=1.E-06
       KCHK=1000
       JOE=1
       DT=0.00005
       TAU2=(10.**DT)+(DT/3.)
       AF=40.
       UN=1.0-EPS
C PHYSICAL PROPERTIES
       TAMB=80.
       TIN=100.
       HTOP=1.E-08
       HBOT=5.
       G=(32.174*3600.*3600.)
C    WAX
       DEN=47.2
       TK=0.087
       CP=0.5
       TTR=73.04
       HTR=22.108
       TMELT=89.8
       HMELT=73.357
       TREF=50.
       BETA=0.00045
       VIS=14.3
       CL=CP
       TKL=TK
C    BOTTOM PLATE DENOTED BY 1
       DEN1=171.
       TK1=93.
       CP1=0.22
```

TABLE C-3. (Continued)

```
C    FIN DENOTED BY 2
       DEN2=171.
       TK2=93.
       CP2=0.22
C    TOP PLATE DENOTED BY 3
       DEN3=72.5
       TK3=0.09
       CP3=0.33
C GEOMETRY PARAMETERS
       W=0.75/12.0
       H=2.625/12.0
       B=5.0/12.0
       S=W/(2.*AM)
       S1=0.032/12.0
       S2=0.008/12.0
       S3=0.25/12.0
       F2JM=1.0/(32.0*S*12.0)
C    VERTICAL RESISTANCES
       RV(1,2)=(S1/(TK1*S2*B))+(2./(HBOT*S2*B))
       DO 10 I=2,MM
    10 RV(I,2)=(S1/(2.*TK1*S*B))+(1./(HBOT*S*B))
       RV(1,3)=(S/(TK2*S2*B))+(S1/(TK1*S2*B))
       DO 20 I=2,MM
    20 RV(I,3)=(1./(2.*TK*B))+(S1/(2.*TK1*S*B))
       DO 30 J=4,NN
    30 RV(1,J)=((2.*S)/(TK2*S2*B))
       DO 40 J=4,NN
       DO 40 I=2,MM
    40 RV(I,J)=(1./(TK*B))
       RV(1,N+3)=(S3/(TK3*S2*B))+(S/(TK2*S2*B))
       DO 50 I=2,MM
       RV(I,N+4) = (S3/(2.*TK3*S*B)) + (1./(HTOP*S*B))
    50 RV(I,N+3)=(S3/(2.*TK3*S*B))+(1./(2.*TK*B))
       RV(1,N+4)=(S3/(TK3*S2*B))+(2./(HTOP*S2*B))
       RV(2,N+4)=(S3/(2.*TK3*B*(S+(S2/2.))))+(1./(HTOP*B*(S+
      1(S2/2.))))
C    HORIZONTAL RESISTANCES
       DO 70 I=2,MM
       RH(I,2) = (S/(TK1*S1*B))
    70 RH(I,N+3)=(S/(TK3*S3*B))
       DO 80 J=3,NN
       DO 80 I=2,MM
    80 RH(I,J) = (1./(TK*B))
       DO 90 J=3,NN
    90 RH(2,J)= (S2/(2.*TK2*S*B)) + (1./(2.*TK*B))
       RH(2,2)=((S2+S)/(2.*TK1*S1*B))
       RH(2,N+3)=((S2+S)/(2.*TK3*S3*B))
       RH(2,N+3)=RH(2,N+3)+RV(1,N+3)
C NODAL CAPACITANCES
       C(1,2)=((DEN1*S1*S2*B*CP1)/2.)
       DO 110 I=2,MM
```

TABLE C-3. (Continued)

```
  110 C(I,2)=(DEN1*S1*S*B*CP1)
      DO 120 J=3,NN
  120 C(1,J)=((DEN2*S2*S*B*CP2)/2.)
      C(1,N+3)=((DEN3*S2*S3*B*CP3)/2.)
      DO 130 I=2,MM
  130 C(I,N+3)=(DEN3*S3*S*B*CP3)
      C(2,N+3)=(S3*B*(S+(S2/2.))*DEN3*CP3)
      DO 140 J=3,NN
      DO 140 I=2,MM
  140 C(I,J)=(DEN*(S**2)*B*CP)
      Q1 = (C(2,3)*(TTR-TREF))
      Q2=Q1+((DEN*(S**2)*B*HTR))
      Q3 = Q2 + ((C(2,3))*(TMELT-TTR))
      Q4=Q3+((DEN*(S**2)*B*HMELT))
C INITIALIZATION OF PERTINENT QUANTITIES
      TIME=0.0
      QMAX=0.0
      QBW=0.0
      QSW=0.0
      QTW=0.0
      QTOP=0.0
      QFTR=0.0
      QTTR=0.0
      V1=0.0
      V2=0.0
      DMO=0.0
      DO 150 J=2,NJ
      DO 150 I=1,MM
  150 T1(I,J)=TIN
      IF(TIN.LT.TTR)QSIN=(C(2,3)*(TIN-TREF))
      IF(TIN.GT.TTR.AND.TIN.LT.TMELT) QSIN=Q2+(C(2,3)*(TIN
     1-TTR))
      IF(TIN.GT.TMELT)QSIN=Q4+((C(2,3))*(TIN-TMELT))
      DO 160 I=1,MM
  160 T1(I,N+4)=TAMB
      DO 170 J=3,NN
      DO 170 I=2,MM
  170 QS(I,J)=QSIN
      DO 199 J=2,NI
      DO 199 I=1,MM
      F(I,J)=0.0
  199 QRAT(I,J)=0.0
      READ(5,11) (TM1(I), I=1,ND)
      READ(5,11) (TM2(I), I=1,ND)
      READ(5,11) (TM3(I), I=1,ND)
      READ(5,11) (TM4(I), I=1,ND)
      READ(5,11) (TIM(I), I=1,ND)
   11 FORMAT(8F10.0)
      DO 910 KTC=1, ND
  910 TIM(KTC)=TIM(KTC)/3600.
      WRITE(6,22) TIME,W,M,N,M
```

TABLE C-3. (Continued)

```
   22 FORMAT(1X,5HTIME=,E15.8,10X,2HW=,E15.8,10X,2HH=,E15.8
     1,10X,2HN=,I2,15X,2HM=,I2)
      WRITE(6,33)Q1,Q2,Q3,Q4
   33 FORMAT(1X,3HQ1=,E15.8,10X,3HQ2=,E15.8,10X,3HQ3=,E15.8
     1,10X,3HQ4=,E15.8)
      WRITE(6,44)
   44 FORMAT(2X,4HI  J,5X,19HVERTICAL RESISTANCE,6X
     1,21HHORIZONTAL RESISTANCE,6X,17HNODAL CAPACITANCE,6X
     2,11HTEMPERATURE,5X,7HQS(I,J))
      DO 200 J=2,NI
      DO 200 I=1,MM
      IF(J.EQ.N+4) GO TO 1
      GO TO 2
    1 QS(I,J)=0.0
      RH(I,J)=1.E08
      C(I,J)=0.0
    2 IF(I.EQ.1) RH(I,J)=1.E08
      IF(J.EQ.2.OR.J.EQ.N+3) QS(I,J)=0.0
      IF(I.EQ.1) QS(I,J)=0.0
      WRITE(6,55)I,J,RV(I,J),RH(I,J),C(I,J),T1(I,J),QS(I,J)
   55 FORMAT(1X,I2,1X,I2,5X,E15.8,10X,E15.8,10X,E15.8,6X
     1,E15.8,4X,E15.8)
  200 CONTINUE
      DO 400 J=3,NJ
      DO 400 I=2,MM
      VR(I,J)=RV(I,J)
  400 HR(I,J)=RH(I,J)
      DO 889 J=3,NN
  889 T3(1,J)=T1(1,J)
C COMPUTATION SECTION   COMPUTATION SECTION COMPUTATION
C       SECTION
    3 TIME=TIME+DT
      DO 210 J=3,NJ
      QRAT(1,J)=((T1(2,J)-T1(1,J))/RH(2,J))+((T1(1,J-1)-T1(1
     1,J))/RV(1,J))+((T1(1,J+1)-T1(1,J))/RV(1,J+1))
      QRAT(MM,J)=((T1(M,J)-T1(MM,J))/RH(MM,J))+((T1(MM,J-1)
     1-T1(MM,J))/RV(MM,J))+((T1(MM,J+1)-T1(MM,J))/RV(MM,J
     2+1))
  210 CONTINUE
      IF(M.EQ.1)GO TO 212
      DO 211 J=3,NJ
      DO 211 I=2,M
      QRAT(I,J)=((T1(I-1,J)-T1(I,J))/RH(I,J))+((T1(I+1,J)-T1
     1(I,J))/RH(I+1,J))+((T1(I,J-1)-T1(I,J))/RV(I,J))+((T1(I
     2,J+1)-T1(I,J))/RV(I,J+1))
  211 CONTINUE
  212 DO 220 J=3,NJ
      DO 220 I=1,MM
  220 QS(I,J)=QS(I,J)+(QRAT(I,J)*DT)
      DO 240 I=2,MM
  240 T2(I,N+3)=T1(I,N+3)+((QRAT(I,N+3)*DT)/C(I,N+3))
```

TABLE C-3. (Continued)

```
      T2(1,N+3)=T2(2,N+3)
      DO 250 J=3,NN
      DO 250 I=2,MM
      IF(QS(I,J).LT.Q1) T2(I,J)=TREF+(QS(I,J)/C(I,J))
      IF(QS(I,J).GE.Q1.AND.QS(I,J).LE.Q2) T2(I,J)=TTR
      IF(QS(I,J).GT.Q2.AND.QS(I,J).LT.Q3) T2(I,J)=TTR+((QS(I
     1,J)-Q2)/C(I,J))
      IF(QS(I,J).GE.Q3.AND.QS(I,J).LE.Q4) T2(I,J)=TMELT
C    WHEN GOING FROM MELT TO FREEZE OR VICE-VERSA CHANGE THE
C       FOLLOWING CA
      IF(QS(I,J).GT.Q3.AND.QS(I,J).LT.Q4) F(I,J)=(Q4-QS(I
     1,J))/(DEN*(S**2)*3*HMELT)
      IF(QS(I,J).GE.Q4) F(I,J)=0.0
      IF(QS(I,J).GT.Q4) T2(I,J)=TMELT+((QS(I,J)-Q4)/C(I,J))
C    WHEN GOING FROM MELT TO FREEZE OR VICE-VERSA CHANGE THE
C       FOLLOWING CA
      IF(QS(I,J).LE.Q3) F(I,J)=1.0
  250 CONTINUE
C SPECIFICATION AND/OR DETERMINATION OF FIN TEMPERATURES
C           THE FOLLOWING DO LOOP ASSUMES FIN TEMPERATURES
C       FOR ITERATION
      DO 255 J=3,NN
  255 T2(1,J)=T3(1,J)
      DO 260 L=1,NDP
      IF(TIME.GE.TIM(L).AND.TIME.LE.TIM(L+1)) GO TO 4
  260 CONTINUE
    4 FAC=(TIME-TIM(L))/(TIM(L+1)-TIM(L))
      T2(1,2)=TM1(L)+((TM1(L+1)-TM1(L))*FAC)
      T2(1,8)=TM2(L)+((TM2(L+1)-TM2(L))*FAC)
      T2(1,15)=TM3(L)+((TM3(L+1)-TM3(L))*FAC)
      T2(1,21)=TM4(L)+((TM4(L+1)-TM4(L))*FAC)
      DO 270 I=1,MM
  270 T2(I,2)=T2(1,2)
C UNSPECIFIED FIN TEMPERATURES DETERMINED BY STEADY STATE
C       EQUATIONS
  256 MCOUNT=MCOUNT+1
      DO 280 J=3,NN
      T3(1,J)=T2(1,J)
      IF(J.EQ.8.OR.J.EQ.15) GO TO 5
      IF(J.EQ.21) GO TO 5
      T2(1,J)=((T2(1,J-1)/RV(1,J))+(T2(2,J)/RH(2,J))+(T2(1,J
     1+1)/RV(1,J+1)))/((1./RV(1,J))+(1./RH(2,J))+(1./RV(1,J
     2+1)))
    5 CONTINUE
  280 CONTINUE
      IF(MCOUNT.GT.MFIN) GO TO 8
      DO 281 J=3,NN
      DIF=T2(1,J)-T3(1,J)
      IF(ABS(DIF).GT.EPS) GO TO 256
  281 CONTINUE
      IF(JOE.EQ.2) GO TO 285
```

TABLE C-3. (Continued)

```
      JOE=JOE+1
      DO 888 J=3,NJ
      DO 888 I=1,MM
888   QS(I,J)=QS(I,J)-(QRAT(I,J)*DT)
      DO 282 J=3,NJ
      QRA2(1,J)=((T2(2,J)-T2(1,J))/RH(2,J))+((T2(1,J-1)-T2(1
     1,J))/RV(1,J))+((T2(1,J+1)-T2(1,J))/RV(1,J+1))
      QRA2(MM,J)=((T2(M,J)-T2(MM,J))/RH(MM,J))+((T2(MM,J-1)
     1-T2(MM,J))/RV(MM,J))+((T2(MM,J+1)-T2(MM,J))/RV(MM,J
     2+1))
282   CONTINUE
      IF(M.EQ.1)GO TO 283
      DO 283 J=3,NJ
      DO 283 I=2,M
      QRA2(I,J)=((T2(I-1,J)-T2(I,J))/RH(I,J))+((T2(I+1,J)-T2
     1(I,J))/RH(I+1,J))+((T2(I,J-1)-T2(I,J))/RV(I,J))+((T2(I
     2,J+1)-T2(I,J))/RV(I,J+1))
283   CONTINUE
      DO 284 J=3,NJ
      DO 284 I=1,MM
284   QRAT(I,J)=(QRAT(I,J)+QRA2(I,J))/2.0
      GO TO 212
285   MCOUNT=1
      DO 401 J=3,NJ
      DO 401 I=2,MM
      IF(F(I,J).GT.EPS.AND.F(I,J).LT.UN) GO TO 402
      IF(F(I,J).GT.UN) GO TO 403
      GO TO 401
403   RV(I,J)=VR(I,J)
      RH(I,J)=HR(I,J)
      GO TO 401
402   RV(I,J)=VR(I,J)/AF
      RH(I,J)=HR(I,J)/AF
      RV(I,J+1)=VR(I,J+1)/AF
      RH(I+1,J)=HR(I+1,J)/AF
401   CONTINUE
      DO 286 I=1,MM
286   QRAT(I,2)=((T2(I,2)-T1(I,2))*C(I,2)/DT)
      DO 287 I=1,MM
287   QS(I,2)=QS(I,2)+(C(I,2)*(T2(I,2)-T1(I,2)))
      DO 290 I=2,MM
      QBW=(T2(I,2)-T2(I,3))/RV(I,3)+QBW
290   QTW=(T2(I,N+3)-T2(I,N+2))/RV(I,N+3)+QTW
      QBT=QBW+((T2(1,2)-T2(1,3))/RV(1,3))
      DO 300 J=3,NN
300   QSW=QSW+((T2(1,J)-T2(2,J))/RH(2,J))
      DO 310 I=1,MM
310   QTOP=((T2(I,N+3)-TAMB)/RV(I,N+4))+QTOP
      DO 311 J=3,NN
311   QFTR=QFTR+QRAT(1,J)
      DO 312 I=1,MM
```

TABLE C-3. (Continued)

```
312 QTTR=QTTR+QRAT(I,NJ)
    QWAX=(QBW+QTW+QSW)*DT+(QWAX)
    RATIO=QSW/QBW
    ERROR=((QBT-(QBW+QSW+QTW+QTOP+QFTR+QTTR))*100.0)/QBT
    DO 930 J=3,NN
    DO 930 I=2,MM
    V2=V2+(F(I,J)*(S**2)*B)
930 CONTINUE
    DAVG=((2.0*V2)/(W*B))*12.0
    QMELT=((V2-V1)*DEN*HMELT)/DT
    QFREZ=QMELT
    V1=V2
    V2=0.0
    IF(KCOUNT.EQ.KCHK) GO TO 6
    KCOUNT=KCOUNT+1
    GO TO 7
  6 WRITE(6,66) TIME, QWAX, ERROR
 66 FORMAT(1X,5HTIME=,E15.8,10X,5HQWAX=,E15.8,10X,6HERROR=
   1,E15.8)
    DO 313 J=3,NN
    AJ=J-3
    BJ=J-2
    IF(F(2,J).GT.F2JM) DFLO=(BJ*S*12.0)
    DFIN=(AJ*S*12.0)
    IF(F(2,J).LT.EPS) GO TO 314
313 CONTINUE
314 DO 315 J=3,NN
    AJ=J-3
    IF(F(MM,J).LT.1.0) DMID=((AJ*S)+(F(MM,J)*S))*12.0
    IF(F(MM,J).LT.1.0) GO TO 316
315 CONTINUE
316 WRITE(6,67) DFIN, DFLO, DAVG, DMID
 67 FORMAT(1X,5HDFIN=,E15.8,10X,5HDFLO=,E15.8,10X,5HDAVG=
   1,E15.8,10X,5HDMID=,E15.8)
    DDOT=(DMID-DMO)/DT
    DMO=DMID
    WRITE(6,69) QFREZ, DDOT
 69 FORMAT(1X,6HQFREZ=,E15.8,10X,5HDDOT=,E15.8)
    WRITE(6,77) QBW, QSW, QTW, QBT, RATIO
 77 FORMAT(1X,4HQBW=,E15.8,3X,4HQSW=,E15.8,3X,4HQTW=,E15.8
   1,3X,4HQBT=,E15.8,3X,6HRATIO=,E15.8)
    WRITE(6,88)
 88 FORMAT(2X,1HI,2X,1HJ,10X,11HTEMPERATURE,10X,15HFRACTIO
   1N MELTED,10X,11HENERGY RATE,10X,13HENERGY STORED)
    DO 320 J=2,NJ
    DO 320 I=1,MM
    WRITE(6,99)I,J,T2(I,J),F(I,J),QRAT(I,J),QS(I,J)
 99 FORMAT(1X,I2,1X,I2,8X,E15.8,8X,E15.8,8X,E15.8,8X
   1,E15.8)
320 CONTINUE
    KCOUNT=1
```

TABLE C-3. (Concluded)

```
  7 QBn=0.0
    QSh=0.0
    QTw=0.0
    QTOP=0.0
    QTTR=0.0
    QFTR=0.0
    DO 330 J=2,NJ
    DO 330 I=1,MM
330 T1(I,J)=T2(I,J)
    JOE=1
    IF(TIME.LT.TAU) GO TO 3
  8 WRITE(6,111) MCOUNT
111 FORMAT(1X,I3)
    STOP
    END
```

NOMENCLATURE

A	Area
ADI	Alternating direction implicit numerical method
Bi	Biot modulus = $\frac{hx}{k}$
C(I,J)	Thermal capacitance of node (I,J)
C_p	Heat capacity
GH	Horizontal Thermal Conductance
GV	Vertical Thermal Conductance
g	Acceleration of gravity
H	Height of PCM in Cell (Figure 31)
h	Convective heat transfer coefficient
h_f	Latent heat of fusion
I	Designation of nodal location (See Figure 31)
J	Designation of nodal location (See Figure 31)
k	Thermal conductivity
L	Distance between bottom surface of cell and liquid-solid interface at center of cell
M	Number of horizontal nodes in PCM (Figure 31)
N	Number of vertical nodes in PCM (Figure 31)
Nu	Nusselt number = $\frac{hx}{k_f}$
PCM	Phase change material
$\dot{q}$	Heat transfer rate
$\dot{q}''$	Heat transfer rate per unit area
Ra	Rayleigh number = $\frac{g\beta x^3 \Delta T}{\nu\alpha}$

NOMENCLATURE (Concluded)

RH	Horizontal thermal resistance
RV	Vertical thermal resistance
S	Nodal spacing PCM
S_1	Thickness of bottom plate
S_2	Thickness of fin
S_3	Thickness of top plate
T	Temperature
t	time
W	Width of PCM in Cell
x	Significant length

GREEK SYMBOLS

α	Thermal diffusivity = $\frac{k}{\rho c_p}$
Δ	Denotes a finite increment
μ	Dynamic viscosity
ν	Kinematic viscosity
ρ	Density

SUBSCRIPTS

f	fusion value
g	Glass
s	Surface

SUPERSCRIPT

'	Denotes calculated value at time t + Δt

TABLE C-4. CINDA COMPUTER PROGRAM FOR FREEZING

```
BCD 3THERMAL LPCS
BCD 9 THERMAL CAPACITOR 52 WAX NODE 3/4 FIN SPACING STUDY
BCD 9 TEST 4(230-7) 20F FLUID INLET NONADECANE PLASTIC BOX
BCD 9 FIRST CELL- 300/65/HR FLUID FLOWRATE-K-PLEXIGLAS=.09
BCD 9 K-WAX=.08 ,4X13 NODES IN WAX-INPUT FIN TEMPS AND BASE
BCD 9 TEMPS FROM TEST DATA
END
BCD 3NODE DATA
    31,100.,.002
GEN 2,4,1,100.,-1.,1.,1.,1.
GEN 8,6,1,100.,-.1,1.,1.,1.
GEN 20,8,1,100.,-.2,2.,1.,1.
GEN 16,2,1,100.,-1.,1.,1.,1.
GEN 28,3,1,100.,-1.,1.,1.,1.
    -1,100.,0.      $BOTTO
    -6,100.,0.      $FIN
    -7,100.,0.      $FI
    -14,100.,0.     $FIN
    -15,100.,0.     $FIN
    -18,100.,0.     $FIN
    -19,100.,0.     $FIN TEMP
GEN -201,52,1,100.,0.,1.,1.,1.
END

BCD 3CONDUCTOR DATA
GEN 2,2,1,1,0,2,1,3.30,1.,1.,1.
GEN 201,4,1,1,0,201,1,.05,1.,1.,1.
GEN 4,24,1,2,1,4,1,1.58,1.,1.,1.
GEN 205,48,1,201,1,205,1,.0313,1.,1.,1.
    301,2,201,.071
GEN 307,2,1,204,1,3,1,.071,1.,1.,1.
GEN 312,2,1,208,1,5,1,.071,1.,1.,1.
GEN 317,2,1,212,1,7,1,.071,1.,1.,1.
GEN 322,2,1,216,1,9,1,.071,1.,1.,1.
GEN 327,2,1,220,1,11,1,.071,1.,1.,1.
GEN 332,2,1,224,1,13,1,.071,1.,1.,1.
GEN 337,2,1,228,1,15,1,.071,1.,1.,1.
GEN 342,2,1,232,1,17,1,.071,1.,1.,1.
GEN 357,2,1,244,1,23,1,.071,1.,1.,1.
GEN 347,2,1,236,1,19,1,.071,1.,1.,1.
GEN 362,2,1,248,1,25,1,.071,1.,1.,1.
GEN 352,2,1,240,1,21,1,.071,1.,1.,1.
    367,252,27,.071
```

TABLE C-4. (Continued)

```
GEN 302,2,1,201,1,202,1,.031,1.,1.,1.
    306,203,204,.031
GEN 309,3,1,205,1,206,1,.031,1.,1.,1.
GEN 314,3,1,209,1,210,1,.031,1.,1.,1.
GEN 319,3,1,213,1,214,1,.031,1.,1.,1.
GEN 324,3,1,217,1,218,1,.031,1.,1.,1.
GEN 329,3,1,221,1,222,1,.031,1.,1.,1.
GEN 334,3,1,225,1,226,1,.031,1.,1.,1.
GEN 339,3,1,229,1,230,1,.031,1.,1.,1.
GEN 344,3,1,233,1,234,1,.031,1.,1.,1.
GEN 349,3,1,237,1,238,1,.031,1.,1.,1.
GEN 354,3,1,241,1,242,1,.031,1.,1.,1.
GEN 359,3,1,245,1,246,1,.031,1.,1.,1.
GEN 364,3,1,249,1,250,1,.031,1.,1.,1.
GEN 253,2,1,249,1,28,2,.0294,1.,1.,1.
    255,251,31,.0294
    256,252,29,.0294
GEN 30,2,1,28,1,30,1,.05,1.,1.,1.
    32,30,31,.05
GEN 28,2,1,26,1,28,1,.02,1.,1.,1.
END

1,0.
2,0.
3,0.
4,0.
5,0.
6,0.
7,0.
8,0.
9,0.
10,0.
11,0.
12,0.
13,0.
14,0.
15,0.
16,0.
```

TABLE C-4. (Continued)

17,0.
18,0.
19,0.
20,0.
21,0.
22,0.
23,0.
24,0.
25,0.
26,0.
27,0.
28,0.
29,0.
30,0.
31,0.
32,0.
33,0.
34,0.
35,0.
36,0.
37,0.
38,0.
39,0.
40,0.
41,0.
42,0.
43,0.
44,0.
45,0.
46,0.
47,0.
48,0.
49,0.
50,0.
51,0.
52,0.
53,0.
54,0.
55,0.
56,0.
57,0.
58,0.
59,0.
60,0.
61,0.
62,0.
63,0.
64,0.
65,0.
66,0.
67,0.
68,0.
69,0.
70,0.
71,0.
72,0.
73,0.
74,0.
75,0.
76,0.
77,0.
78,0.
79,0.
80,0.
81,0.
82,0.
83,0.
84,0.
85,0.
86,0.
87,0.
88,0.
89,0.
90,0.
91,0.
92,0.
93,0.
94,0.
95,0.
96,0.
97,0.
98,0.
99,0.
100,0.
101,0.
102,0.
103,0.
104,0.
105,0.
106,0.
107,0.
108,0.
109,0.
110,0.
111,0.
112,0.
113,0.
114,0.
115,0.
116,0.
117,0.
118,0.
119,0.
120,0.
121,0.
122,0.
123,0.
124,0.
125,0.
126,0.
127,0.
128,0.
129,0.
130,0.
131,0.
132,0.
133,0.
134,0.
135,0.
136,0.
137,0.
138,0.
139,0.
140,0.
141,0.
142,0.
143,0.
144,0.
145,0.
146,0.
147,0.
148,0.
149,0.
150,0.
151,0.

TABLE C-4. (Continued)

152,0.
153,0.
154,0.
155,0.
156,0.
157,0.
158,0.
159,0.
160,0.
161,0.
162,0.
163,0.
164,0.
165,0.
166,0.
167,0.
168,0.
169,0.
170,0.
171,0.
172,0.
173,0.
174,0.
175,0.
176,0.
177,0.
178,0.
179,0.
180,0.
181,0.
182,0.
183,0.
184,0.
185,0.
186,0.
187,0.
188,0.
189,0.
190,0.
191,0.
192,0.
193,0.
194,0.
195,0.
196,0.
197,0.
198,0.
199,0.
200,0.
201,0.
202,0.
203,0.
204,0.
205,0.
206,0.
207,0.
208,0.
209,0.
210,0.
211,0.
212,0.
213,0.
214,0.
215,0.
216,0.
217,0.
218,0.
219,0.
220,0.
221,0.
222,0.
223,0.
224,0.
225,0.
226,0.
227,0.
228,0.
229,0.
230,0.
231,0.
232,0.
233,0.
234,0.
235,0.
236,0.
237,0.
238,0.
239,0.
240,0.
241,0.
242,0.
243,0.
244,0.
245,0.
246,0.
247,0.
248,0.
249,0.
250,0.
251,0.
252,0.
253,0.
254,0.
255,0.
256,0.
257,0.
258,0.
259,0.
260,0.
261,0.
262,0.
263,0.
264,0.
265,0.
266,0.
267,0.
268,0.
269,0.
270,0.
271,0.
272,0.
273,0.
274,0.
275,0.
276,0.
277,0.
278,0.
279,0.
280,0.
281,0.
282,0.
283,0.
284,0.
285,0.
286,0.
287,0.
288,0.
289,0.

TABLE C-4. (Continued)

290,0.
291,0.
292,0.
293,0.
294,0.
295,0.
296,0.
297,0.
298,0.
299,0.
300,0.
301,0.
302,0.
303,0.
304,0.
305,0.
306,0.
307,0.
308,0.
309,0.
310,0.
311,0.
312,0.
313,.617
314,.617
315,.617
316,.617
317,.617
318,.617
319,.617
320,.617
321,.617
322,.617
323,.617
324,.617
325,.617
326,.617
327,.617
328,.617
329,.617
330,.617
331,.617
332,.617
333,.617
334,.617
335,.617
336,.617
337,.617
338,.617
339,.617
340,.617
341,.617
342,.617
343,.617
344,.617
345,.617
346,.617
347,.617
348,.617
349,.617
350,.617
351,.617
352,.617
353,.617
354,.617
355,.617
356,.617
357,.617
358,.617
359,.617
360,.617
361,.617
362,.617
363,.617
364,.617

TABLE C-4. (Continued)

```
     DAMPA=.3 $ARITH NODE DAMPING
     DAMPD=.3
     NLOOP=41 $A
     ARLXCA=.01 $RELAXATION CRITERIA
     DRLXCA=.01
     DTIMEI=.00825
     CSGFAC=10.
     TIMEND=4.0
     OUTPUT= 0.1
 END
 BCD $ARRAY DATA
     1 $ TEMP VS Q(BTU) OF WAX REF -50-F
     0.,50.,.0492,73.,.1672,73.,.2036,90.,.5952,90.
     .7236,150.,END   $ Q PER NODE VERSUS TEMP
     -2 $ LABEL ARRAY FOR WAX
     Q-WAX,DQ*TIM,Q*TIM,TWAX,END
     -3 $ LABEL TEMPS EXCEPT WAX
      T1,T2,T3,T4,T5,T6,T7,T8,T9,T10,T11
      T12,T13,T14,T15,T16,T17,T18,T19,T20,T21,T22
      T23,T24,T25,T26,T27,T28,T29,T30,T31,END
     4,0.,100.,.139,94.0,.278,91.6,.417,91.3,.556,91.5,.696,91.0
      .834,90.6,.973,90.2,1.112,88.5,1.261,86.5,1.390,84.3,1.529
      82.1,1.674,80.0,1.813,78.8,1.946,77.2,2.085,75.0,2.224,72.8
      2.363,71.6,2.502,70.0,END
 REM   MIDDLE FIN NODE -TEST TEMP T26
     5,0.,100.0,.139,96.4,.278,95.2,.417,91.7,.556,91.0,.695,90.6
      .834,90.3,.973,90.4,1.112,90.3,1.261,90.6,1.390,90.4,1.529
      90.6,1.674,90.0,1.813,89.9,1.946,89.4,2.085,88.2,2.224,85.7
      2.363,83.6,2.502,81.3,END
 REM    MIDDLE FIN NODE TEST TEMP T27
     6,0.,100.0,.139,98.5,.278,95.5,.417,93.2,.556,92.1,.695,91.0
      .834,90.7,.937,91.1,1.112,90.9,1.261,91.3,1.390,91.2,1.529
      91.6,1.674,91.0,1.813,90.8,1.946,90.6,2.085,90.8,2.224,90.3
      2.363,90.7,2.502,90.0,END
 REM    TOP FIN NODE  TEST TEMP 28
     7,0.,100.0,.139,80.8,.278,75.6,.417,70.3,.556,67.7,.695,65.8
      .834,63.8,.973,62.9,1.112,60.9,1.261,59.4,1.390,58.4,1.529
      57.8,1.674,56.4,1.813,55.7,1.946,54.7,2.085,53.6,2.224,52.3
      2.363,51.3,2.502,50.4,END
 REM    PLATE NODE TEMP TEST DATA T33
 END
 BCD $EXECUTION
DIMENSION X(100)                                                    F
NDIM=100                                                            F
NTH=0                                                               F
     CSGDMP
     CNFWRK
 END
```

TABLE C-4. (Continued)

```
BCD 3VARIABLES 1
     QMETER(T1,T201,G201,K1)
     QMETER(T2,T201,G301,K2)
     QMETER(T205,T201,G205,K3)
     QMETER(T202,T201,G302,K4)
     QMETER(T1,T202,G202,K5)
     QMETER(T201,T202,G302,K6)
     QMETER(T206,T202,G206,K7)
     QMETER(T203,T202,G303,K8)
     QMETER(T1,T203,G203,K9)
     QMETER(T202,T203,G303,K10)
     QMETER(T207,T203,G207,K11)
     QMETER(T204,T203,G306,K12)
     QMETER(T1,T204,G204,K13)
     QMETER(T203,T204,G306,K14)
     QMETER(T208,T204,G208,K15)
     QMETER(T3,T204,G307,K16)
     QMETER(T201,T205,G205,K17)
     QMETER(T4,T205,G308,K18)
     QMETER(T209,T205,G209,K19)
     QMETER(T206,T205,G309,K20)
     QMETER(T202,T206,G206,K21)
     QMETER(T205,T206,G309,K22)
     QMETER(T210,T206,G210,K23)
     QMETER(T207,T206,G310,K24)
     QMETER(T203,T207,G207,K25)
     QMETER(T206,T207,G310,K26)
     QMETER(T211,T207,G211,K27)
     QMETER(T208,T207,G311,K28)
     QMETER(T204,T208,G208,K29)
     QMETER(T207,T208,G311,K30)
     QMETER(T212,T208,G212,K31)
     QMETER(T5,T208,G312,K32)
     QMETER(T205,T209,G209,K33)
     QMETER(T6,T209,G313,K34)
     QMETER(T213,T209,G213,K35)
     QMETER(T210,T209,G314,K36)
     QMETER(T206,T210,G210,K37)
     QMETER(T209,T210,G314,K38)
     QMETER(T214,T210,G214,K39)
     QMETER(T211,T210,G315,K40)
     QMETER(T207,T211,G211,K41)
     QMETER(T210,T211,G315,K42)
     QMETER(T215,T211,G215,K43)
     QMETER(T212,T211,G316,K44)
     QMETER(T208,T212,G212,K45)
     QMETER(T211,T212,G316,K46)
     QMETER(T216,T212,G216,K47)
     QMETER(T7,T212,G317,K48)
     QMETER(T209,T213,G213,K49)
     QMETER(T8,T213,G318,K50)
     QMETER(T217,T213,G217,K51)
     QMETER(T214,T213,G319,K52)
     QMETER(T210,T214,G214,K53)
     QMETER(T213,T214,G319,K54)
     QMETER(T218,T214,G218,K55)
     QMETER(T215,T214,G320,K56)
     QMETER(T211,T215,G215,K57)
     QMETER(T214,T215,G320,K58)
     QMETER(T219,T215,G219,K59)
     QMETER(T216,T215,G321,K60)
     QMETER(T212,T216,G216,K61)
     QMETER(T215,T216,G321,K62)
     QMETER(T220,T216,G220,K63)
     QMETER(T9,T216,G322,K64)
     QMETER(T213,T217,G217,K65)
     QMETER(T10,T217,G323,K66)
     QMETER(T221,T217,G221,K67)
     QMETER(T218,T217,G324,K68)
     QMETER(T214,T218,G218,K69)
     QMETER(T217,T218,G324,K70)
     QMETER(T222,T218,G222,K71)
     QMETER(T219,T218,G325,K72)
     QMETER(T215,T219,G219,K73)
     QMETER(T218,T219,G325,K74)
     QMETER(T223,T219,G223,K75)
     QMETER(T220,T219,G326,K76)
     QMETER(T216,T220,G220,K77)
     QMETER(T219,T220,G326,K78)
     QMETER(T224,T220,G224,K79)
     QMETER(T11,T220,G327,K80)
     QMETER(T217,T221,G221,K81)
     QMETER(T12,T221,G328,K82)
     QMETER(T225,T221,G225,K83)
     QMETER(T222,T221,G329,K84)
     QMETER(T218,T222,G222,K85)
     QMETER(T221,T222,G329,K86)
     QMETER(T226,T222,G226,K87)
     QMETER(T223,T222,G330,K88)
     QMETER(T219,T223,G223,K89)
```

TABLE C-4. (Continued)

```
GMETER(T222,T223,G330,K90)
GMETER(T227,T223,G227,K91)
GMETER(T224,T223,G331,K92)
GMETER(T220,T224,G224,K93)
GMETER(T223,T224,G331,K94)
GMETER(T228,T224,G228,K95)
GMETER(T13,T224,G332,K96)
GMETER(T221,T225,G225,K97)
GMETER(T14,T225,G333,K98)
GMETER(T229,T225,G229,K99)
GMETER(T226,T225,G334,K100)
GMETER(T222,T226,G226,K101)
GMETER(T225,T226,G334,K102)
GMETER(T230,T226,G230,K103)
GMETER(T227,T225,G335,K104)
GMETER(T223,T227,G227,K105)
GMETER(T226,T227,G335,K106)
GMETER(T231,T227,G231,K107)
GMETER(T228,T227,G336,K108)
GMETER(T224,T228,G228,K109)
GMETER(T227,T228,G336,K110)
GMETER(T232,T228,G232,K111)
GMETER(T15,T228,G337,K112)
GMETER(T225,T229,G229,K113)
GMETER(T15,T229,G338,K114)
GMETER(T233,T229,G233,K115)
GMETER(T230,T229,G339,K116)
GMETER(T226,T230,G230,K117)
GMETER(T229,T230,G339,K118)
GMETER(T234,T230,G234,K119)
GMETER(T231,T230,G340,K120)
GMETER(T227,T231,G231,K121)
GMETER(T230,T231,G340,K122)
GMETER(T235,T231,G235,K123)
GMETER(T232,T231,G341,K124)
GMETER(T228,T232,G232,K125)
GMETER(T231,T232,G341,K126)
GMETER(T236,T232,G236,K127)
GMETER(T17,T232,G342,K128)
GMETER(T229,T233,G233,K129)
GMETER(T18,T233,G343,K130)
GMETER(T237,T233,G237,K131)
GMETER(T234,T233,G344,K132)
GMETER(T230,T234,G234,K133)
GMETER(T233,T234,G344,K134)
GMETER(T238,T234,G238,K135)
GMETER(T235,T234,G345,K136)
GMETER(T231,T235,G235,K137)
GMETER(T234,T235,G345,K138)
GMETER(T239,T235,G239,K139)
GMETER(T236,T235,G346,K140)
GMETER(T232,T236,G236,K141)
GMETER(T235,T236,G346,K142)
GMETER(T240,T236,G240,K143)
GMETER(T19,T236,G347,K144)
GMETER(T233,T237,G237,K145)
GMETER(T20,T237,G348,K146)
GMETER(T241,T237,G241,K147)
GMETER(T238,T237,G349,K148)
GMETER(T234,T238,G238,K149)
GMETER(T237,T238,G349,K150)
GMETER(T242,T238,G242,K151)
GMETER(T239,T238,G350,K152)
GMETER(T235,T239,G239,K153)
GMETER(T238,T239,G350,K154)
GMETER(T243,T239,G243,K155)
GMETER(T240,T239,G351,K156)
GMETER(T236,T240,G240,K157)
GMETER(T239,T240,G351,K158)
GMETER(T244,T240,G244,K159)
GMETER(T21,T240,G352,K160)
GMETER(T237,T241,G241,K161)
GMETER(T22,T241,G353,K162)
GMETER(T245,T241,G245,K163)
GMETER(T242,T241,G354,K164)
GMETER(T238,T242,G242,K165)
GMETER(T241,T242,G354,K166)
GMETER(T246,T242,G246,K167)
GMETER(T243,T242,G355,K168)
GMETER(T239,T243,G243,K169)
GMETER(T242,T243,G355,K170)
GMETER(T247,T243,G247,K171)
GMETER(T244,T243,G356,K172)
GMETER(T240,T244,G244,K173)
GMETER(T243,T244,G356,K174)
GMETER(T248,T244,G248,K175)
GMETER(T23,T244,G357,K176)
GMETER(T241,T245,G245,K177)
GMETER(T24,T245,G358,K178)
GMETER(T249,T245,G249,K179)
```

TABLE C-4. (Continued)

```
GMETER(T246,T245,G359,K180)
GMETER(T242,T246,G246,K181)
GMETER(T245,T246,G359,K182)
GMETER(T250,T246,G250,K183)
GMETER(T247,T246,G360,K184)
GMETER(T243,T247,G247,K185)
GMETER(T246,T247,G360,K186)
GMETER(T251,T247,G251,K187)
GMETER(T248,T247,G361,K188)
GMETER(T244,T248,G248,K189)
GMETER(T247,T248,G361,K190)
GMETER(T252,T248,G252,K191)
GMETER(T25,T248,G362,K192)
GMETER(T245,T249,G249,K193)
GMETER(T26,T249,G363,K194)
GMETER(T28,T249,G253,K195)
GMETER(T250,T249,G364,K196)
GMETER(T246,T250,G250,K197)
GMETER(T249,T250,G364,K198)
GMETER(T30,T250,G254,K199)
GMETER(T251,T250,G365,K200)
GMETER(T247,T251,G251,K201)
GMETER(T250,T251,G365,K202)
GMETER(T31,T251,G255,K203)
GMETER(T252,T251,G366,K204)
GMETER(T248,T252,G252,K205)
GMETER(T251,T252,G366,K206)
GMETER(T29,T252,G256,K207)
GMETER(T27,T252,G367,K208)
ADD(K1,K2,K3,K4,K209)
ADD(K5,K6,K7,K8,K210)
ADD(K9,K10,K11,K12,K211)
ADD(K13,K14,K15,K16,K212)
ADD(K17,K18,K19,K20,K213)
ADD(K21,K22,K23,K24,K214)
ADD(K25,K26,K27,K28,K215)
ADD(K29,K30,K31,K32,K216)
ADD(K33,K34,K35,K36,K217)
ADD(K37,K38,K39,K40,K218)
ADD(K41,K42,K43,K44,K219)
ADD(K45,K46,K47,K48,K220)
ADD(K49,K50,K51,K52,K221)
ADD(K53,K54,K55,K56,K222)
ADD(K57,K58,K59,K60,K223)
ADD(K61,K62,K63,K64,K224)
ADD(K65,K66,K67,K68,K225)
ADD(K69,K70,K71,K72,K226)
ADD(K73,K74,K75,K76,K227)
ADD(K77,K78,K79,K80,K228)
ADD(K81,K82,K83,K84,K229)
ADD(K85,K86,K87,K88,K230)
ADD(K89,K90,K91,K92,K231)
ADD(K93,K94,K95,K96,K232)
ADD(K97,K98,K99,K100,K233)
ADD(K101,K102,K103,K104,K234)
ADD(K105,K106,K107,K108,K235)
ADD(K109,K110,K111,K112,K236)
ADD(K113,K114,K115,K116,K237)
ADD(K117,K118,K119,K120,K238)
ADD(K121,K122,K123,K124,K239)
ADD(K125,K126,K127,K128,K240)
ADD(K129,K130,K131,K132,K241)
ADD(K133,K134,K135,K136,K242)
ADD(K137,K138,K139,K140,K243)
ADD(K141,K142,K143,K144,K244)
ADD(K145,K146,K147,K148,K245)
ADD(K149,K150,K151,K152,K246)
ADD(K153,K154,K155,K156,K247)
ADD(K157,K158,K159,K160,K248)
ADD(K161,K162,K163,K164,K249)
ADD(K165,K166,K167,K168,K250)
ADD(K169,K170,K171,K172,K251)
ADD(K173,K174,K175,K176,K252)
ADD(K177,K178,K179,K180,K253)
ADD(K181,K182,K183,K184,K254)
ADD(K185,K186,K187,K188,K255)
ADD(K189,K190,K191,K192,K256)
ADD(K193,K194,K195,K196,K257)
ADD(K197,K198,K199,K200,K258)
ADD(K201,K202,K203,K204,K259)
ADD(K205,K206,K207,K208,K260)
D1DEG1(K313,A1,T201)
D1DEG1(K314,A1,T202)
D1DEG1(K315,A1,T203)
D1DEG1(K316,A1,T204)
D1DEG1(K317,A1,T205)
D1DEG1(K318,A1,T206)
D1DEG1(K319,A1,T207)
D1DEG1(K320,A1,T208)
D1DEG1(K321,A1,T209)
D1DEG1(K322,A1,T210)
D1DEG1(K323,A1,T211)
```

TABLE C-4. (Continued)

```
D1DEG1(K324,A1,T212)
D1DEG1(K325,A1,T213)
D1DEG1(K326,A1,T214)
D1DEG1(K327,A1,T215)
D1DEG1(K328,A1,T216)
D1DEG1(K329,A1,T217)
D1DEG1(K330,A1,T218)
D1DEG1(K331,A1,T219)
D1DEG1(K332,A1,T220)
D1DEG1(K333,A1,T221)
D1DEG1(K334,A1,T222)
D1DEG1(K335,A1,T223)
D1DEG1(K336,A1,T224)
D1DEG1(K337,A1,T225)
D1DEG1(K338,A1,T226)
D1DEG1(K339,A1,T227)
D1DEG1(K340,A1,T228)
D1DEG1(K341,A1,T229)
D1DEG1(K342,A1,T230)
D1DEG1(K343,A1,T231)
D1DEG1(K344,A1,T232)
D1DEG1(K345,A1,T233)
D1DEG1(K346,A1,T234)
D1DEG1(K347,A1,T235)
D1DEG1(K348,A1,T236)
D1DEG1(K349,A1,T237)
D1DEG1(K350,A1,T238)
D1DEG1(K351,A1,T239)
D1DEG1(K352,A1,T240)
D1DEG1(K353,A1,T241)
D1DEG1(K354,A1,T242)
D1DEG1(K355,A1,T243)
D1DEG1(K356,A1,T244)
D1DEG1(K357,A1,T245)
D1DEG1(K358,A1,T246)
D1DEG1(K359,A1,T247)
D1DEG1(K360,A1,T248)
D1DEG1(K361,A1,T249)
D1DEG1(K362,A1,T250)
D1DEG1(K363,A1,T251)
D1DEG1(K364,A1,T252)
MLTPLY(K209,DTIMEU,K261)
MLTPLY(K210,DTIMEU,K262)
MLTPLY(K211,DTIMEU,K263)
MLTPLY(K212,DTIMEU,K264)
MLTPLY(K213,DTIMEU,K265)
MLTPLY(K214,DTIMEU,K266)
MLTPLY(K215,DTIMEU,K267)
MLTPLY(K216,DTIMEU,K268)
MLTPLY(K217,DTIMEU,K269)
MLTPLY(K218,DTIMEU,K270)
MLTPLY(K219,DTIMEU,K271)
MLTPLY(K220,DTIMEU,K272)
MLTPLY(K221,DTIMEU,K273)
MLTPLY(K222,DTIMEU,K274)
MLTPLY(K223,DTIMEU,K275)
MLTPLY(K224,DTIMEU,K276)
MLTPLY(K225,DTIMEU,K277)
MLTPLY(K226,DTIMEU,K278)
MLTPLY(K227,DTIMEU,K279)
MLTPLY(K228,DTIMEU,K280)
MLTPLY(K229,DTIMEU,K281)
MLTPLY(K230,DTIMEU,K282)
MLTPLY(K231,DTIMEU,K283)
MLTPLY(K232,DTIMEU,K284)
MLTPLY(K233,DTIMEU,K285)
MLTPLY(K234,DTIMEU,K286)
MLTPLY(K235,DTIMEU,K287)
MLTPLY(K236,DTIMEU,K288)
MLTPLY(K237,DTIMEU,K289)
MLTPLY(K238,DTIMEU,K290)
MLTPLY(K239,DTIMEU,K291)
MLTPLY(K240,DTIMEU,K292)
MLTPLY(K241,DTIMEU,K293)
MLTPLY(K242,DTIMEU,K294)
MLTPLY(K243,DTIMEU,K295)
MLTPLY(K244,DTIMEU,K296)
MLTPLY(K245,DTIMEU,K297)
MLTPLY(K246,DTIMEU,K298)
MLTPLY(K247,DTIMEU,K299)
MLTPLY(K249,DTIMEU,K301)
MLTPLY(K248,DTIMEU,K300)
MLTPLY(K250,DTIMEU,K302)
MLTPLY(K251,DTIMEU,K303)
MLTPLY(K252,DTIMEU,K304)
MLTPLY(K253,DTIMEU,K305)
MLTPLY(K254,DTIMEU,K306)
MLTPLY(K255,DTIMEU,K307)
MLTPLY(K256,DTIMEU,K308)
MLTPLY(K257,DTIMEU,K309)
MLTPLY(K258,DTIMEU,K310)
MLTPLY(K259,DTIMEU,K311)
```

TABLE C-4. (Continued)

```
MLTPLY(K260,DTIMEU,K312)
ADD(K261,K313,K313)
ADD(K262,K314,K314)
ADD(K263,K315,K315)
ADD(K264,K316,K316)
ADD(K265,K317,K317)
ADD(K266,K318,K318)
ADD(K267,K319,K319)
ADD(K268,K320,K320)
ADD(K269,K321,K321)
ADD(K270,K322,K322)
ADD(K271,K323,K323)
ADD(K272,K324,K324)
ADD(K273,K325,K325)
ADD(K274,K326,K326)
ADD(K275,K327,K327)
ADD(K276,K328,K328)
ADD(K277,K329,K329)
ADD(K278,K330,K330)
ADD(K279,K331,K331)
ADD(K280,K332,K332)
ADD(K281,K333,K333)
ADD(K282,K334,K334)
ADD(K283,K335,K335)
ADD(K284,K336,K336)
ADD(K285,K337,K337)
ADD(K286,K338,K338)
ADD(K287,K339,K339)
ADD(K288,K340,K340)
ADD(K289,K341,K341)
ADD(K290,K342,K342)
ADD(K291,K343,K343)
ADD(K292,K344,K344)
ADD(K293,K345,K345)
ADD(K294,K346,K346)
ADD(K295,K347,K347)
ADD(K296,K348,K348)
ADD(K297,K349,K349)
ADD(K298,K350,K350)
ADD(K299,K351,K351)
ADD(K300,K352,K352)
ADD(K301,K353,K353)
ADD(K302,K354,K354)
ADD(K303,K355,K355)
ADD(K304,K356,K356)
ADD(K305,K357,K357)
ADD(K306,K358,K358)
ADD(K307,K359,K359)
ADD(K308,K360,K360)
ADD(K309,K361,K361)
ADD(K310,K362,K362)
ADD(K311,K363,K363)
ADD(K312,K364,K364)
D1DEG1(TIMEN,A4,T6)
D1DEG1(TIMEN,A4,T7)
D1DEG1(TIMEN,A5,T14)
D1DEG1(TIMEN,A5,T15)
D1DEG1(TIMEN,A6,T18)
D1DEG1(TIMEN,A6,T19)
D1DEG1(TIMEN,A7,T1)
END
```

TABLE C-4. (Continued)

```
BCD 3VARIABLES 2
END
BCD 30UTPUT CALLS
     STNDRD
     PRINTL(A2,K209,K261,K313,T201)
     PRINTL(A2,K210,K262,K314,T202)
     PRINTL(A2,K211,K263,K315,T203)
     PRINTL(A2,K212,K264,K316,T204)
     PRINTL(A2,K213,K265,K317,T205)
     PRINTL(A2,K214,K266,K318,T206)
     PRINTL(A2,K215,K267,K319,T207)
     PRINTL(A2,K216,K268,K320,T208)
     PRINTL(A2,K217,K269,K321,T209)
     PRINTL(A2,K218,K270,K322,T210)
     PRINTL(A2,K219,K271,K323,T211)
     PRINTL(A2,K220,K272,K324,T212)
     PRINTL(A2,K221,K273,K325,T213)
     PRINTL(A2,K222,K274,K326,T214)
     PRINTL(A2,K223,K275,K327,T215)
     PRINTL(A2,K224,K276,K328,T216)
     PRINTL(A2,K225,K277,K329,T217)
     PRINTL(A2,K226,K278,K330,T218)
     PRINTL(A2,K227,K279,K331,T219)
     PRINTL(A2,K228,K280,K332,T220)
     PRINTL(A2,K229,K281,K333,T221)
     PRINTL(A2,K230,K282,K334,T222)
     PRINTL(A2,K231,K283,K335,T223)
     PRINTL(A2,K232,K284,K336,T224)
     PRINTL(A2,K233,K285,K337,T225)
     PRINTL(A2,K234,K286,K338,T226)
     PRINTL(A2,K235,K287,K339,T227)
     PRINTL(A2,K236,K288,K340,T228)
     PRINTL(A2,K237,K289,K341,T229)
     PRINTL(A2,K238,K290,K342,T230)
     PRINTL(A2,K239,K291,K343,T231)
     PRINTL(A2,K240,K292,K344,T232)
     PRINTL(A2,K241,K293,K345,T233)
     PRINTL(A2,K242,K294,K346,T234)
     PRINTL(A2,K243,K295,K347,T235)
     PRINTL(A2,K244,K296,K348,T236)
     PRINTL(A2,K245,K297,K349,T237)
     PRINTL(A2,K246,K298,K350,T238)
     PRINTL(A2,K247,K299,K351,T239)
     PRINTL(A2,K248,K300,K352,T240)
     PRINTL(A2,K249,K301,K353,T241)
```

TABLE C-4. (Concluded)

```
      PRINTL(A2,K250,K302,K354,T242)
      PRINTL(A2,K251,K303,K355,T243)
      PRINTL(A2,K252,K304,K356,T244)
      PRINTL(A2,K253,K305,K357,T245)
      PRINTL(A2,K254,K306,K358,T246)
      PRINTL(A2,K255,K307,K359,T247)
      PRINTL(A2,K256,K308,K360,T248)
      PRINTL(A2,K257,K309,K361,T249)
      PRINTL(A2,K258,K310,K362,T250)
      PRINTL(A2,K259,K311,K363,T251)
      PRINTL(A2,K260,K312,K364,T252)
      PRINTL(A3,T1,T2,T3,T4,T5,T6,T7,T8,T9,T10,T11,T12,T13,T14
            T15,T16,T17,T18,T19,T20,T21,T22,T23,T24,T25,T26,T27
            T28,T29,T30,T31)
END
```

APPENDIX D

TEST DATA

Introduction

Test data for twenty phase change tests run at Marshall Space Flight Center's Test Division are included herein. These data includes temperatures and phase change position time histories. Data for 1.9-cm (3/4-in.) and 0.635-cm (1/4-in.) cells for twenty tests are given. Of these, nine tests are melting runs and eleven tests are freezing runs. Data are divided into four sections; Section I, freeze temperatures; Section II, freeze front position height; Section III, melt temperatures; and Section IV, melt front position height. Figure D-1 gives a presentation of temperature instrumentation location for all runs. Only data from the last 1.9-cm (3/4-in.) and the center 0.635-cm (1/4-in.) cells are presented.

General Data Description

Temperature plots for test 230-5 through 230-15 were hand plotted, and all subsequent tests were computer plotted. Although numerous additional temperature data were acquired, only the fin and cell temperatures for the center 0.635-cm (1/4-in.) cell and the last 1.9-cm (3/4-in.) cell (i.e., at fluid outlet) are presented. Thermocouple T31 through T33 represent fluid

temperatures not used in analyses and T-34 represents the lower plate temperature. The phase change position data were visually read from filmed data using a film analyzer. Readings were recorded and stored on computer cards. These cards were input to a 4020 computer plotter to generate position versus time plots. Position data for center of cell readings are given for all tests. In some cases, the phase change position on the upstream fins are also given, these data are represented by starred and unstarred lines, respectively. In the case of the 0.635-cm (1/4-in.) cell, when only one set of data is given for both fin and center cell, this indicates that these two heights coincide. In some cases the data were truncated when the cells were completely melted, in others the data plotting was continued. In the later case, this can be easily seen by the flatting of the data plots.

Across the top of some data plots the following information parameters are given; test type, internal test designation (official test designation), test duration, date the test was run, initial paraffin temperature and fluid inlet temperature.

In test 230-52 only 2000 seconds of data is available because of improper camera positioning. In test 230-7 the 1.9-cm (3/4-in.) cell data were inadvertently lost. For this case the smoothed data are presented in lieu of raw data.

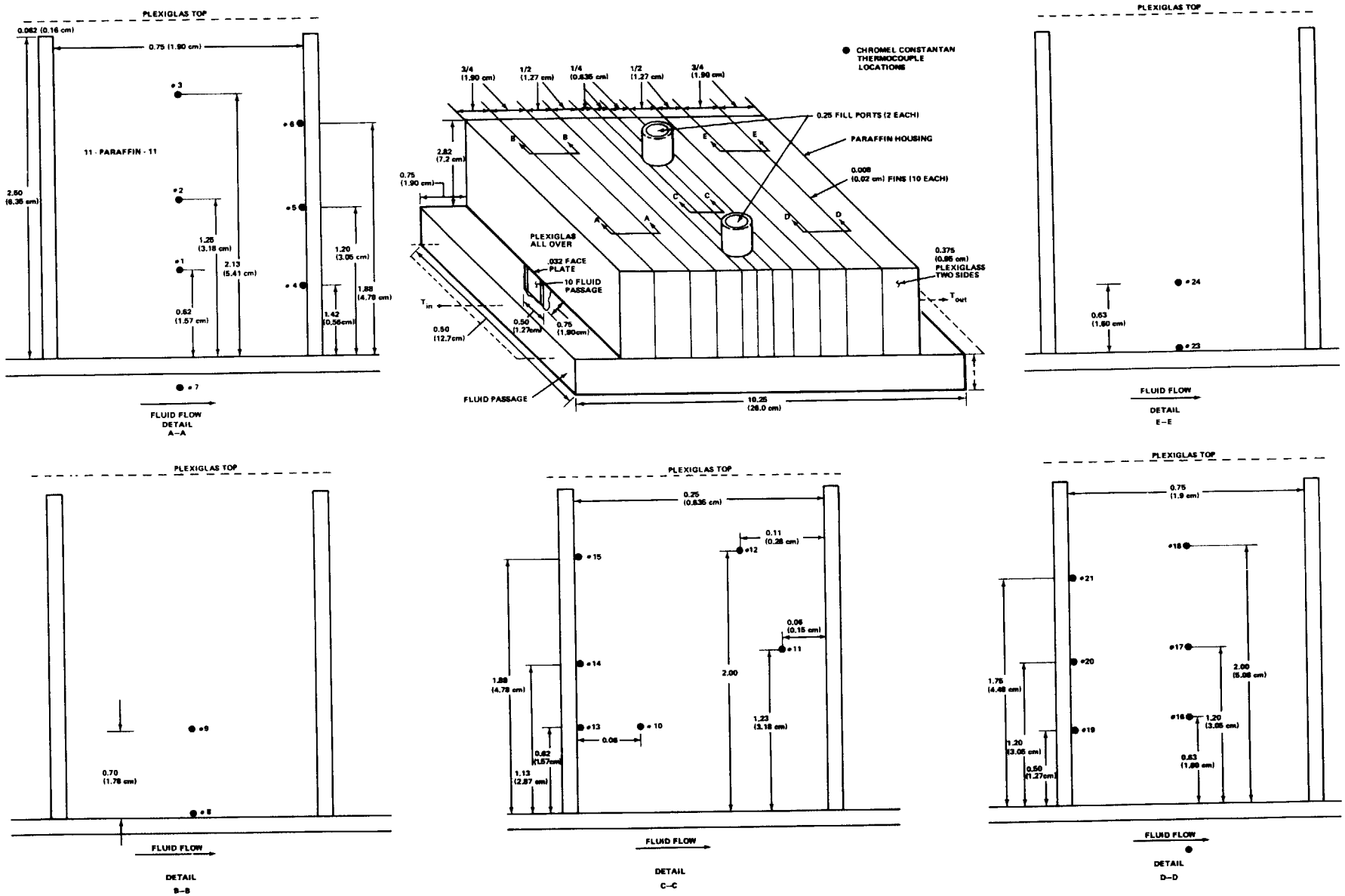

Figure D-1. Temperature instrumentation.

SECTION I

FREEZE TEMPERATURE DATA FOR FINNED THERMAL CAPACITORS

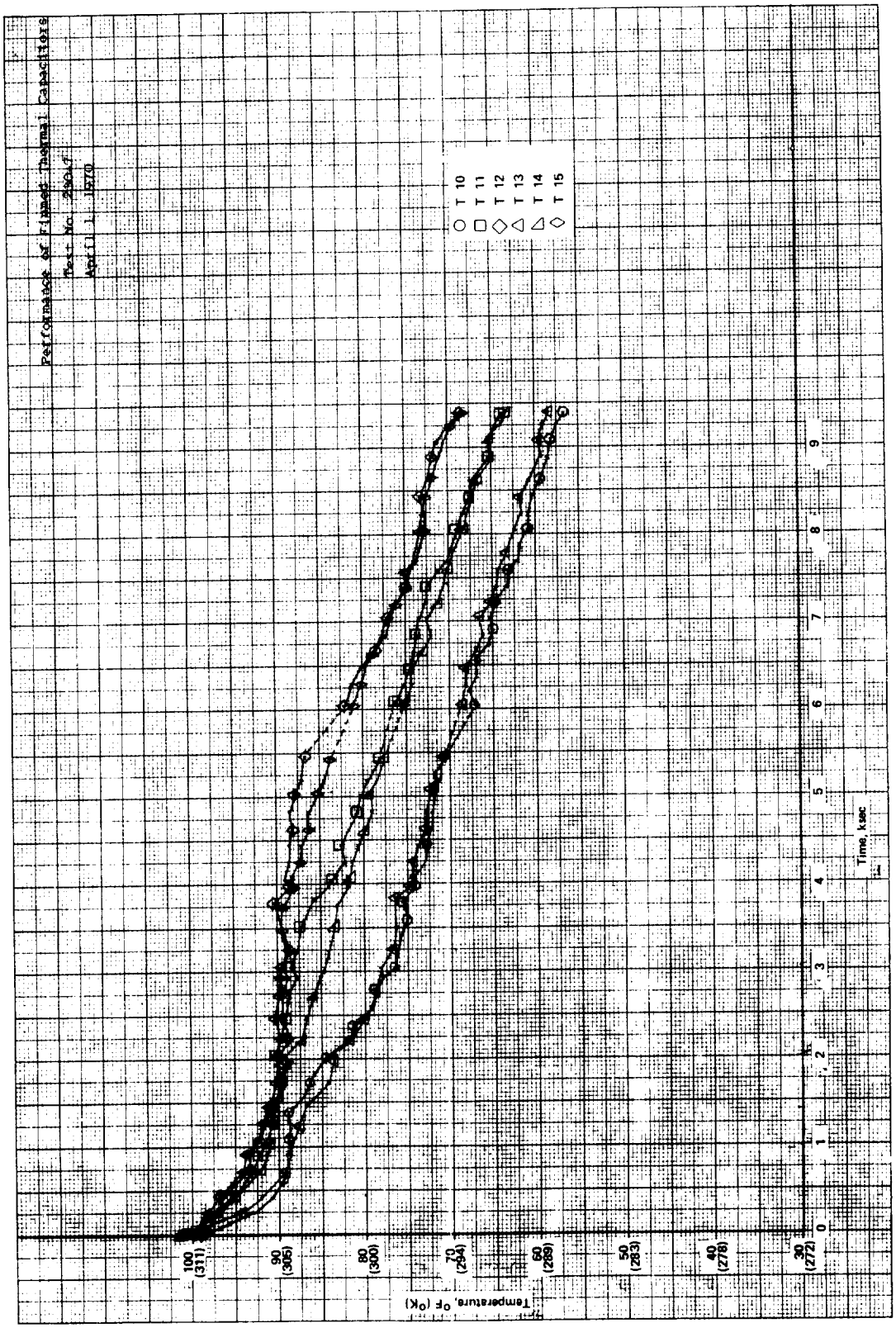

Figure D-2. Freeze temperature data for finned thermal capacitor (test no. 230-7).

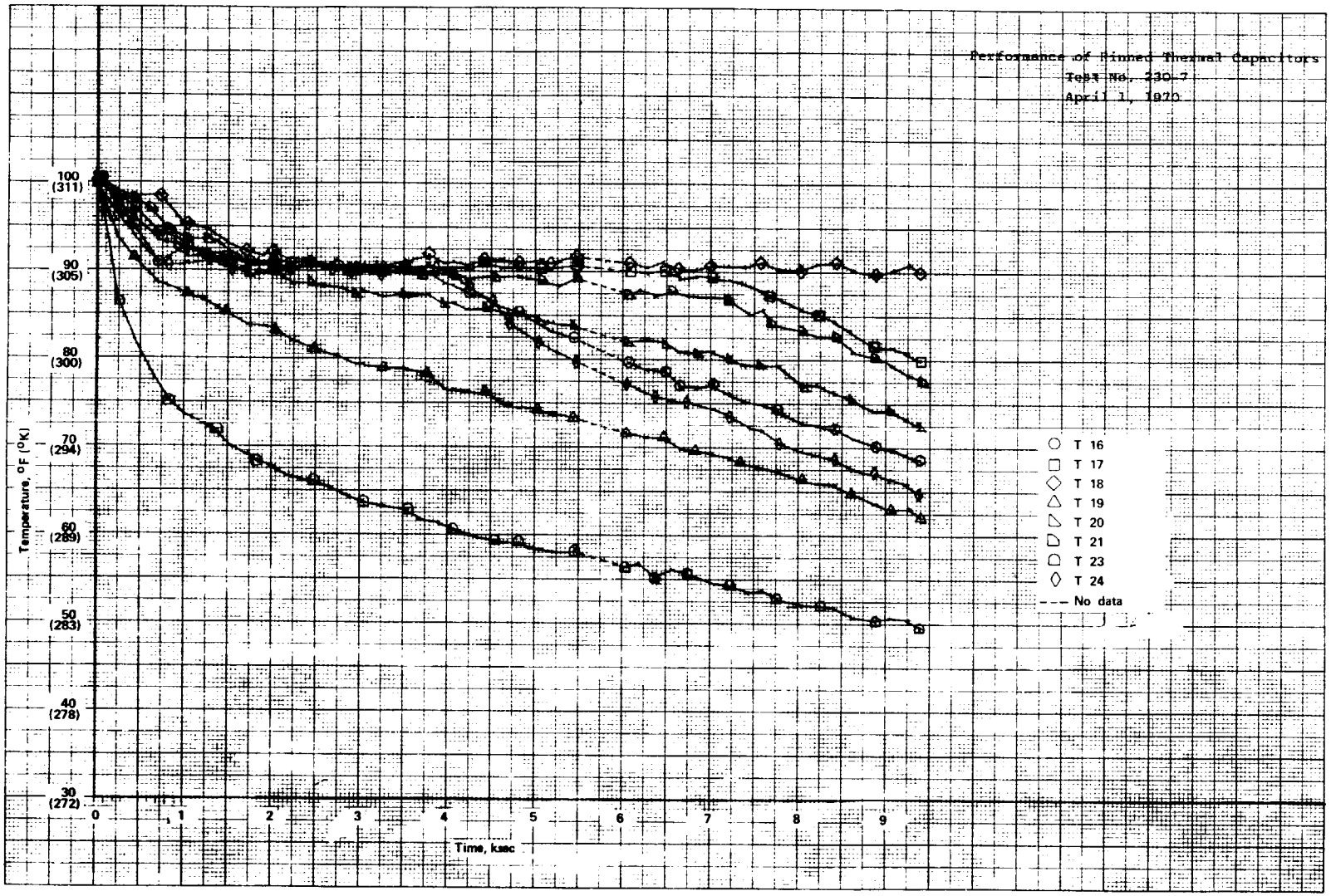

Figure D-3. Freeze temperature data for finned thermal capacitor (test no. 230-7).

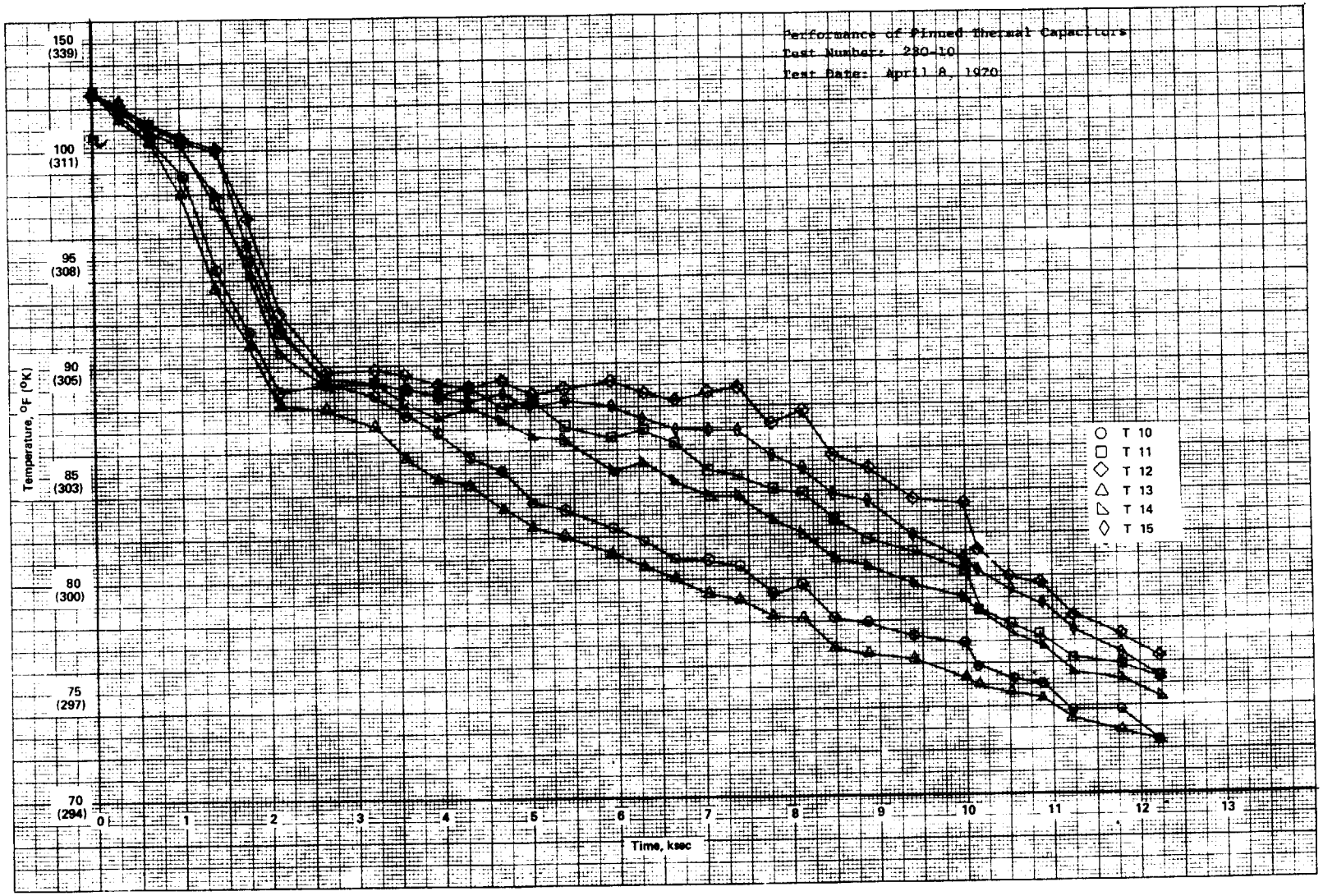

Figure D-4. Freeze temperature data for finned thermal capacitor (test no. 230-10).

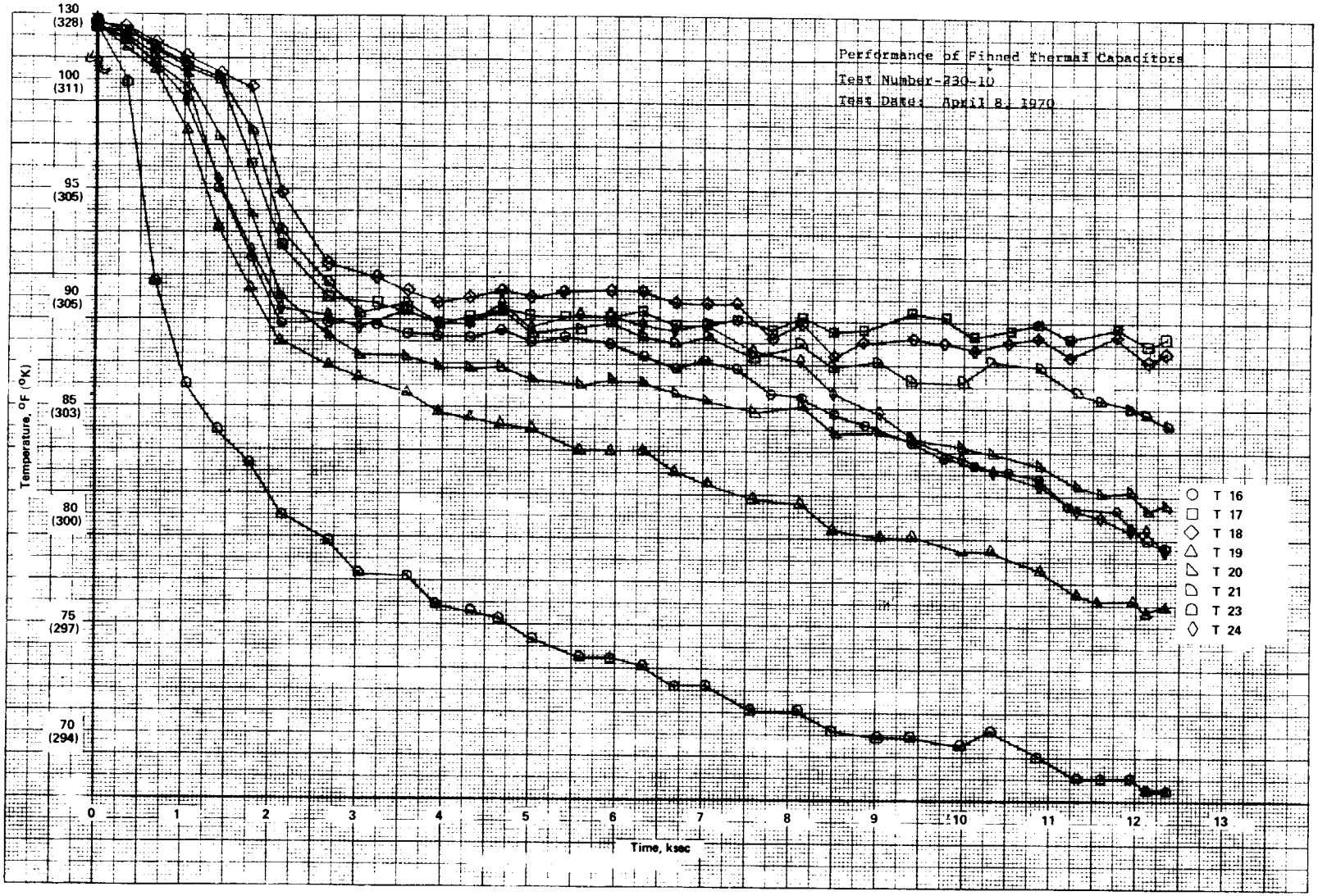

Figure D-5. Freeze temperature data for finned thermal capacitor (test no. 230-10).

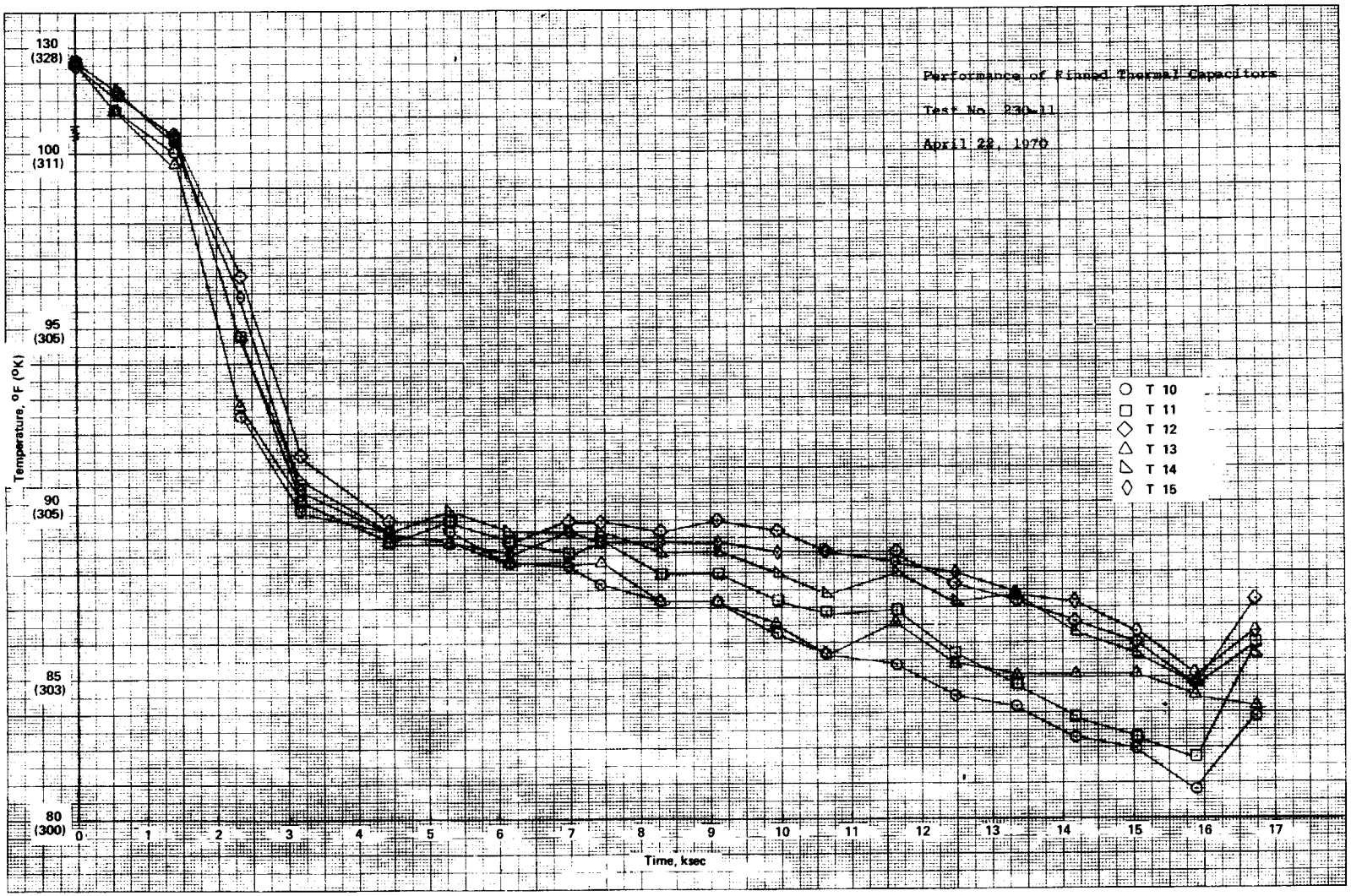

Figure D-6. Freeze temperature data for finned thermal capacitor (test no. 230-11).

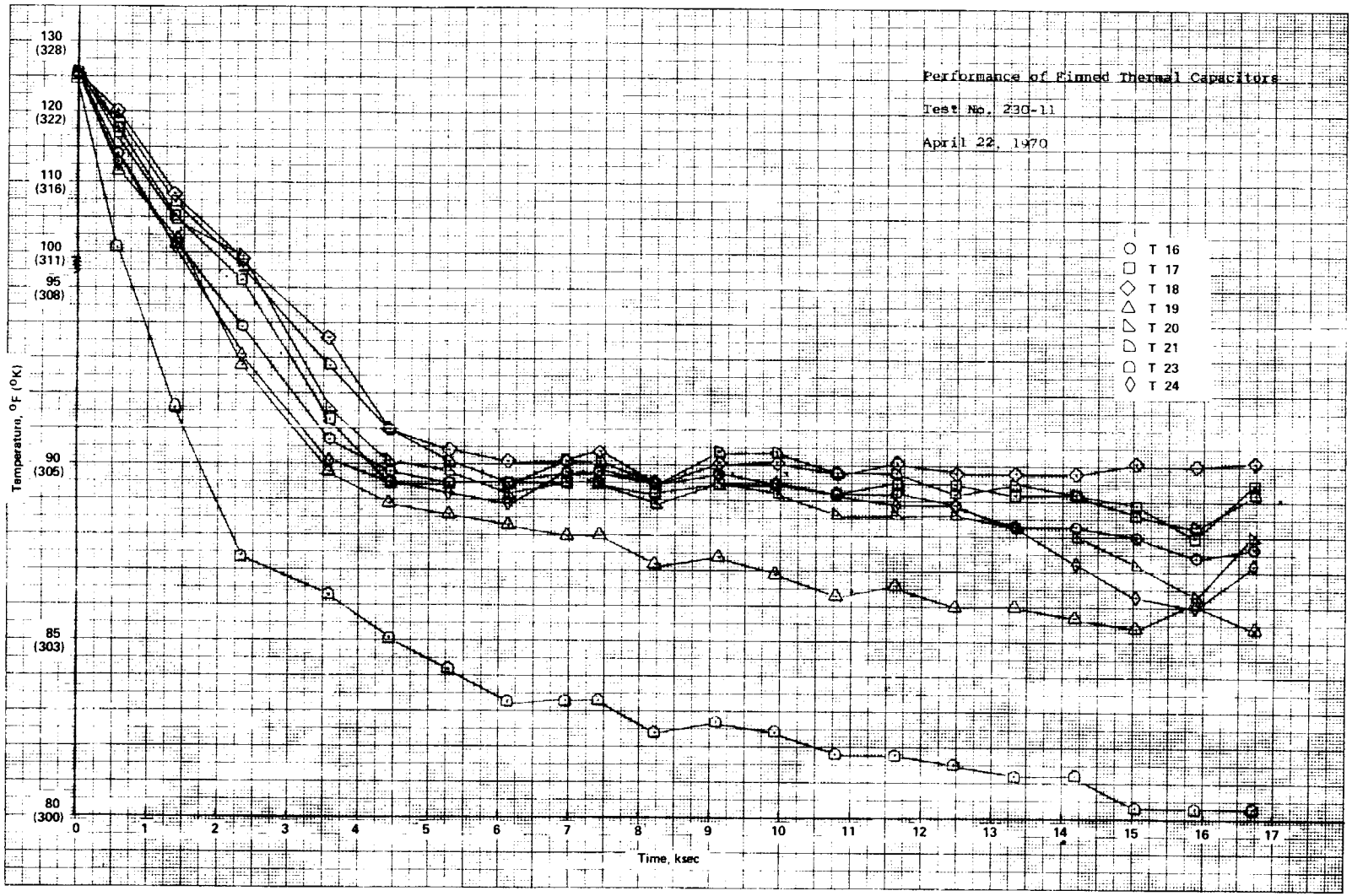

Figure D-7. Freeze temperature data for finned thermal capacitor (test no. 230-11).

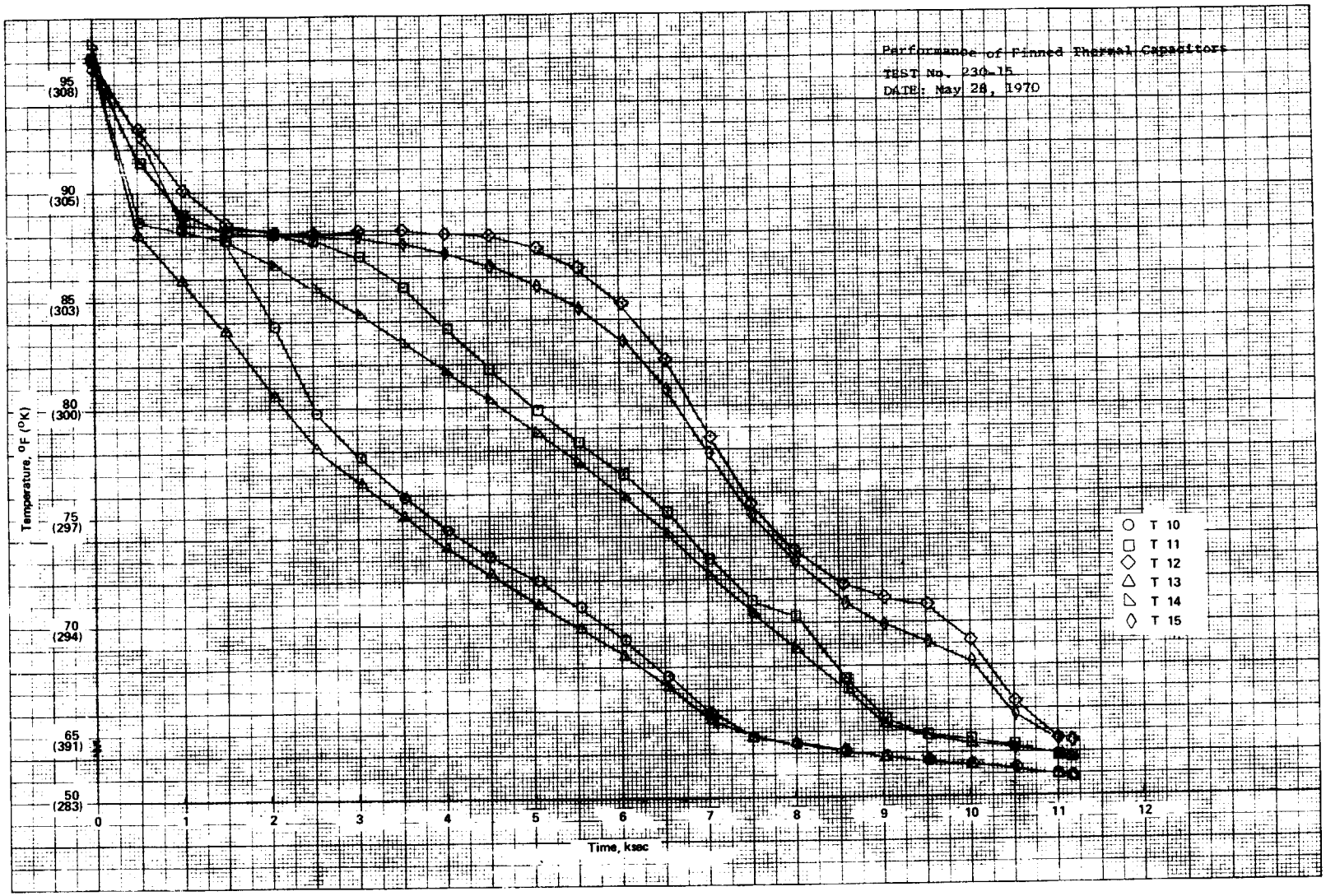

Figure D-8. Freeze temperature data for finned thermal capacitor (test no. 230-15)

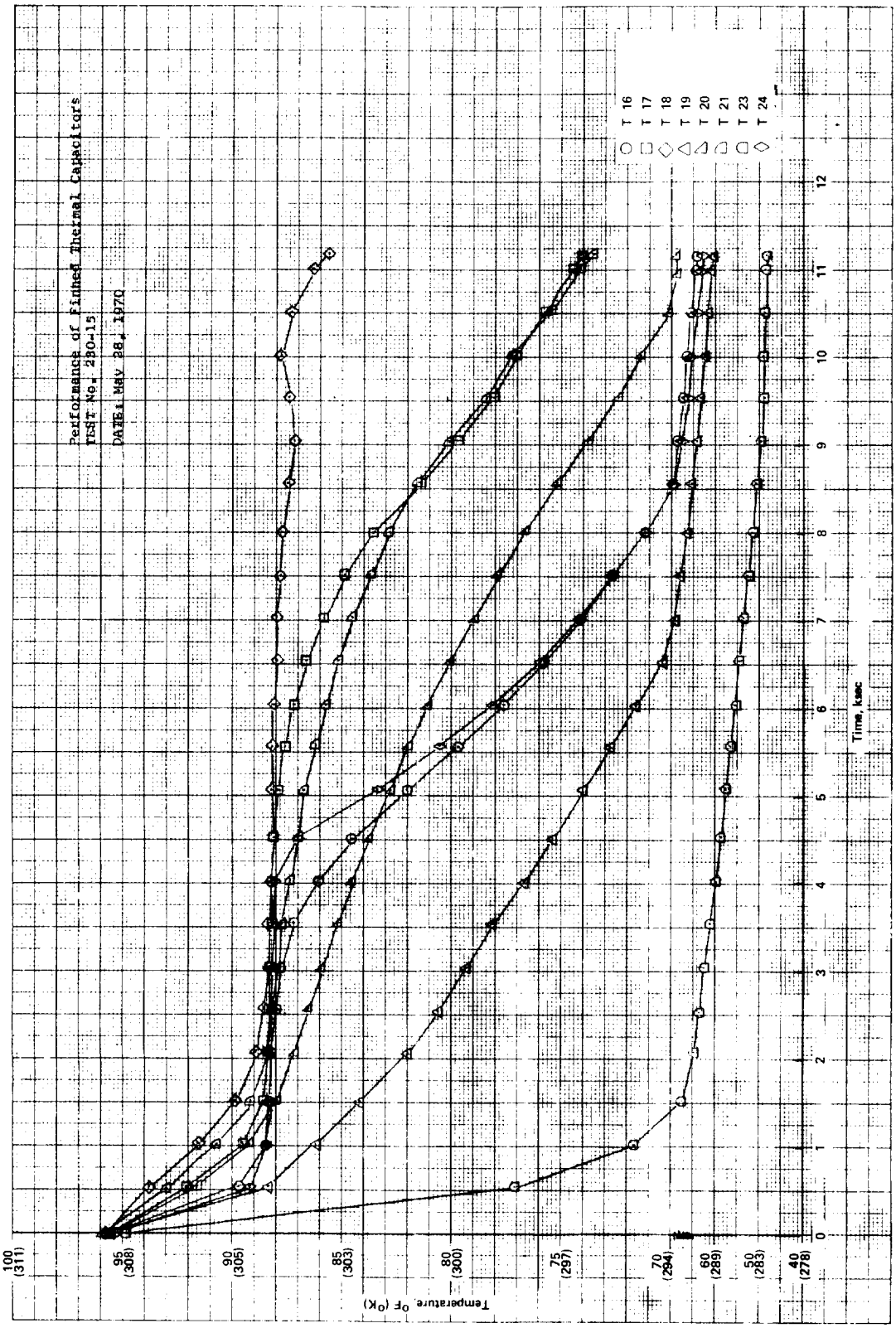

Figure D-9. Freeze temperature data for finned thermal capacitor (test no. 230-15).

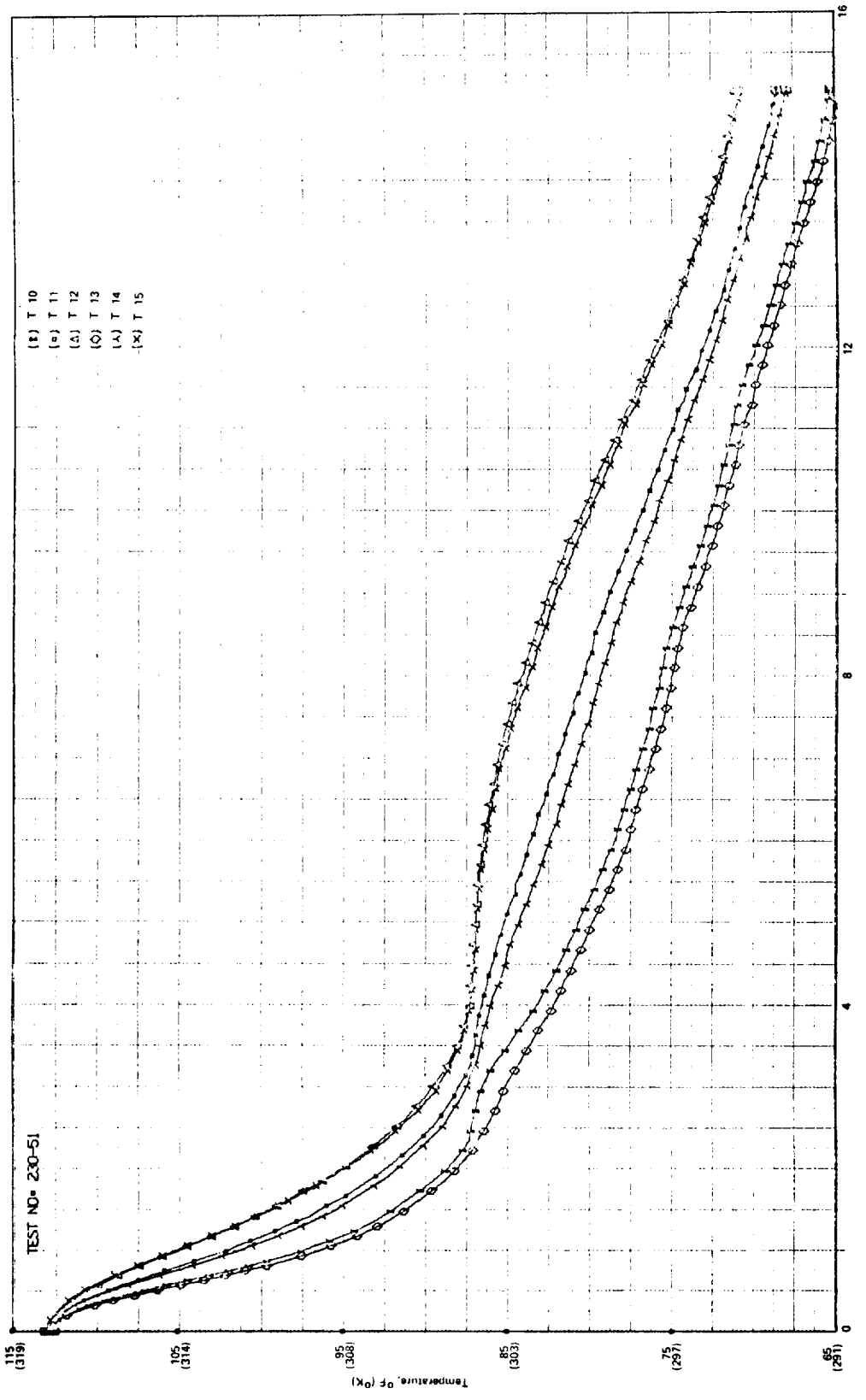

Figure D-10. Freeze temperature data for finned thermal capacitor (test no. 230-51).

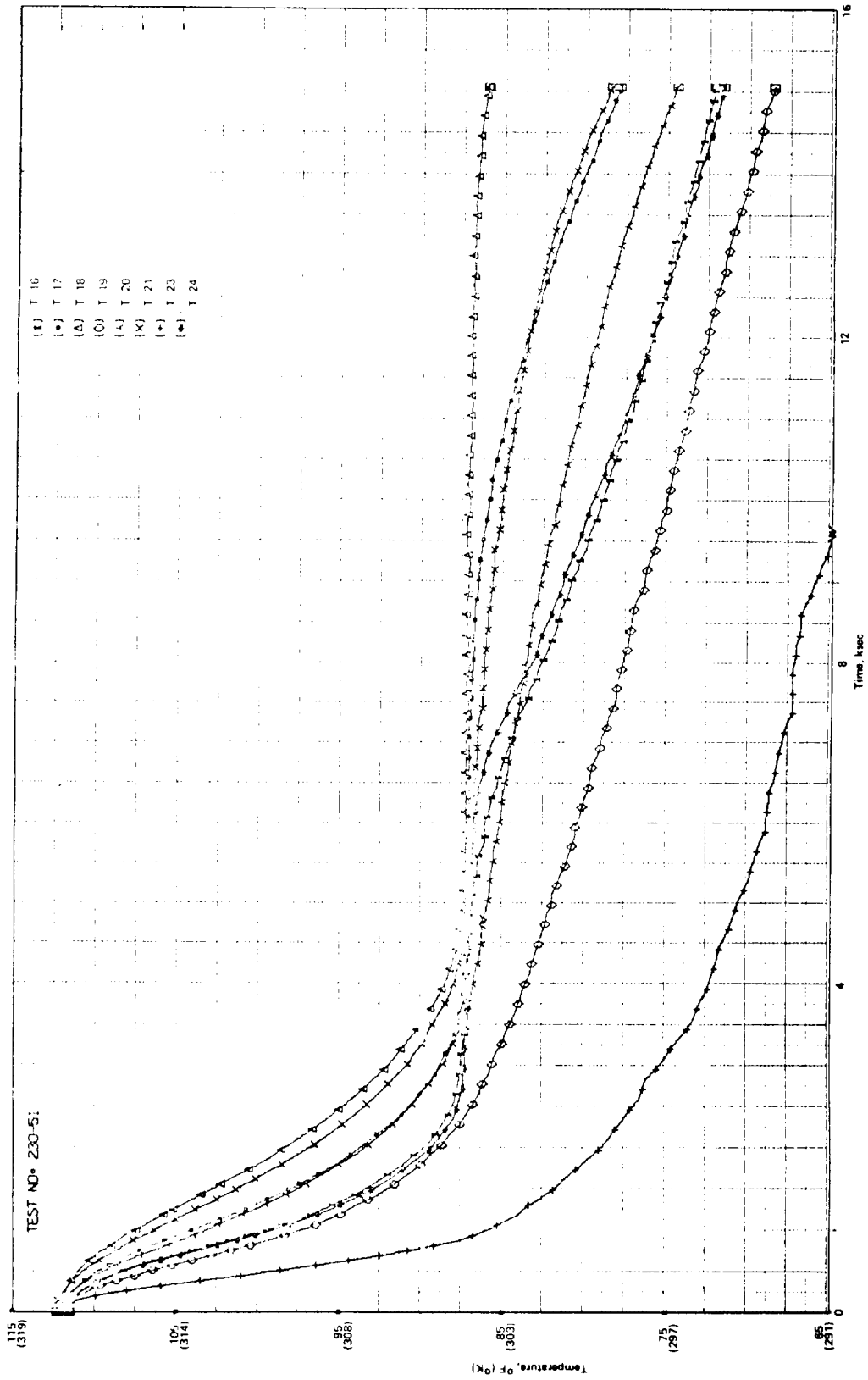

Figure D-11. Freeze temperature data for finned thermal capacitor (test no. 230-51).

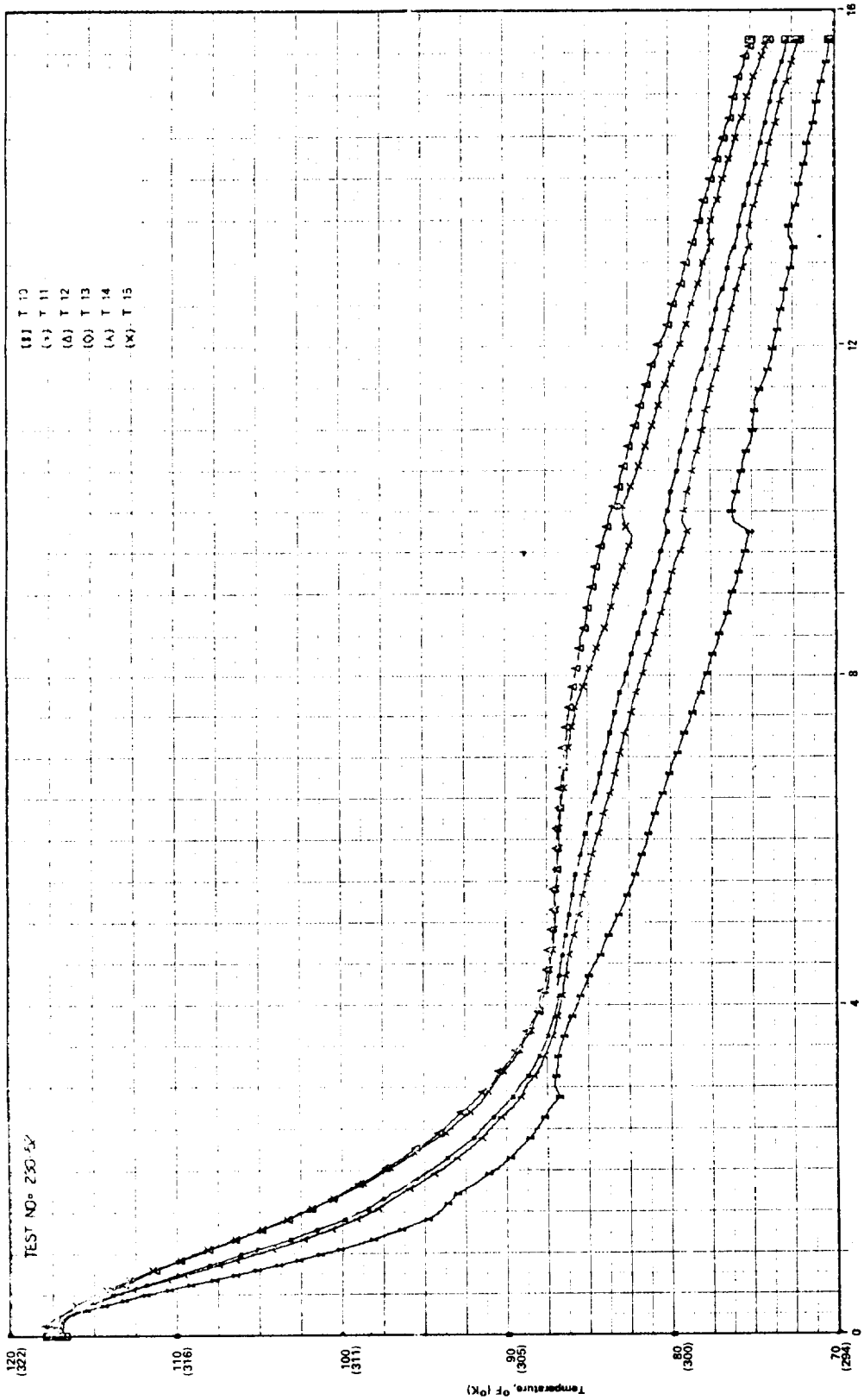

Figure D-12. Freeze temperature data for finned thermal capacitor (test no. 230-52).

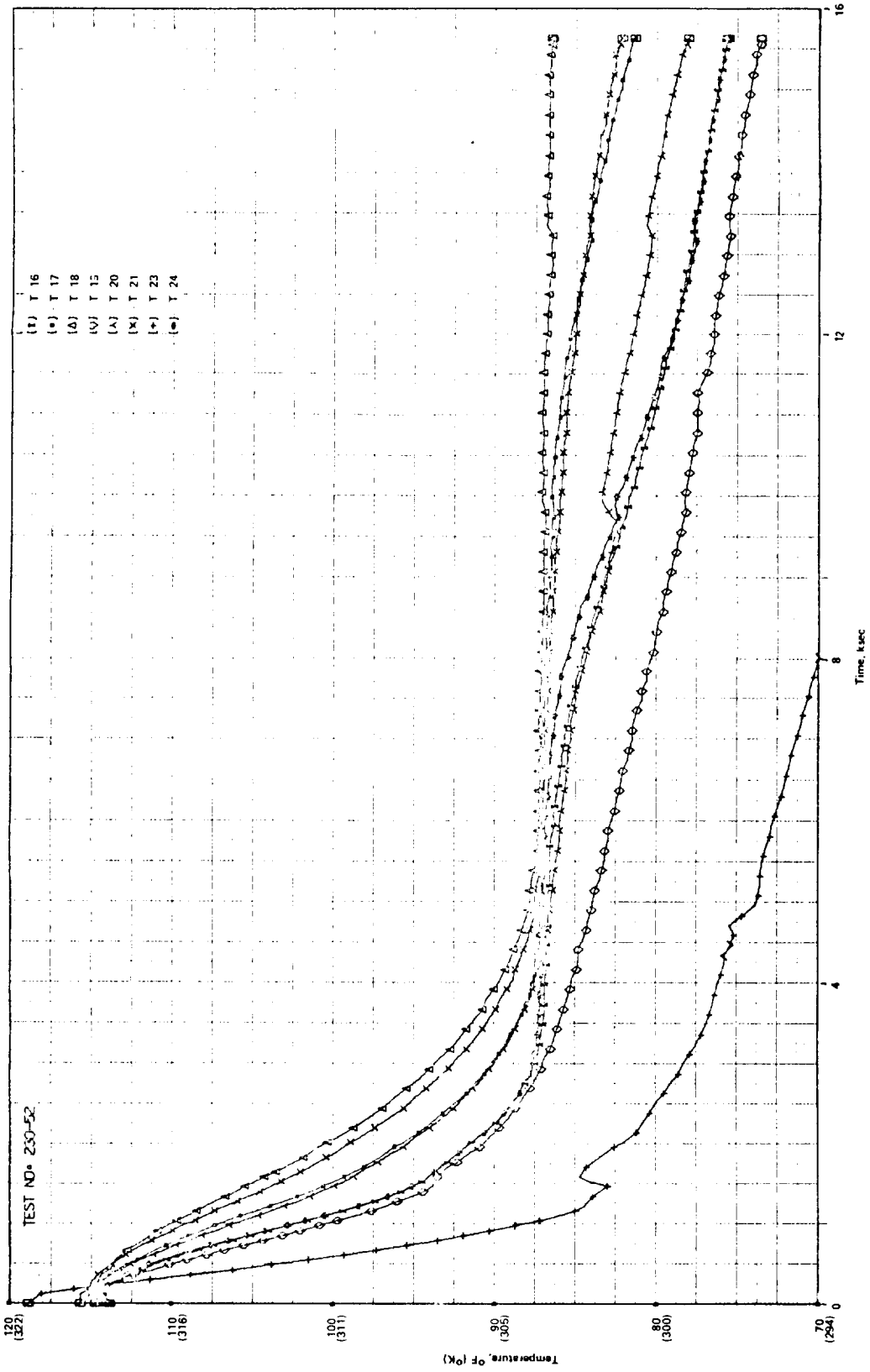

Figure D-13. Freeze temperature data for finned thermal capacitor (test no. 230-52).

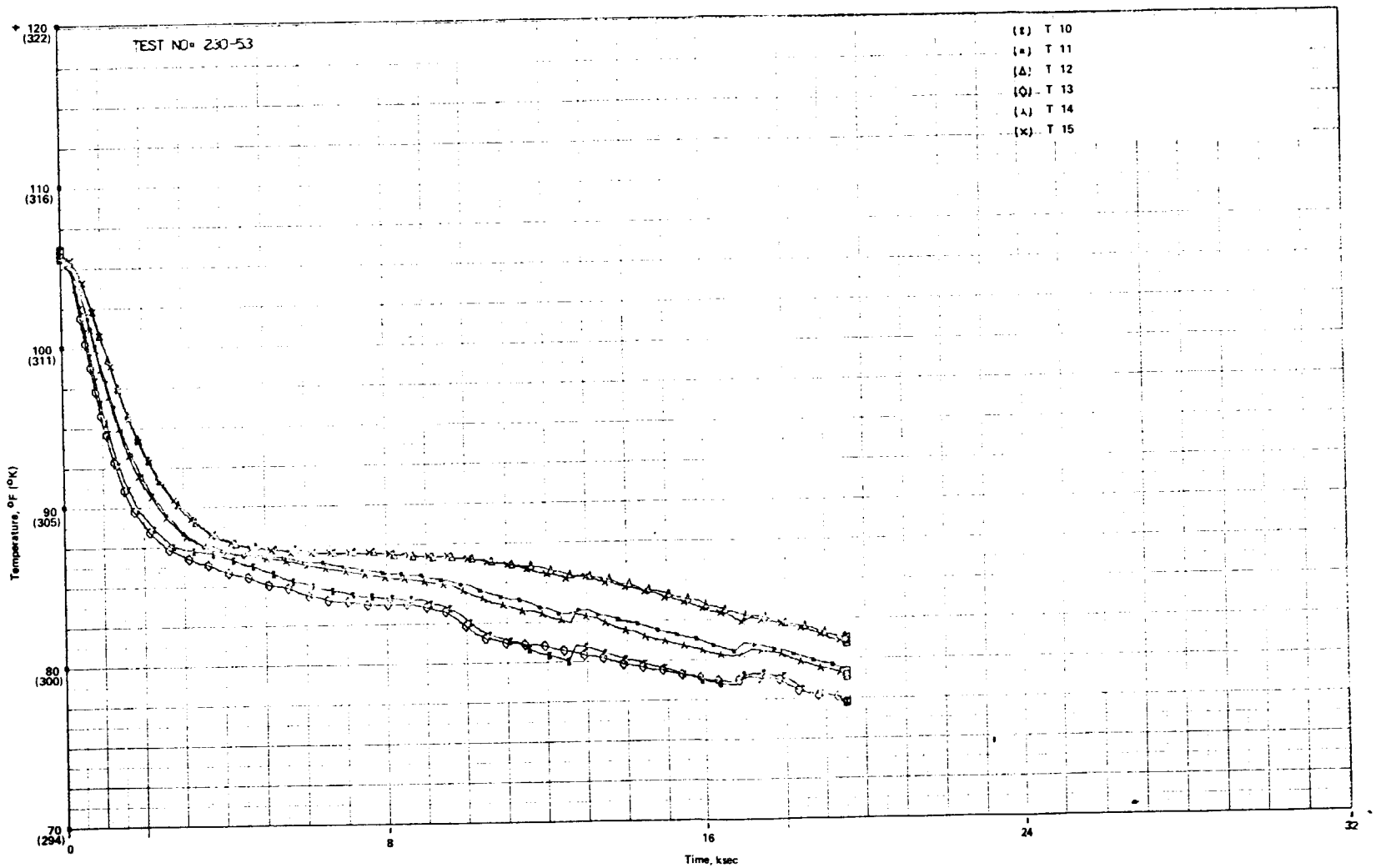

Figure D-14. Freeze temperature data for finned thermal capacitor (test no. 230-53).

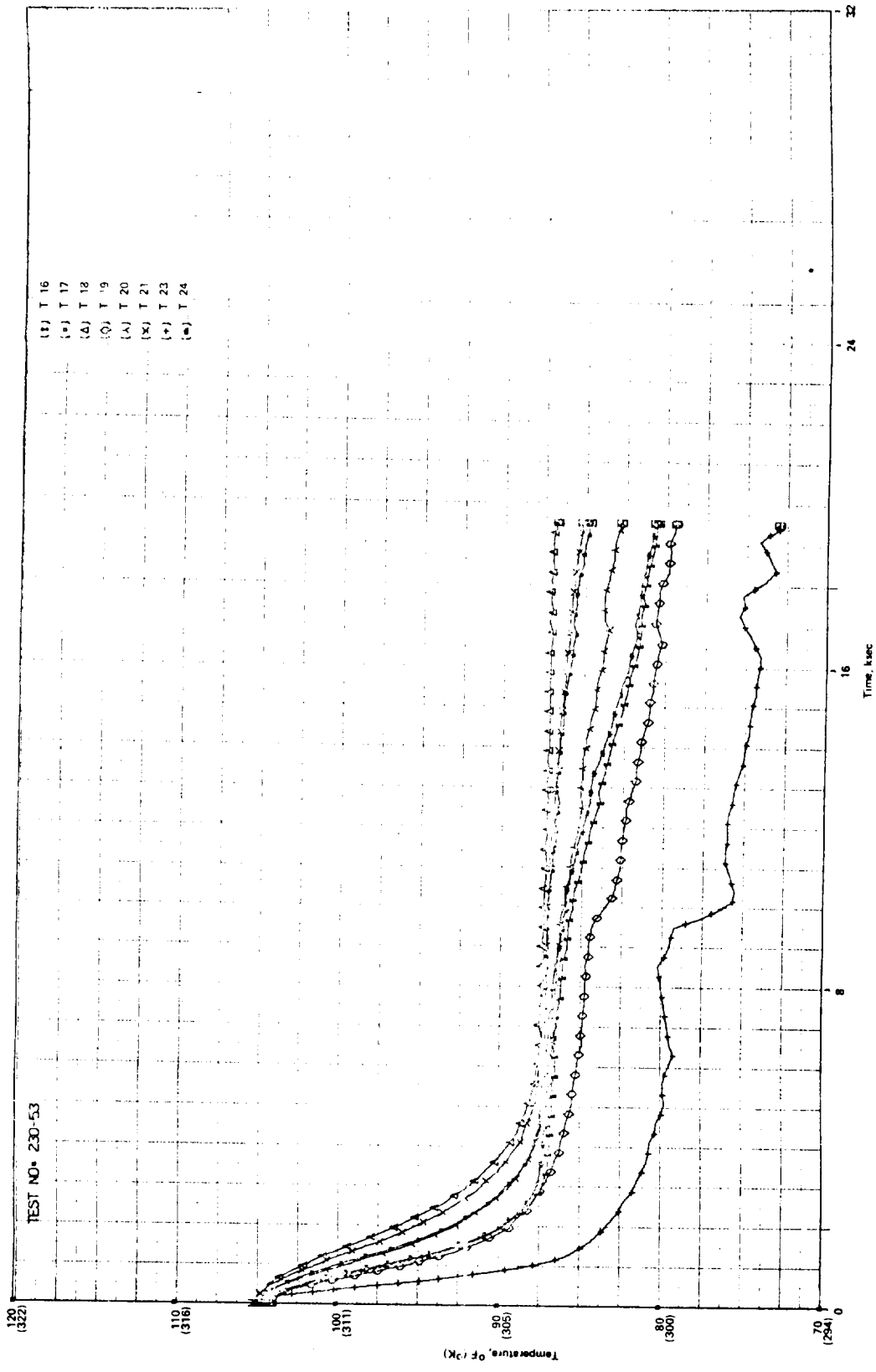

Figure D-15. Freeze temperature data for finned thermal capacitor (test no. 230-53).

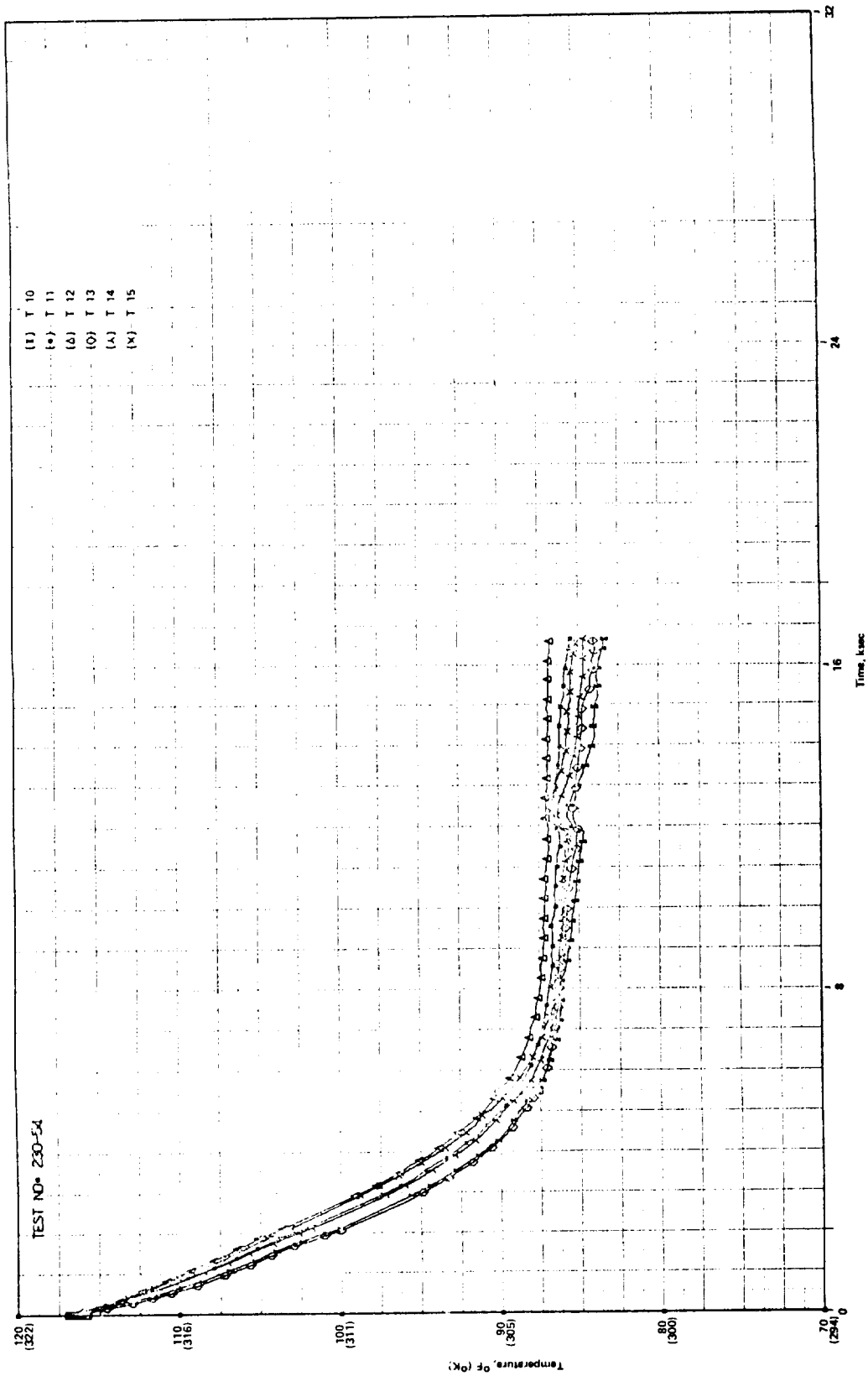

Figure D-16. Freeze temperature data for finned thermal capacitor (test no. 230-54).

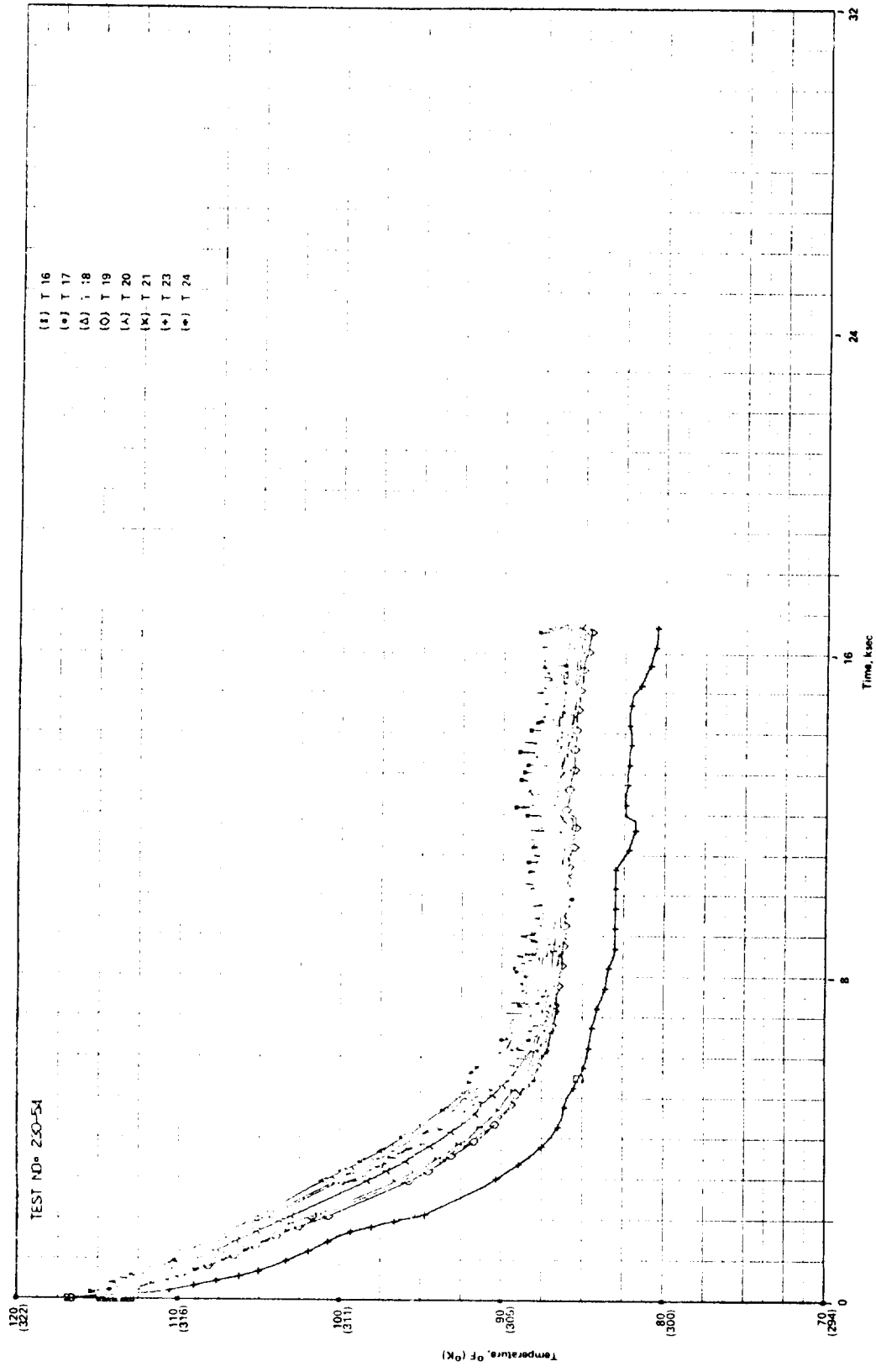

Figure D-17. Freeze temperature data for finned thermal capacitor (test no. 230-54).

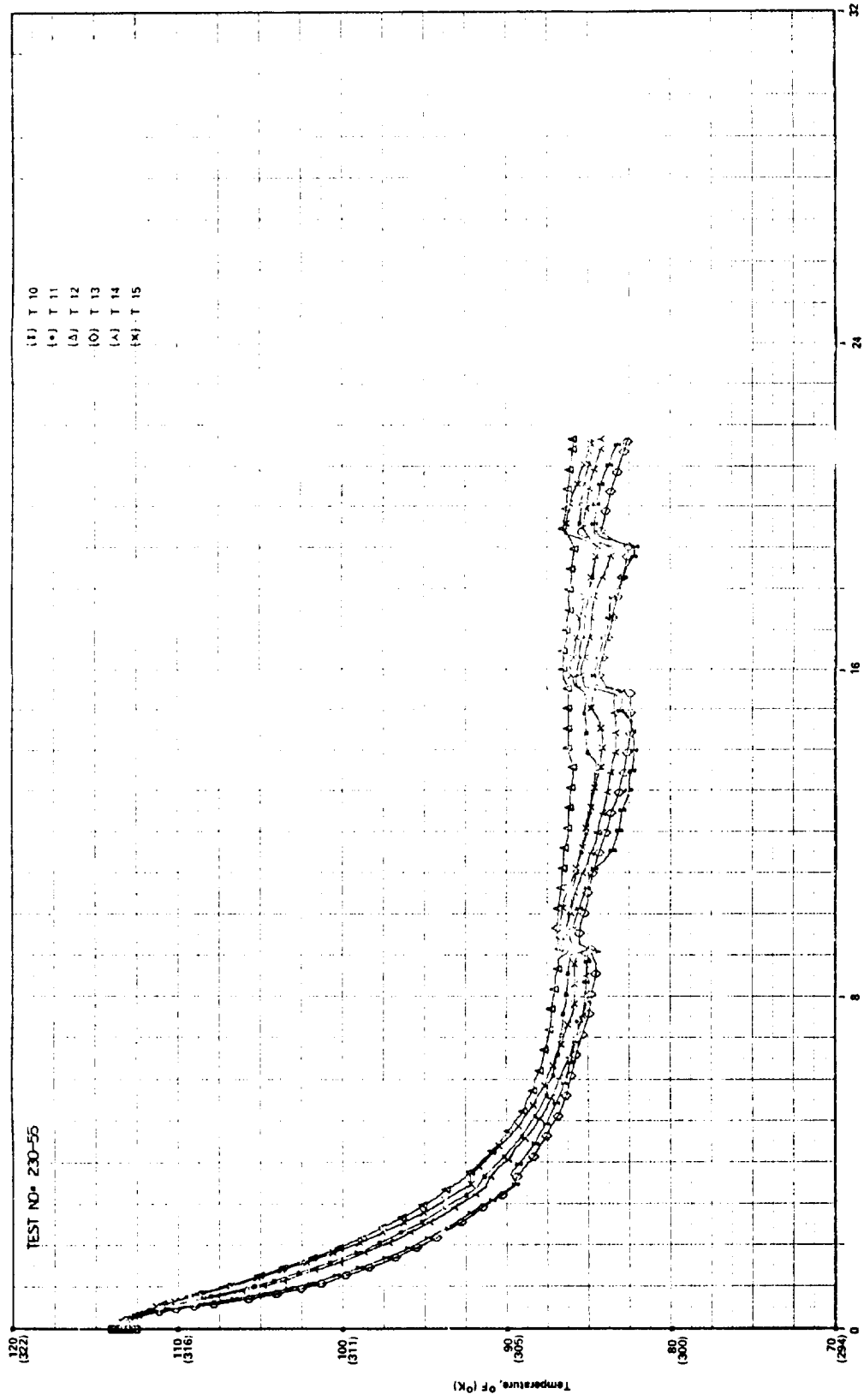

Figure D-18. Freeze temperature data for finned thermal capacitor (test no. 230-55).

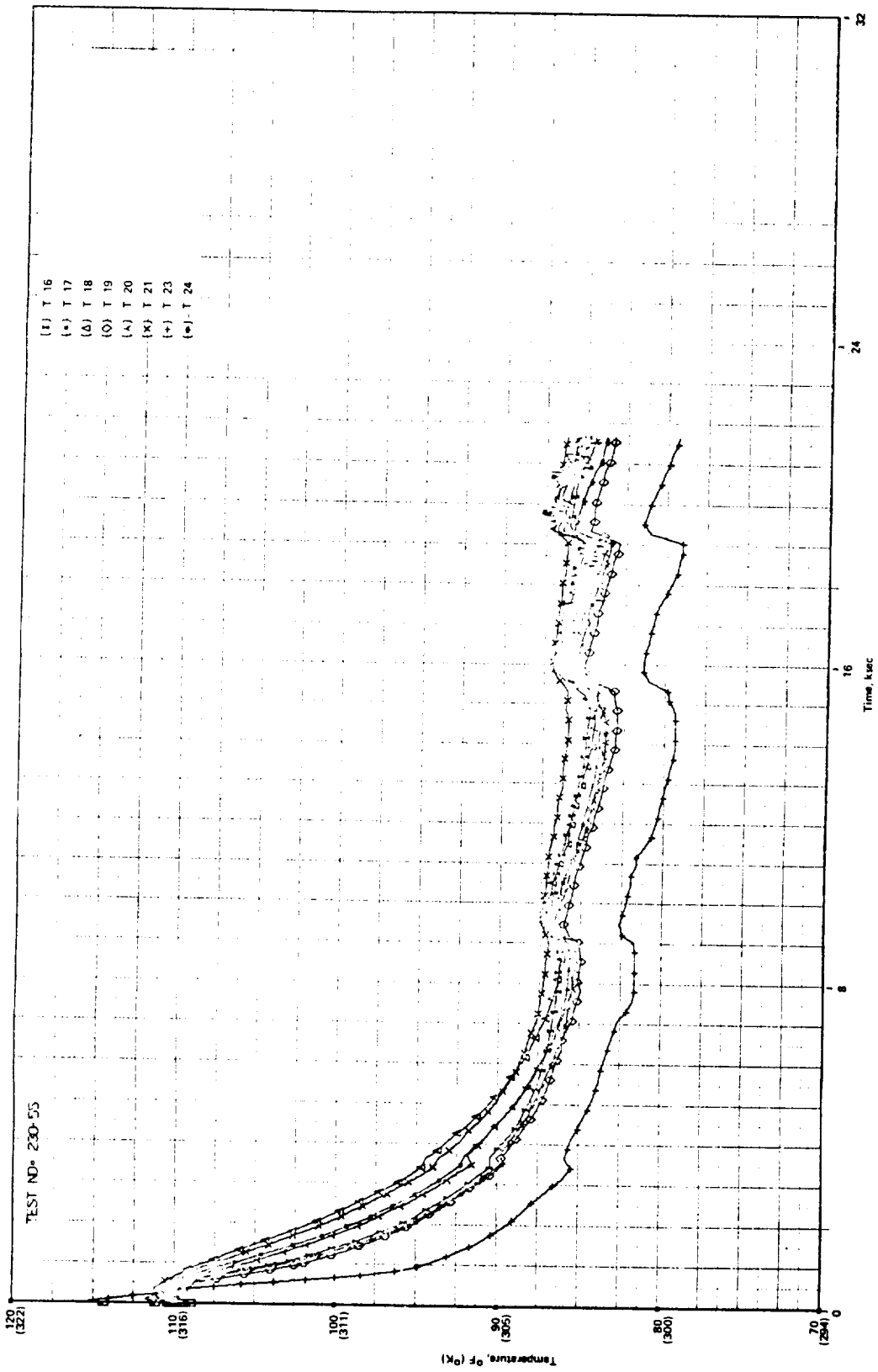

Figure D-19. Freeze temperature data for finned thermal capacitor (test no. 230-55).

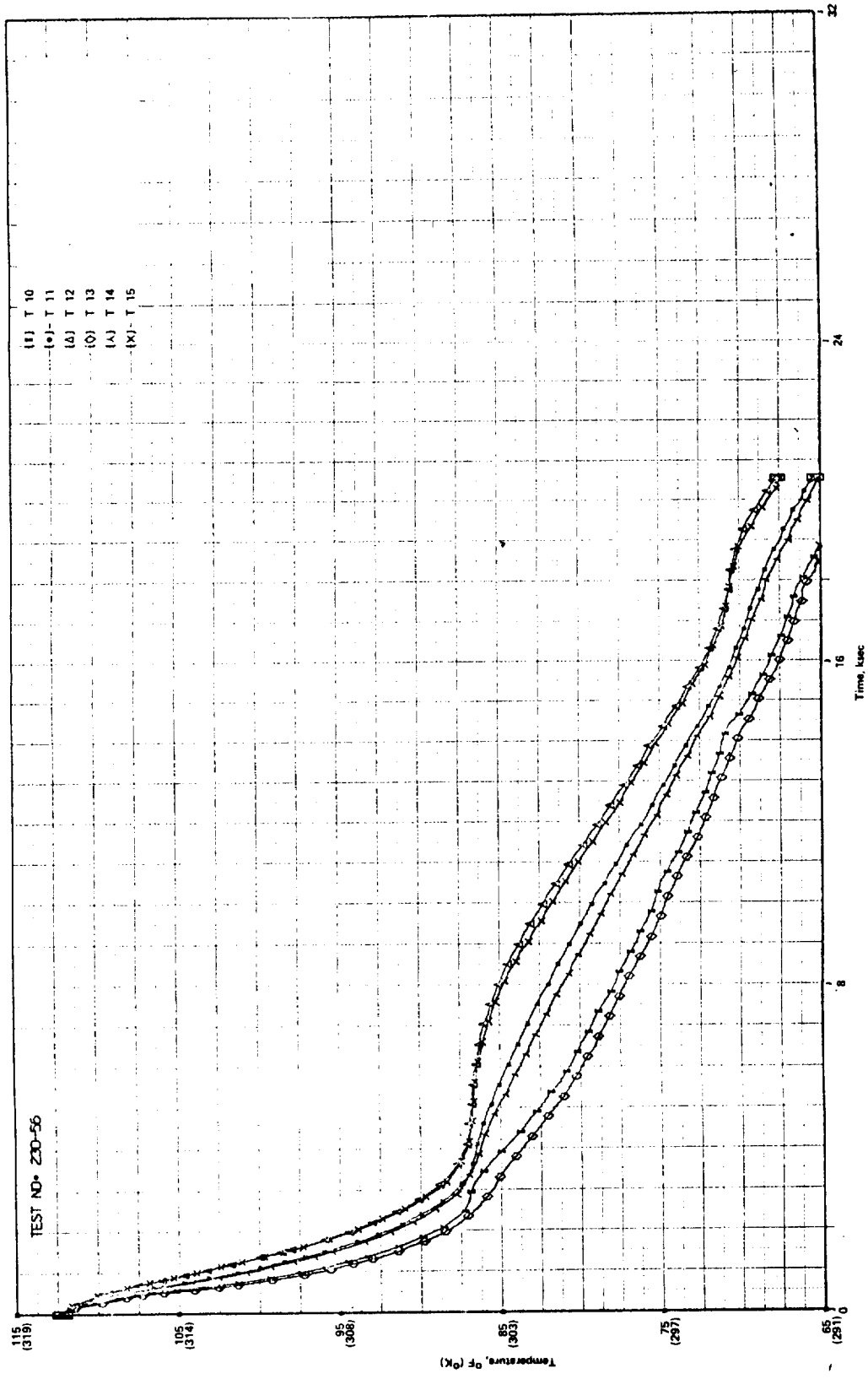

Figure D-20. Freeze temperature data for finned thermal capacitor (test no. 230-56).

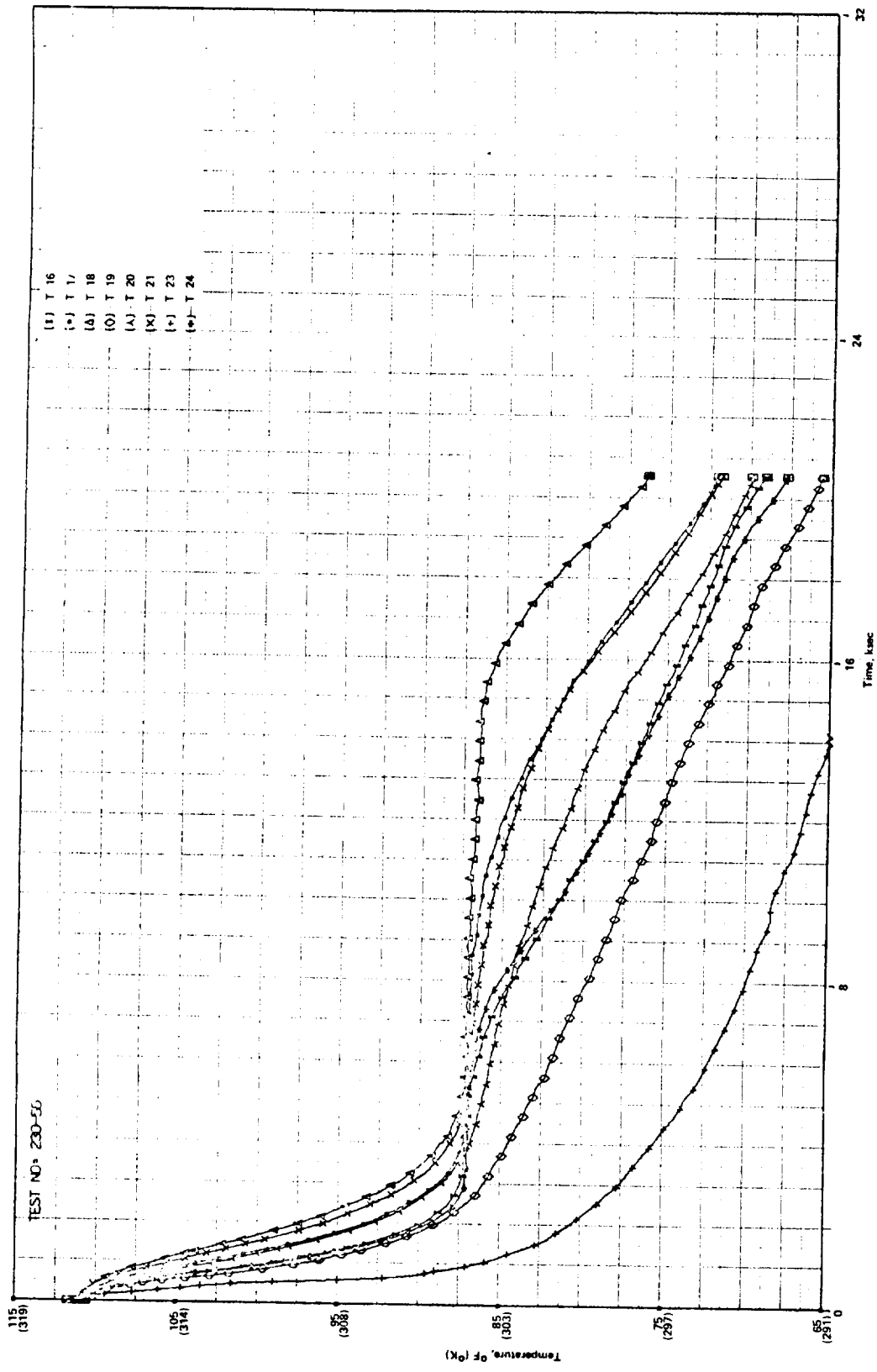

Figure D-21. Freeze temperature data for finned thermal capacitor (test no. 230-56).

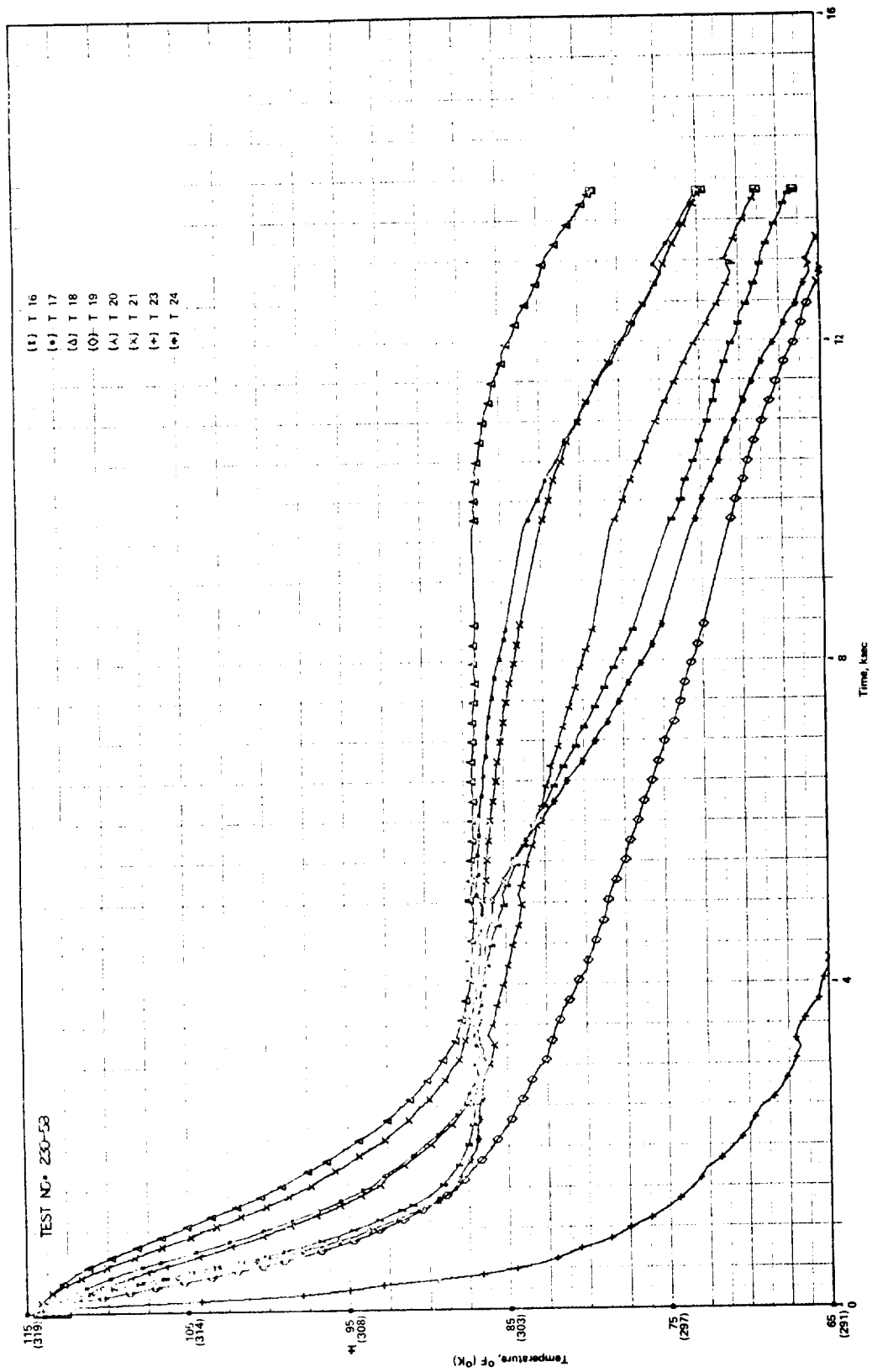

Figure D-22. Freeze temperature data for finned thermal capacitor (test no. 230-58).

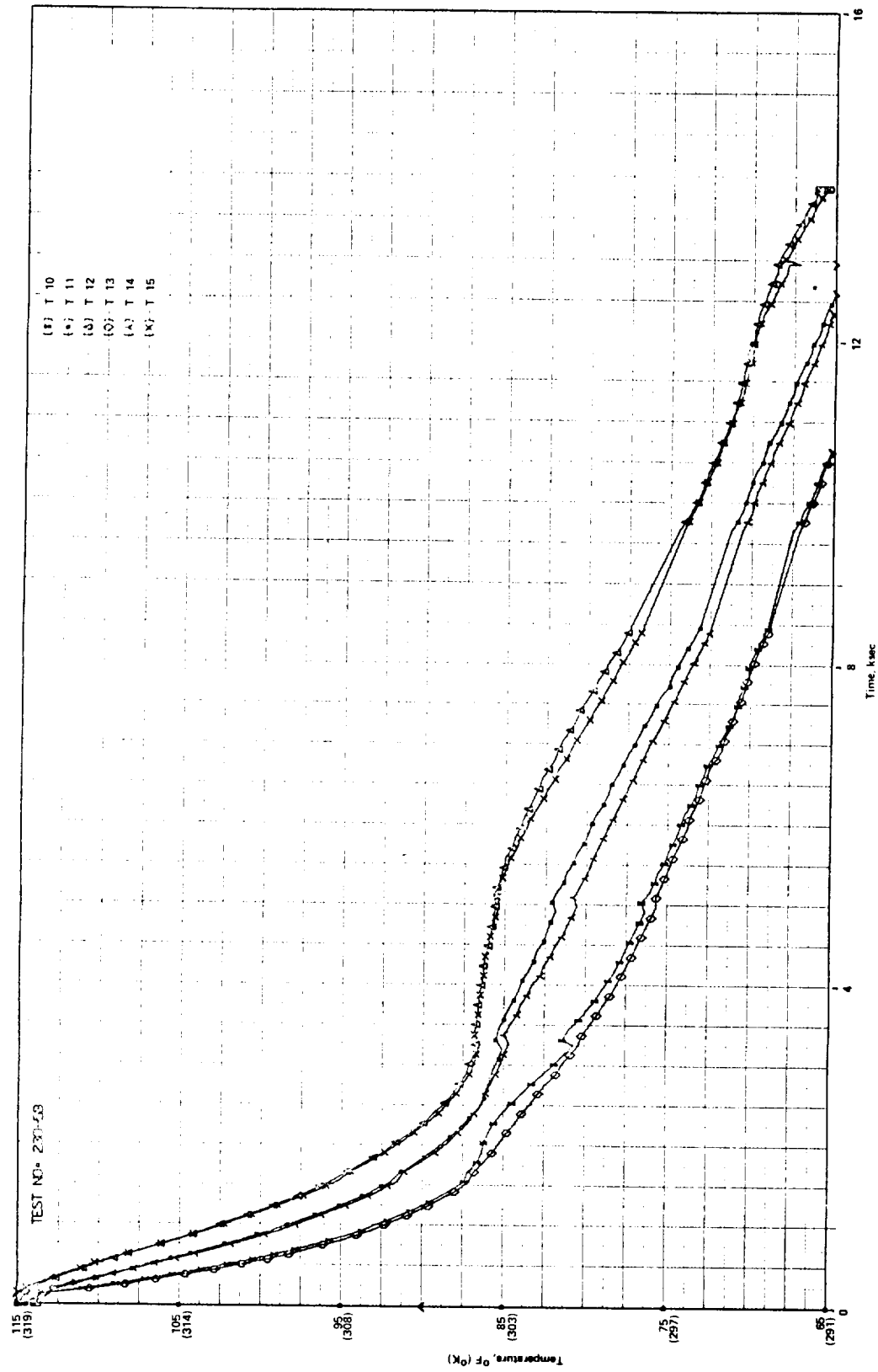

Figure D-23. Freeze temperature data for finned thermal capacitor (test no. 230-58).

SECTION II

FREEZE FRONT POSITION DATA FOR FINNED THERMAL CAPACITORS

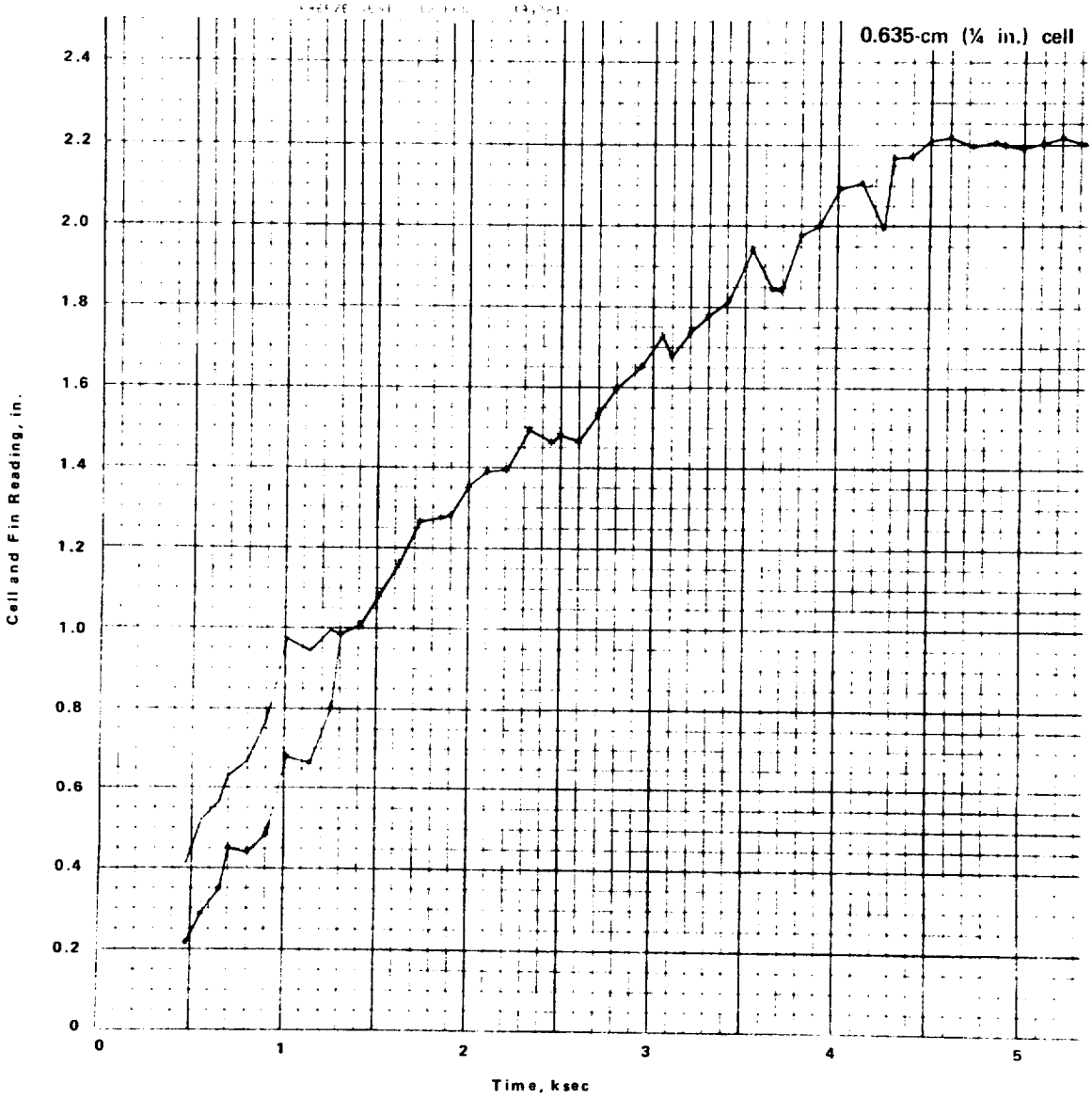

Figure D-24. Freeze front position data (test no. 230-7).

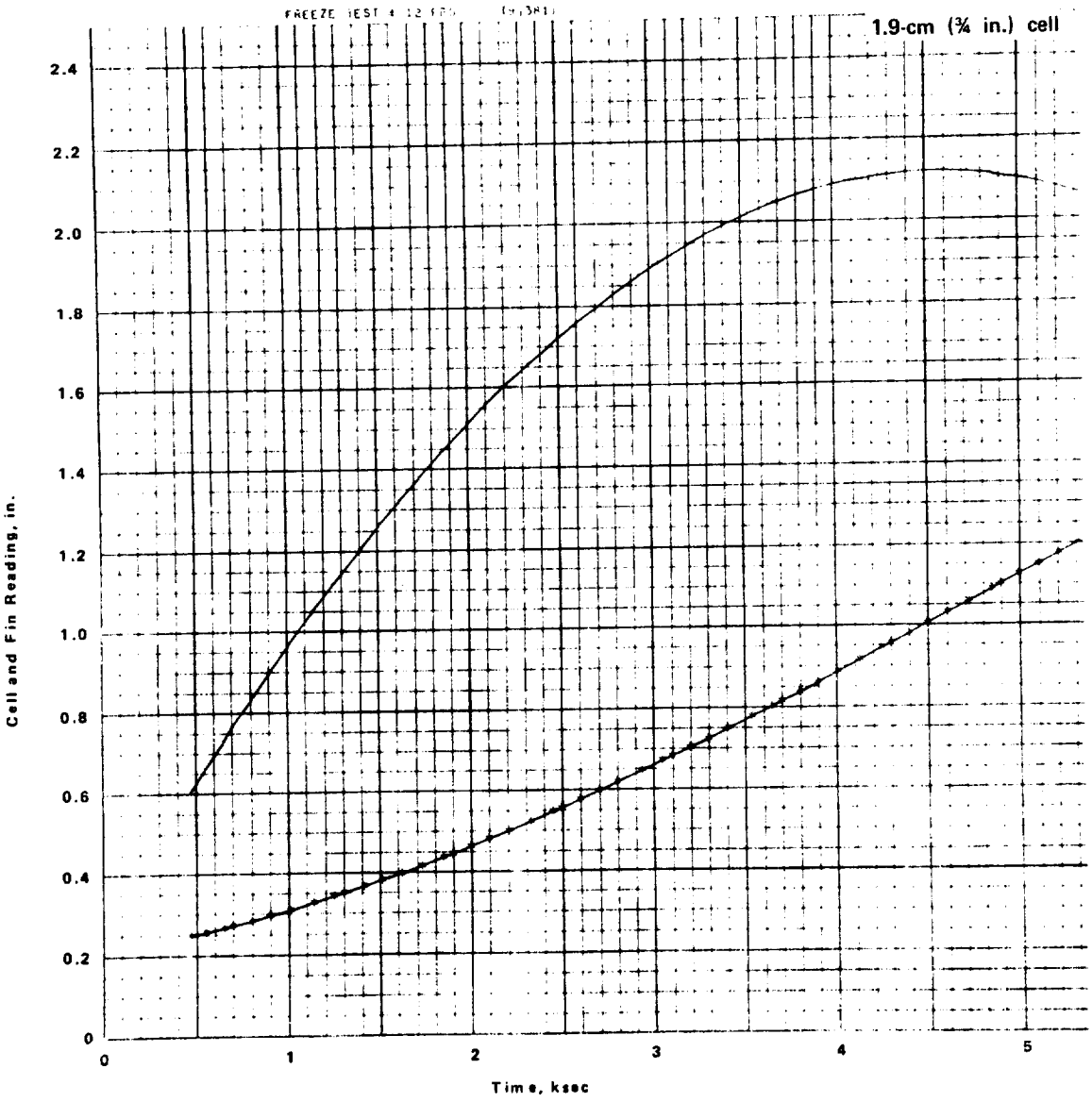

Figure D-25. Freeze front position data (test no. 230-7).

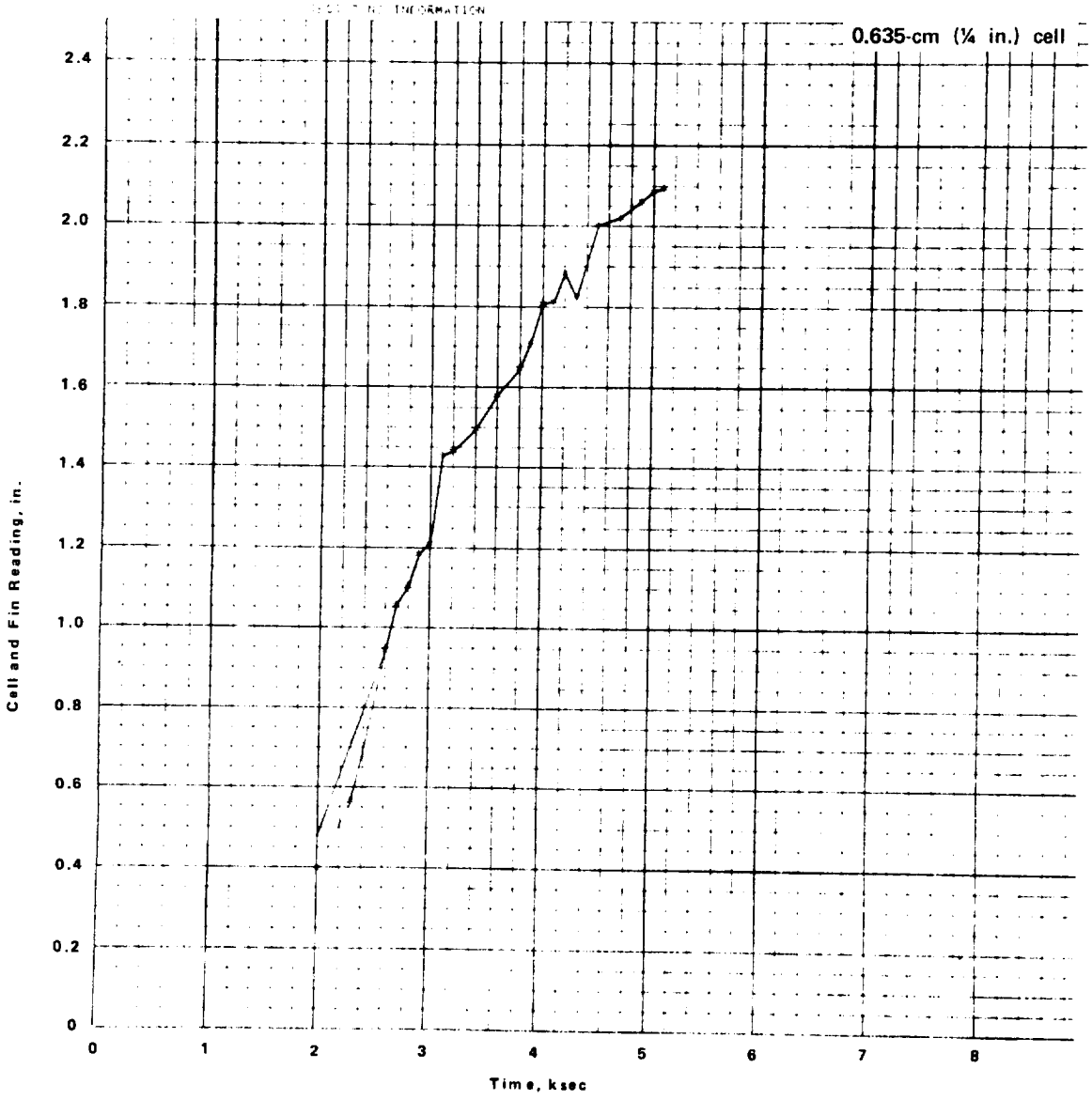

Figure D-26. Freeze front position data (test no. 230-10).

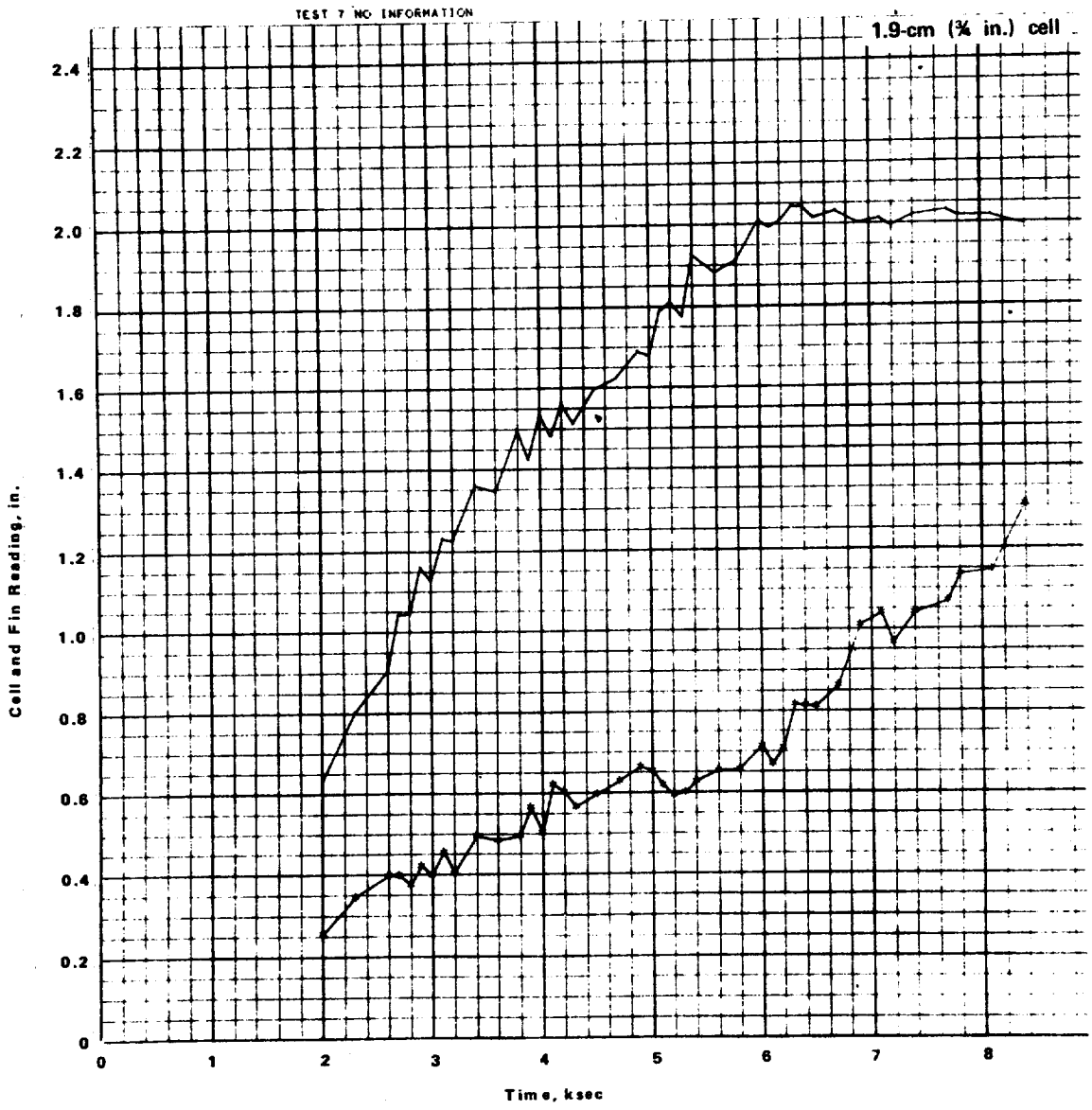

Figure D-27. Freeze front position data (test no. 230-10).

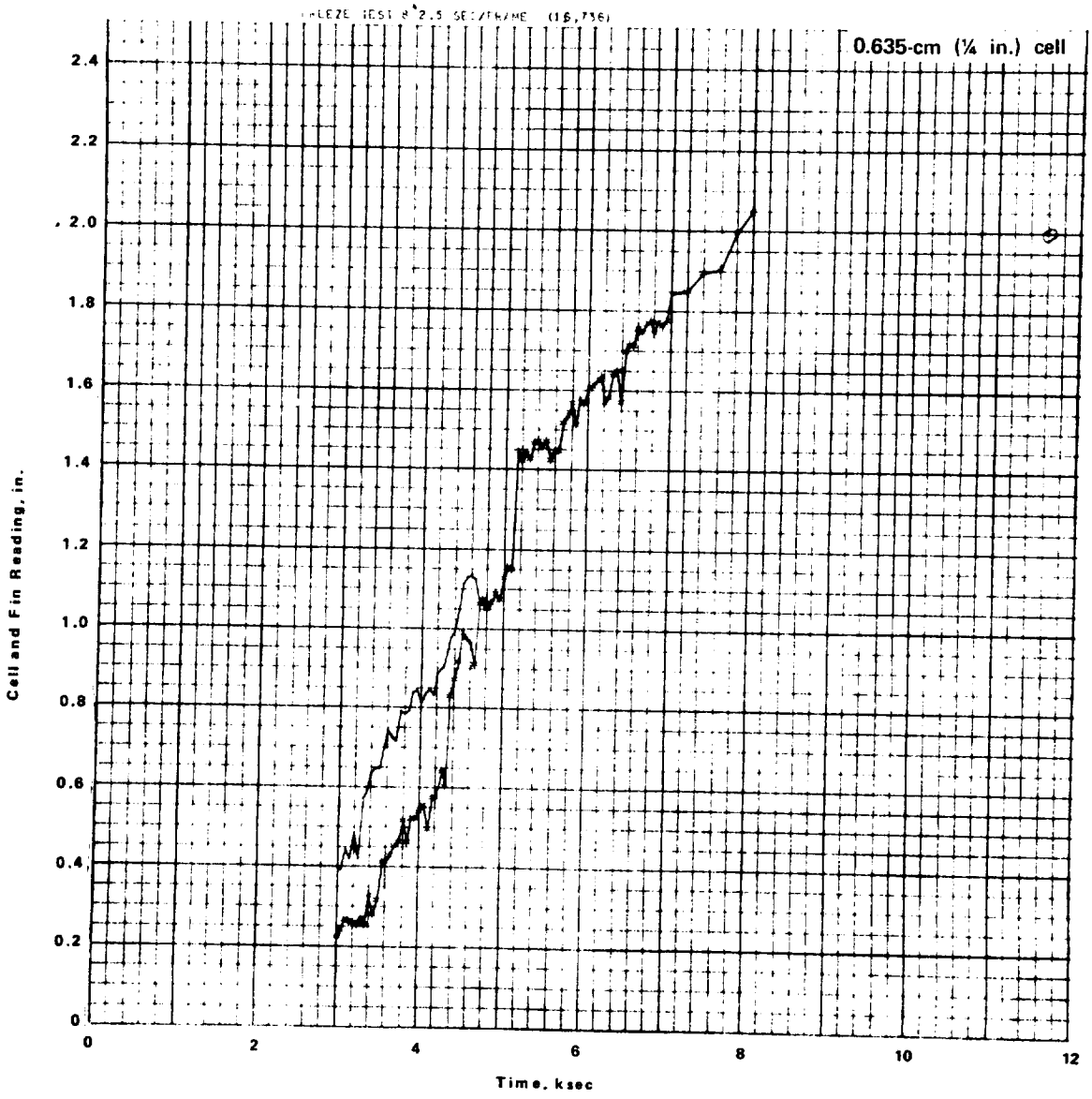

Figure D-28. Freeze front position data (test no. 230-11).

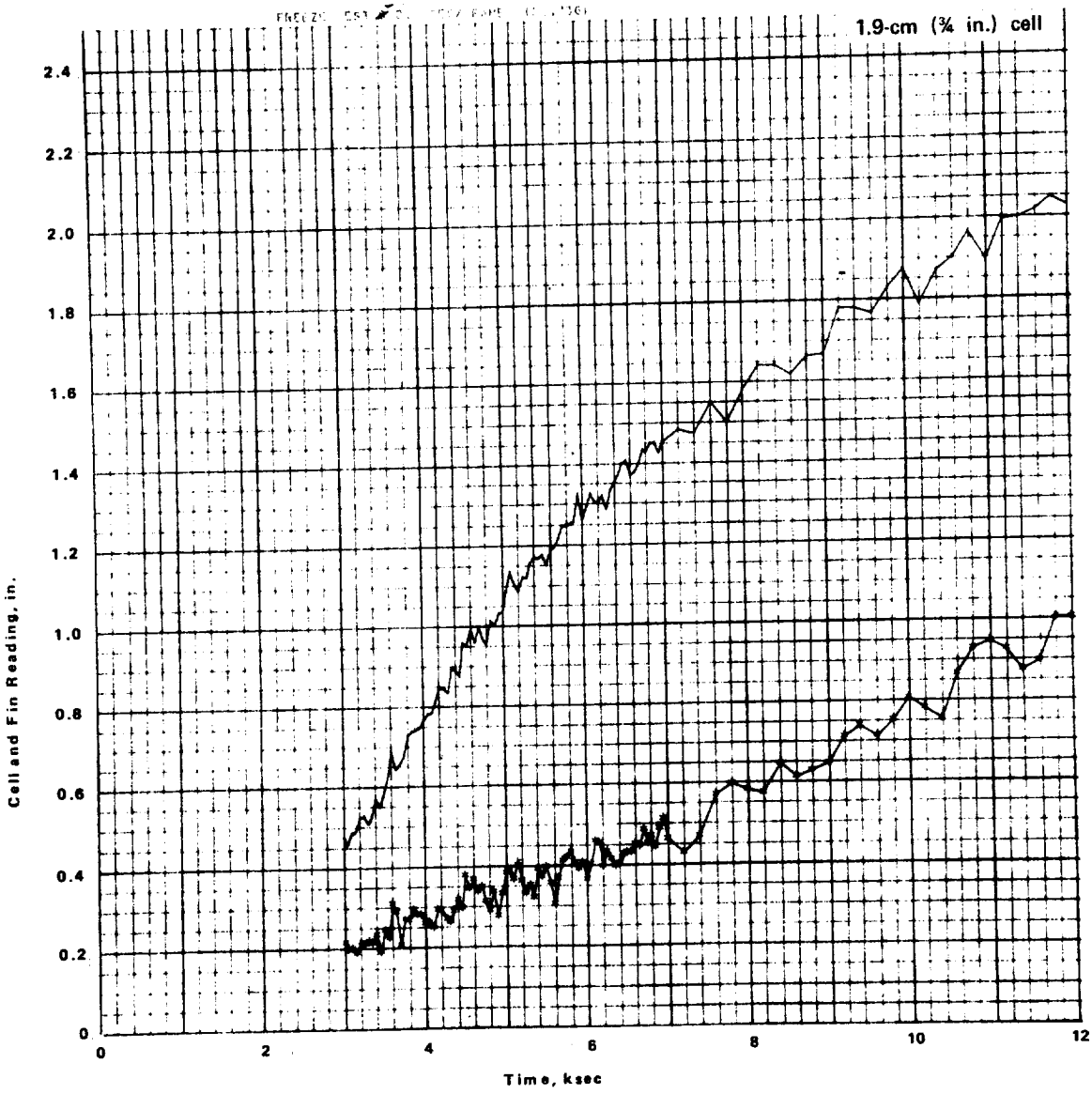

Figure D-29. Freeze front position data (test no. 230-11).

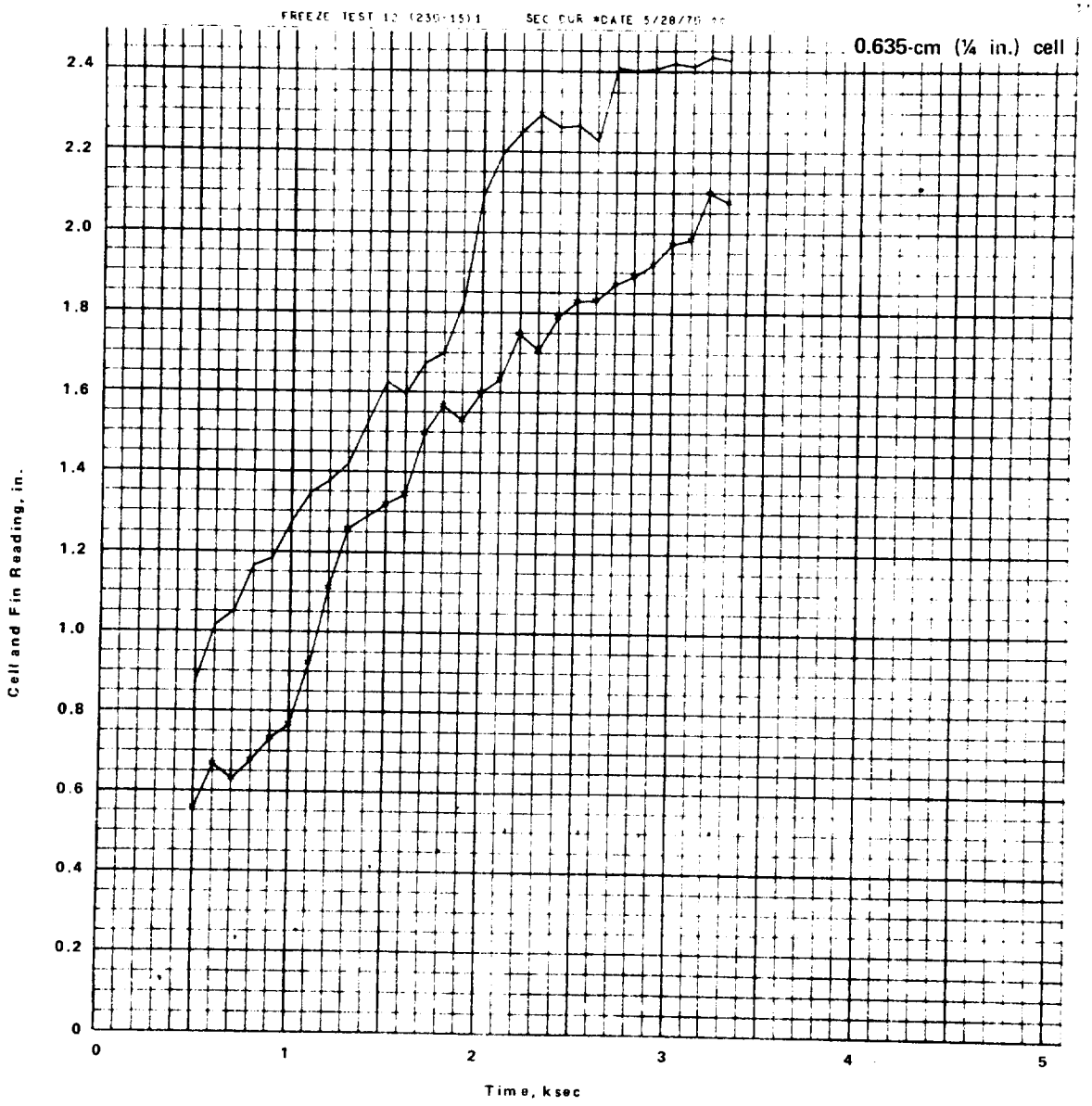

Figure D-30. Freeze front position data (test no. 230-15).

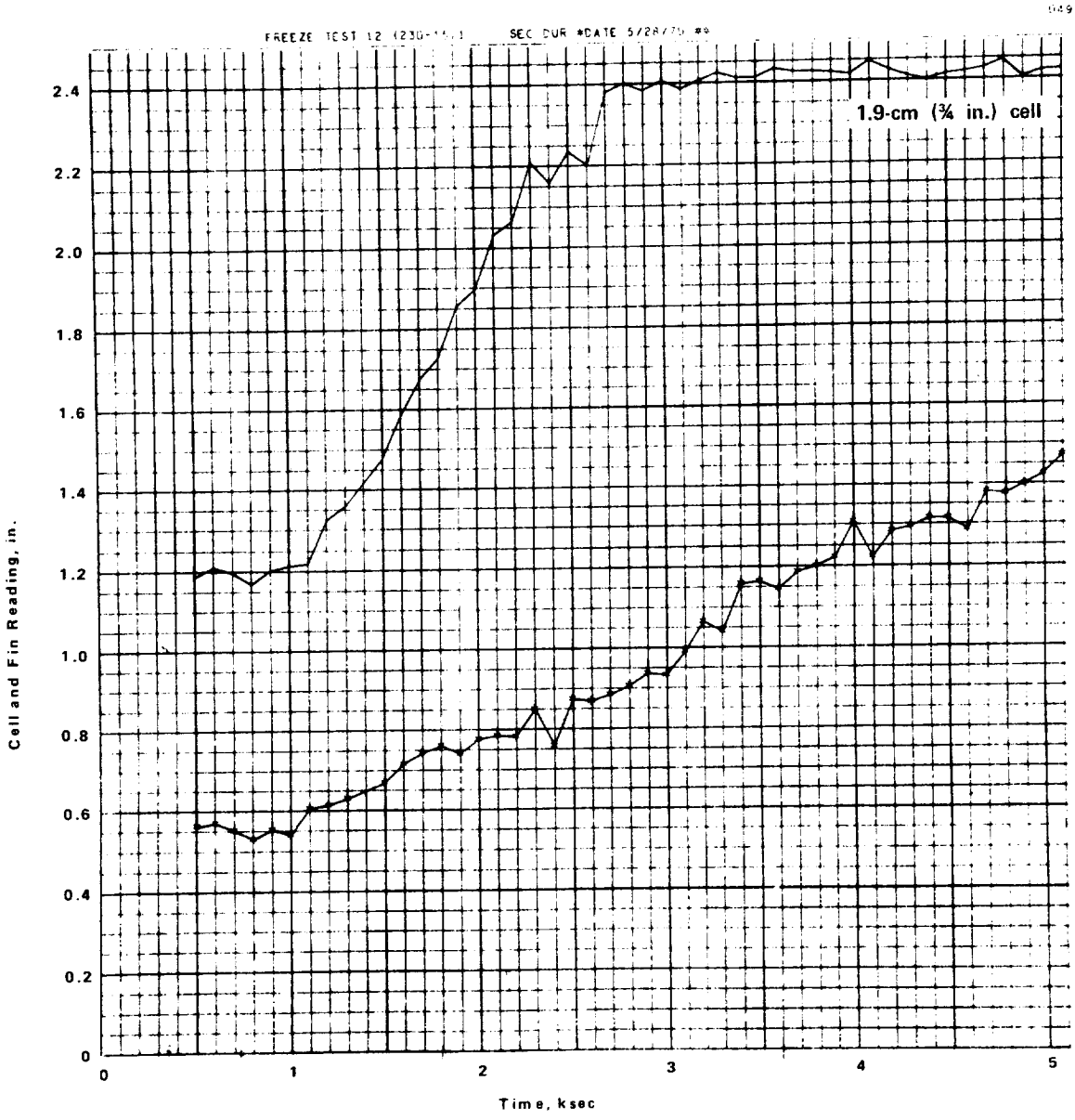

Figure D-31. Freeze front position data (test no. 230-15).

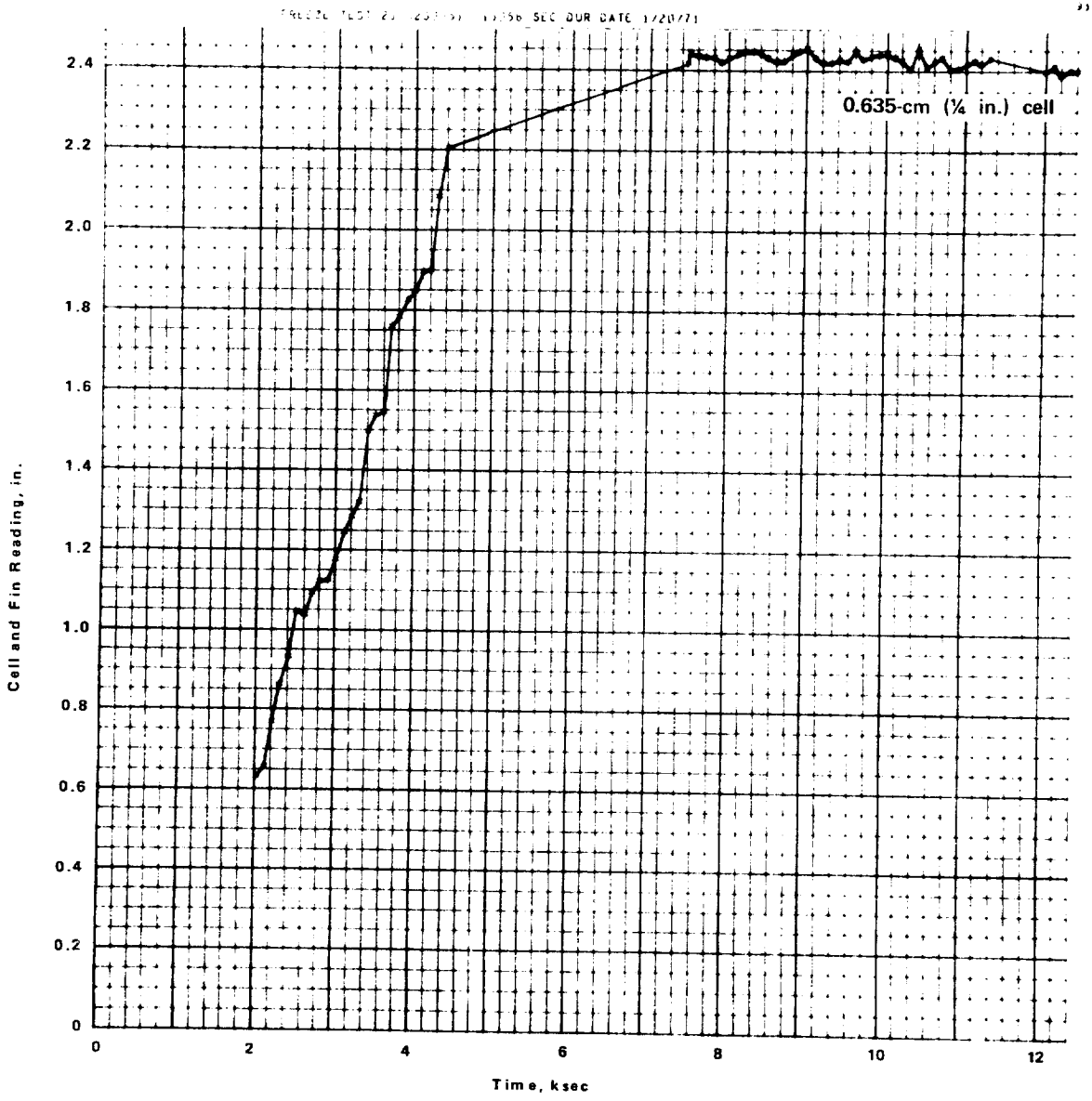

Figure D-32. Freeze front position data (test no. 230-51).

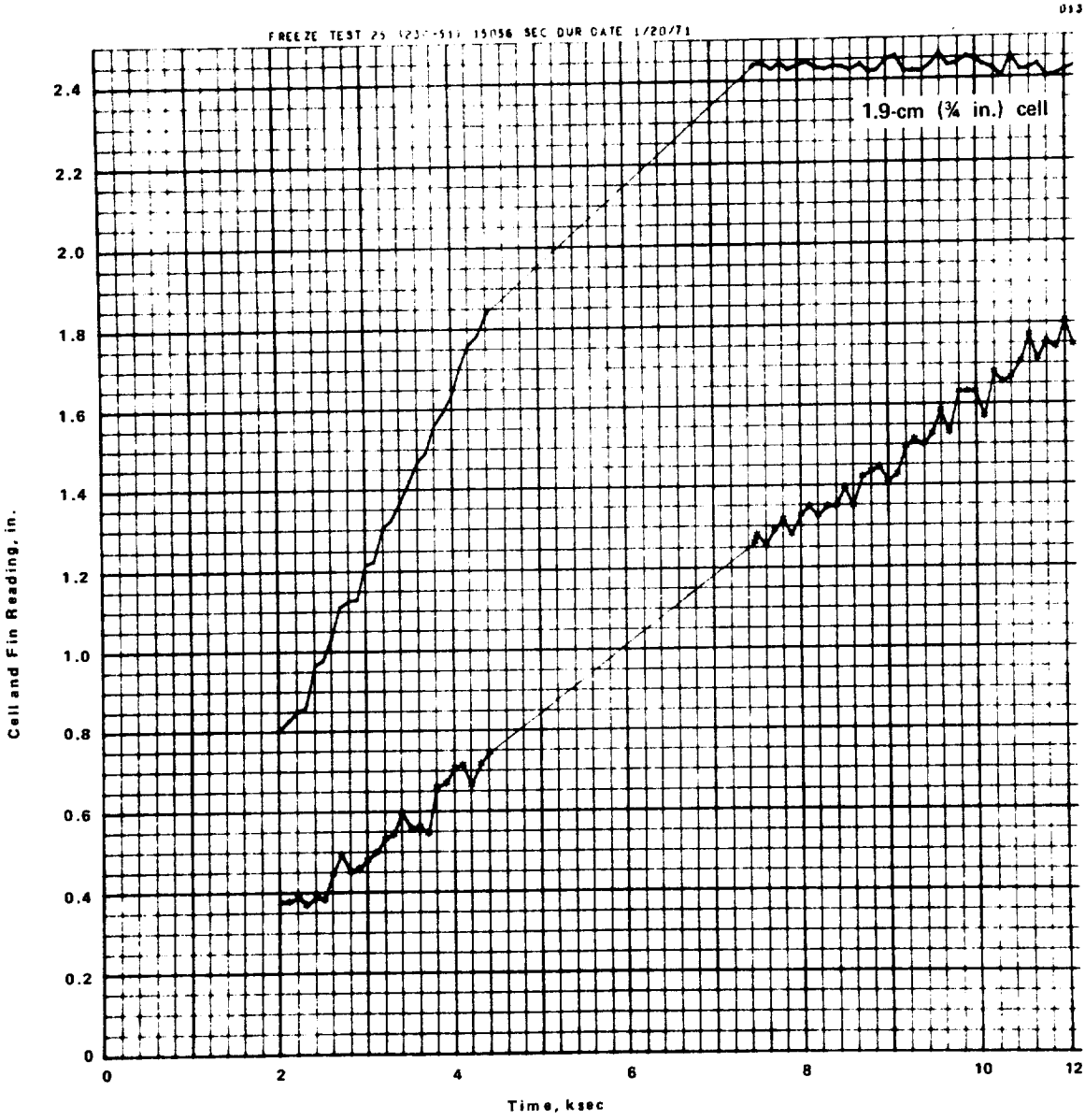

Figure D-33. Freeze front position data (test no. 230-51).

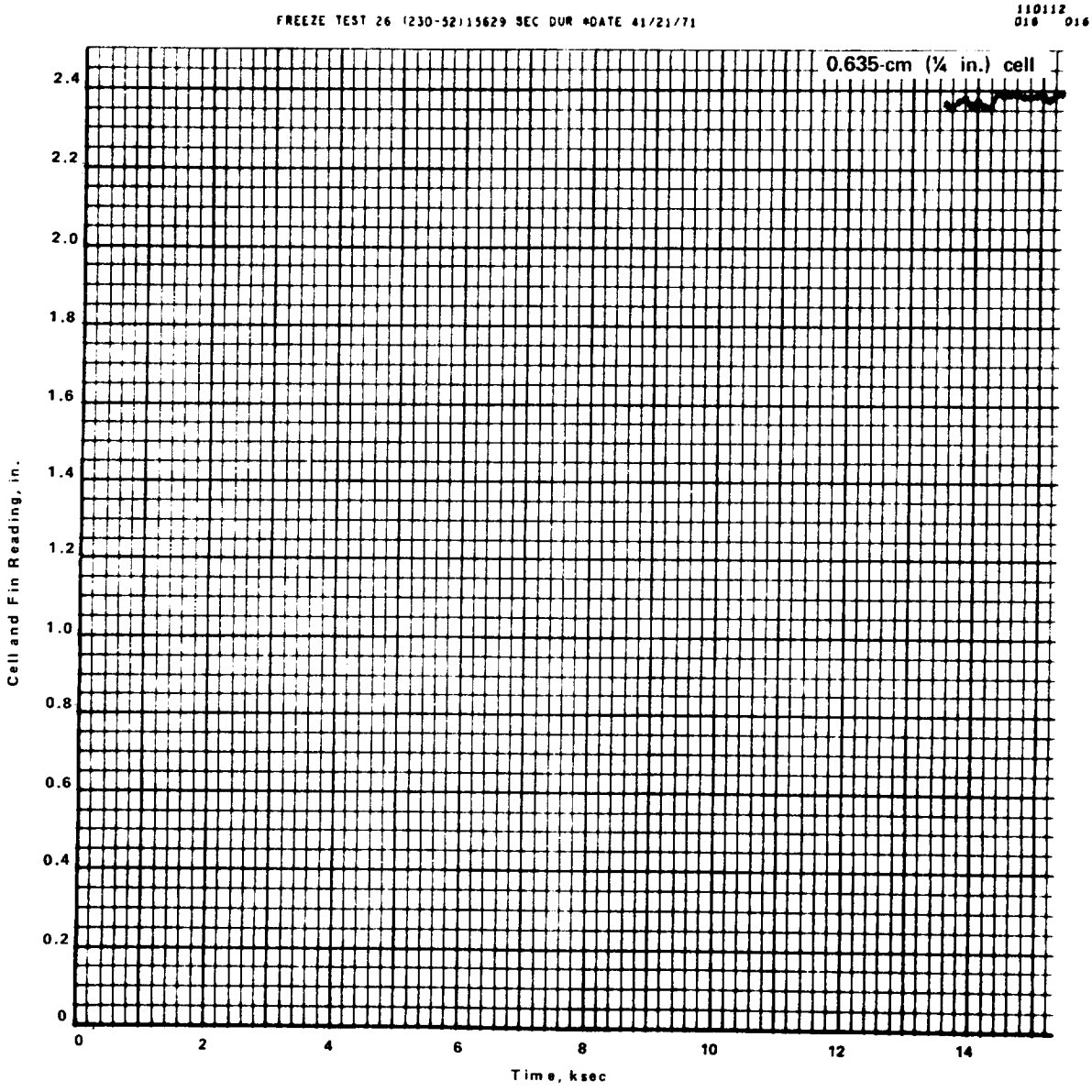

Figure D-34. Freeze front position data (test no. 230-52).

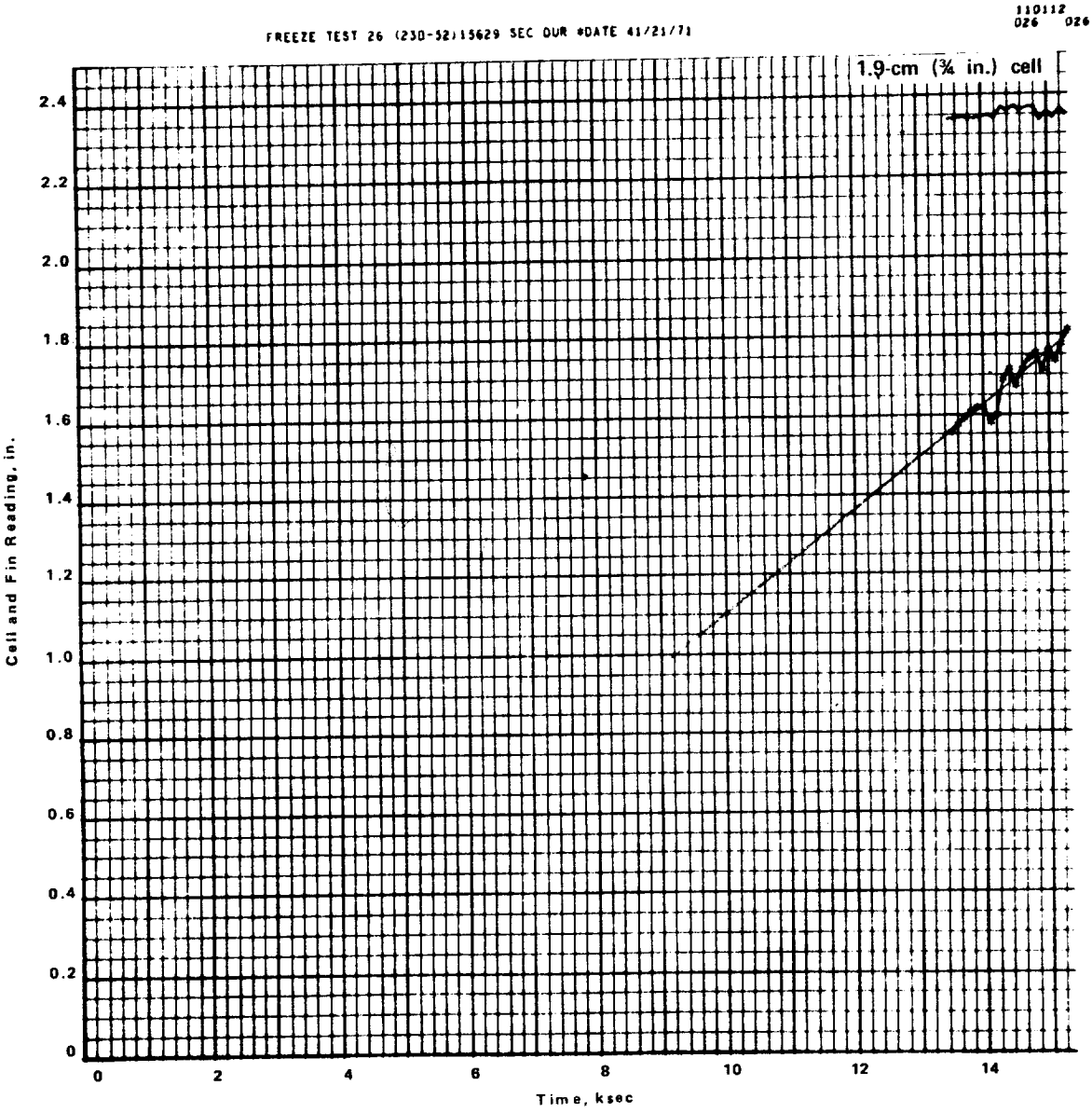

Figure D-35. Freeze front position data (test no. 230-52).

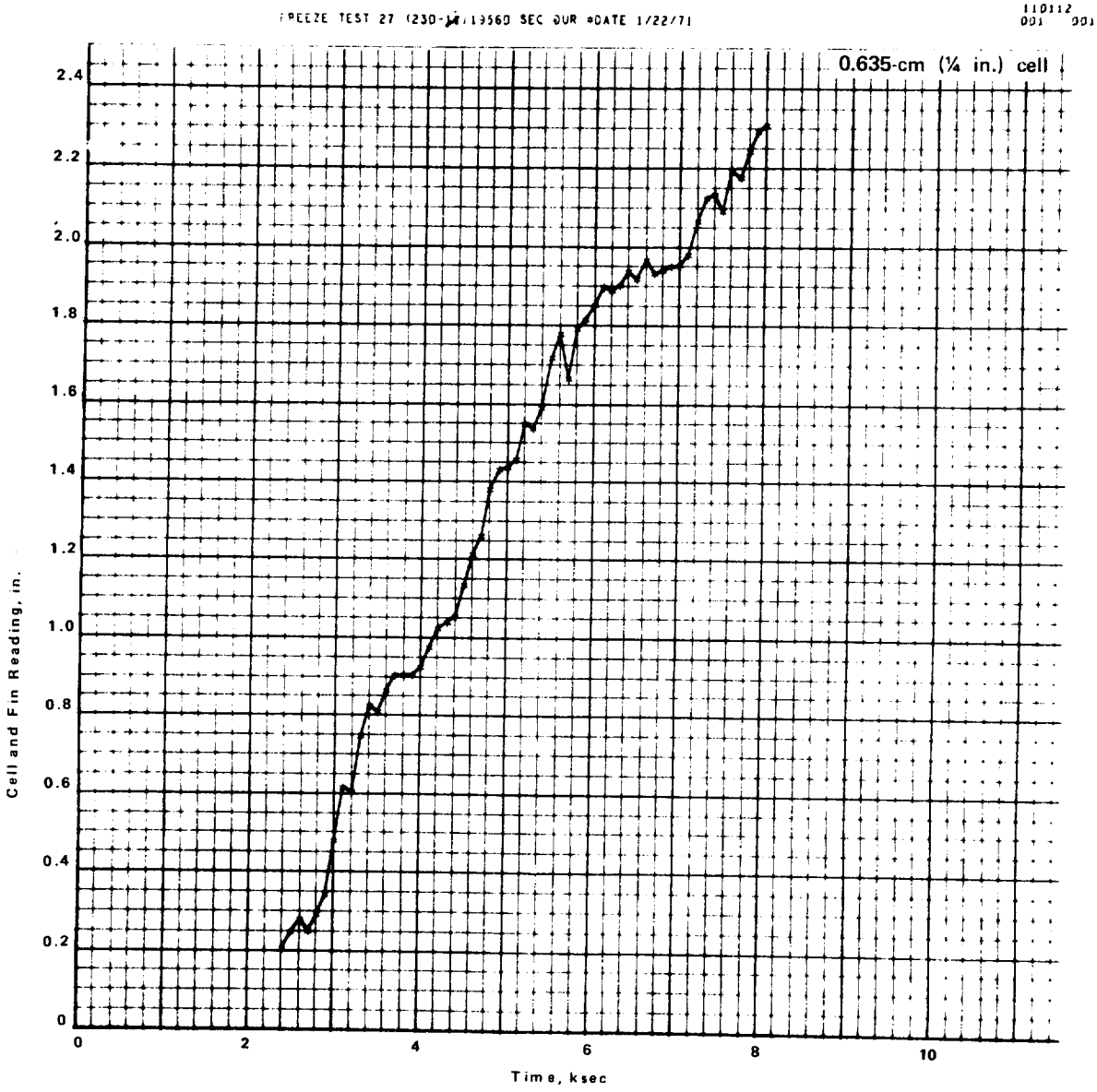

Figure D-36. Freeze front position data (test no. 230-57).

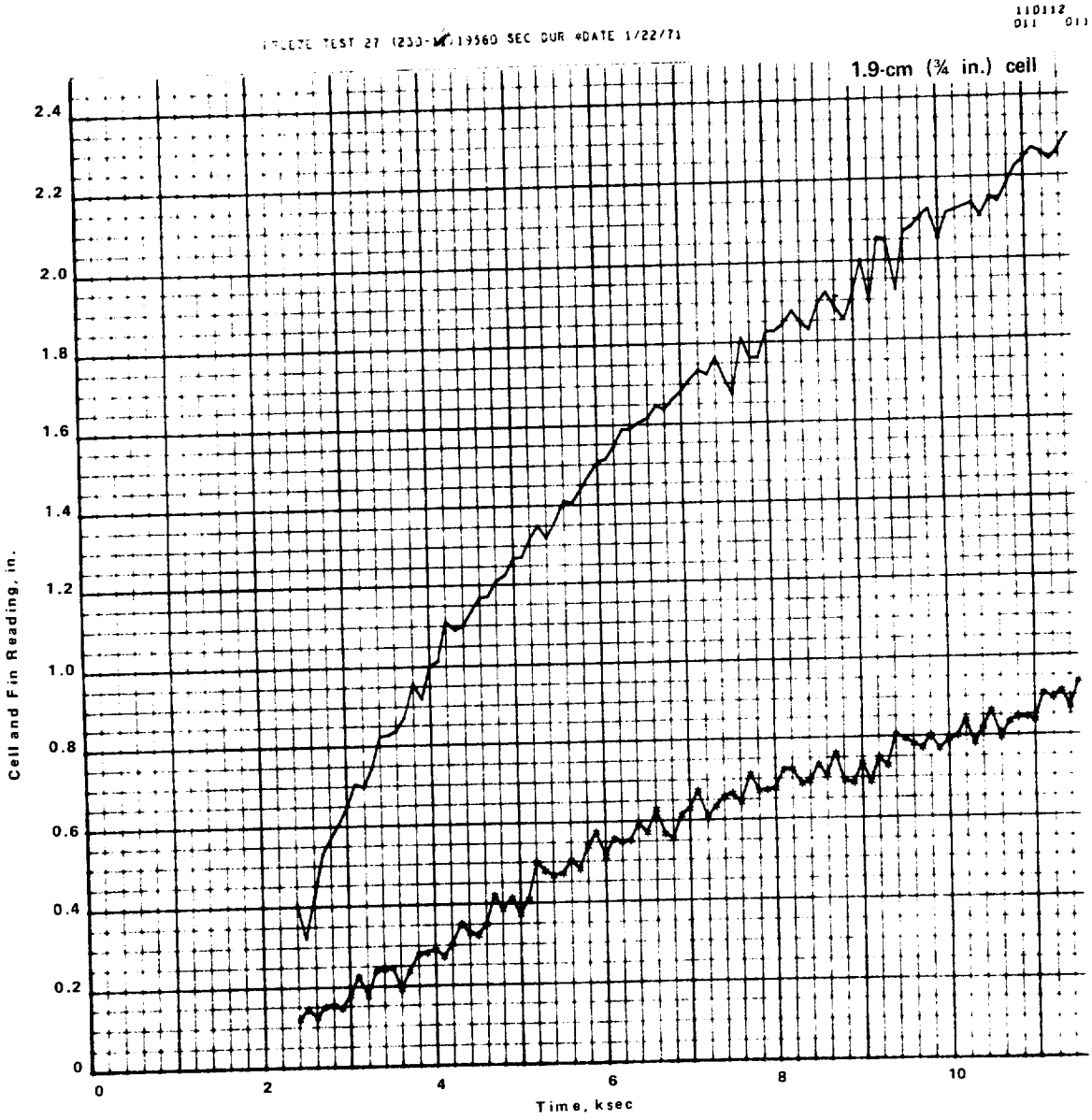

Figure D-37. Freeze front position data (test no. 230-57).

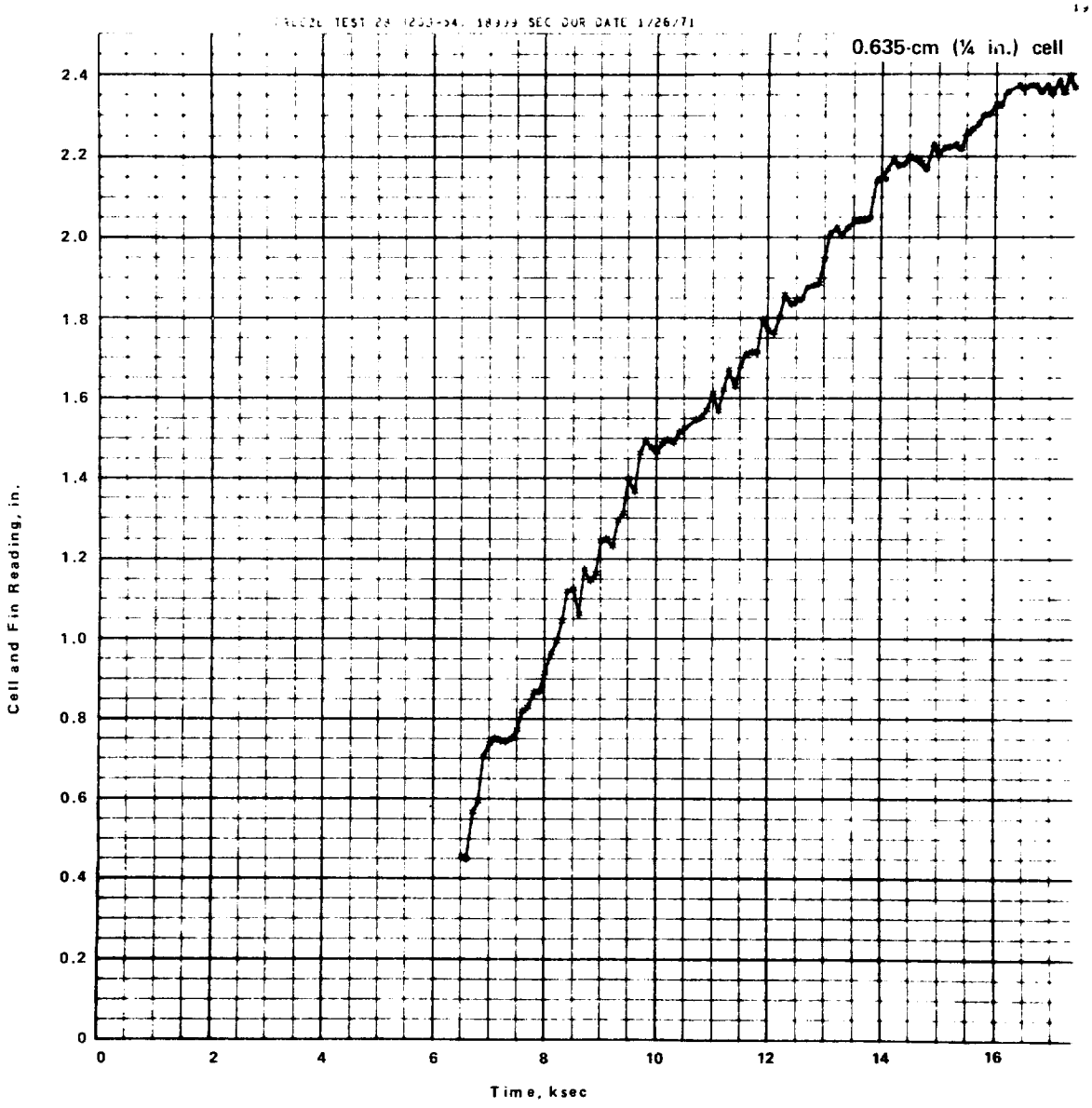

Figure D-38. Freeze front position data (test no. 230-54).

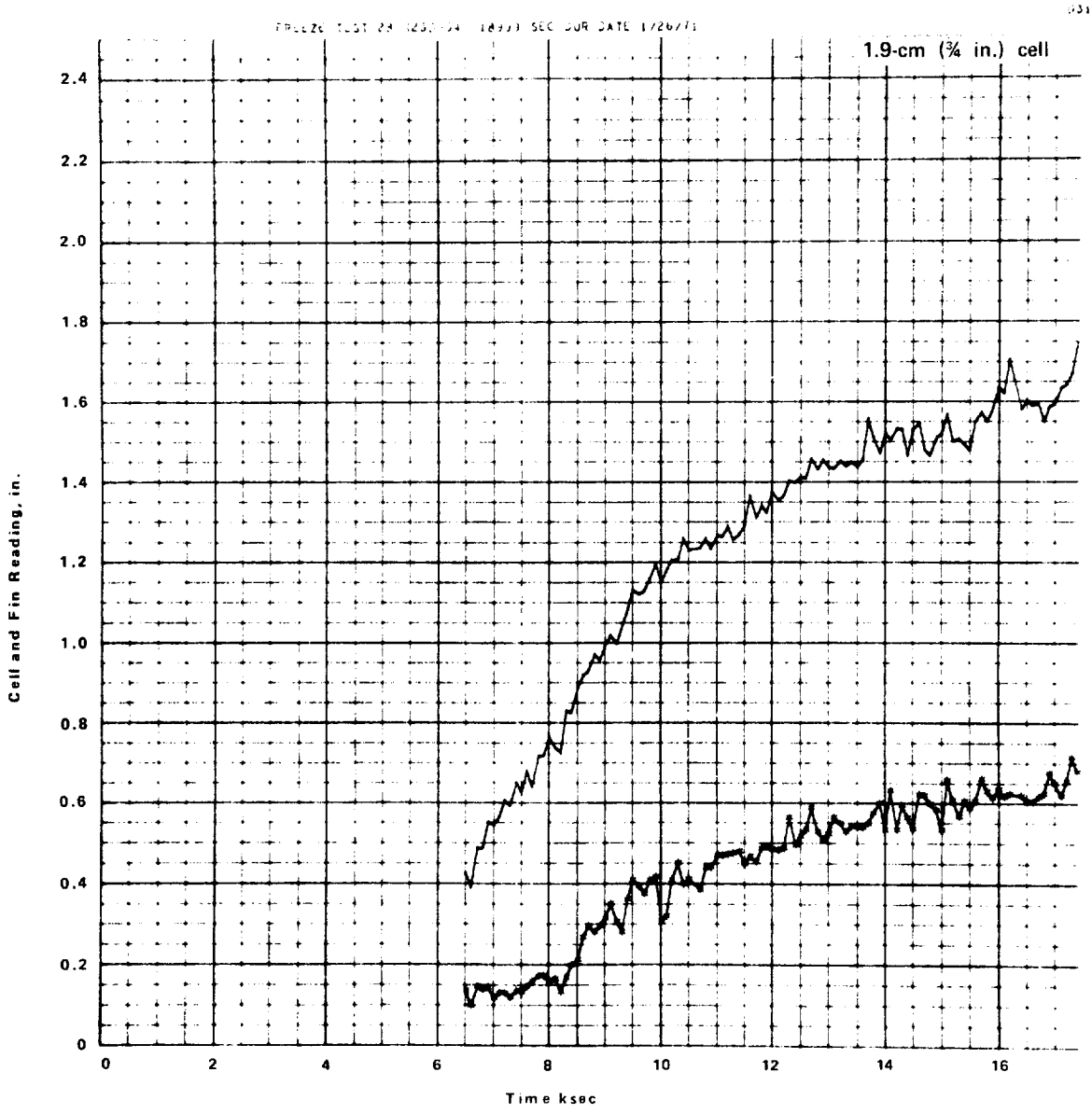

Figure D-39. Freeze front position data (test no. 230-54).

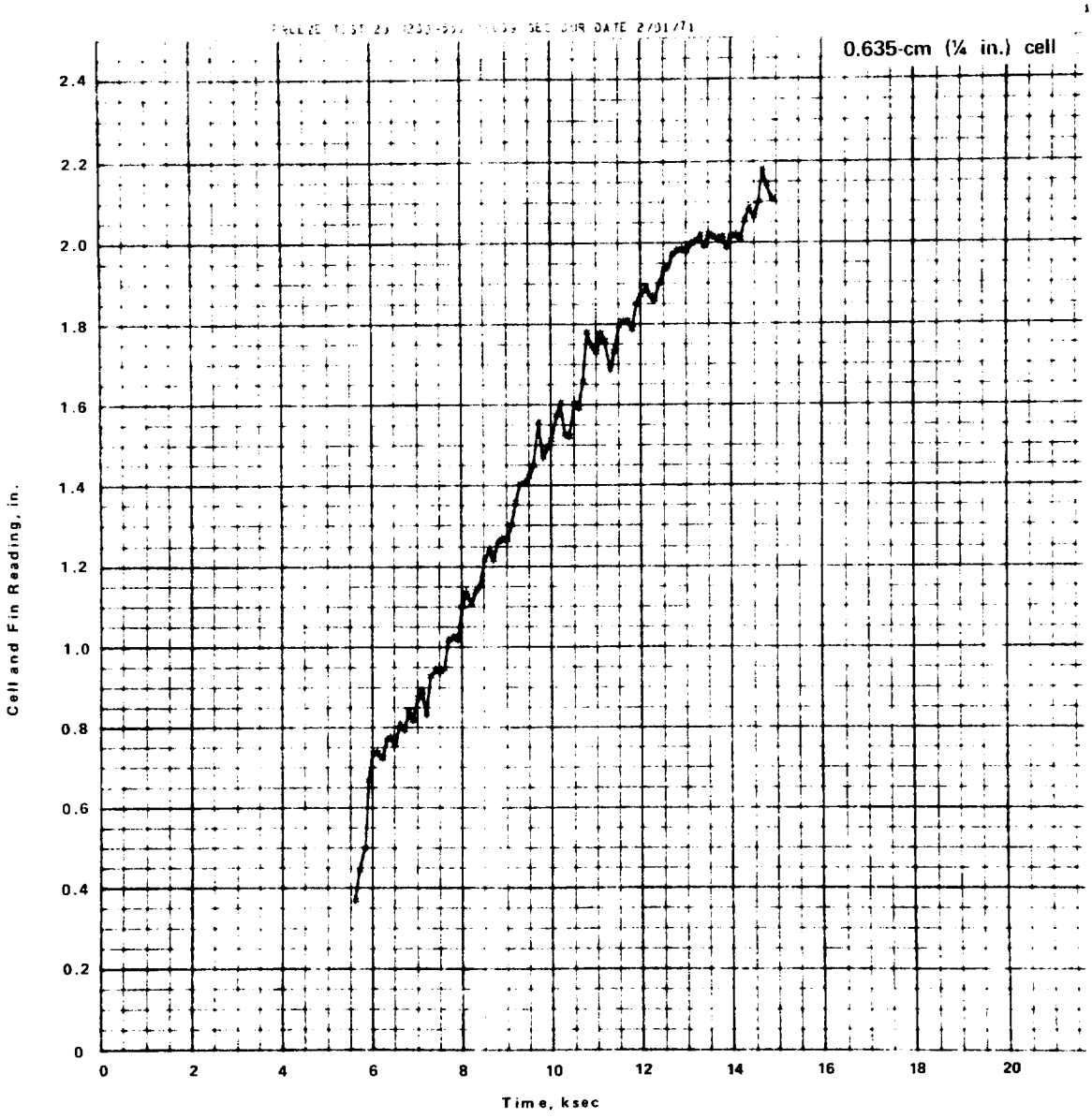

Figure D-40. Freeze front position data (test no. 230-55).

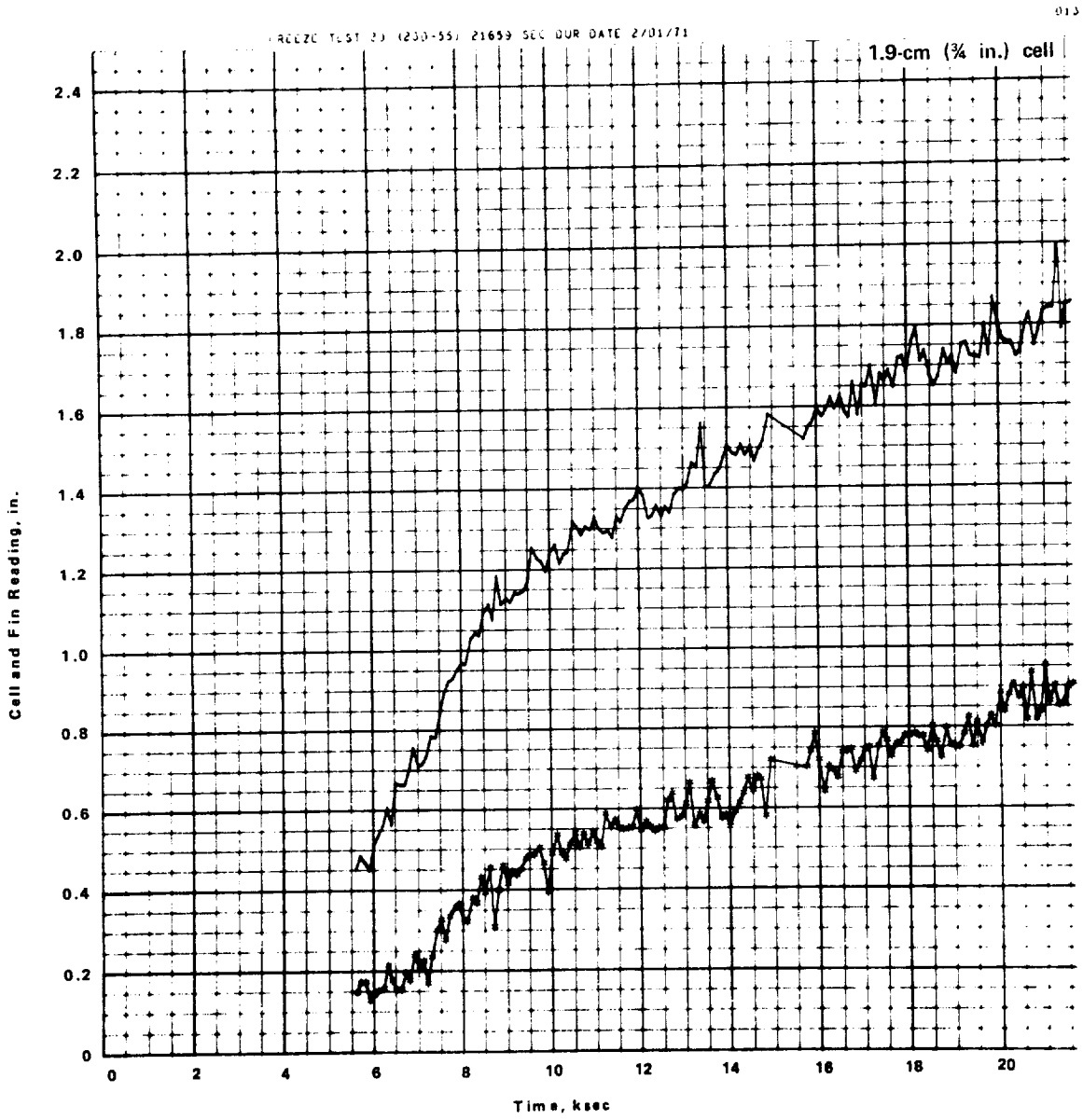

Figure D-41. Freeze front position data (test no. 230-55).

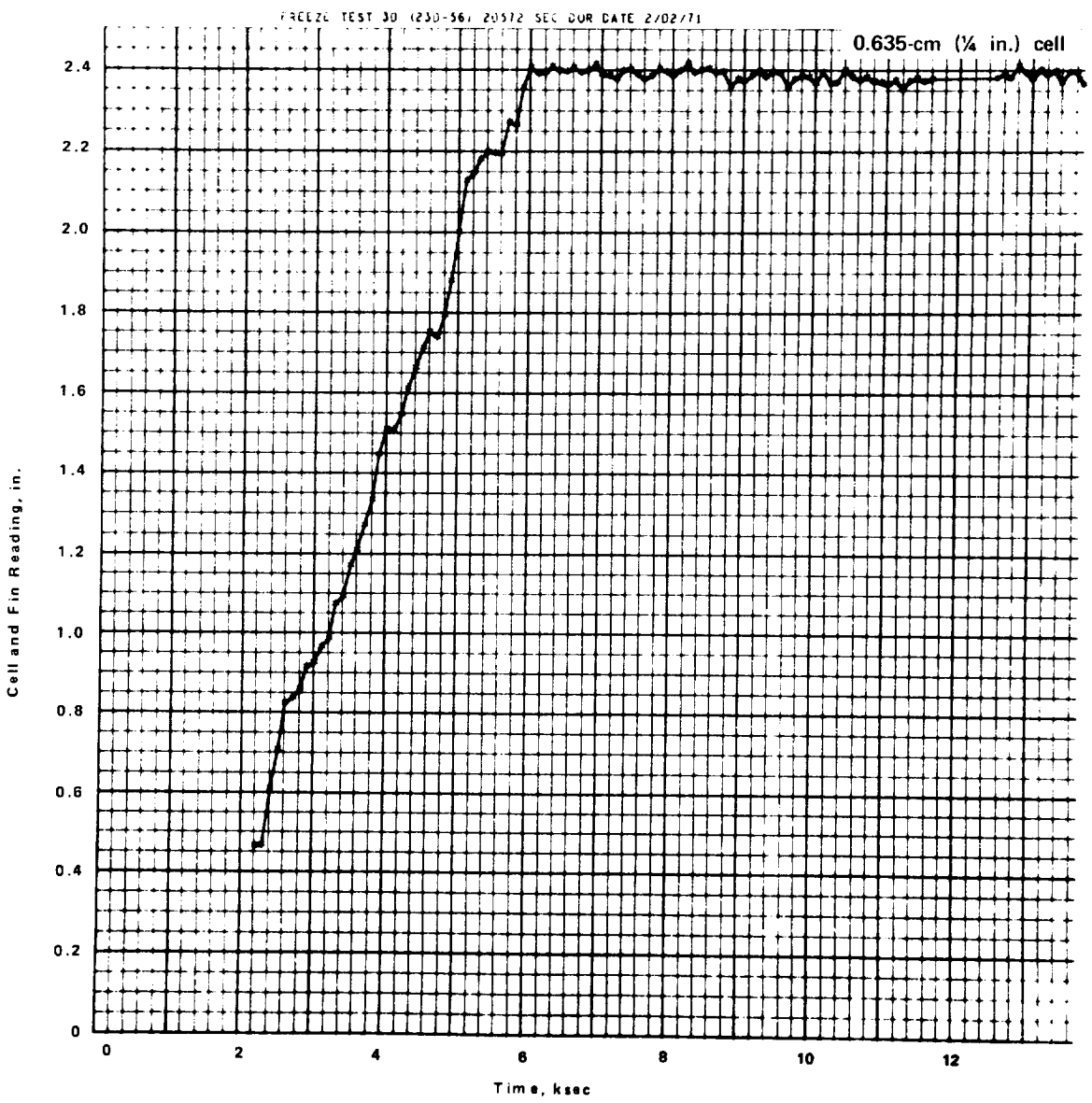

Figure D-42. Freeze front position data (test no. 230-56).

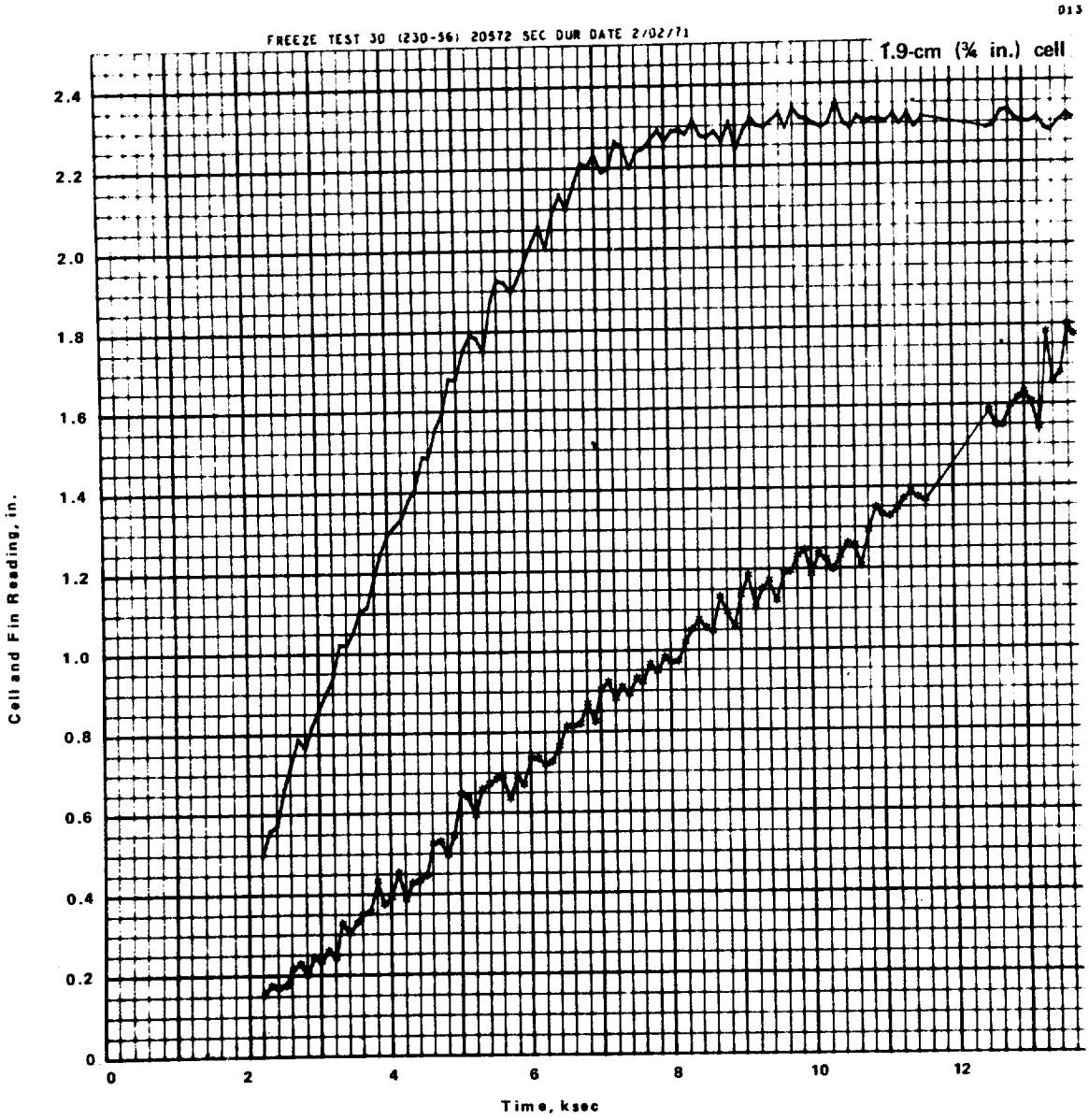

Figure D-43. Freeze front position data (test no. 230-56).

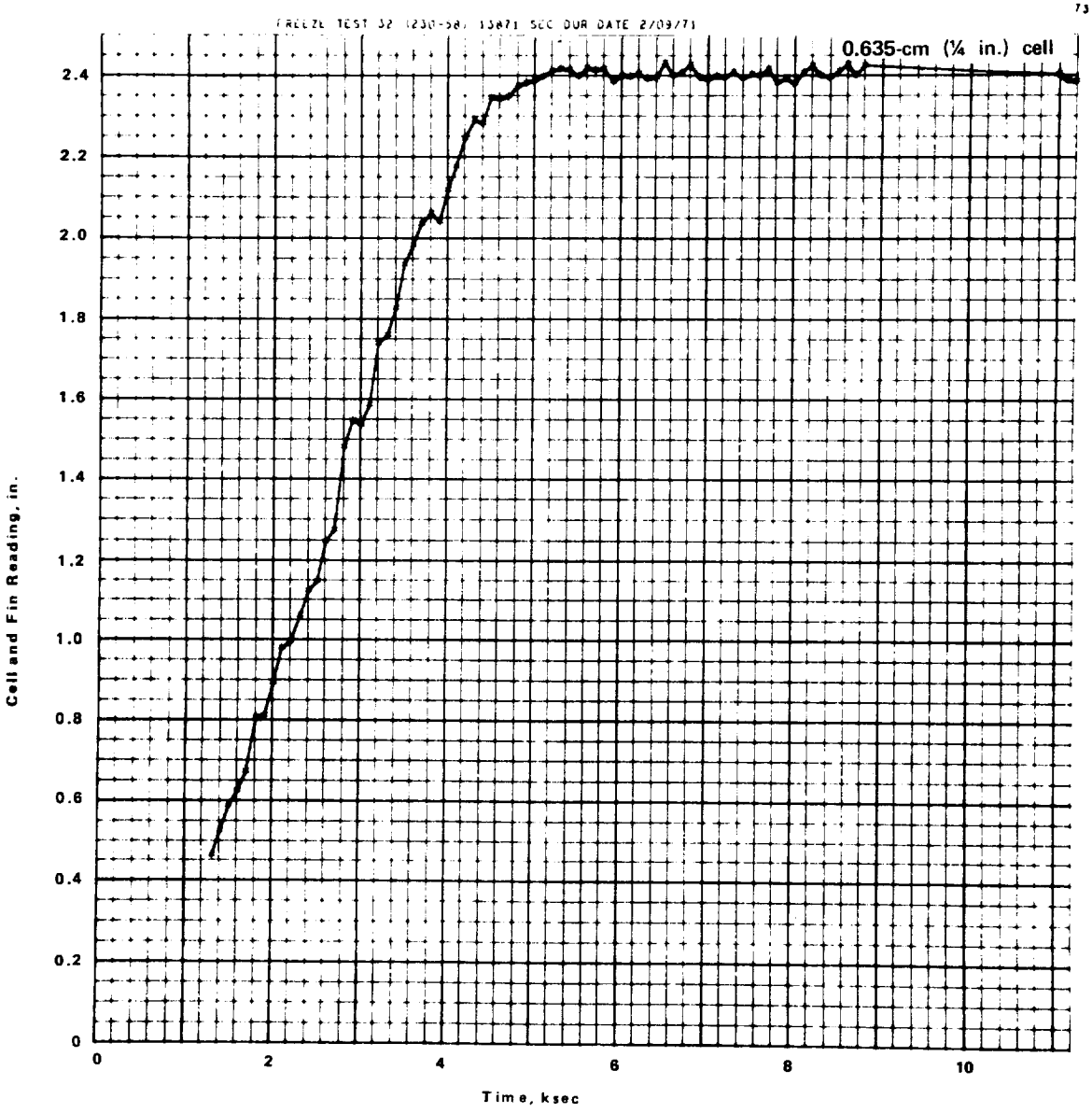

Figure D-44. Freeze front position data (test no. 230-58).

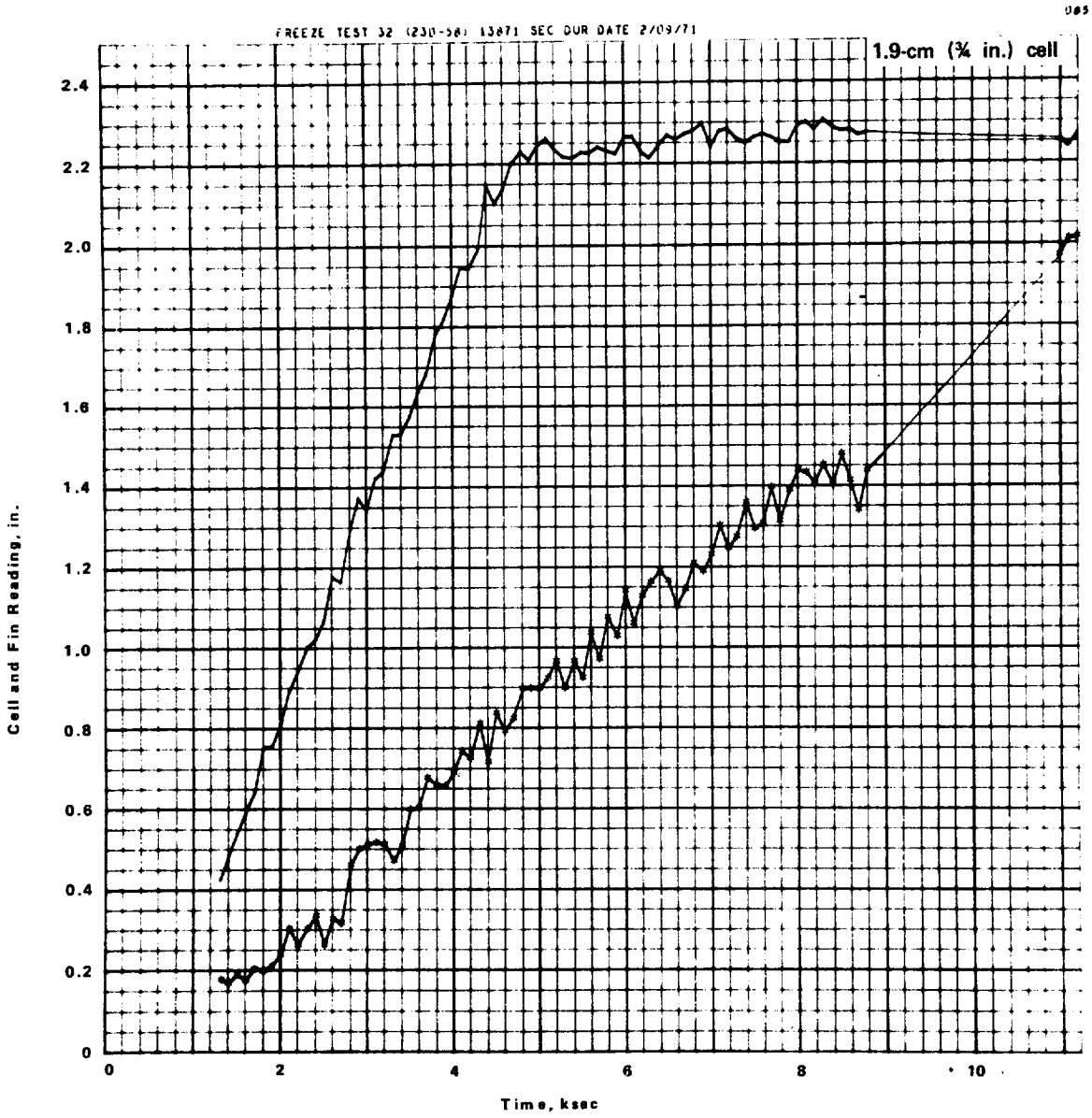

Figure D-45. Freeze front position data (test no. 230-58).

SECTION III

MELT TEMPERATURE DATA FOR FINNED THERMAL CAPACITORS

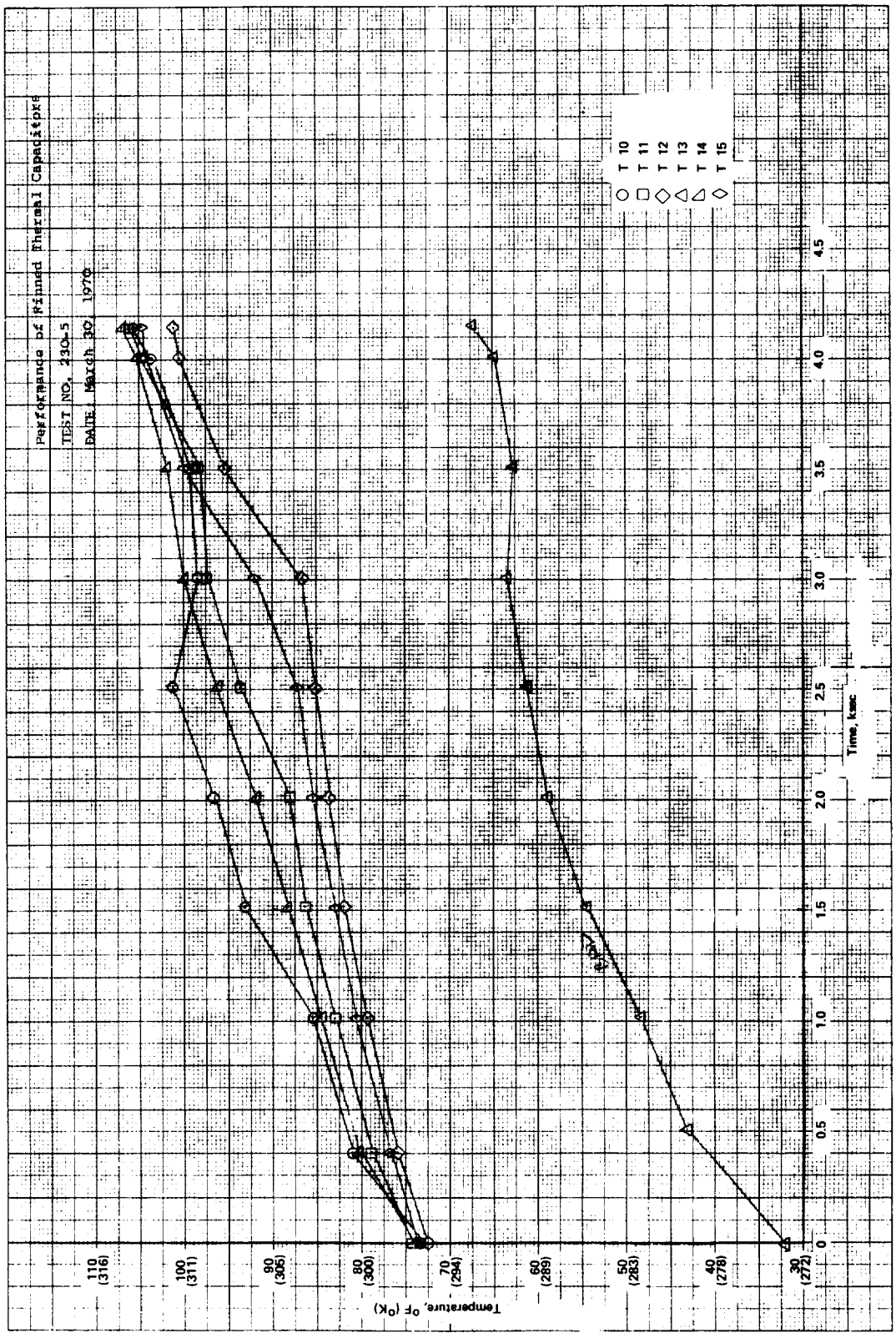

Figure D-46. Melt temperature data for finned thermal capacitor (test no. 230-5).

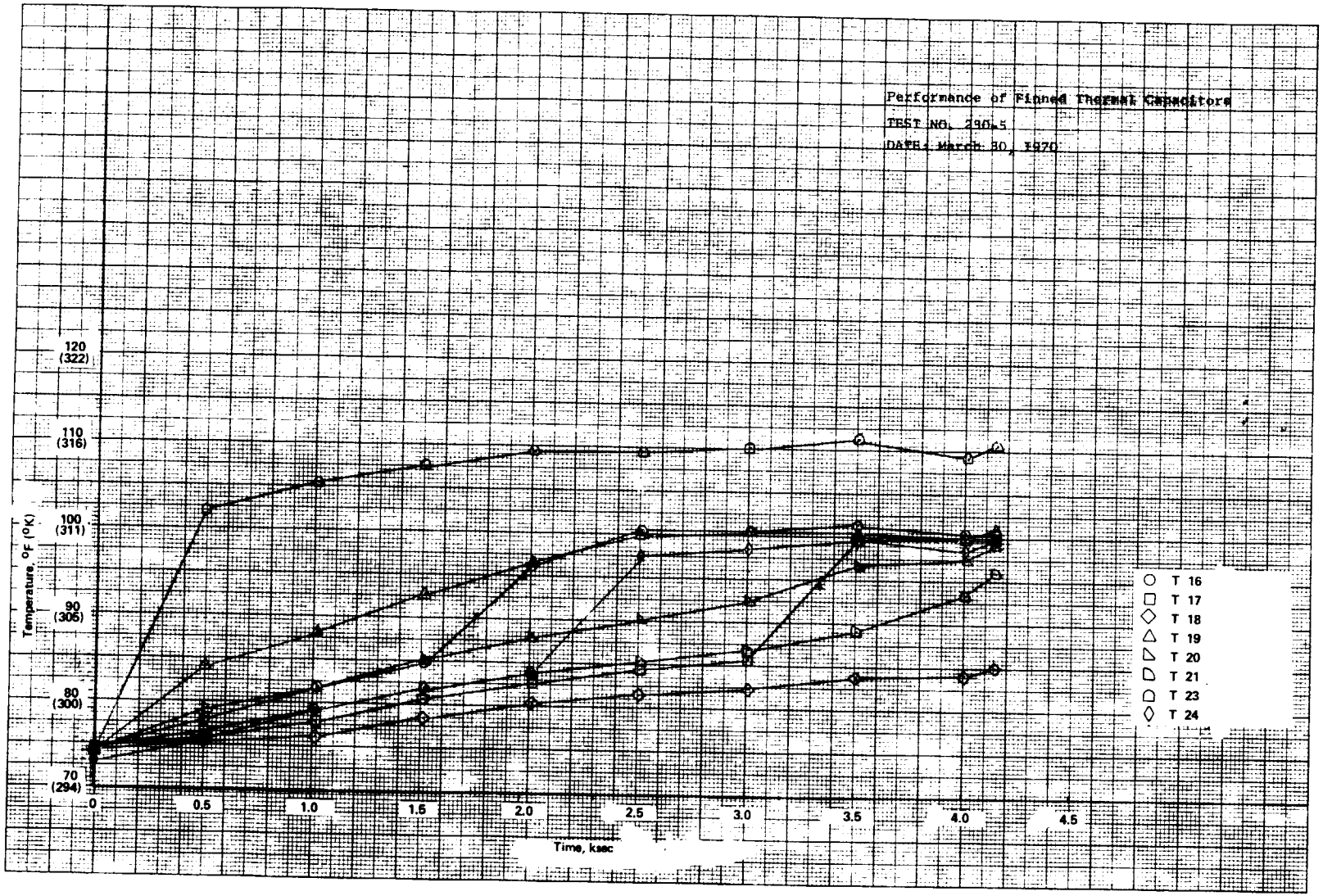

Figure D-47. Melt temperature data for finned thermal capacitor (test no. 230-5).

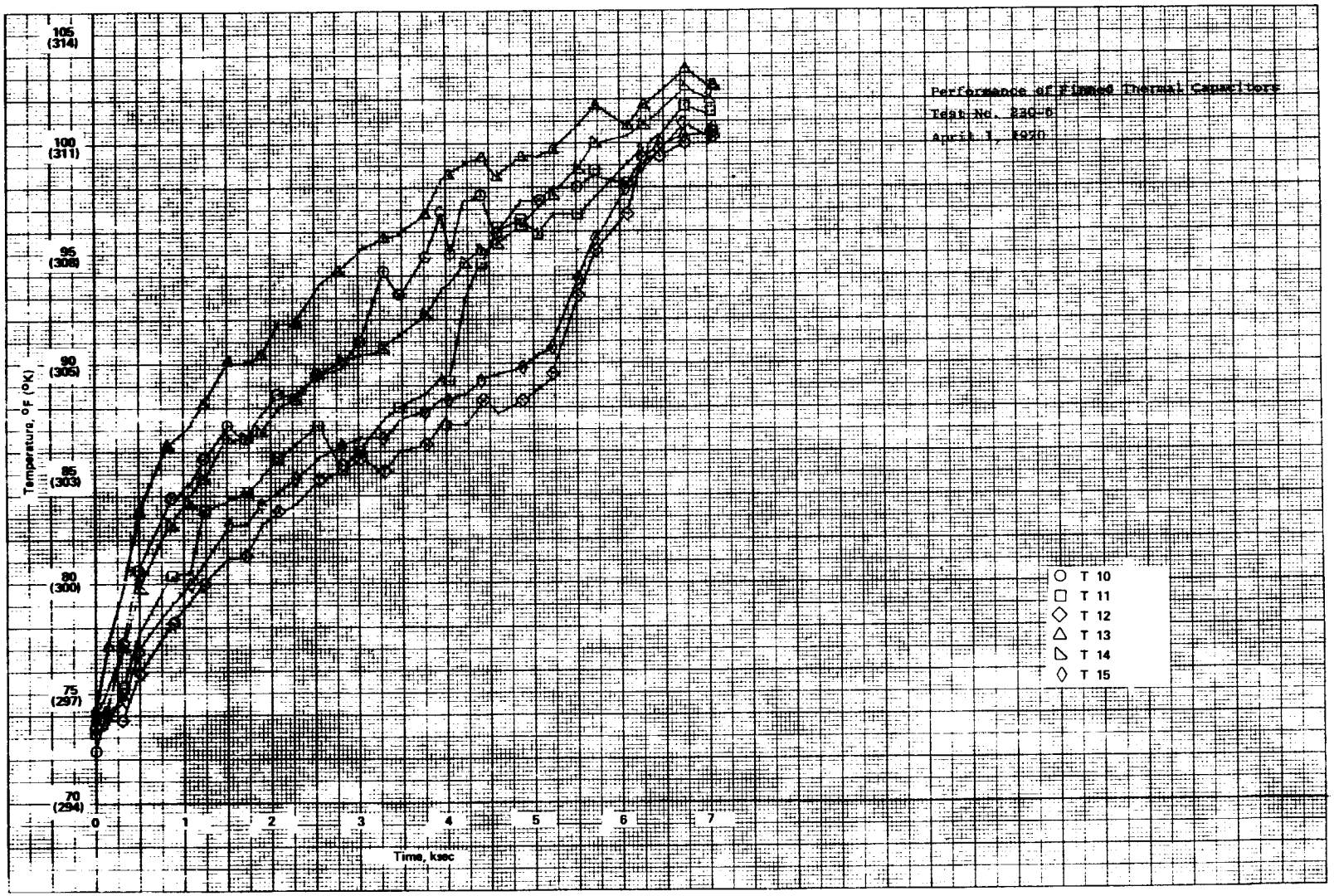

Figure D-48. Melt temperature data for finned thermal capacitor (test no. 230-6).

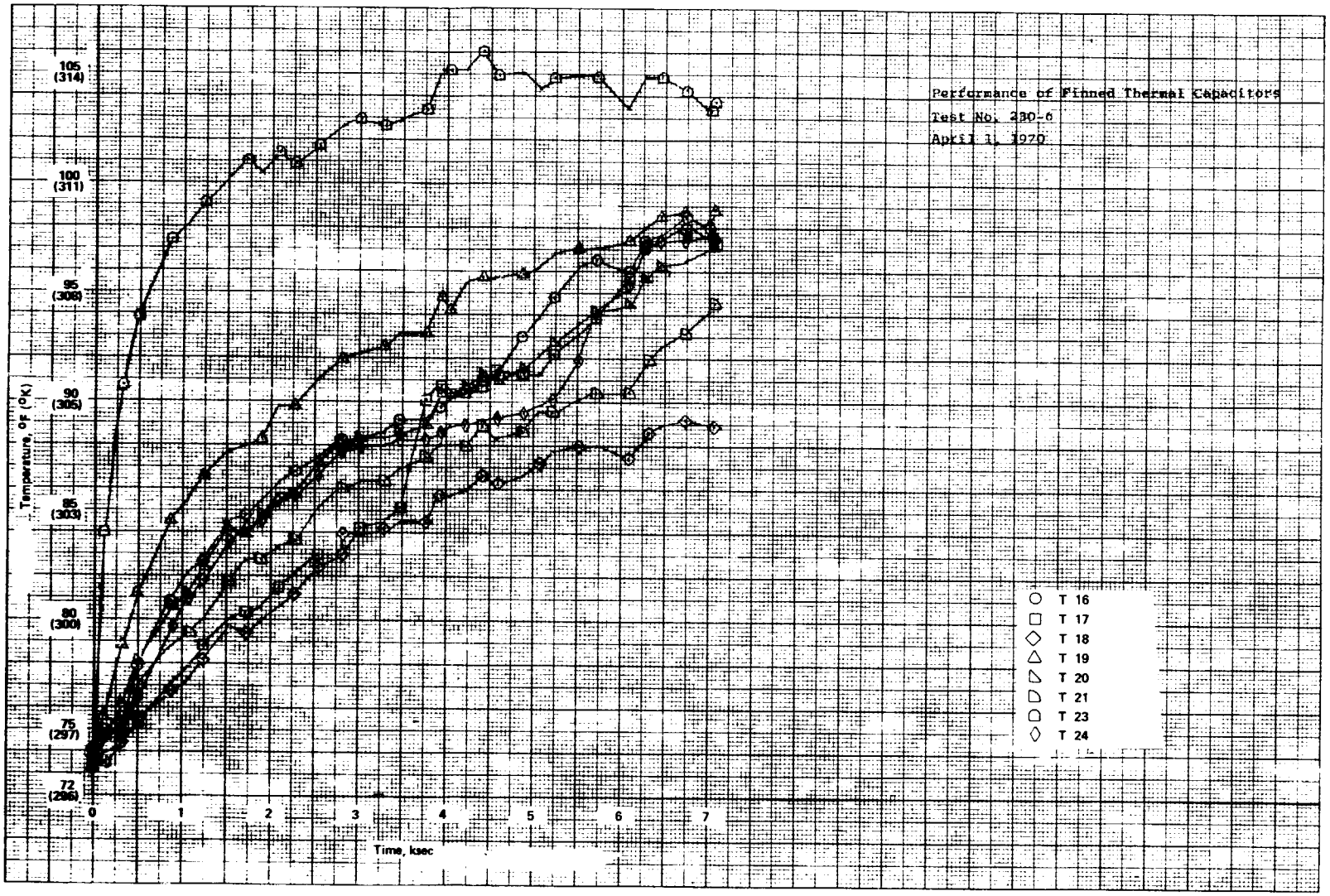

Figure D-49. Melt temperature data for finned thermal capacitor (test no. 230-6).

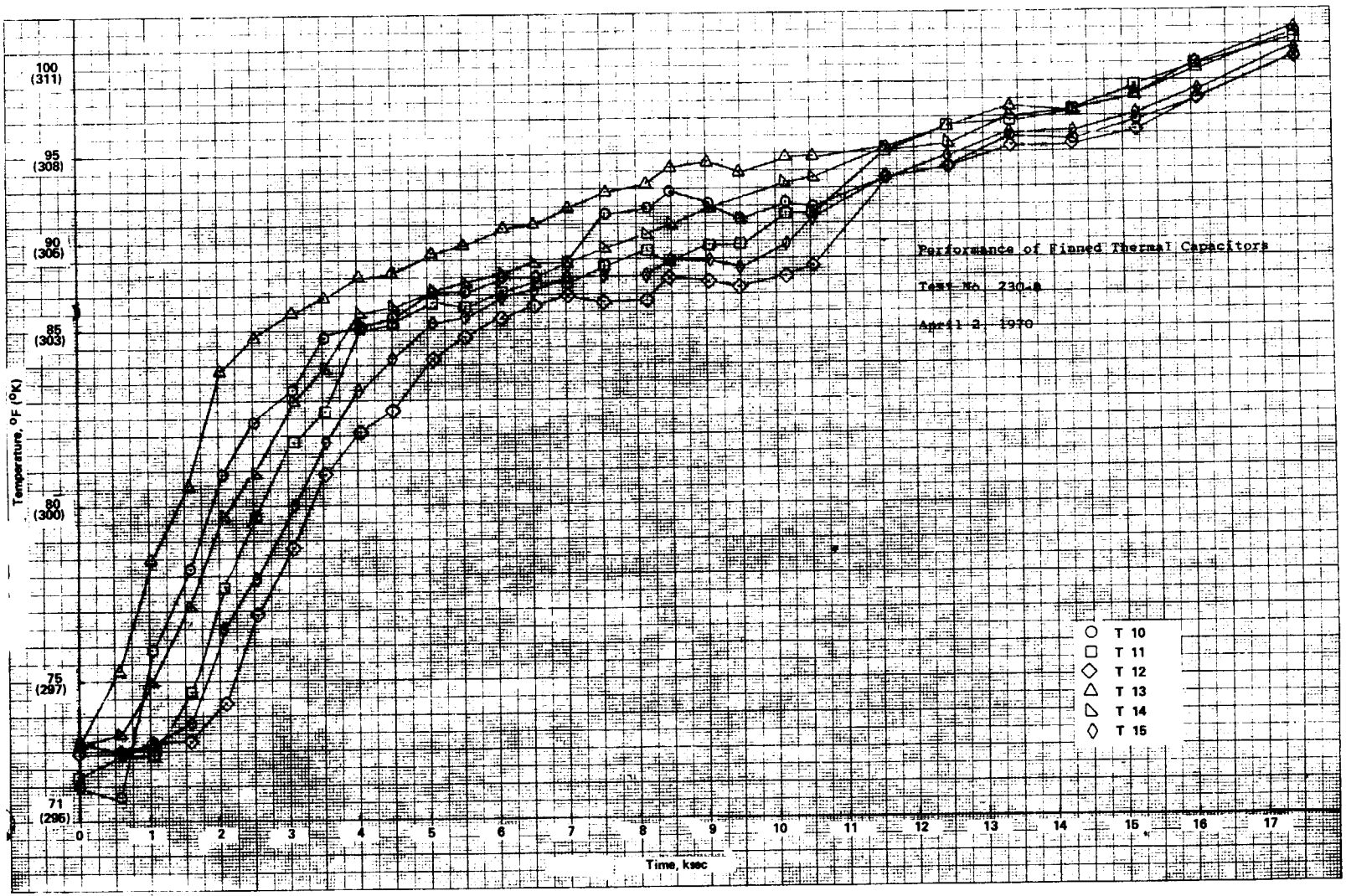

Figure D-50. Melt temperature data for finned thermal capacitor (test no. 230-8).

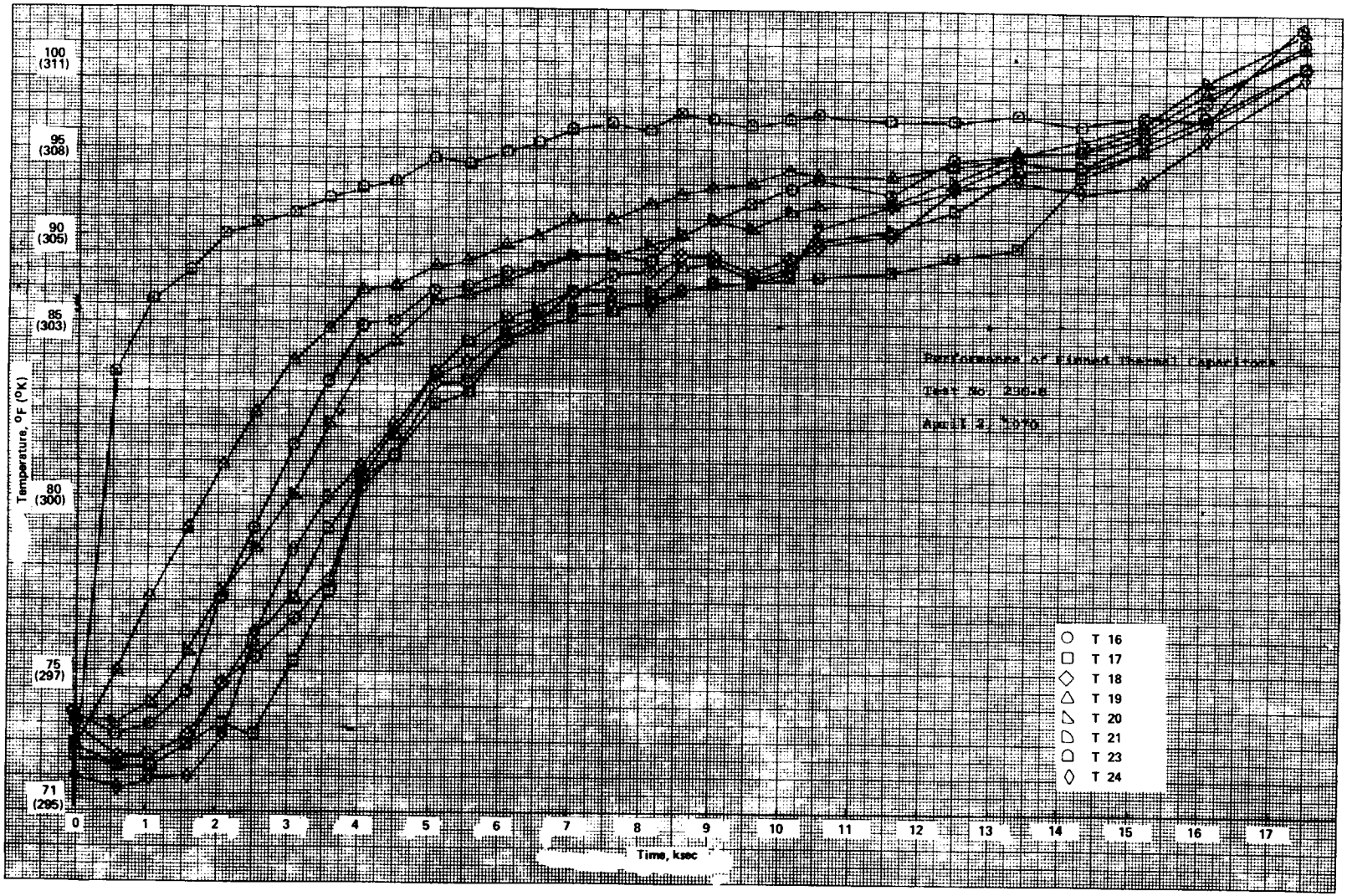

Figure D-51. Melt temperature data for finned thermal capacitor (test no. 230-8).

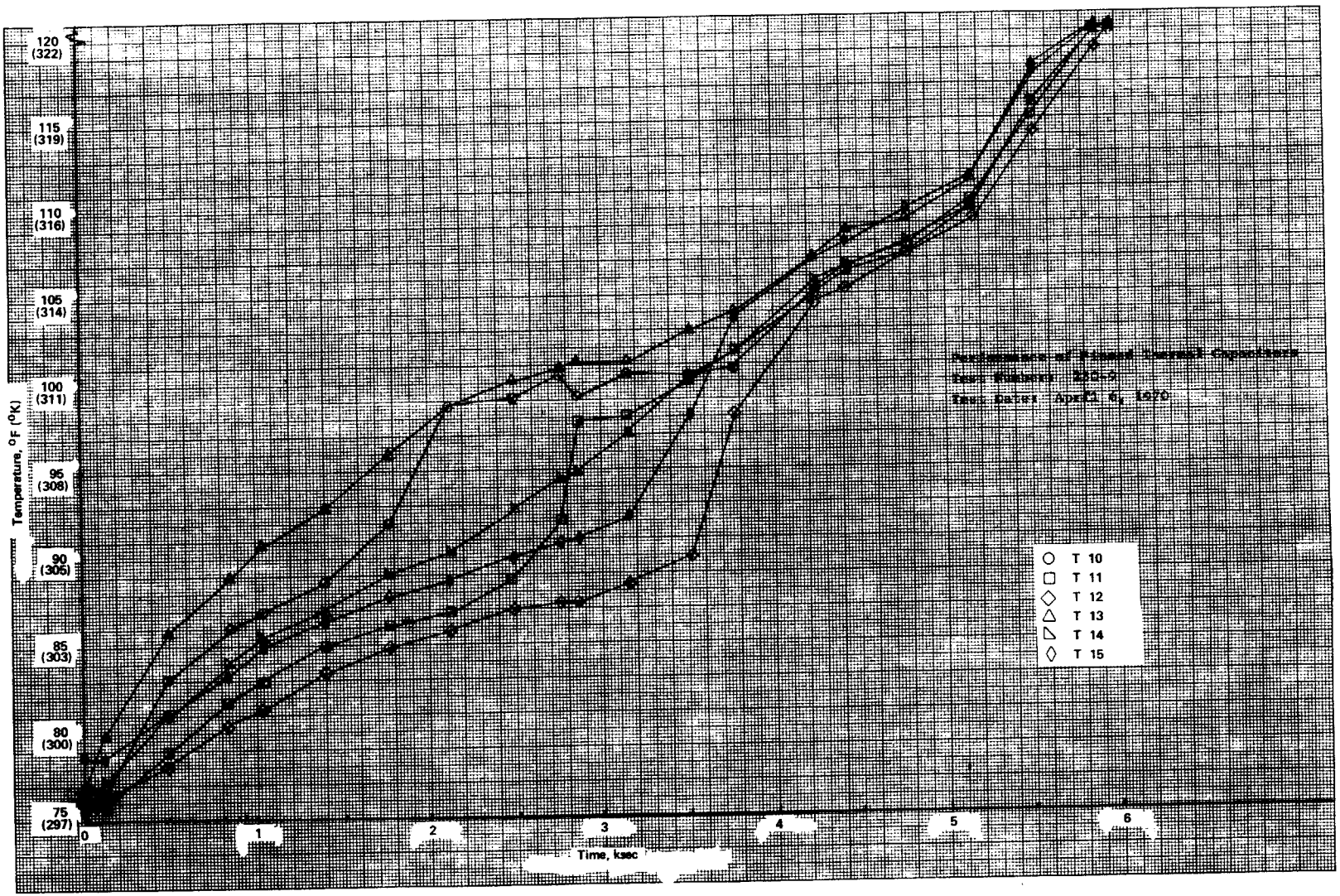

Figure D-52. Melt temperature data for finned thermal capacitor (test no. 230-9).

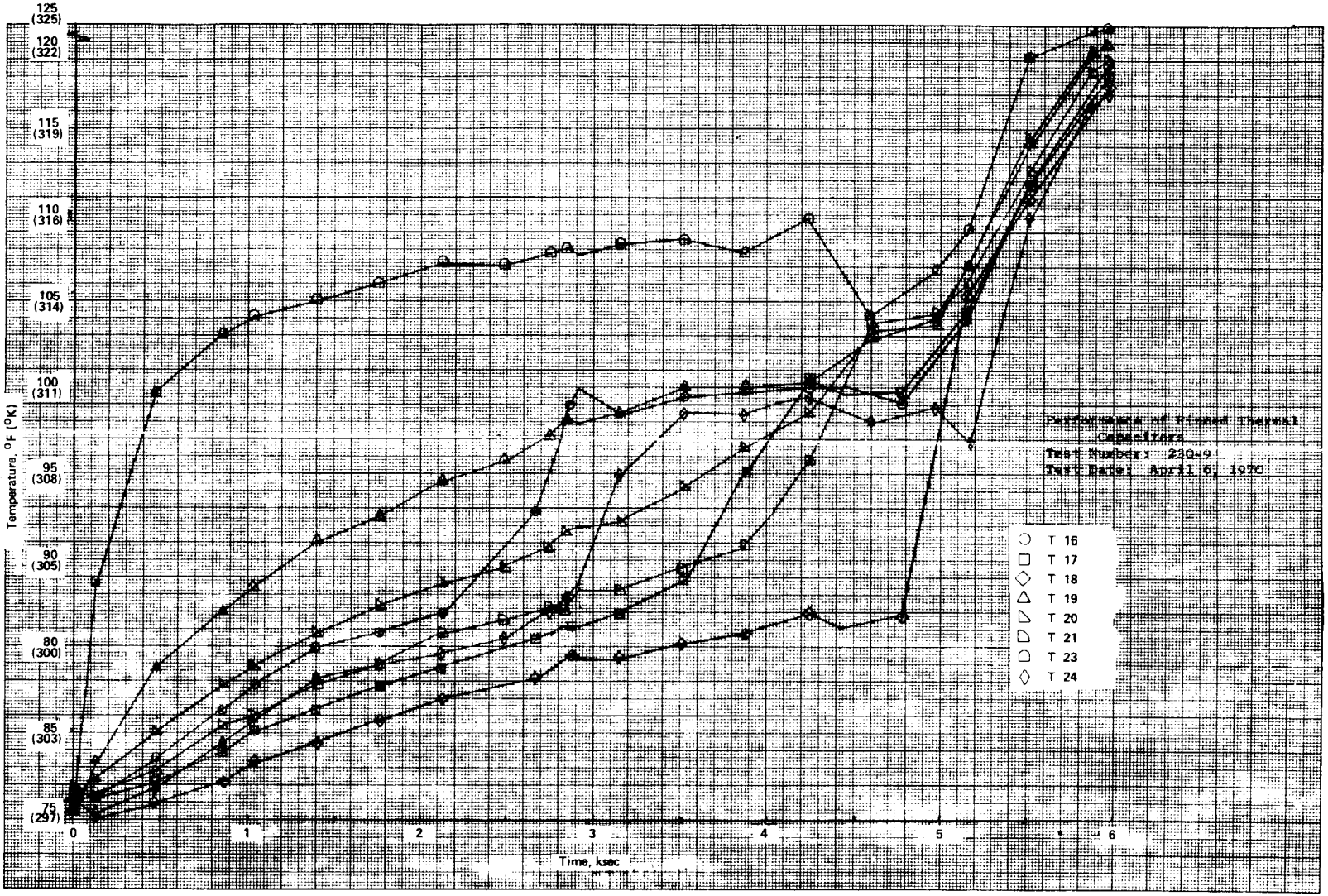

Figure D-53. Melt temperature data for finned thermal capacitor (test no. 230-9).

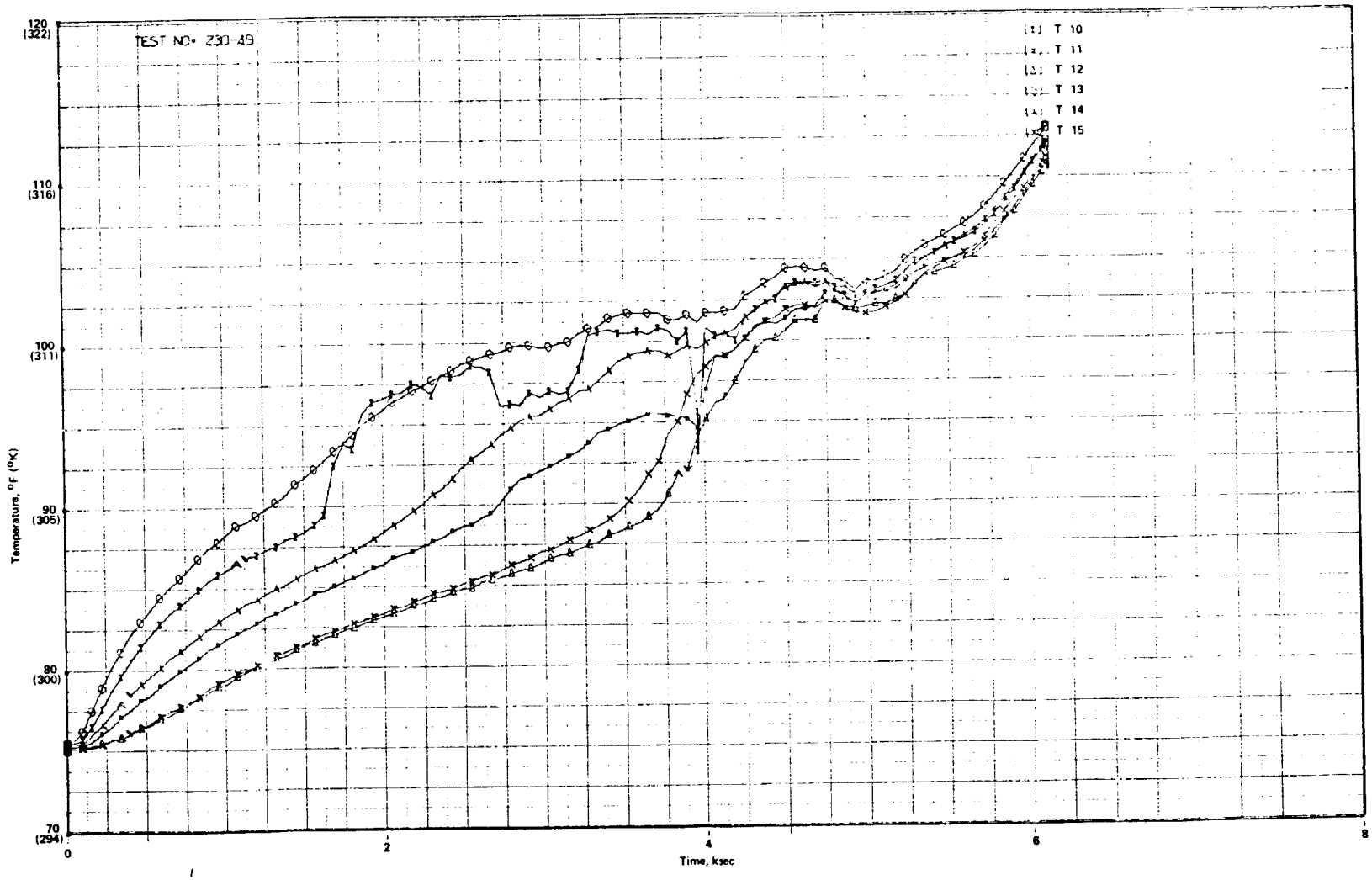

Figure D-54. Melt temperature data for finned thermal capacitor (test no. 230-49).

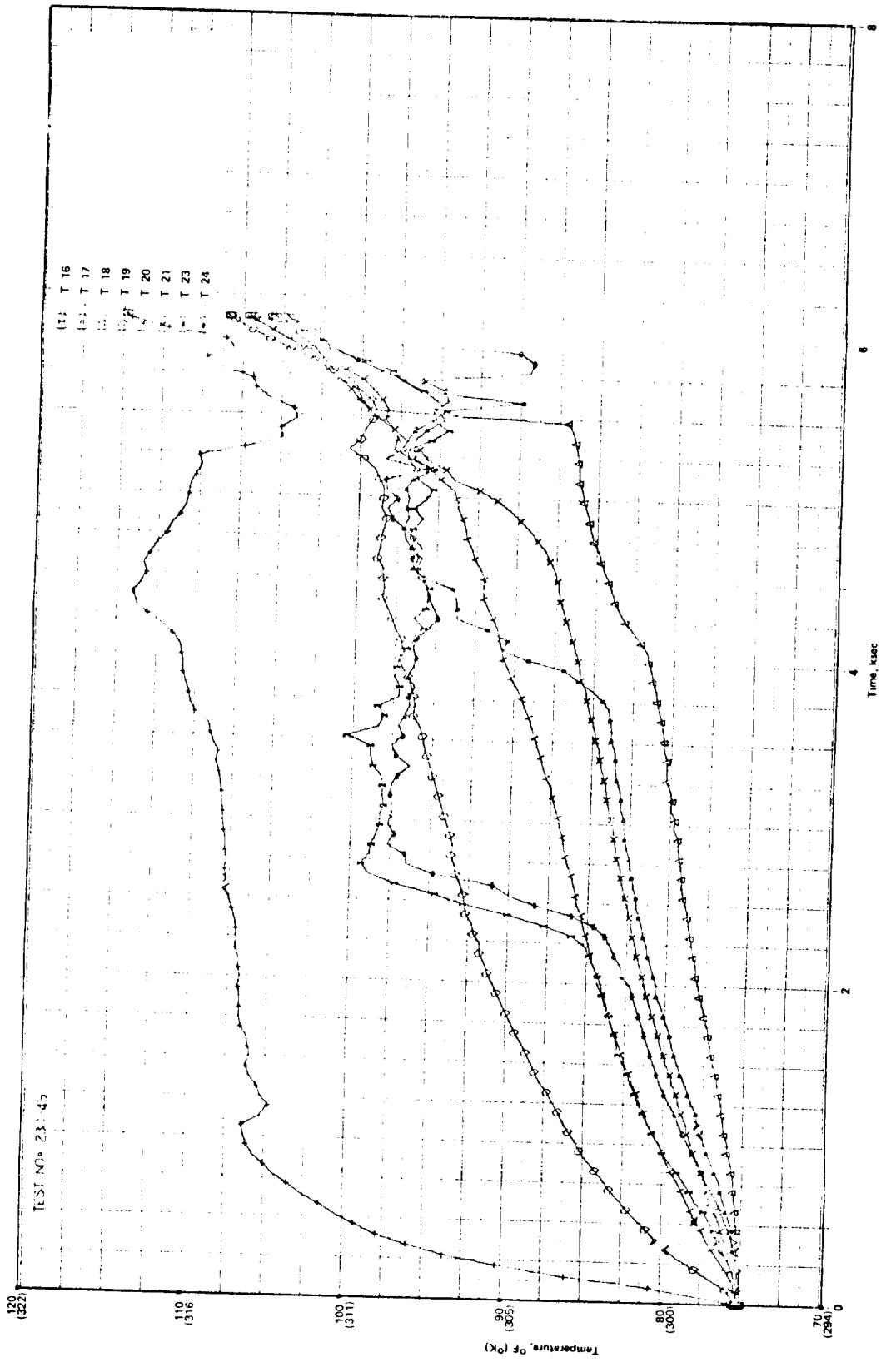

Figure D-55. Melt temperature data for finned thermal capacitor (test no. 230-49).

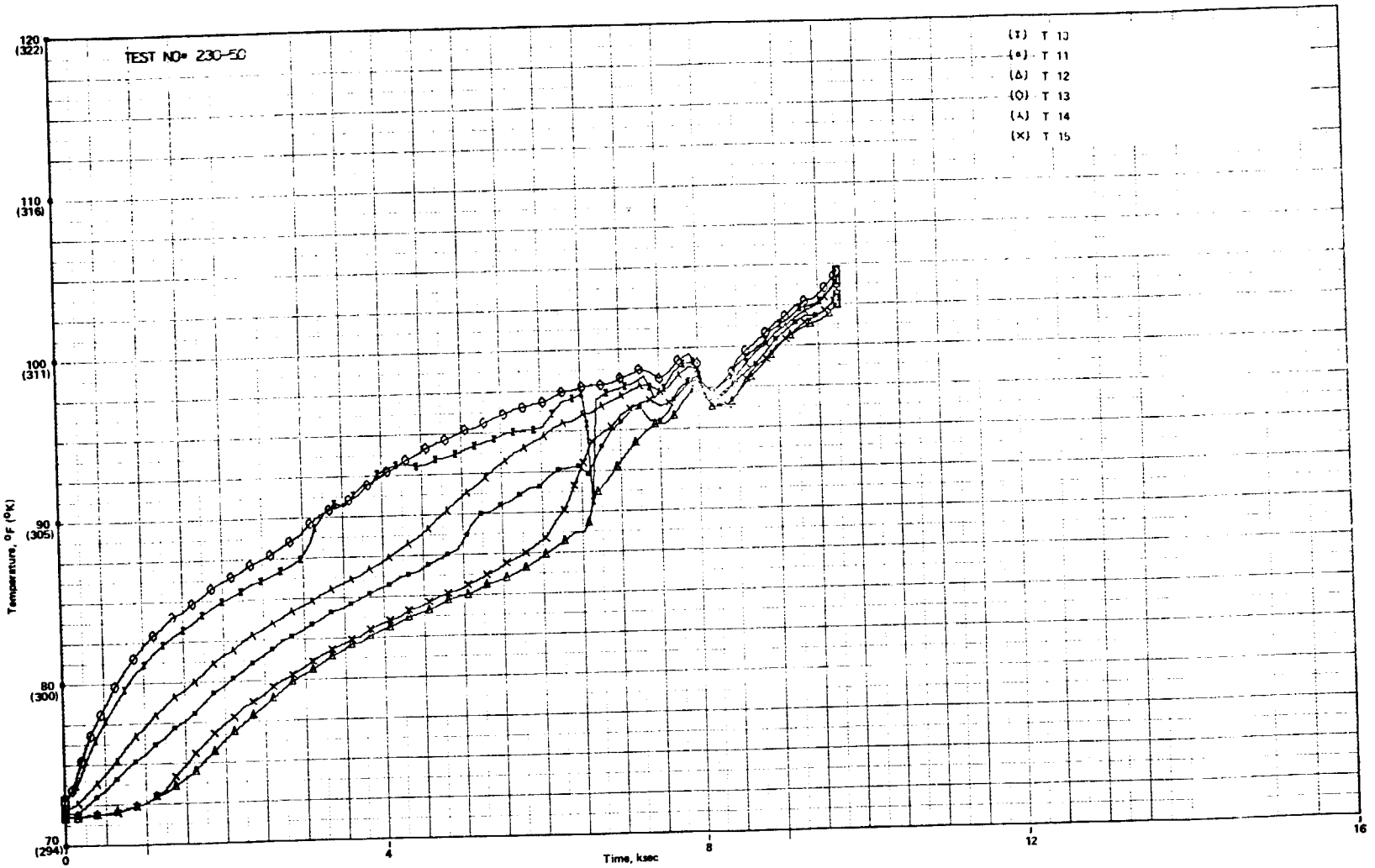

Figure D-56. Melt temperature data for finned thermal capacitor (test no. 230-50).

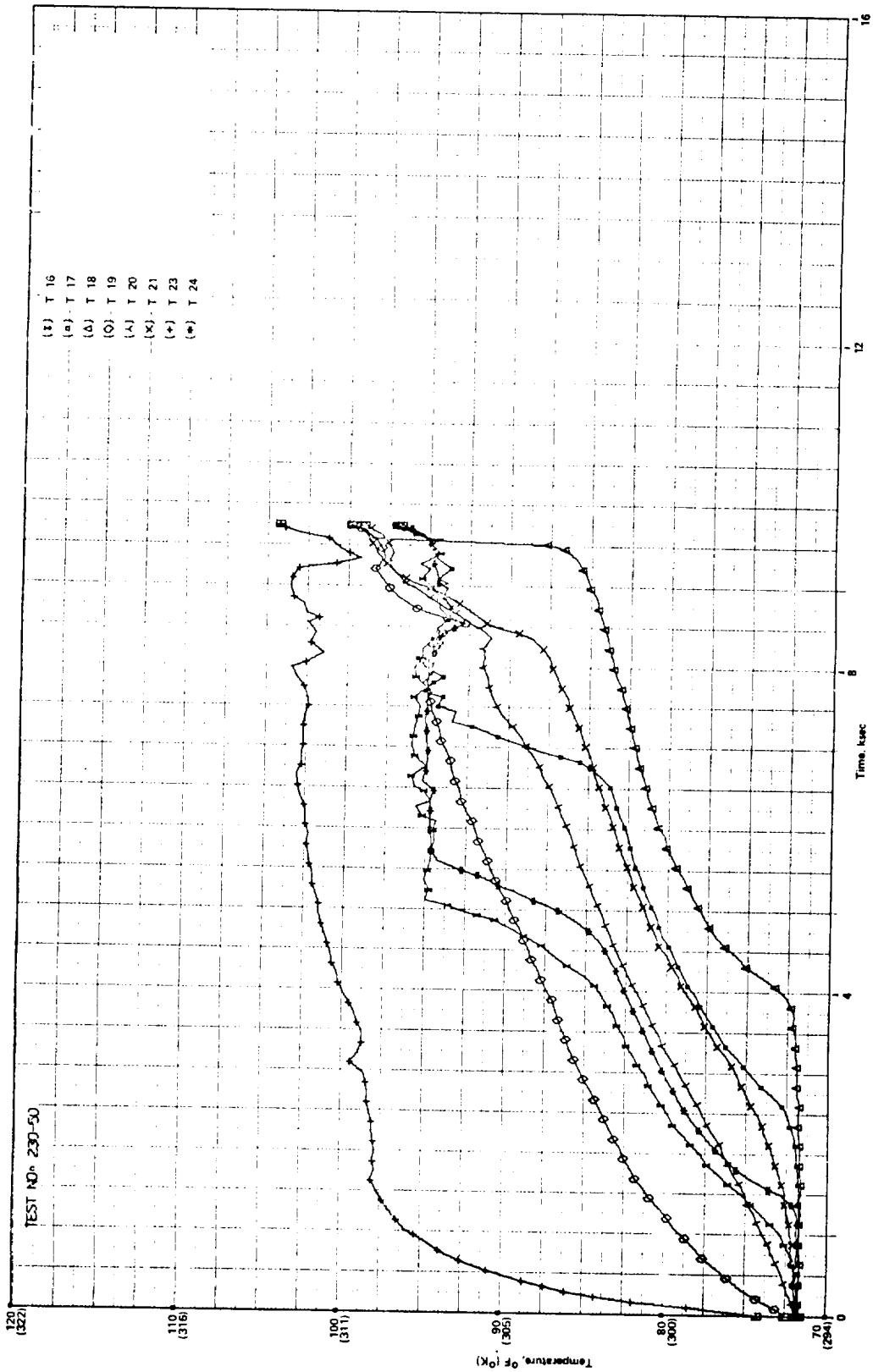

Figure D-57. Melt temperature data for finned thermal capacitor (test no. 230-50).

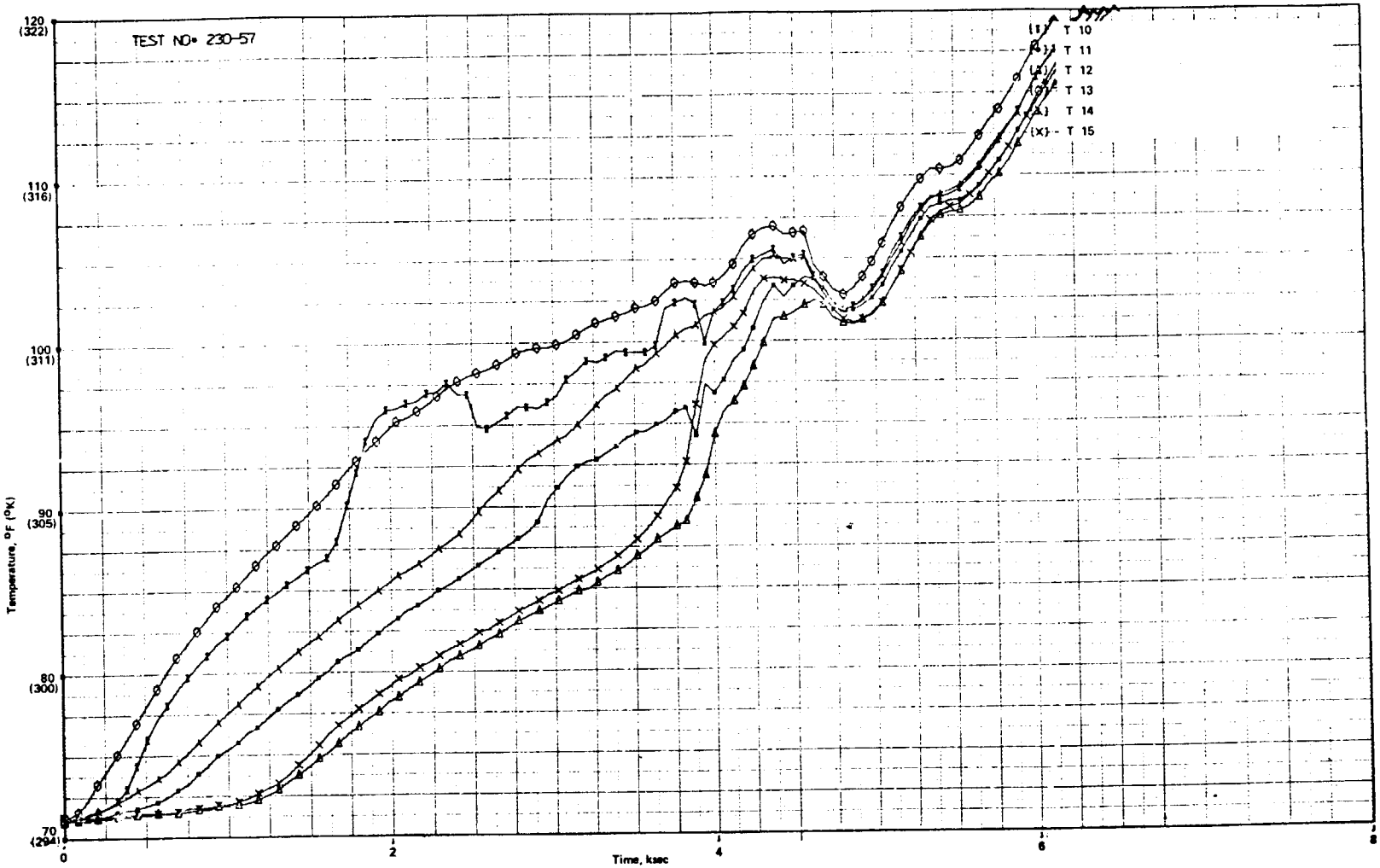

Figure D-58. Melt temperature data for finned thermal capacitor (test no. 230-57).

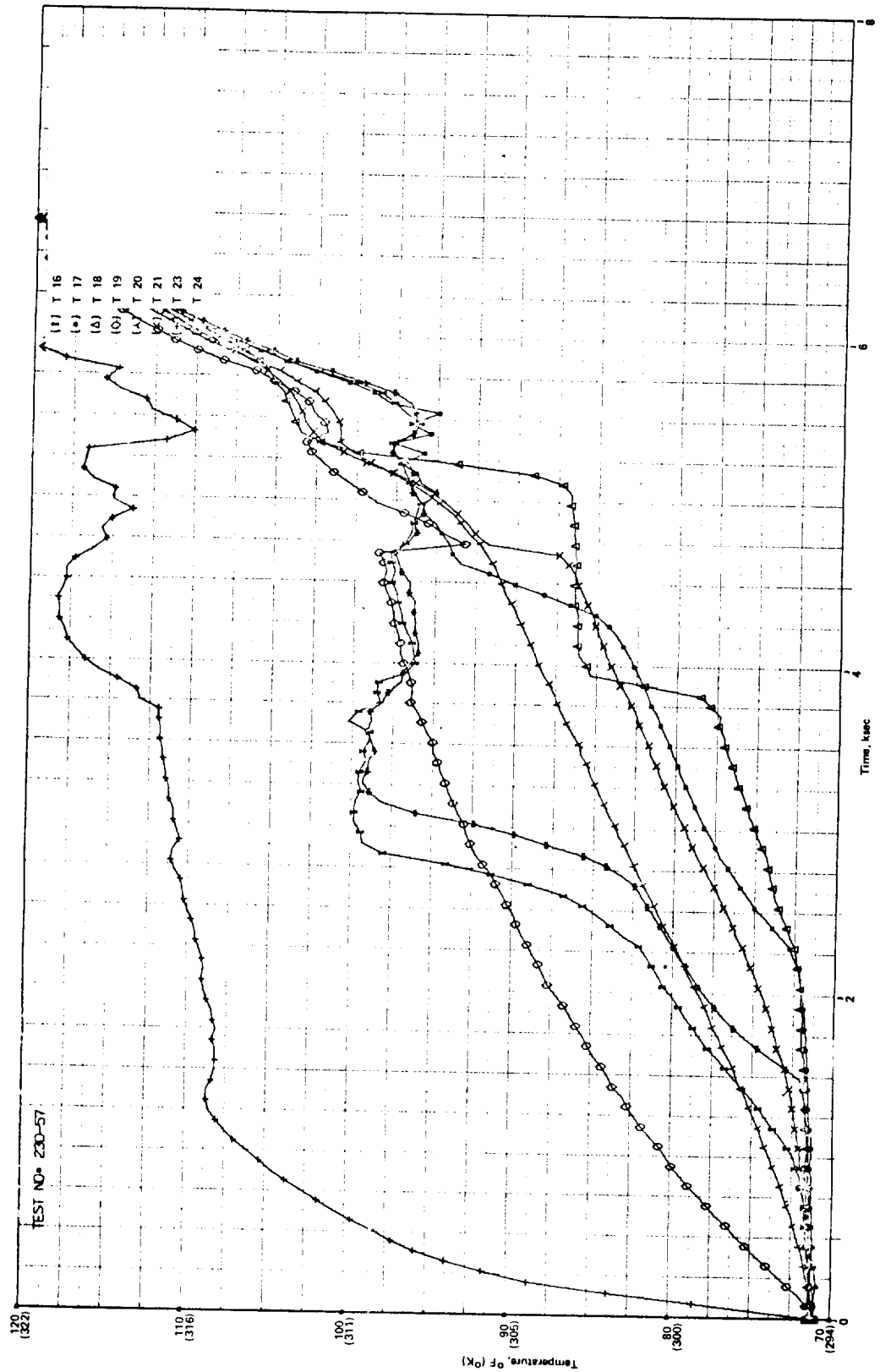

Figure D-59. Melt temperature data for finned thermal capacitor (test no. 230-57).

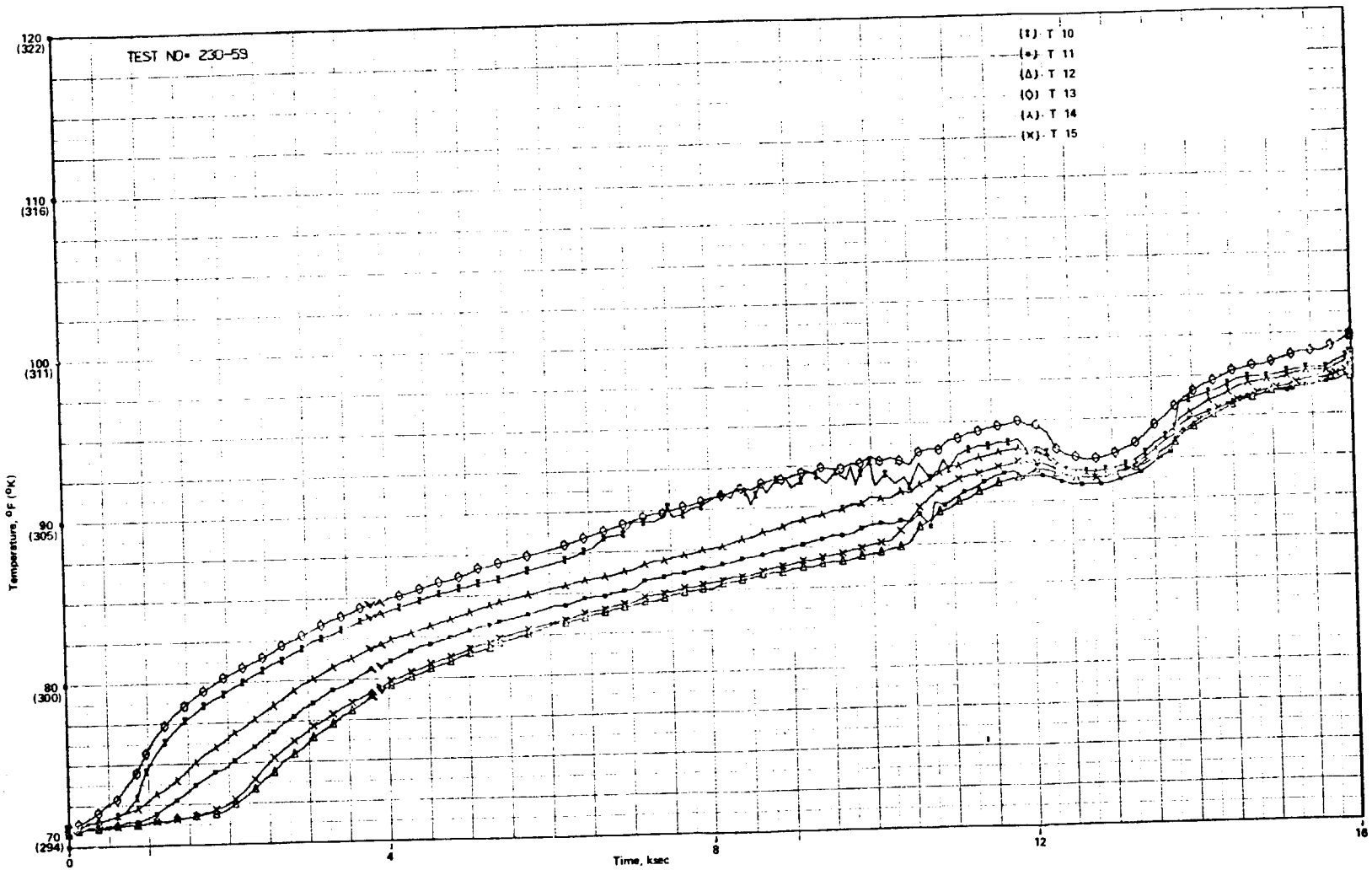

Figure D-60. Melt temperature data for finned thermal capacitor (test no. 230-59).

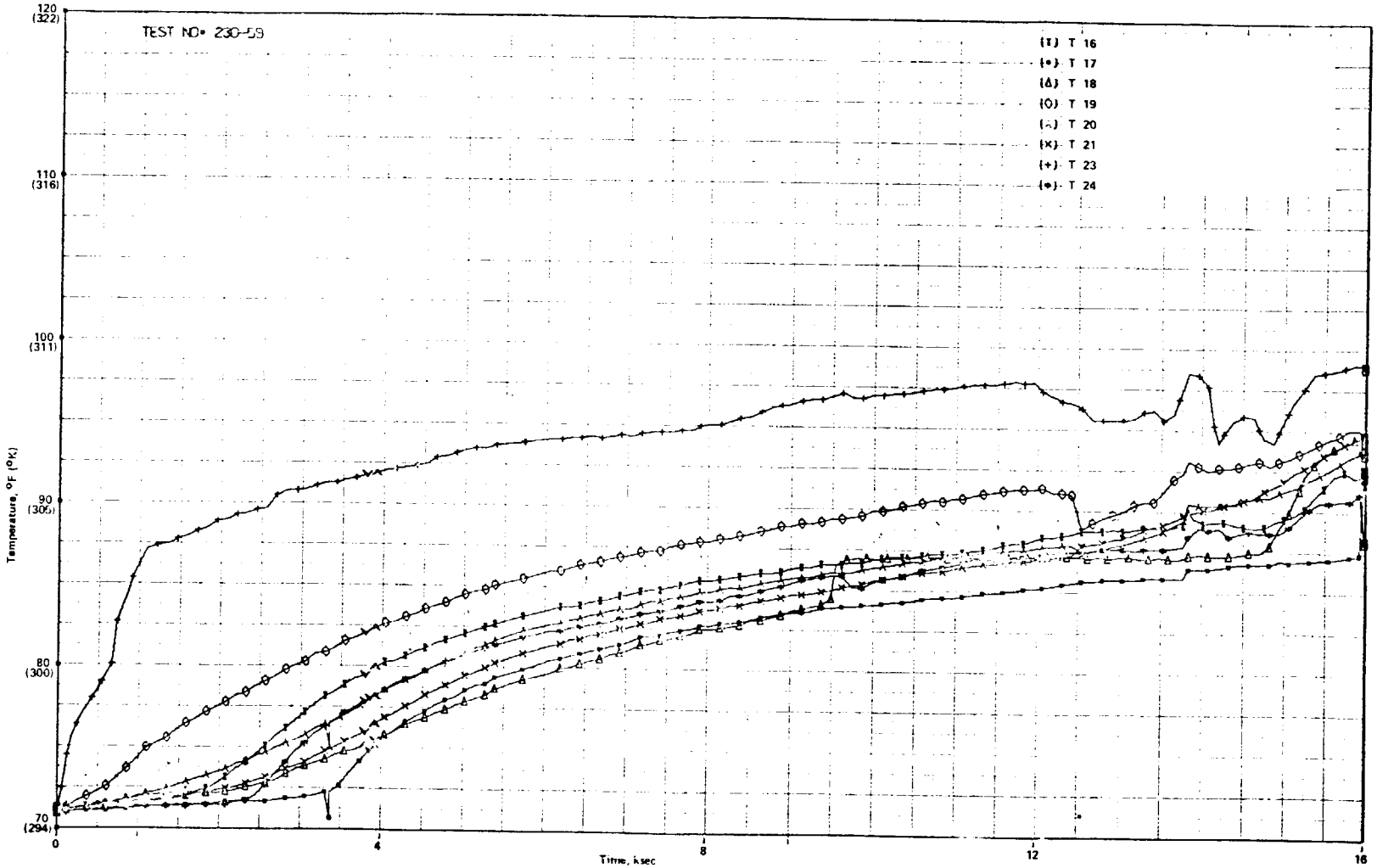

Figure D-61. Melt temperature data for finned thermal capacitor (test no. 230-59).

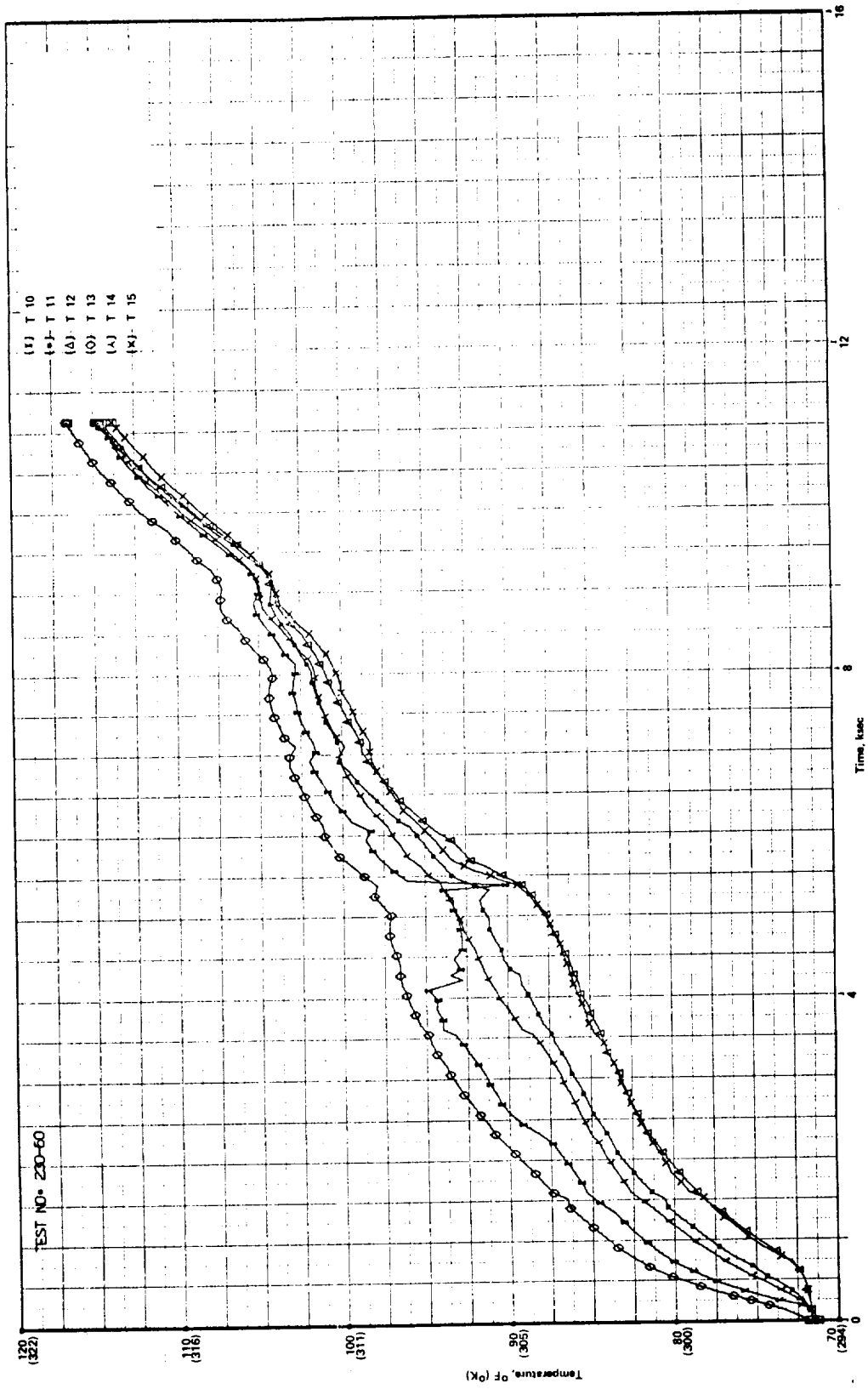

Figure D-62. Melt temperature data for finned thermal capacitor (test no. 230-60).

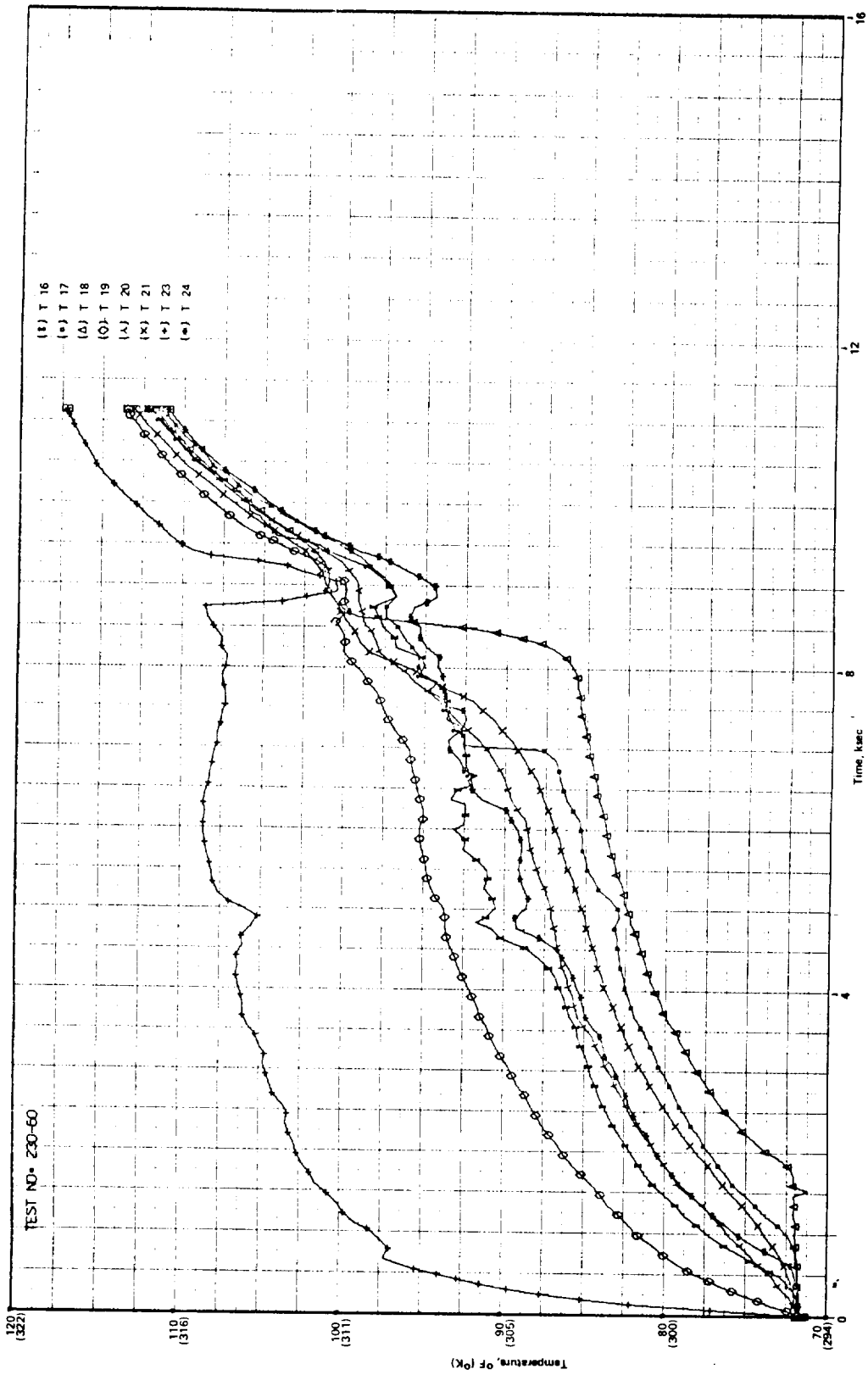

Figure D-63. Melt temperature data for finned thermal capacitor (test no. 230-60).

SECTION IV

MELT FRONT POSITION DATA FOR FINNED THERMAL CAPACITORS

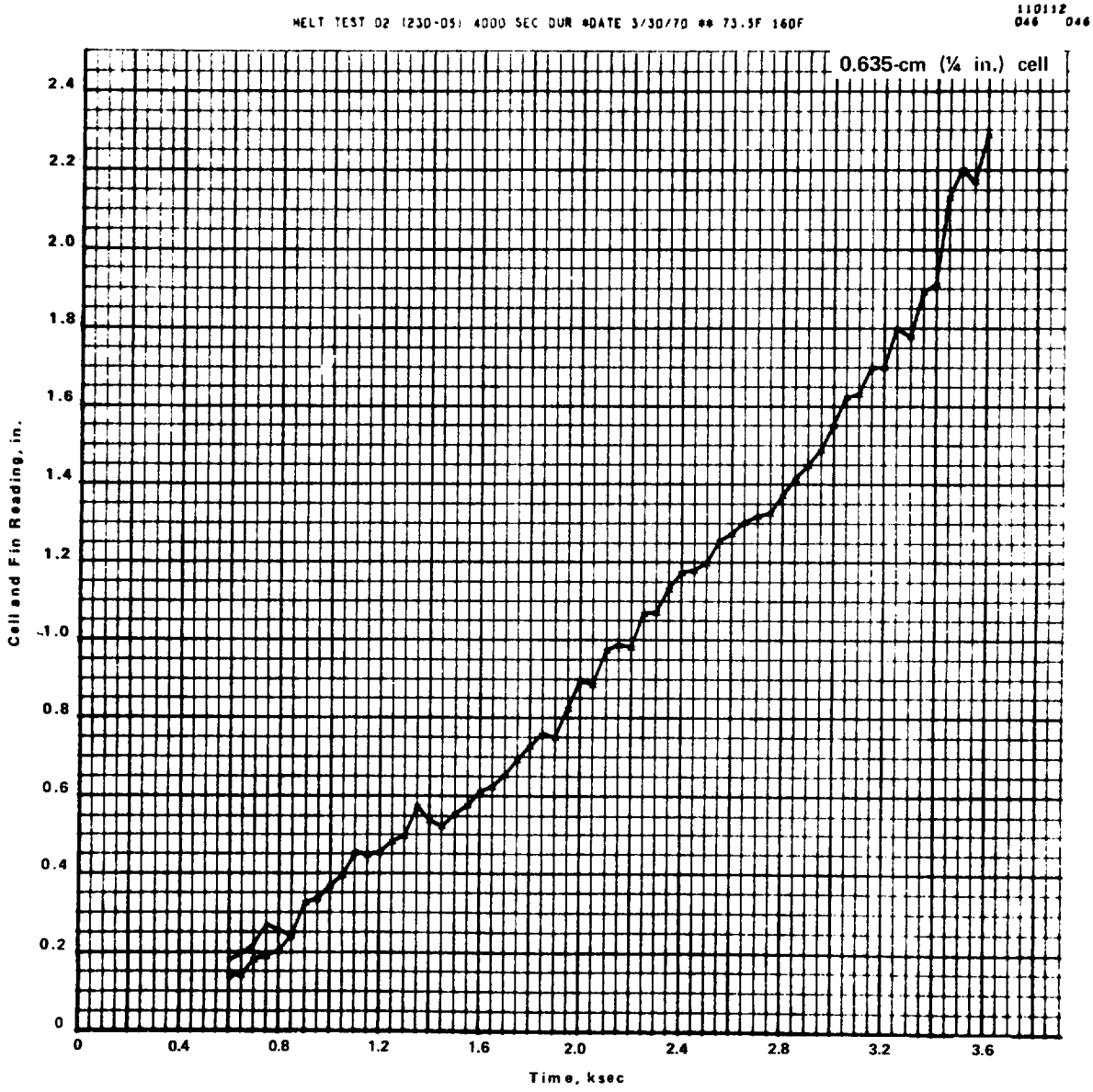

Figure D-64. Melt front position data (test no. 230-5).

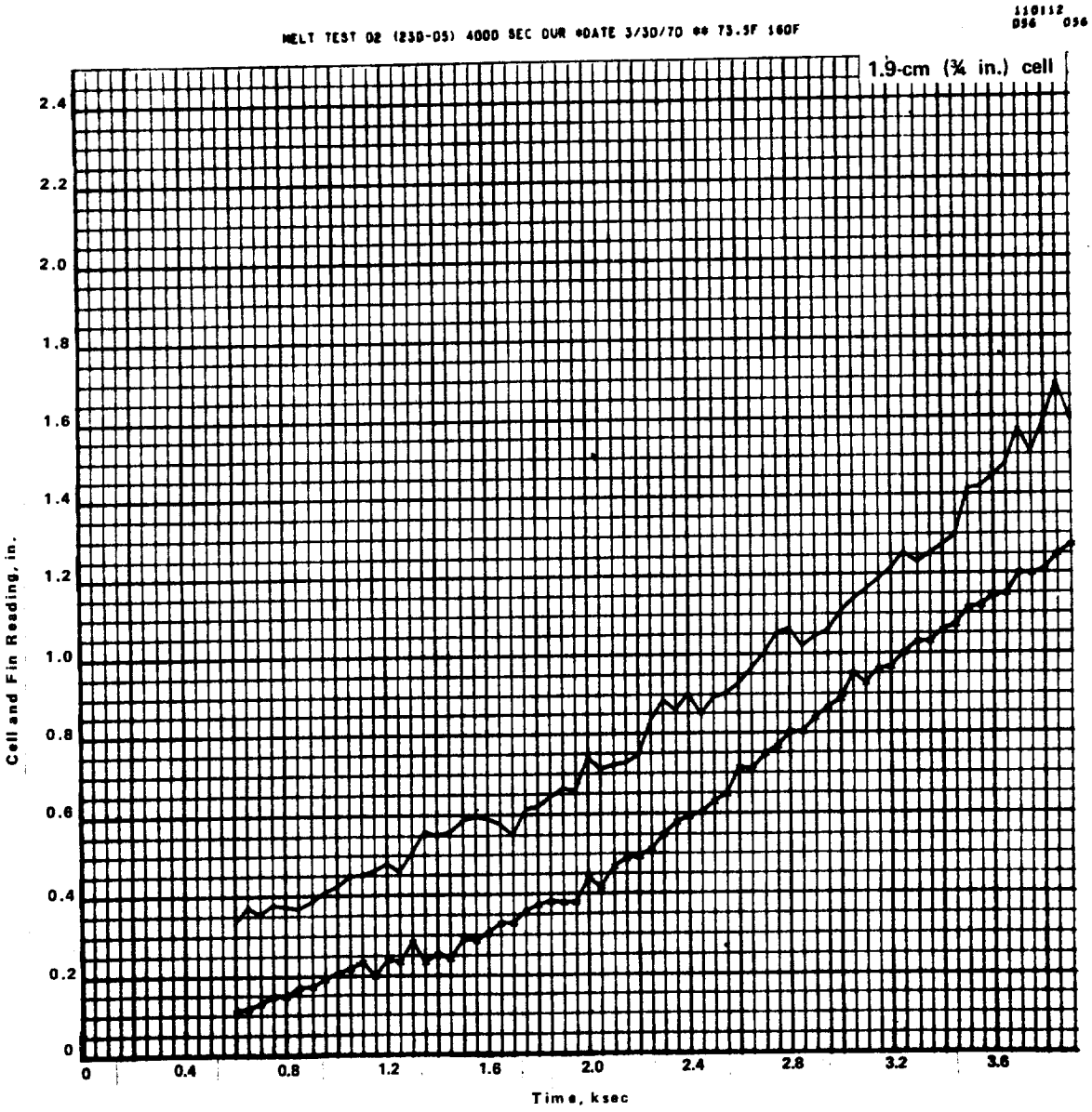

Figure D-65. Melt front position data (test no. 230-5).

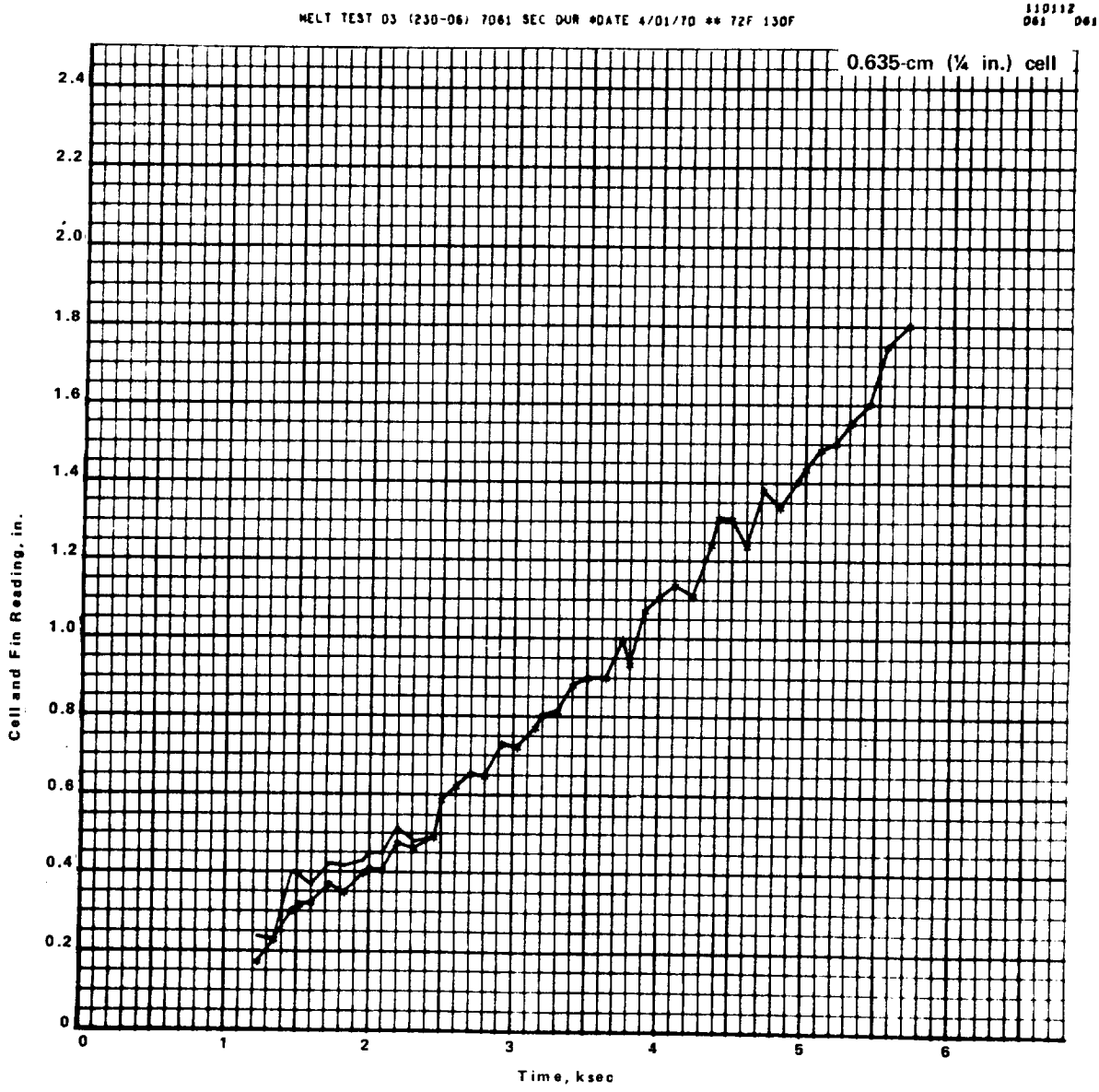

Figure D-66. Melt front position data (test no. 230-6).

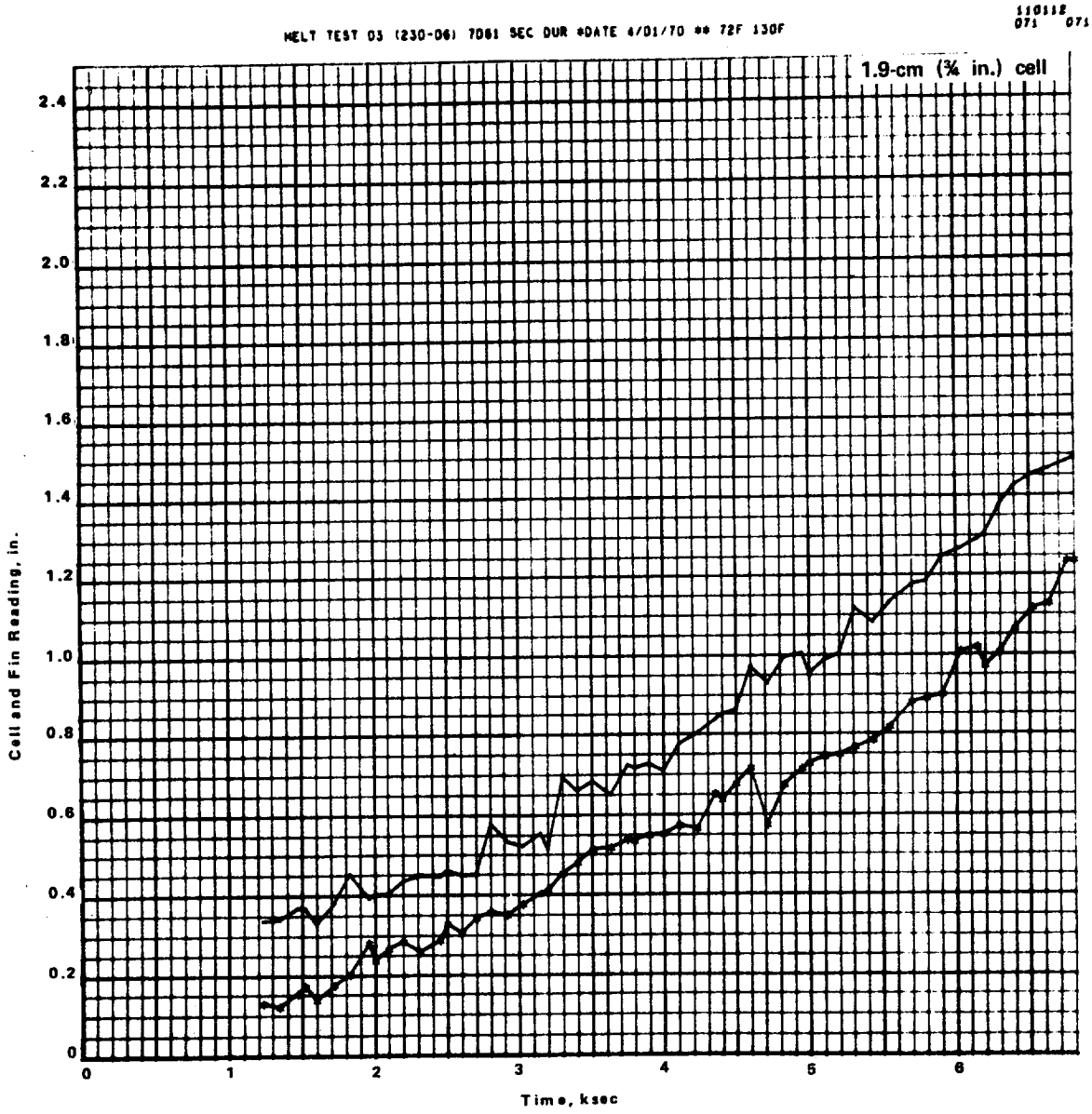

Figure D-67. Melt front position data (test no. 230-6).

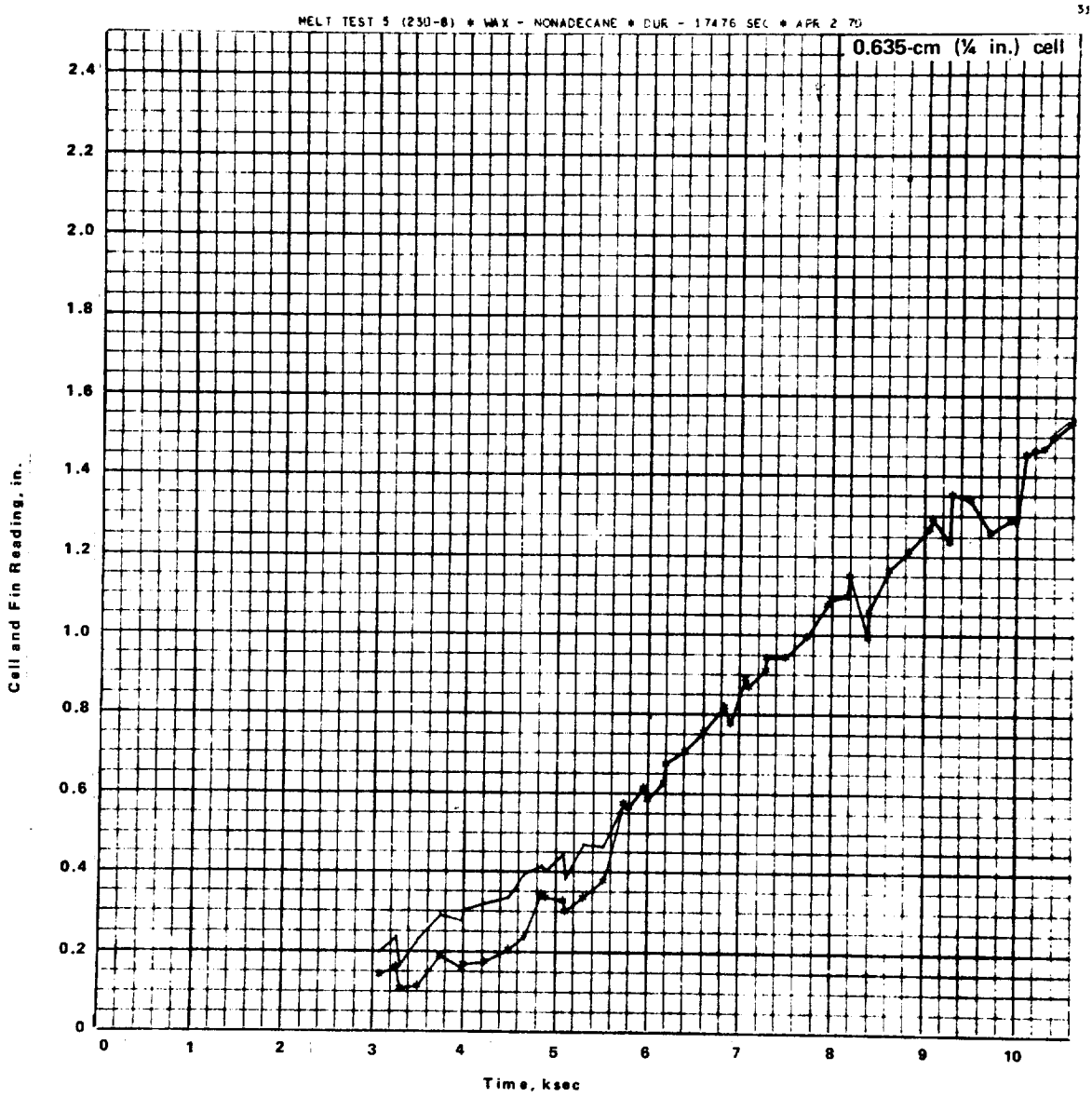

Figure D-68. Melt front position data (test no. 230-8).

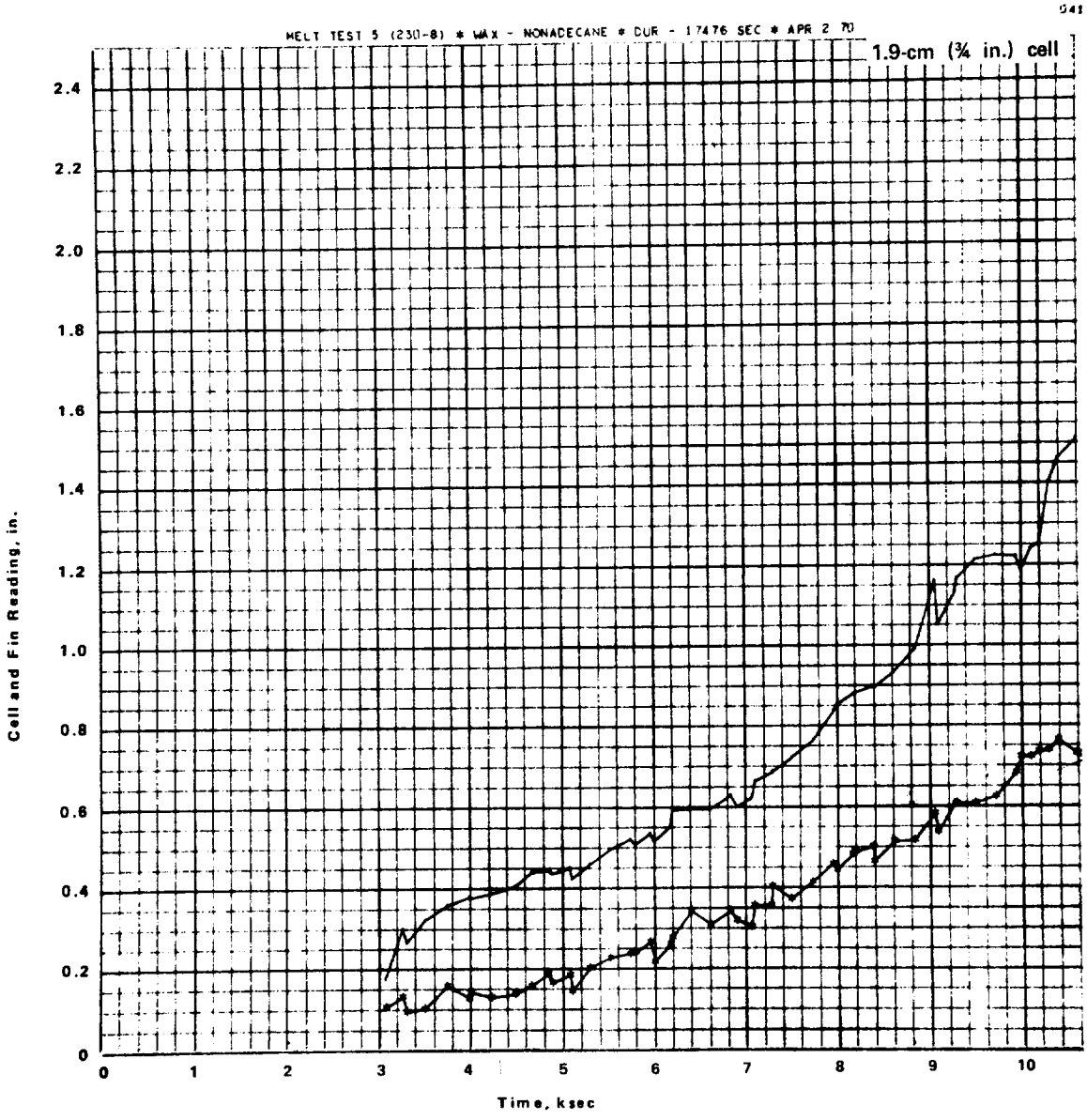

Figure D-69. Melt front position data (test no. 230-8).

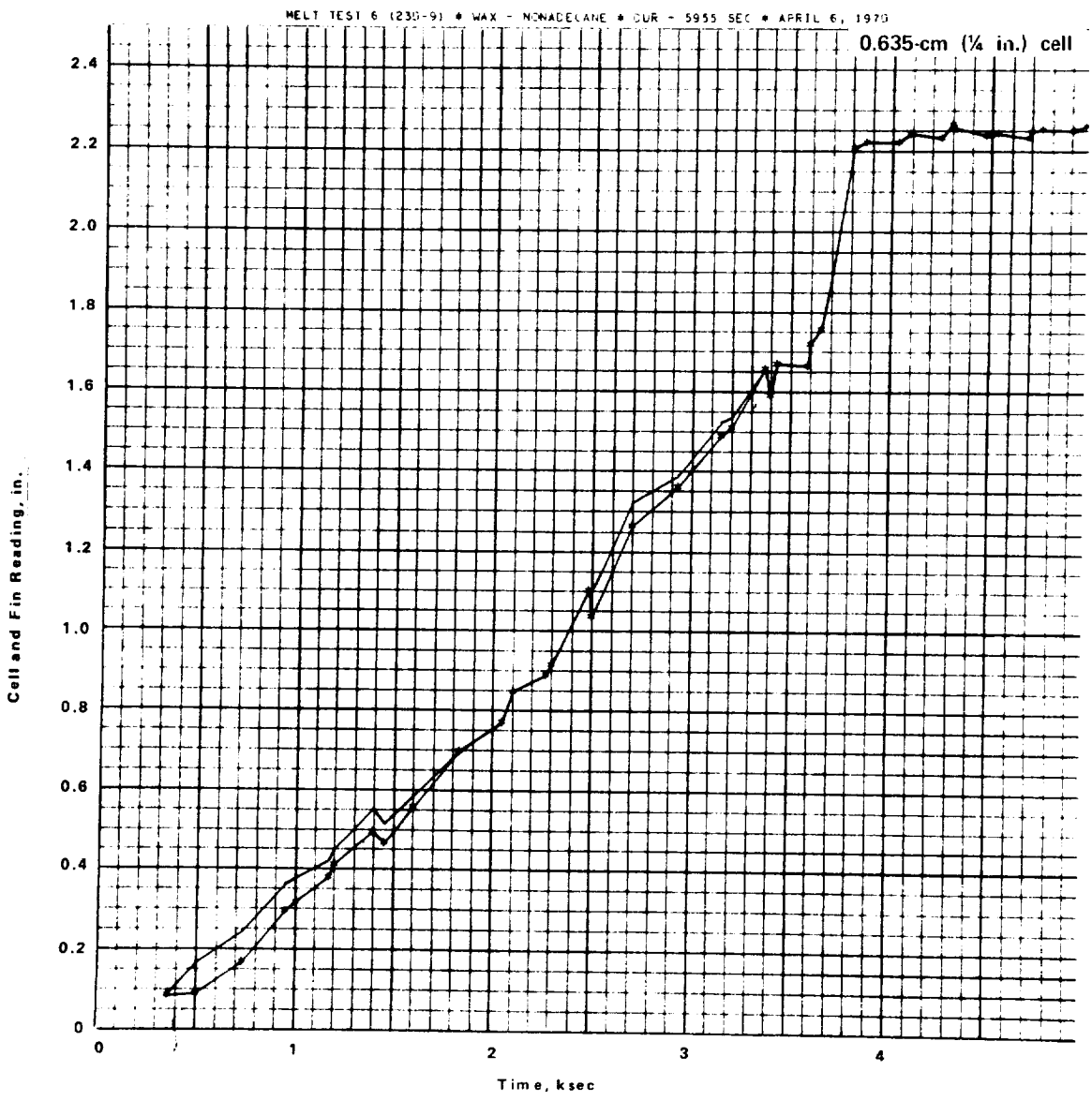

Figure D-70. Melt front position data (test no. 230-9).

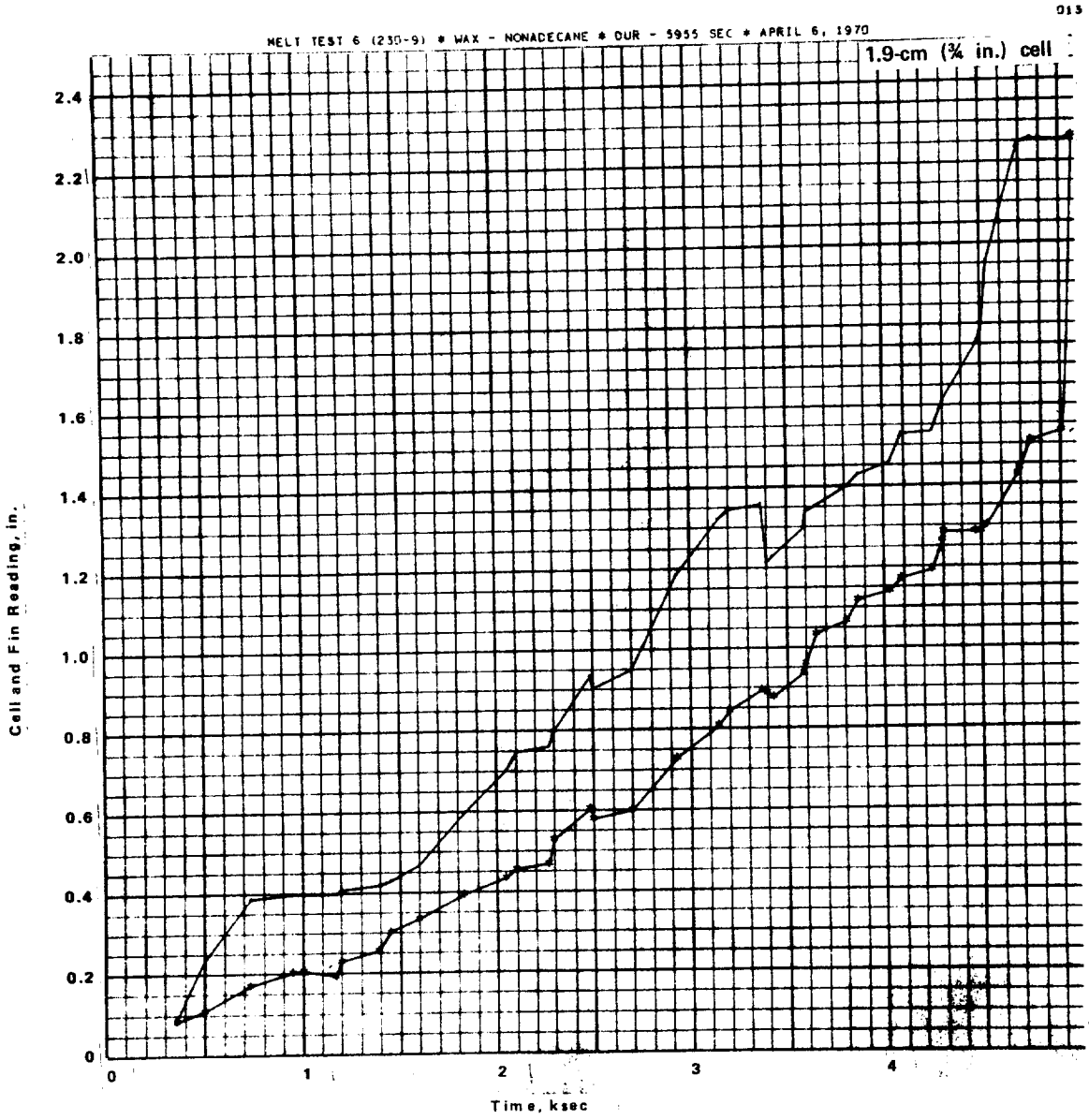

Figure D-71. Melt front position data (test no. 230-9).

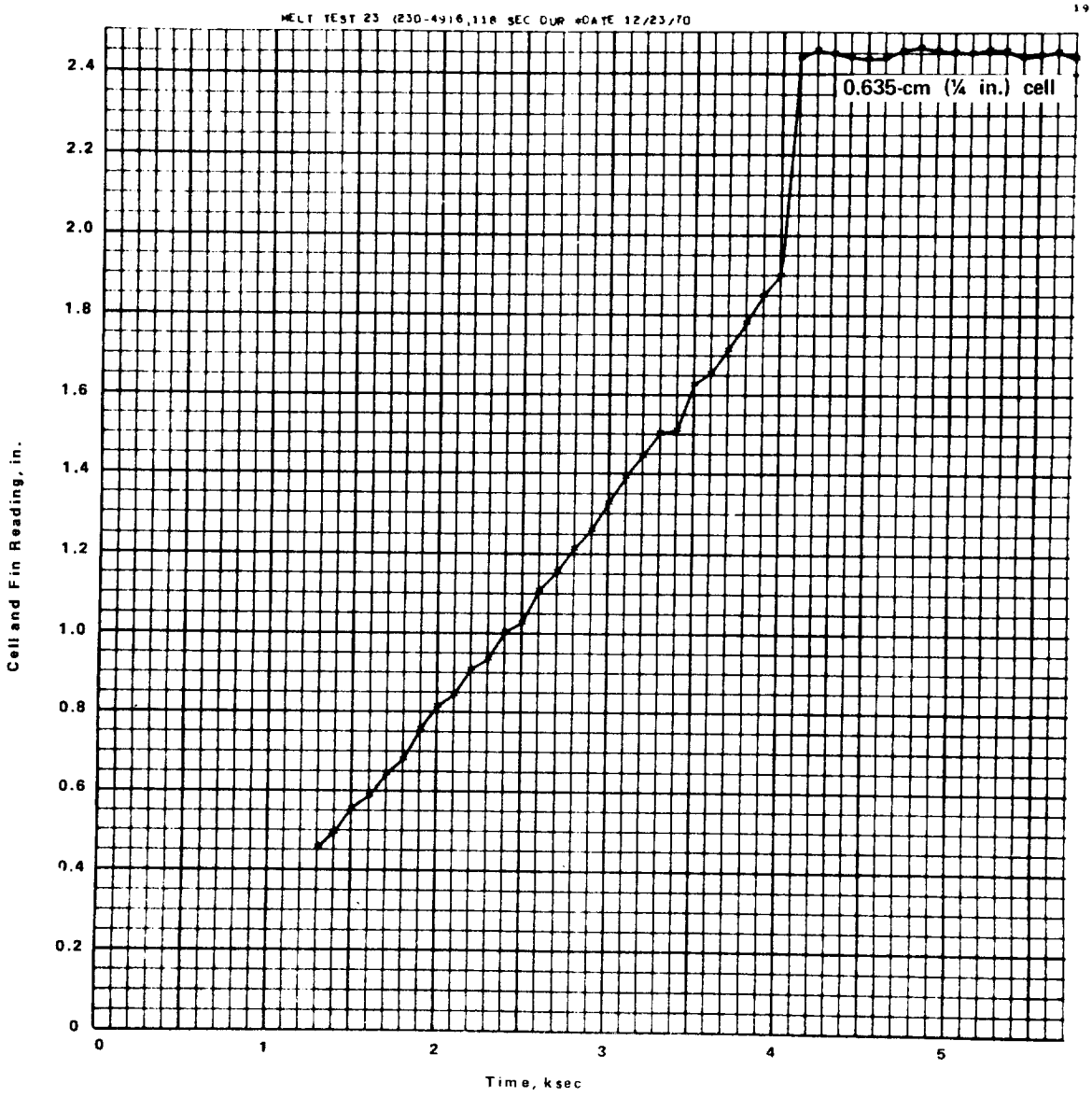

Figure D-72. Melt front position data (test no. 230-49).

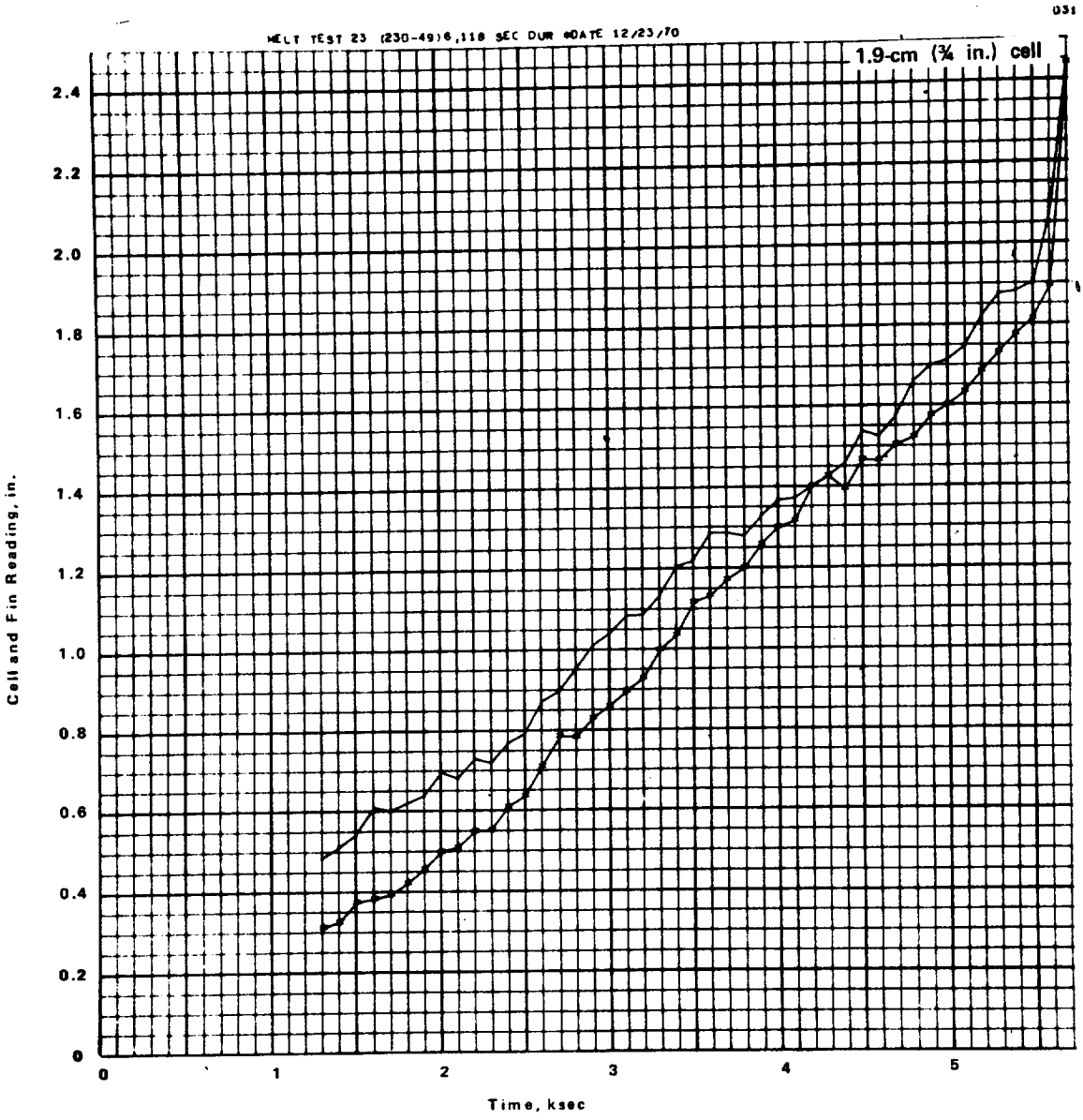

Figure D-73. Melt front position data (test no. 230-49).

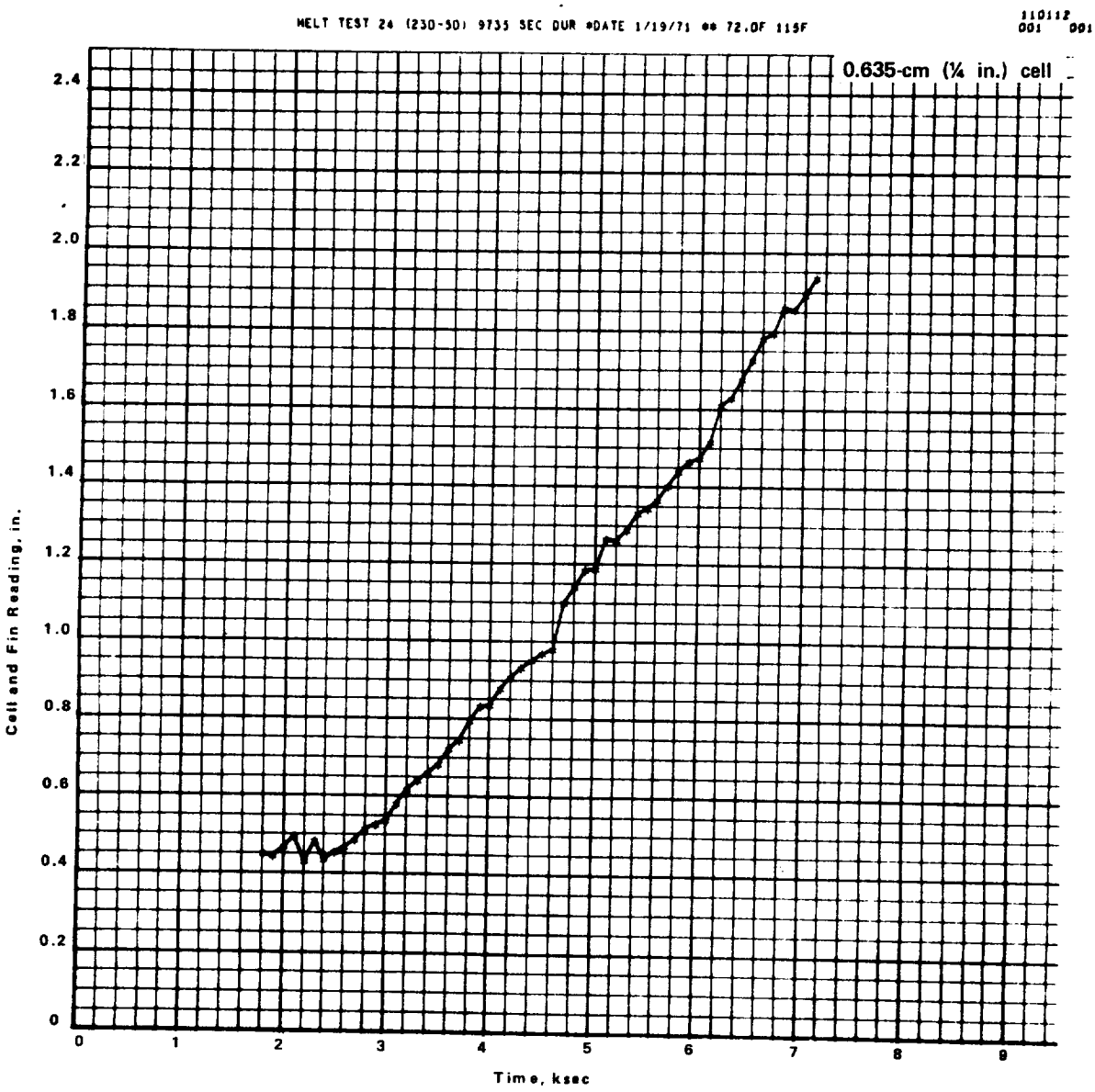

Figure D-74. Melt front position data (test no. 230-50).

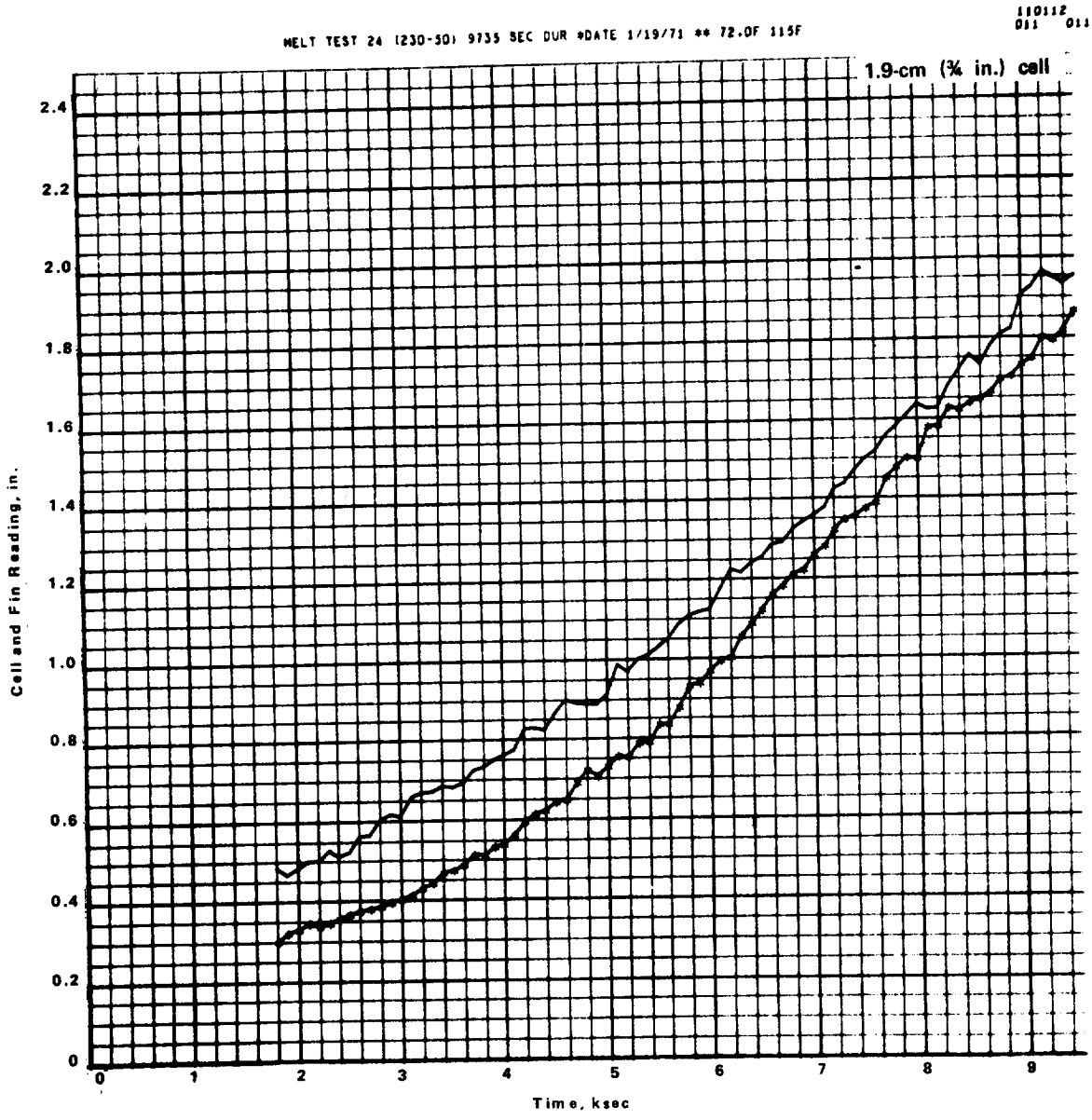

Figure D-75. Melt front position data (test no. 230-50).

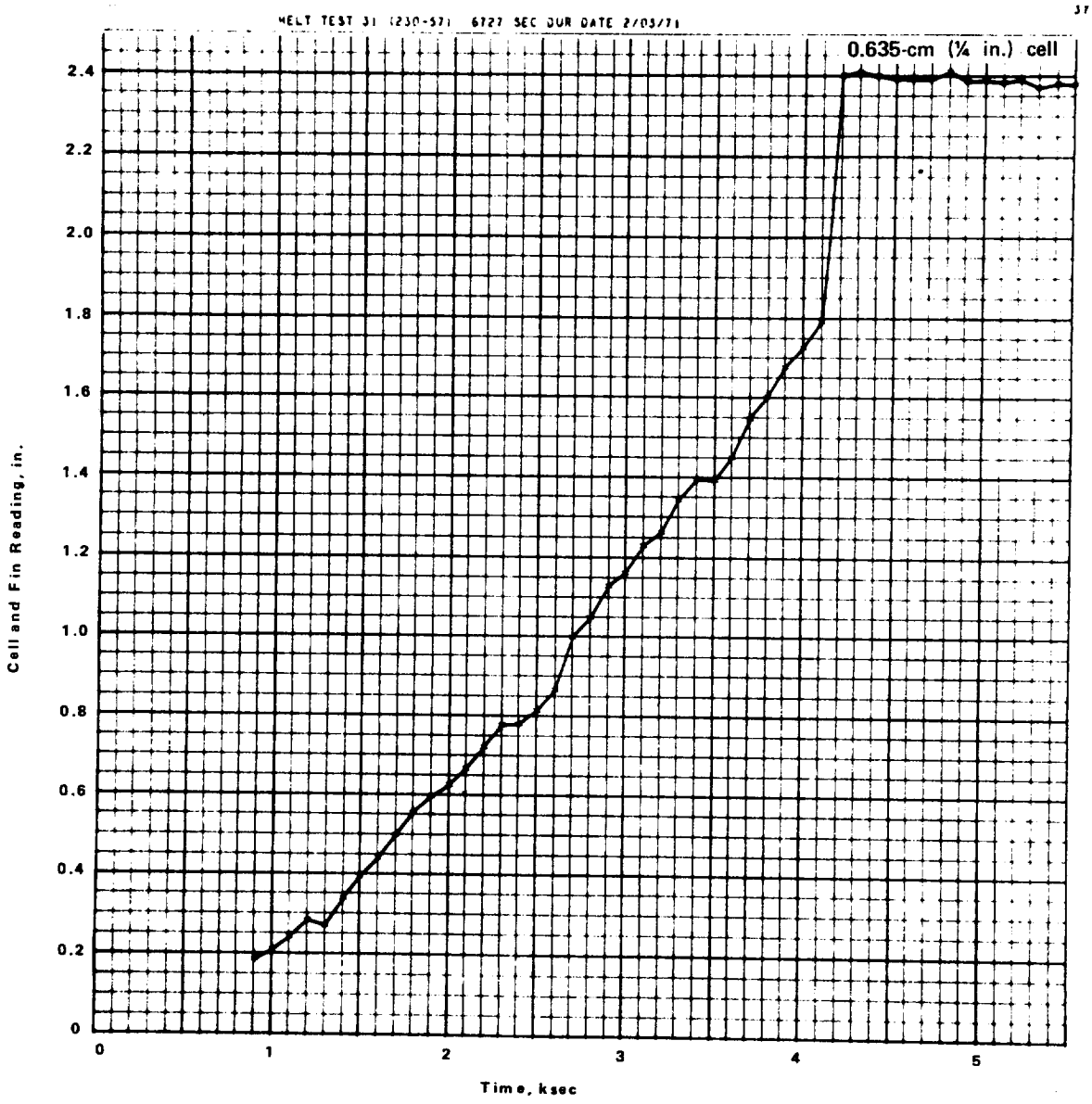

Figure D-76. Melt front position data (test no. 230-57).

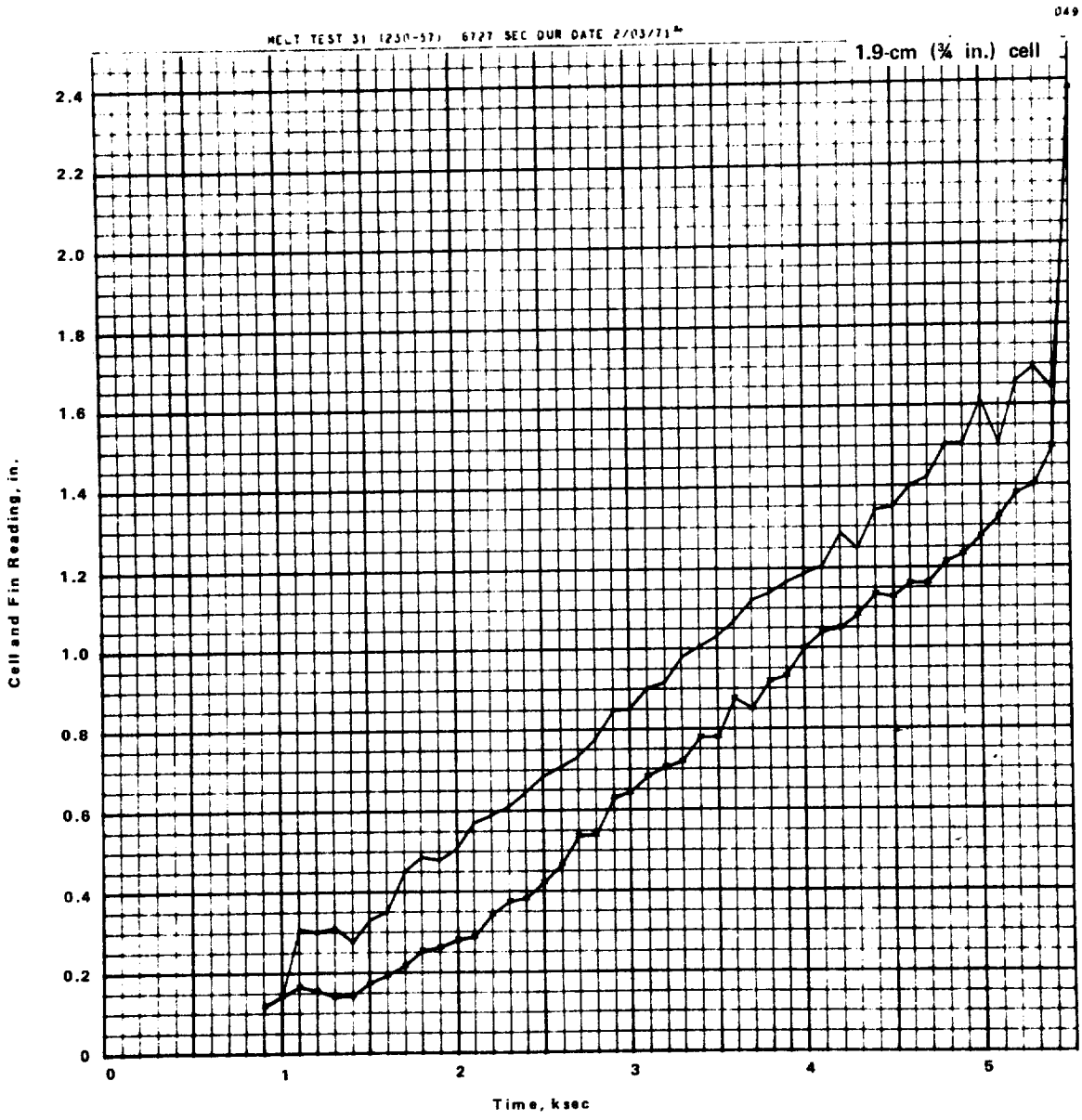

Figure D-77. Melt front position data (test no. 230-57).

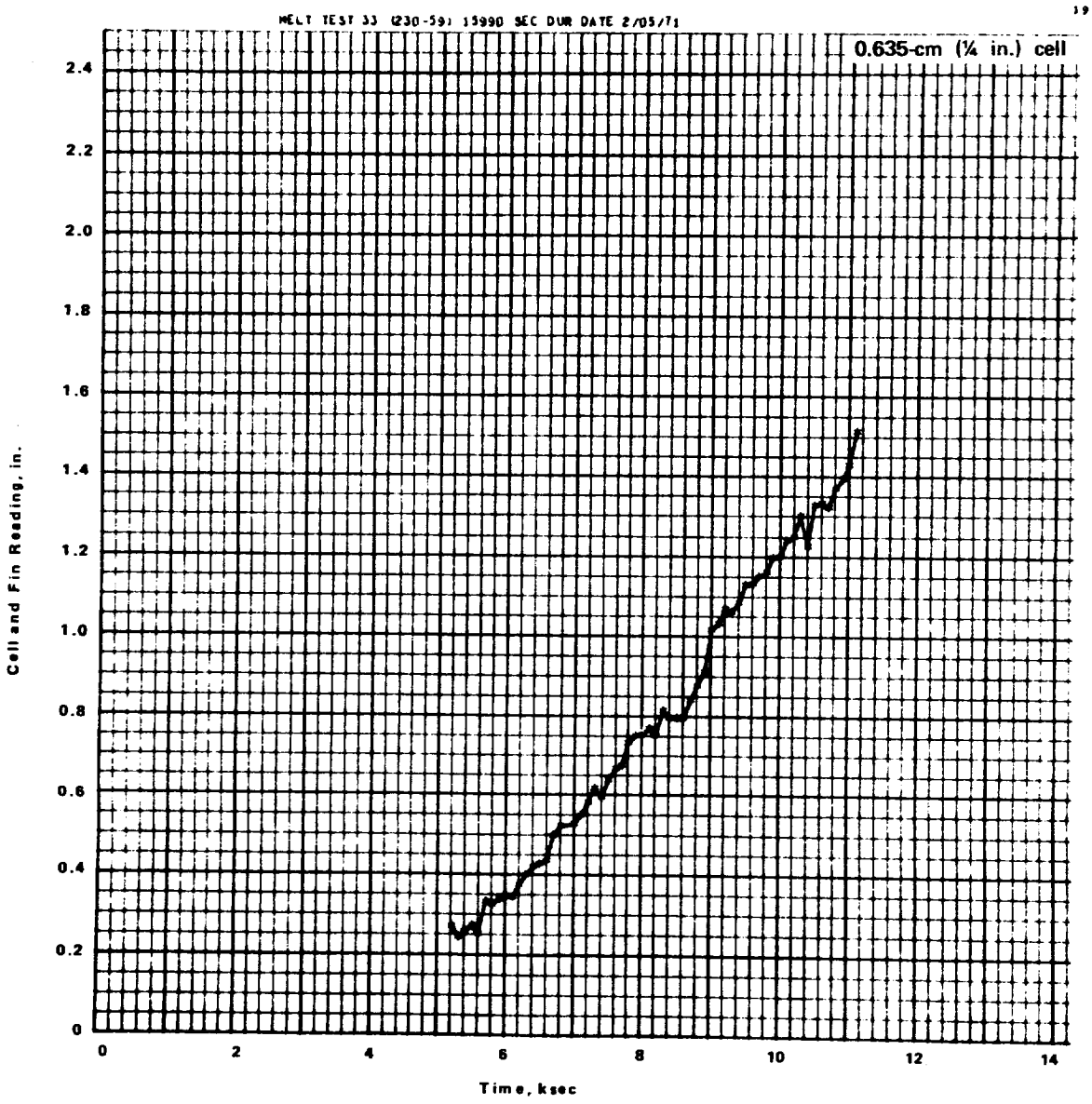

Figure D-78. Melt front position data (test no. 230-59).

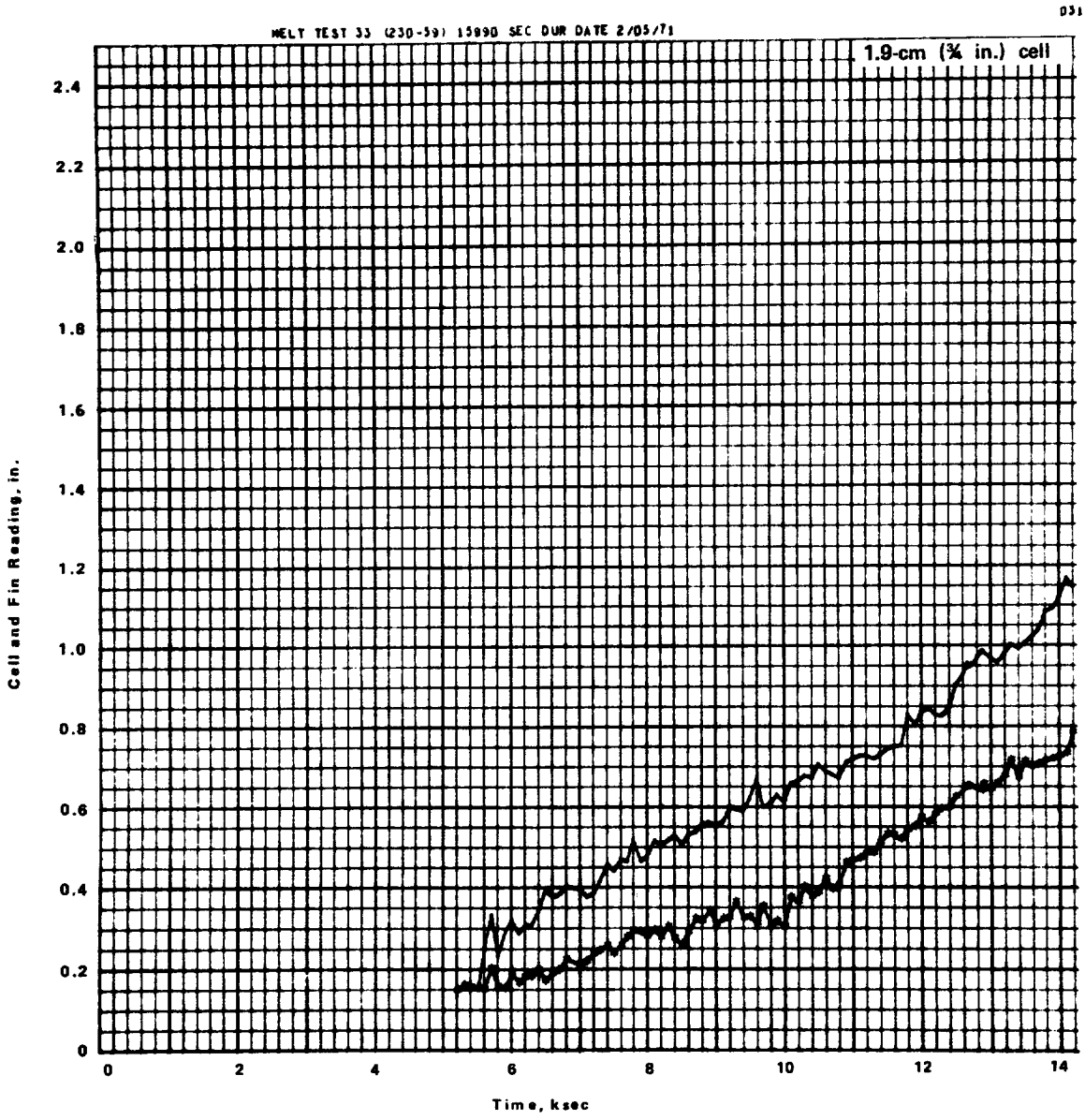

Figure D-79. Melt front position data (test no. 230-59).

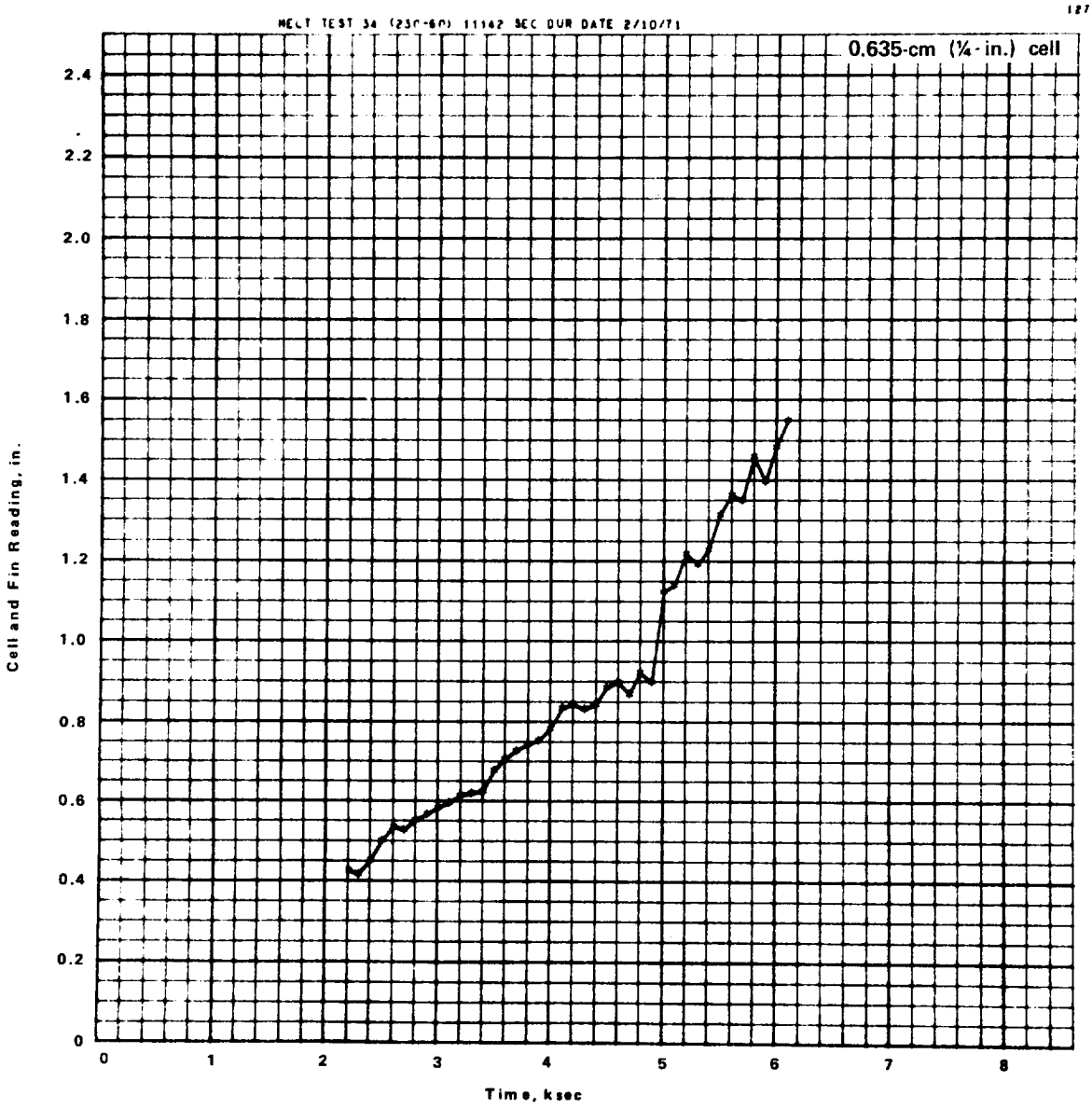

Figure D-80. Melt front position data (test no. 230-60).

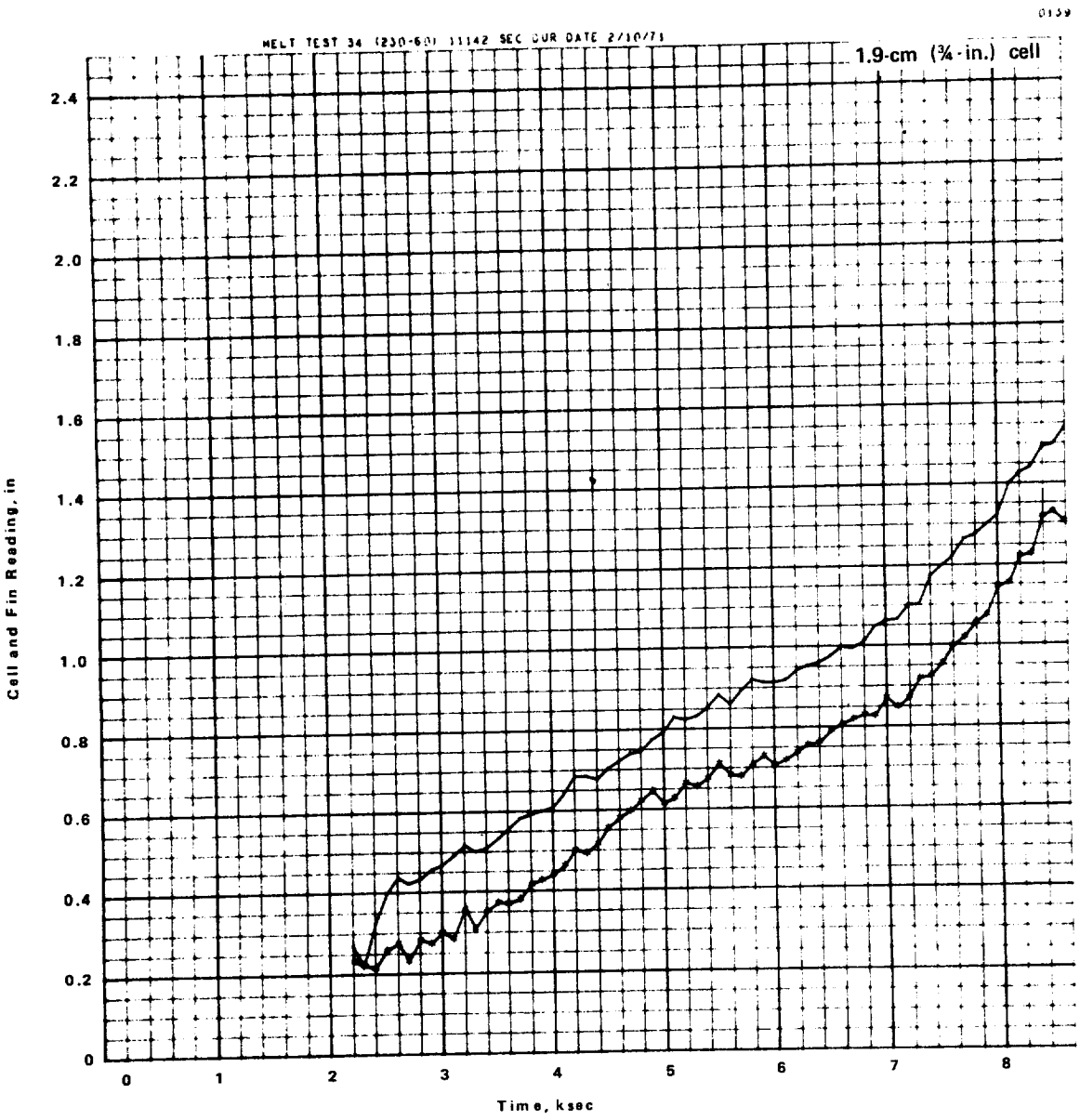

Figure D-81. Melt front position data (test no. 230-60).

APPENDIX E

DERIVATION OF INTERFACE BOUNDARY CONDITION*

An observer on the interface at $S(x', t)$ moves with the velocity $\frac{\partial S}{\partial t}$ in the y direction. He observes $\rho \frac{\partial S}{\partial t}\ \delta x\ \delta t$ mass change phase during the time interval δt in the distance interval $x' - \frac{\delta x}{2} \leq x \leq x' + \frac{\delta x}{2}$. The heat liberated because of the change in phase is $\rho \Delta H \frac{\delta x}{\delta t}$ and is equal to the net heat conducted away from the interface between $x' - \frac{\delta x}{2}$ and $x' + \frac{\delta x}{2}$ during δt.

In the y direction, the heat conducted away is given by

$$\left[- K_L \frac{\partial T_L}{\partial y} - \left(- K_S \frac{\partial T_S}{\partial y} \right) \right] \delta x\ \delta t \quad , \tag{E-1}$$

for

$$y = S(x', t) \quad .$$

In the X direction the heat conducted away is given by

$$\left[- K_L \frac{\partial T_L}{\partial x} - \left(- K_S \frac{\partial T_S}{\partial x} \right) \right] \left(- \frac{\partial S}{\partial x}\ \partial x\ \partial t \right) \tag{E-2}$$

for

$$y = S(x', t) \quad .$$

Equating the net heat conducted away from the interface and the heat librated due to phase change gives

---

*K. A. Rathjen; and L. M. Jiji: Heat Conduction with Melting or Freezing in a Corner. Trans. of ASME, Journal of Heat Transfer, February 1971.

$$- K_S \frac{\partial T_S}{\partial x} \frac{\partial S}{\partial x} \partial x \partial t + K_L \frac{\partial T_L}{\partial x} \frac{\partial S}{\partial x} \partial x \partial t$$

$$- K_L \frac{\partial T_L}{\partial y} \delta x \delta t + K_S \frac{\partial T_S}{\partial y} \delta x \delta t = \rho \Delta H \frac{\partial S}{\partial t} \delta t \delta x$$

for

$$y = S(x', t)$$

rearranging and dividing by $\delta x \, \delta t$ we have

$$K_S \frac{\partial T_S}{\partial y} - K_L \frac{\partial T_L}{\partial y} + K_L \frac{\partial T_L}{\partial x} \frac{\partial S}{\partial x} - K_S \frac{\partial T_S}{\partial x} \frac{\partial S}{\partial x} = \rho \Delta H \frac{\partial S}{\partial t} \quad ,$$

for

$$y = S(x', t) \quad . \tag{E-3}$$

We know the total differential is given by

$$dT_S = \frac{\partial T_S}{\partial x} dx + \frac{\partial T_S}{\partial y} dy + \frac{\partial T_S}{\partial t} dt \quad .$$

However, along the interface $T_S = T_F$, a constant, so that

$$0 = \frac{\partial T_S}{\partial x} dx + \frac{\partial T_S}{\partial y} dy + \frac{\partial T_S}{\partial t} dt \quad ,$$

for

$$y = S(x, t) \quad , \tag{E-4}$$

and we also know

$$dy = \frac{\partial S}{\partial x} dx + \frac{\partial S}{\partial t} dt \quad , \tag{E-5}$$

for

$$y = S(x, t) \quad .$$

Putting (E-5) into (E-4) gives

$$\left(\frac{\partial T_S}{\partial x} + \frac{\partial T_S}{\partial y}\frac{\partial S}{\partial x}\right) dx + \left(\frac{\partial T_S}{\partial t} + \frac{\partial T_S}{\partial y}\frac{\partial S}{\partial t}\right) dt = 0 \quad , \qquad (E\text{-}6)$$

for

$$y = S(x,t) \quad .$$

Since x and t are independent

$$\frac{\partial T_S}{\partial x} = -\frac{\partial T_S}{\partial y}\frac{\partial S}{\partial x} \quad , \qquad (E\text{-}7)$$

for

$$y = S(x,t) \quad ,$$

and

$$\frac{\partial T_S}{\partial t} = -\frac{\partial T_S}{\partial y}\frac{\partial S}{\partial t} \qquad (E\text{-}8)$$

from equation (E-6), for $y = S(x,t)$.

Also by the same method

$$\frac{\partial T_L}{\partial x} = -\frac{\partial T_L}{\partial y}\frac{\partial S}{\partial x} \quad , \qquad (E\text{-}9)$$

for

$$y = S(x,t) \quad ,$$

and

$$\frac{\partial T_L}{\partial t} = -\frac{\partial T_L}{\partial y}\frac{\partial S}{\partial t} \quad , \text{ for } y = S(x,t) \quad . \qquad (E\text{-}10)$$

Substituting (E-7) and (E-9) into (E-3), we obtain

$$K_S \frac{\partial T_S}{\partial y} - K_L \frac{\partial T_L}{\partial y} - K_L \frac{\partial T_L}{\partial y} \left(\frac{\partial S}{\partial x}\right)^2$$

$$+ K_S \frac{\partial T_S}{\partial y} \left(\frac{\partial S}{\partial x}\right)^2 = \rho \Delta H \frac{\partial S}{\partial t} \quad ,$$

for

$$y = S(x,t) \quad .$$

Since x' is a general coordinate

$$\left(K_S \frac{\partial T_S^*}{\partial y} - K_L \frac{\partial T_L^*}{\partial y}\right) \left[1 + \left(\frac{\partial S}{\partial x}\right)^2\right] = \rho \Delta H \frac{\partial S}{\partial t} \quad ,$$

for

$$y = S(x,t) \quad ,$$

If the dimensionless temperatures T_S^* and T_L^* are introduced, the desired boundary condition form is obtained,

where:

$$T_S^* = \frac{T_S - T_F}{T_F - T_W} \quad ,$$

$$T_L^* = \frac{K_L}{K_S} \left(\frac{T_L - T_F}{T_F - T_W}\right) \quad ,$$

T_F = Fusion temperature,

T_S = Solid Temperature,

T_L = Liquid temperature, and

T_W = Wall temperature.

REFERENCES

1. Chalmers, B.: Principles of Solidification. John Wiley and Sons, New York, New York, 1964.

2. Grodzka, P. B.: Thermal Control by Freezing and Melting; Second Interim Report on Space Thermal Control Study. Lockheed Missiles and Space Company, D148619, NASA Contract NAS 8-21123, May, 1969.

3. Fixler, S.: Satellite Thermal Control Using Phase-Change Materials, AIAA Journal of Spacecraft, vol. 3, no. 9, September 1966.

4. Bannister, T. C.: Space Thermal Control Using Phase Change. NASA TMX-53402, March, 1966.

5. Grodzka, P. B.; and Fan, C.: Thermal Control by Freezing and Melting; First Interim Report on Space Thermal Control Study. Lockheed Missiles and Space Company, A791342, NASA Contract NAS8-21123, March, 1968.

6. Broadhurst, M. G.: Analysis of the Solid Phase Behavior of Normal Paraffins. Journal of Research (NBS), vol. 66A, no. 3, May - June, 1962.

7. Shlosinger, A. P.; and Bentilla, B. W.: Research and Development Study on Thermal Control by Use of Fusible Materials. Interim Report NSL-16, NASA Contract NAS8-11163, February, 1965.

8. Bentilla, E. W.; Sterrett, K. F.; and Karre, L. E.: Research and Development Study on Thermal Control by Use of Fusible Materials. Final Report, NASA Contract No. NAS 8-11163, NSL 65-16, April, 1966.

9. Prenger, F. C.: Freezing for Selected Hydrocarbon Wax Mixtures. Martin-Marietta Report TM 0-478-70-4, July, 1970.

10. American Petroleum Institute: Selected Values of Physical and Thermodynamic Properties of Hydrocarbons and Related Compounds. Research Project 44, Carnegie Press, Pittsburgh, Penn., 1953.

11. Timmerans, J.: Physio-Chemical Constants of Pure Organic Compounds. vol. 1, Elsevier Publishing Company, Inc., New York, N. Y., 1950.

12. Timmerans, J.: Physio-Chemical Constants of Pure Organic Compounds. vol. II, Elsevier Publishing Company, Inc., New York, N. Y., 1960.

13. Hale, D. V.; Hoover, M. J.; and O' Neill, M. J.: Phase Change Materials Handbook. Lockheed Missiles and Space Company, NASA Report CR-61363, September, 1971.

14. Phillips Petroleum Company: Reference Data for Hydrocarbons and Petro-Sulfur Compounds. Special Products Division, Bartlesville, Oklahoma, 1972.

15. Elliott, R. G.; Paoletti, C. J.; and Britt, M. A.: Lunar Roving Vehicle Thermal Control System. ASME Inter-Society EC/LSS Conference, August, 1972.

16. Rayleigh, Lord: On Connection Currents in a Horizontal Layer of Fluid, When the Higher Temperature is on the Under Side. Phil. Mag. and Journal of Science, vol. 32, no. 192, December 1916.

17. Knudsen, J. G.; and Katz, D. L.: Fluid Dynamics and Heat Transfer. McGraw-Hill Book Co., Inc., New York, N. Y., 1958.

18. Schmidt, E.; and Silveston, P. L.: Natural Convection in Horizontal Fluid Layers. Chemical Engineering Progress Symposium Series, vol. 55, no. 29, 1959.

19. Glober, S.; and Dropkin, D.: Natural-Convection Heat Transfer in Liquids Confined by Two Horizontal Plates and Heated From Below. Journal of Heat Transfer, vol. 81, 1959.

20. Silveston, P. L.: Warmedurchgarg in Waagerechten Flussigkeitsschichten," Part 1, Forsch Ing. Wes.; vol. 24, 1958.

21. Edwards, D. K.: Suppression of Cellular Convection by Lateral Walls. Journal of Heat Transfer, ASME, Series C, vol. 91, no. 1, February, 1969, pp. 145-150.

22. Sammuels, M. R.; and Churchill, S. W.: Stability of a Fluid in a Rectangular Region Heated from Below. AICHE Journal, vol. 13, no. 1, 1967, pp. 77-85.

23. Davis, S. H.: Convection in a Box, Linear Theory, Journal of Fluid Mechanics, vol. 30, part 3, 1967, pp. 465-478.

24. Sun, W.M.; and Edwards, D. K.: Natural Convection in Cells with Finite Conducting Wide Walls Heated from Below. Heat Transfer, Fourth International Heat Transfer Conference, vol. 4, paper NC 23, Elsevier Publishing Co., Amsterdam, 1970, pp. 1-11.

25. Ostrach, S.; and Pmueli, D.: The Thermal Instability of Completely Confined Fluids Inside Some Particular Configurations. Journal of Heat Transfer, Trans. ASME, vol. 4, series c, November, 1963, pp. 346-354.

26. Sherman, M.; and Ostrach, S.: Lower Bounds to the Critical Rayleigh Number in Completely Confined Regions. Journal of Applied Mechanics, Trans. ASME, vol. 34, series E, no. 2, June 1967, pp. 308-312.

27. Catton, I.; and Edwards, D. K.: Effect of Side Walls on Natural Convection Between Horizontal Plates Heated from Below. Journal of Heat Transfer, Trans. ASME, vol. 80, series c, no. 4, November, 1967, pp. 295-299.

28. Heitz, W. L.; and Westwater, J. W.: Critical Rayleigh Numbers for Natural Convection of Water Confined in Square Cells with L/D from 0.5 to 8. Journal of Heat Transfer, Trans. ASME, May, 1971, pp. 188-196.

29. Gershuni, G. Z.; and Zhuklovitskii, E. M.: Convection Instability of Horizontal Fluid Layers Bounded by Thermal Interaction. PPM, vol. 32, no. 3, 1968.

30. O' Toole, J. L.; and Silveston, P. L. : Correlation of Convective Heat Transfer in Confined Horizontal Layers. Chemical Engineering Progress Symposium Series, vol. 57, no. 32, 1961.

31. Edwards, D. K.; and Catton, I.: Prediction of Heat Transfer in Liquids Confined by Two Horizontal Plates and Heated From Below. Journal of Heat Transfer, vol. 81, 1959.

32. Bénard, H.: Les Tourbillion Cellulaires Dans Une Nappe Liquide Transport-Aut de La chaleur Par Convection in Régime Permanent. Ann. Chem. Phy., vol. 23, 1901, pp. 62-144.

33. Block, M. J.: Surface Tension as the Cause of Bénard Cells and Surface Deformation in a Liquid Film. Nature, vol. 178, September, 1956.

34. Pearson, J. R. A.: On Convection Induced by Surface Tension. Journal of Fluid Mechanics, vol. 4, 1958.

35. Scriven, L. E.; and Sternling, C. V.: The Marangoni Effects. Nature, vol. 187, July, 1960.

36. Sternling, C. V.; and Scriven, L. E.: Interfacial Turbulence; Hydrodynamic instability and the Marangoni Effect. American Institute of Chemical Engineers Journal, December, 1956.

37. Marangoni, C. S. M.: Il Nuovo Cimento Journal, Series 2.516 1872, p. 239.

38. Young N. O.; Goldstein, J. S.; and Block, M. J.: "The Motion of Bubbles in a Vertical Temperature Gradient." Jour. of Fluid Mechanics, vol. 6, 1959.

39. Gambrill, W. R.: Surface Tension for Pure Liquids. Chem. Eng., April, 1958.

40. Hershey, A. V.: The Physical Review, vol. 56, 1939, p. 204.

41. McGrew, J. L.; and Larkin, B. K.: Cryogenic Liquid Experiments in Orbit — vol. III Bubble Mechanics. Boiling Heat Transfer and Propellant Tank Venting in a Zero Gravity Environment, NASA Report CR 652, December, 1966.

42. Nields, D. A.: Surface Tension and Buoyance Effects in Cellular Convection. Journal of Fluid Mechanics, vol. 19, 1964.

43. Grodzka, P. G.: Zero Gravity Solidification. Lockheed Final Report D148619, NASA Contract NAS8-21123, March, 1970.

44. Tien, R. H.; and Koump, V.: Effect of Density Change on the Solidification of Alloys. ASME Journal of Heat Transfer, February 1970, pp. 11-16.

45. Bannister, T. C.: Heat Flow and Convection Demonstration (Apollo 14). Marshall Space Flight Center Internal Report, July 1971.

46. Grodzka, P. G.; Fan, C.; and Hedden, R. O.: The Apollo 14 Heat Flow Convection Demonstration Experiments — Final Results of Data Analysis. Lockheed Missiles and Space Company Report D225333, NASA Contract NAS8-25577, September 1971.

47. Altman, M.; Ross, D. P.; and Chang, H.: The Prediction of Transient Heat Transfer Performance of Thermal Energy Storage Devices.

48. Fixler, S. Z.:"Passive Thermal Control by Phase Change Material." Space Aeronautics, February 1966.

49. Leatherman, R. A.: Component Thermal Control Via Heat of Fusion Radiator. ASME, 63-AHGT-12, March 1963.

50. Kaye, J.; Fand, R. M.; Nance, W. G.; and Nickerson, R. J.: Final Report on Heat-Storage Cooling of Electronic Equipment. WADC TR 56-473, February 1957.

51. Golden, J. O.; and Stermole, A.: A Microscopic and Thermal Study of the Solidfication of Hexodecane. Annual Summary Report No. 1, NAS8-30511, Colorado School of Mines, Golden, Colorado, December 1969.

52. Bannister, T. C.; and Richards, B. E.: Microscopic Observations of Interfacial Phenomena. AIAA Paper No. 69-95, AIAA 7th Aerospace Sciences Meeting, New York, N. Y., January 1969.

53. Thomas, L. J.; and Westwater, J. W.: Microscopic Study of Solid-Liquid Interfaces During Melting and Freezing. Chemical Engineering Prog. Symposium Series, vol. 59, no. 41, 1963.

54. Hahn, H.: Mushroom Co-Op Finds Thaw Indicator Big Asset in Building Sales. Quick Frozen Foods Magazine, November 1971.

55. Telkes, M.: "A Review of Solar House Heating," Heating and Ventilation, no. 46, September 1949, pp. 68-75.

56. Telkes, M.: "Storing Heat in Chemicals." Heating and Ventilation, no. 46, November 1946, pp. 79-86.

57. Telkes, M.; Space Heating with Solar Energy. "Proceedings of United Nations Scientific Conference on the Conservation and Utilization of Resources, no. 3, 1951, pp. 215-222.

58. Schafer, C. F.; and Bannister, T. C.: Pegasus Thermal Control Coating Experiment. AIAA Paper No. 66-419, 1966.

59. Elliott, R. G.; Paoletti, C. J.; and Britt, M.A.: Lunar Roving Vehicle Thermal Control System. ASME Intersociety Conference, 1972.

60. McDonnel Douglas Company (Eastern Division): Study of Structural Active Cooling and Heat Sink Systems for Shuttle. First Quarterly Progress Report, MDC-E0479, October, 1971.

61. Shelden, B. G.; and Golden, J. O.: Development of a Phase Change Thermal Control Device. AIAA Paper 72-287, April, 1972.

62. Vaselou, K. Y.; Kalisheva, L. U.; and Telepin, M. L.: Using Phase Transitions to Improve Thermostatic Control of Instruments. NAS Tech. Trans. NASA TTF-467, May, 1, 1967.

63. Bird, R.B.; Stewart, W. E.; and Lightfoot, E. N.: Transport Phenomena. Third Edition, John Wiley and Sons, Inc., New York, N.Y., 1963.

64. Stefan, J.: Uber Die Theorie Der Eisbildung Insebesondere Uber Die Eis-building in Polarmaere. Annalen Physik und Chemie, N. F., vol. 42, 1891.

65. Neumann, F.: "Die Partiellen Differentialgleichungen Der Mathematischen Physik." Lecture Notes, 1860's.

66. Carslaw, H. S.; and Jaeger, J. C.: Conduction of Heat in Solids. Second Edition, Oxford Press (London), 1959.

67. Muehlbauer, J. C.; and Sunderland, J. E.: Heat Conduction with Freezing or Melting. Applied Mechanics Review, vol. 18, no. 12, December 1965, pp. 951-955.

68. Sunderland, J. E.; Bailey, J. A.; and Liao, C.: Thermal Capacitor Design Rationale. NASA Cooperative Agreement with North Carolina State University, Interim Report No. 1, August, 1972

69. Sharma, O. P.; Rotenberg, M.; and Penner, S. S.: Phase Change Problems, with Variable Surface Temperatures. AIAA Journal, vol. I, no. 4, pp. 677-682, 1967.

70. Tien, C.; and Yen, Y. C.: Appoximate Solution of a Melting Problem with Natural Convection. Chem. Engr. Progress, Symposium Series, vol. 62, no. 64, 1966.

71. Bain, R. L.; Stermole, F. J.; and Golden, J. O.: The Effect of Gravity Induced Free Convection upon the Melting Phenomena of a Finite Paraffin Slab for Thermal Control, Colorado School of Mines, Annual Report No. 1, NASA Contract NAS 8-30511, June 1971.

72. White, S. P.; Golden, J. O.; and Stermole, F. J.: An Experimental and Theoretical Evaluation of Increased Thermal Diffusivity Phase Change Device. Colorado School of Mines Report CSM-CPR-R472, Golden, Colorado, Summary Report, NASA Contract NAS 8-30511, January 1972.

73. Pujado, P. R.: Melting of a Finite Paraffin Slab. Thesis No. NDT-1215, Colorado School of Mines, Golden, Colorado, 1968.

74. Ukanwa, A. O.; Stermole, F. J.; and Golden, J. O.: Phase Change Solidifications Phenomena for Thermal Control, Colorado School of Mines, Golden Colorado, Annual Report, NASA Contract NAS 8-30511, December, 1969.

75. Rathjen, K. A.; and Jiji, L. M.: Heat Conduction with Melting or Freezing in a Corner . Trans of ASME, Journal of Heat Transfer, February, 1971.

76. Boger, J. W.: The Effects of Bouyance Forces on the Melting and Freezing Process. PHD Thesis, University of Illinois, 1966.

77. Chrysler Corporation: Chrysler Improved Numerical Differencing Analyzer-CINDA. Chrysler Technical Note TN-AP-66-15, 1968.

78. Griggs, E. I.: A Study of the Heat Transfer Characteristics of a PCM Thermal Capacitor. First Progress Report, Cooperative Agreement with NASA/MSFC, Tennessee Technological University, March, 1971.

79. Jones, G. D.; and Smith, L. F.: Optimum Arrangement of Rectangular Fins on Horizontal Surfaces for Free Convection Heat Transfer. Journal of Heat Transfer, vol. 7, February, 1970.

80. Defay, R; Prigogine, R. ; Bellemaus, A.; and Everett, D. H.: Surface Tension and Absorption. John Wiley and Sons, New York, N. Y., 1966.

81. Reynolds, W. C.; Saad, M. A.; and Satterlee, H. M.: Capillary Hydrostatics and Hydrodynamics at Low g. National Science Foundation Technical Report LG-3, September, 1964

82. Schaerer, A. A.; Basso, C. J.; Smith, A. E.; and Skinner, L. B.: Properties of Pure Normal Alkanes in the C_{17} to C_{36} Range. Chemical Society, 77, 1955.

☆ U.S. GOVERNMENT PRINTING OFFICE: 1974—739-162/146